Effects of Pressure and Dissolved Carbon Dioxide on the Rheological Properties of Molten Polymers

By

Hee Eon Park

Department of Chemical Engineering

McGill University, Montreal

May 2005

A thesis submitted to McGill University in partial fulfilment of the requirements of the degree of Doctor of Philosophy

Your file Votre référence
ISBN: 978-0-494-21686-6
Our file Notre référence
ISBN: 978-0-494-21686-6

Dedicated to my father, H.D. Park (1945-2004).

아버님 영전에 부족한 저의 졸업논문을 바칩니다.

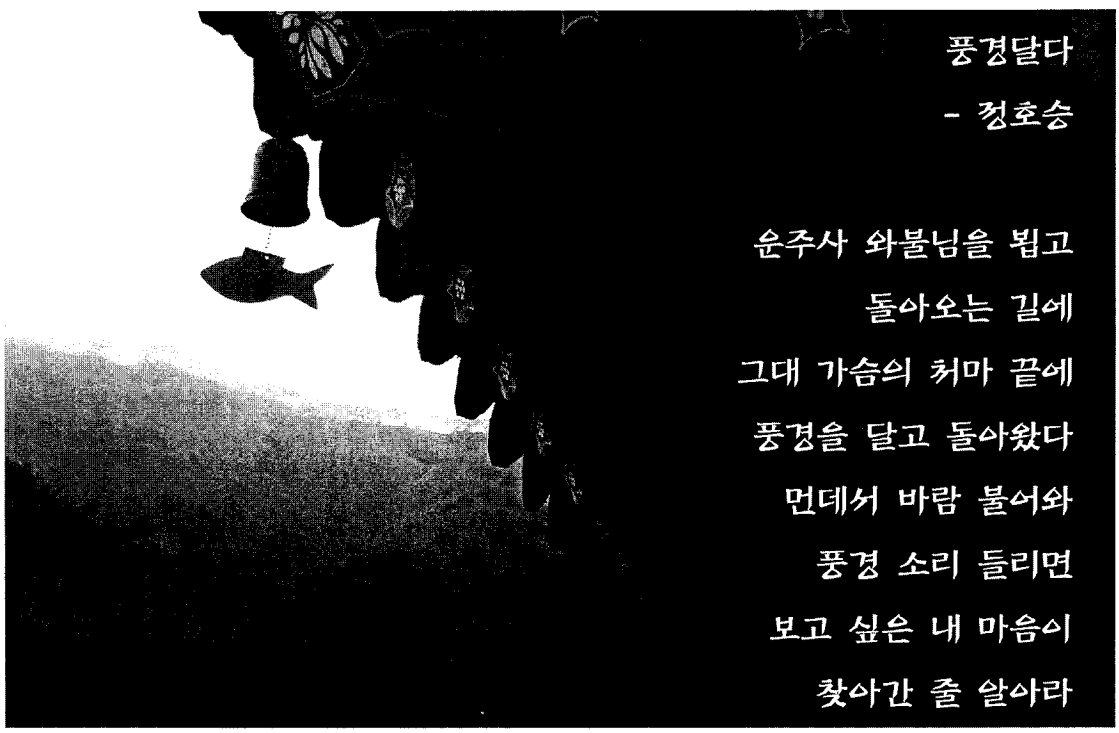

Abstract

Supercritical carbon dioxide (SC-CO_2) is used as a physical blowing agent in the manufacture of plastic foam and as a plasticizer to reduce melt viscosity during processing. Pressure is also an important variable for processing, and the combined effects of dissolved SC-CO_2 and pressure on rheological properties must be known to achieve optimum processing conditions. However, until recently there was no method to measure these effects accurately. A high-pressure sliding plate rheometer in which the shear rate, temperature, pressure, and CO_2 concentration are uniform, was used in the present study. The effects of CO_2 and pressure on the viscosity, stress growth function, and creep compliance of a high density polyethylene (HDPE) were determined. To separate the effects of pressure and CO_2, samples were first pressurized without CO_2, and then pressurized and saturated with CO_2. It was possible to use shift factors for pressure and CO_2 concentration to obtain a master curve. For the purpose of comparison, the effect of nitrogen on the viscosity is also determine. Another important concern in plastics processing is molecular structure, which has a strong effect on melt flow properties. The effects of long- and short-chain branching and side groups on the pressure sensitivity of viscosity were also determined in this project.

Résumé

Le carbone dioxyde supercritique (SC-CO_2) est utilisé comme agent physique d'expansion dans la manufacture de mousses plastiques et comme plastifiant pour réduire la viscosité à l'état fondu durant le traitement. La pression est aussi une variableimportante pour la transformation, et les effets combinés du SC-CO_2 dissout et de la pression sur les propriétés rhéologiques doivent être connu pour obtenir des conditions de traitements optimales. Cependant, jusqu'à récemment il n'y avait pas de méthode pour mesurer ces effets de façon précise. Un rhéomètre àplaque glissante haute pression,dans laquelle la température, la pression, et la concentration en CO_2 sont uniformes a été utilisé dans cette étude. Les effets du CO_2 et de la pression sur la viscosité, la fonction d'augmentation du stress, conformité de rampement, du polyéthylène à haute densité (HDPE) ont été déterminés. Pour séparer les effets du a la pression et au CO_2, des échantillons ont été d'abord pressurisé sans CO_2, et ensuite pressurisé et saturé en CO_2. Il a été possible d'utiliser des facteurs de glissement pour la pression et la concentration en CO_2 pour obtenir une courbe maîtresse. Un autre point important dans le traitement des plastiques est la structure moléculaire, qui a e un important effets sur les propriétés d'écoulement. Les effets de branchage des longues et courtes chaînes et des groupes latéraux sur la sensibilité à la pression de la viscosité on aussi été déterminé au cours de ce projet.

Acknowledgement

It is my greatest honor to express appreciation to my mentor Prof. John M. Dealy. His full support, including advice for academic research, patience, concerns, understanding, financial support, and opportunity for research, is too valuable for words.

I would like to express my thank to Mr. Charles Dolan, who helped me take care of mechanical tasks. Special thanks must go to Prof. M.R. Kamal and Nitin Borse, who allowed me to access the *PVT* apparatus and training on the instrument. I also highly thank Prof. Park and Guangming Li at University of Toronto for letting me use of the MSB instrument and training on this device. I show my appreciation to Mr. Yoshito Sasaki at Japan Polyolefins Co., who supplied HDPE.

I would like to thank Alan Gagnon and Lou Cusmich for their prompt support concerning mechanical or electrical situations. I also appreciate the cooperation of Ms. H. Campbell for SEM images and Hyuk Ho Shin for optical microscopy images. I appreciate Dr. Stewart McGlashan, Dr. Francois Koran, and Dr. Frank Bubic for their advice on the high-pressure sliding plate rheometer.

I would like to show my thank to Prof. Paula Wood-Adams for giving me precious suggestions, criticism, and encouragement. I am also grateful to my former and present laboratory fellows, Dr. Seungoh Kim, Dr. Stéphane Costeux, Dr. Benoît Blottière, Dr. Sung Taek Lim, Chunxia He, Siripon Anantawaraskul, Yufeng Ye, Junke Xu, Nan Nan Liu, Miguel Baqueiro, Fabricio Smillo, Matthew Campbell, Jen Tiang, and Michelle Si Wan Li, for their academic advice, and it has been a great time and experience to work and stay with them. Specially, I am indebted to Dr. Sung Taek Lim for our collaboration. He suggested many

solutions to setbacks in this research, and his academic advice was priceless. I would also like to specially thank Dr. Seungoh Kim for training on DSC measurements and advice on not only thermodynamics but also personal life and Jen Tiang for his help for my thermodynamic study.

I would also like to thank professors at Pohang University of Science and Technology for their encouragement and advice. Profs. Young Gul Kim, Kyung Hee Lee, Sun Bok Lee, and Jong Moon Park always encouraged me to pursue my studies and helped me pick up valuable information. Prof. In-Sik Nam, who was my Bachelor thesis supervisor, not only consulted with me about my future but also has gave me a bill for my future haircut, and I keep the bill as a kind of a charm against evils. Prof. Jin Kon Kim, who is the research director in the Polymer Nano-Rheology Lab, gave me a lot of information regarding rheology studies.

I would also like to thank alumni from POSTECH who provided me with lots of scientific documents and books. Jeongman The-Man Son, who was a graduate student in the Polymer Nano-Rheology Lab, never complained about my endless requests. The wonderful retrospections with Woosung Adrian Jung have greatly stimulated me. Great memories, which will ever last, shared with Sunyoung Bbox Park have been powerful driving force for my work and life. The fantastic time with Minseok Song, Yong-Woo Shin, and Jiyoung Na also has been a big solace. Daehyun Park, who was my last roommate at POSTECH, assisted me a lot. Hyejin Kim, who always shows an active attitude to everything, promoted my diligence. Sangsook Cecily Kim and Hyunmi Timy Baek also offered my needs so many times, and the wonderful time with them will be unforgettable.

Finally, I must thank my ancestor for giving me life. Undoubtedly my ultimate thanks must go to my family: my parents, brother, sister-in-law, nephew, and my wife, Sujn Oh. Without them, I could not even exist and finish my Ph.D. work.

Table of Contents

List of Figures

Chapter 1. Introduction

Chapter 2. Pressure-Volume-Temperature Behavior of HDPE

Chapter 3. Solubility of CO_2 and Swollen Volume of HDPE

Chapter 4. Previous Work on the Effects of Temperature, Pressure and Concentration

Chapter 5. Rotational Rheometry

Chapter 6. Effects of Pressure, Temperature, and Concentration on Rheological Properties

Chapter 7. Effect of Molecular Structure on Temperature and Pressure Sensitivity of Viscosity

Appendices

List of Tables

Chapter 7. Effect of Molecular Structure on Temperature and Pressure Sensitivity of Viscosity

Appendices

1. Introduction

1.1 Motivations

Supercritical (SC) fluids have been evaluated as solvents and extraction agents in the food, pharmaceutical, and chemical industries [1-10] and are also used in the plastics industry [11-15]. In particular, supercritical carbon dioxide (CO_2) has been used as a physical blowing agent in plastic foam production and as a plasticizer to reduce melt viscosity for melt processing. Since elevated pressures are involved in plastics forming processes, the combined effects of dissolved SC-CO_2 and pressure on rheological properties must be known to achieve optimum processing conditions. Data reported previously were obtained using capillary or slit rheometers, and the temperature, pressure, and shear rate are not uniform in these instruments.

A high-pressure sliding plate rheometer (HPSPR) was modified and used in the present study. In this instrument the temperature, pressure, CO_2 concentration, and shear rate are all uniform. It is thus possible to generate a simple shear flow in which the hydrostatic pressure and CO_2 concentration can be controlled independently of the shear rate. The shear stress is measured using a shear stress transducer, which senses the stress in the center of the sample so that edge effects are not a problem.

Another important concern in plastic processing industry is molecular structure, since the structure has a strong effect on flow properties. The effect of short- and long-chain branching and a benzene side group on the temperature and pressure sensitivity of the viscosity were also studied in this project.

1.2 Objectives

The overall objective of this research was:

1. To determine the effects of pressure and dissolved CO_2 on rheological properties.

To achieve this objective, the following sub-objectives were established:

1.1. To develop a technique to study the effect of dissolved CO_2 on the

rheological behavior of molten plastics.

1.2. To determine pressure-volume-temperature (*PVT*) behavior of a high density polyethylene (HDPE), CO_2, and HDPE/CO_2 mixture.

1.3. To determine the solubility of CO_2 in HDPE.

A secondary objective was:

2. To determine the effects of molecular structure on the temperature and pressure sensitivity of the viscosity.

1.3 Organization of the Thesis

The various chapters describe the methods used to achieve the objectives.

Chapter 2: The *PVT* behavior of HDPE was determined in order to (1) interpret the CO_2 solubility data and (2) ensure that HDPE is in molten state at all the pressures used. The data were fitted to the Tait and the Sanchez-Lacombe equations. The *PVT* data were also used (3) to determine the vertical shift factor for density.

Chapter 3: The solubility of CO_2 in HDPE was determined by use of a magnetic suspension balance. To interpret the data and to determine the swollen volume of HDPE, a simulation was carried out using the Sanchez-Lacombe equation along with data. The vertical shift factor for concentration [1] was determined.

Chapter 4: This chapter summarizes previous work on the effects of temperature, pressure, and concentration of dissolved CO_2 on rheological properties.

Chapter 5: Two rotational rheometers were used to determine (1) dependency of test results on fixture geometry and gap, (2) thermal stability, (3) zero-

1) Two types of concentrations are used in this thesis. One is that of CO_2 in polymer/CO_2 mixture, and the other is that of polymer in the mixture. A variable simply C stands for the concentration of CO_2, and C_{pol} is that of polymer. A horizontal concentration shift factor a_C is conventionally expressed as a function of concentration of CO_2, because the amount of gas is a controlled variable in a process with gas. A vertical concentration shift factor b_C is commonly shown as a function of concentration of polymer, because this factor is to describe the density change of polymer due to dissolved gas.

shear viscosity, (4) the range of shear-rates for the determination of viscosity, (5) the effect of temperature on the linear [2] viscoelastic (LVE) properties, and (6) the need for a vertical shift factor.

Chapter 6: Development of a new technique to determine the effects of pressure and CO_2 on the rheological properties of HDPE. The following issues are addressed: (1) reproducibility, (2) effects of pressure and CO_2 on the viscosity, stress growth function and the creep compliance, (3) need for a vertical shift factor, (4) comparison of the temperature shift factor from steady simple-shear tests with that from dynamic experiments (LVE), and (5) comparison of the viscosity with the complex viscosity.

Chapter 7: Four polyethylenes, two polystyrenes, and one polypropylene were used to determine the effects of molecular structure on the temperature and pressure dependence of the viscosity as well as the relative influence of temperature and pressure. The structural features examined were short- and long-chain branching and benzene side group.

1.4 Materials Studied

1.4.1 High Density Polyethylene

A high-density polyethylene was chosen due to its simple chemical structure. The HDPE was provided by Japan Polyolefins (formerly Nippon Petrochemicals) and is a general-purpose film resin. The same material has been previously studied by Sato *et al.* [16], who reported the solubility and diffusion coefficient for CO_2 in this HDPE. A Mettler Toledo AB204 Balance was used to determine the density of the HDPE. Appendix 1 describes the procedure used. The melting/crystallization temperatures

2) In this thesis, the term "linear" is used to indicate (1) a polymer molecule having no long-chain branching, (2) that the viscosity is independent of shear rate, and Boltzmann superposition principle can be applied, (3) that regression of curve fitting involves a linear model, which is linear in the parameters, (4) that a line on a plot is straight, *i.e.* a function is linear, and (5) swelling in one direction.

were determined at 1 atm by use of a Perkin Elmer Pyris 1 Differential Scanning Calorimeter (DSC) with a heating/cooling rate of 10℃/min. Two melting temperatures were identified, one ($T_{m,h}$) from the peak in the endothermic curve and the other ($T_{m,e}$) from the end of the peak (Fig. 1.1). Crystallization temperatures were defined in the same manner. The physical properties of the HDPE are summarized in Table 1.1. The polymers used for the molecular structure study are described in Chapter 7.

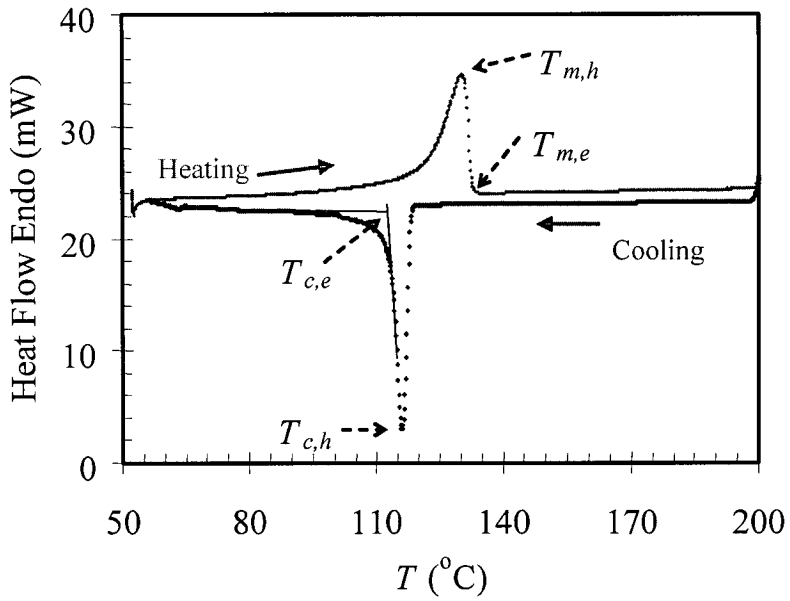

Figure 1.1. Endothermic DSC curve of HDPE.

Table 1.1. Physical properties of HDPE.

Code	Grade name	Density	M_w (kg/mol) [16]	M_w/M_n [16]	$T_{m,h}$ (℃)	$T_{m,e}$ (℃)	$T_{c,e}$ (℃)	$T_{c,h}$ (℃)
HDPE	J-Rex HD KF251A	0.945	111	13.6	130.5	134.4	113.1	115.7

1.4.2 Supercritical Fluid and Carbon Dioxide

A compound that is gaseous at atmospheric pressure and room temperature shows

supercritical behavior when heated and compressed above its critical temperature (T_c) and pressure (P_c) (Fig. 1.2 [17-19]). The physical properties of a supercritical fluid (SCF) are between those of a gas and a liquid. The solubility and density of a SCF are higher than those of a gas, and its diffusion coefficient is higher than that of a liquid. Due to these characteristics, SCFs have applications in extraction and separation.

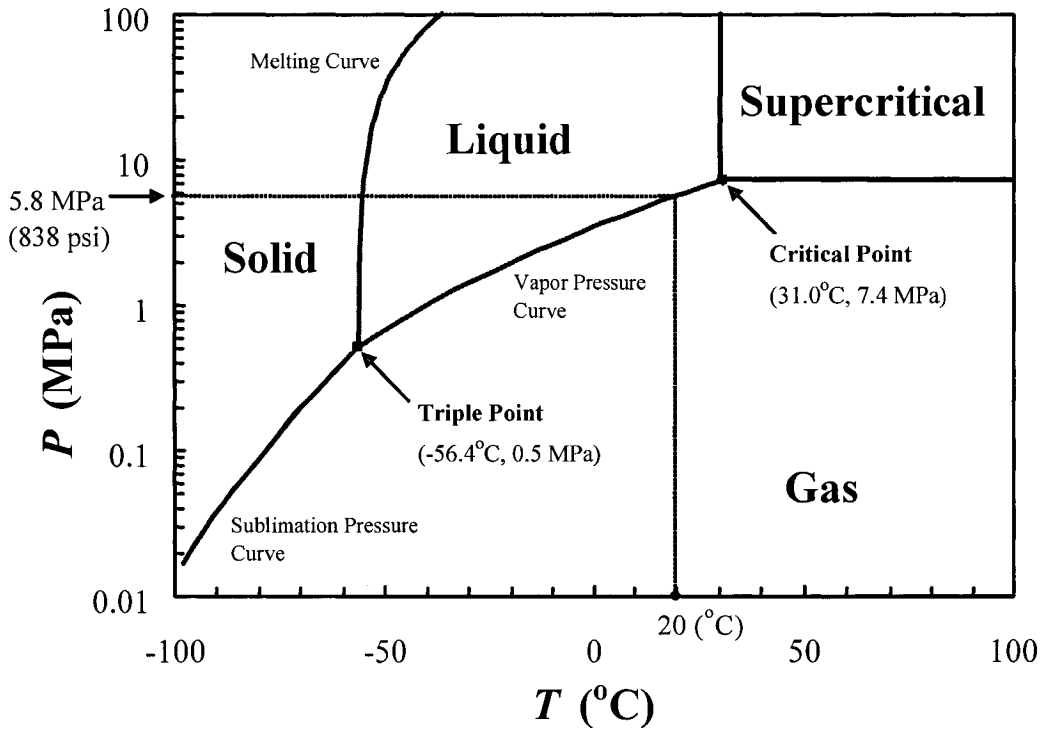

Figure 1.2. Pressure-temperature phase diagram for CO_2 [17-19].

Supercritical fluids have the following characteristics:

- The diffusion rate is higher than those of common liquids, which have similar density, by two orders of magnitude (Fig. 1.3).
- The viscosity is lower than those of common liquids, which have similar density, by an order of magnitude (Fig. 1.4).
- Solubility in a polymer can be controlled by changing the temperature or pressure.
- It is easily removed from solution by decompression or heating.

Table 1.2 [19] provides data for several compounds that have critical properties of potential interest in the polymer industry.

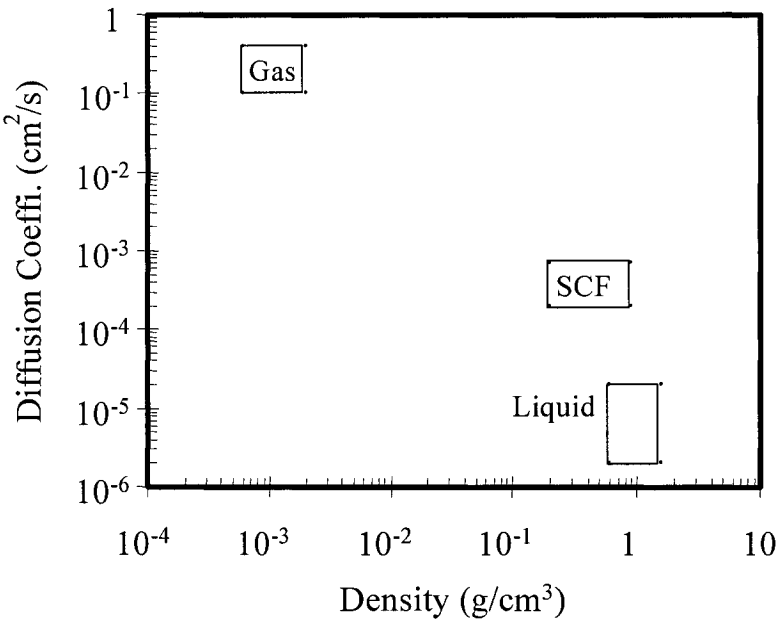

Figure 1.3. Ranges of diffusion coefficients versus density for three physical states. A box shows the range of properties.

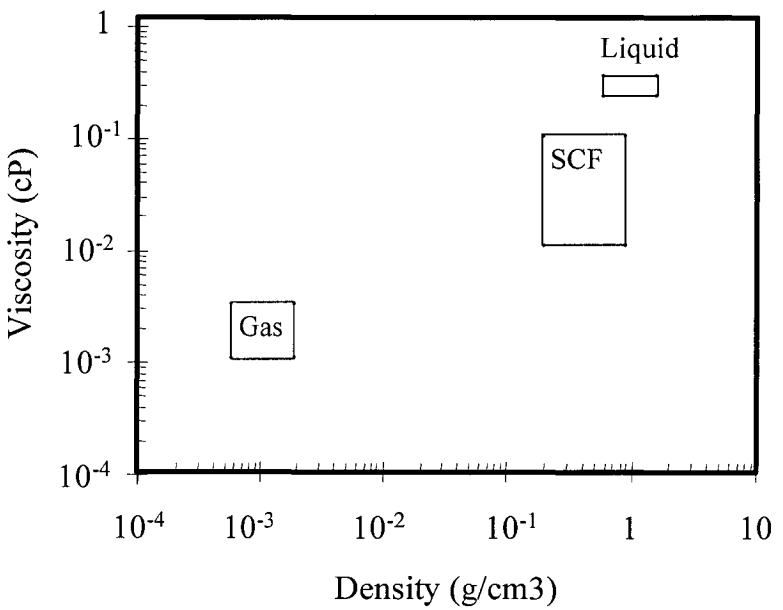

Figure 1.4. Ranges of viscosity and density for three physical states. A box shows the range of properties.

Table 1.2. Critical properties of selected fluids [19].

	T_c (℃)	P_c (MPa)	v_c (cm^3/mol)		T_c (℃)	P_c (MPa)	v_c (cm^3/mol)
He	-267.96	0.227	57	NH_3	132.35	11.35	72
H_2	-240.18	1.293	65	C_4H_8 (1-butane)	146.35	4.020	241
N_2	-146.94	3.39	90	SO_2	157.65	7.884	122
O_2	-118.56	5.043	73	CH_3OH	239.35	8.084	117
CH_4	-82.59	4.599	99	H_2O	373.99	22.06	56
Xe	16.62	5.841	118	CHF_3 (HFC-23)	25.83	4.82	133
CO_2	30.98	7.375	94	CH_2F_2 (HFC-32)	78.41	5.83	123
C_2H_6	32.18	4.872	146	CHF_2Cl (HCFC-22)	96.35	5.035	164
N_2O	36.42	7.255	97	CF_2Cl_2 (CFC-12)	111.8	41.36	217
C_3H_8	96.68	4.248	200	$CFCl_3$ (CFC-11)	197.95	4.47	247

It is known that a dissolved SCF reduces melt viscosity even at elevated pressures, and this makes it possible to process some polymers that are normally hard to process due to a high melt viscosity. For example an SCF can dissolve fluoropolymers that are insoluble in most solvents [20] except SCFs and chloro-fluorocarbons (CFCs). Releasing CFCs into the atmosphere has been found to enhance global warming and damage the ozone layer [21] (Appendix 2), and the Montreal Protocol (1987) and Copenhagen Amendment (1992) [22] mandated phaseout of the use of CFCs by 1996. Hydrogen and hydrocarbons are highly flammable, and their use requires special safety precautions. The global warming potential of hydrocarbons is higher than that of CO_2 (Appendix 2). Oxygen and

water cause or enhance the oxidation of processing equipment. Nitrous oxide (N_2O) has critical properties similar to those of CO_2 but has a small permanent dipole, while CO_2 has no dipole. Carbon dioxide can thus be used with non-polar polymers. Although methanol has a high solvent power, its flammability and high T_c limit its application to polymers. Ammonia (NH_3) is not desirable due to its corrosive and toxic properties. Nitrogen has much less solubility than that of CO_2, and this gives CO_2 an advantage for plastics applications, even though N_2 has a lower critical temperature and pressure. Carbon dioxide is also easy to obtain and remove, cheap, and nontoxic and causes no ozone depletion. For the above reasons, SC-CO_2 is a very attractive SCF for the polymer industry.

Unlike nonliquefied gases, of which critical temperatures are lower than room temperature, the maximum pressure in a CO_2 cylinder is only 5.8 MPa at 20℃ (Fig. 1.2), since CO_2 is a liquefied gas, of which critical temperature is higher than room temperature. To use CO_2 at elevated pressure; room temperature, a compressor or liquid pump is required. This will be discussed in detail in Section 6.4.4.1. A Coleman Instrument 99.99% grade (Matheson Gas Products) of CO_2 was used for solubility measurement, and a bone dry 99.80% grade (Matheson Gas Products) was used for viscosity and creep measurements.

Diffusion data are necessary to estimate the experimental saturation time, because all measurements can only be performed at saturation. The solubility is also required to describe the effect of CO_2 on the rheological properties in terms of its concentration in HDPE. Tables 1.3 and 1.4 show the diffusion coefficient and the solubility measured by Sato *et al.* [16] using the pressure decay method. However, the pressure range of their solubility data are limited, and solubility measurements were thus carried out at the higher pressures used in this study.

Table 1.3. Diffusion coefficient of CO_2 in HDPE at 180℃ [16].

Average weight fraction of CO_2 × 10^3	P (MPa)		Diffusion coefficient × 10^5 (cm^2/s)
	Initial	Final	
8.2	0.000	3.005	10.6
21	3.005	4.925	9.2
29	4.925	6.614	9.2
40	6.614	8.515	9.1
53	8.515	10.97	9.1
68	10.97	12.53	10.7
76	12.53	15.43	16.3

Table 1.4. Solubility of CO_2 in HDPE at 180℃ [16].

P (MPa)	Solubility (g-CO_2 / kg-HDPE)
7.055	35.0
11.326	67.1
14.013	89.0
15.762	100.5
16.896	109.4
18.123	119.8

1.5 References

1. J.M.L. Penninger, M. Radosz, M.A. McHug, and V.J. Krukonis, *Supercritical Fluid Technology*, Elsevier, Amsterdam, 1985.
2. T. Clifford, *Fundamentals of Supercritical Fluids*, Oxford Univ. Press, Oxford, 1999.
3. M.D.L. De Castro, M. Valcárcel, and M.T. Tena, *Analytical Supercritical Fluid Extraction*, Springer-Verlag, Berlin, 1994.
4. L.T. Taylor, *Supercritical Fluid Extraction*, John Wiley & Sons, New York, 1996.
5. M.A. McHugh and V.J. Krukonis, *Supercritical Fluid Extraction*, 2nd Ed., Elsevier, Amsterdam, 1994.
6. J.M. DeSimone and W. Tumas, *Green Chemistry Using Liquid and Supercritical Carbon Dioxid*, Oxford Univ. Press, Oxford, 2003.
7. J. McHardy and S.P. Sawan, *Supercritical Fluid Cleaning*, Noyes Pub., Westwood, 1998.
8. J.R. Dean, *Applications of Supercritical Fluids in Industrial Analysis*, Blackie Academic & Professional, London, 1993.
9. K.P. Johnston and J.M.L. Penninger, *Supercritical Fluid Science and Technology*, American Chemical Society, Washington, 1989.
10. J.M. DeSimone, "Practical Approaches to Green Solvents," *Science* 297:799 (2002).
11. D.L. Tomasko, H. Li, D. Liu, X. Han, M.J. Wingert, L.J. Lee, and K.W. Koelling, "A Review of CO_2 Applications in the Processing of Polymers," *Ind. Eng. Chem. Res.* 42:6431 (2003).
12. J.M. DeSimone, Z. Guan, and C.S. Elsbernd, "Synthesis of fluoropolymers in supercritical carbon dioxide," *Science* 257:945 (1992).
13. K.C. Khemani, *Polymeric Foams*, American Chemical Society, Washington, 1997.
14. A.H. Landrock, *Handbook of Plastic Foams*, Noyes Pub., Park Ridge, 1995.
15. K.T. Okamoto, *Microcellular Processing*, Hanser, Munich, 2003.
16. Y. Sato, K. Fujiwara, T. Takikawa, Sumarno, S. Takishima, and H. Masuoka, "Solubilities and diffusion coefficients of carbon dioxide and nitrogen in polypropylene, high-density polyethylene, and polystyrene under high pressures and temperatures," *Fluid Phase Equilibria* 162:261 (1999).
17. Thermodynamic Tables Project, *International Thermodynamics Tables of the Fluid State Carbon Dioxide*, Pergamon Press, Oxford, 1973.
18. K. Ražnjević, *Handbook of Thermodynamic Tables and Charts*, Hemisphere

Publishing Corp., Washington, 1976.

19. *CRC Handbook of Chemistry and Physics*, 81st Edition, CRC Press, Cleveland, 2000/2001.

20. L. Wall, "Fluoropolymers," in *High Polymers Ser.*, Vol. 25, Wiley-Interscience, New York, 1972.

21. S. Solomon, R.R. Carcia, F. Sherwood, and J. Wuebbles, "On the depletion of Antarctic ozone," *Nature* 321:755 (1986).

22. E.A. Parson, *Protecting the Ozone Layer*, Oxford University Press, Oxford, 2003.

2. Pressure-Volume-Temperature Behavior of HDPE

2.1 Introduction

Since the melting point T_m increases with pressure, to prevent pressure-induced crystallization, the high-pressure measurements must be carried out at temperatures well above the elevated T_m. The pressure dependencies of T_m must thus be known to establish the minimum operating temperature. These dependencies can be determined by carrying out pressure-volume-temperature (*PVT*) measurements. In addition, to determine the solubility of the gas in the polymer, the *PVT* behavior of pure polymer, pure gas, and the mixture are required. The *PVT* data of polymer can also be used to calculate the vertical shift factor for viscosity, which is often assumed to be one.

A Gnomix *PVT* apparatus was used to determine the *PVT* behavior of the polymer, and the data were fitted to the empirical Tait equation and the theoretical Sanchez-Lacombe equation.

2.2 Theory and Equations

Several models have been proposed to describe the *PVT* behavior of polymeric liquids. Equations of state for polymers are either empirical or theoretical. The most popular empirical equation is the Tait equation [1]. Theoretical models are at the molecular level and are of a statistical nature. Over several decades, theories based on lattice or hole concepts have been developed. These include the lattice theory of Flory [2] and Huggins [3], the cell model of Prigogine [4], the lattice fluid model of Sanchez and Lacombe[5-7] and Panayiotou and Vera [8], the modified cell theory of Dee and Walsh [9,10], the non-equilibrium lattice fluid (NEFL) model of Doghieri and Sarti [11], the group-contribution lattice fluid model of Parekh and Danner [12], and the lattice hole theory of Simha and Somcynsky [13,14].

More recently, so-called integral equation theories have been developed. In these theories, a property is expressed as a sum of contributions from repulsion, attraction,

and chain structure. Numerous models have been obtained by modifying previous models; these include the thermodynamic perturbation theory (TPT) of Wertheim [15-18], the statistical associating fluid theory (SAFT) of Chapman *et al.* [19,20], the modified SAFT model of Huang and Radosz [21,22], and the perturbed hard-sphere chain (PHSC) theory of Song *et al.* [23]. The SAFT model has attracted much attention and has been used in hundreds of articles published in the past 15 years.

Most theoretical models: (1) describe mixtures by using mixing rules for the parameters without changing the basic structure of the model, and (2) make use of reduced variables scaled by characteristic parameters. Zoller [24], Cho and Sanchez [25], and Rodgers [26] have reviewed work on the *PVT* behavior of polymers and compared the predictions of the various models.

Rodgers [26] reviewed *PVT* models for molten polymers and performed model fitting for published *PVT* data. He also fitted *PVT* data published by Hellwege *et al.* [27] for a HDPE. He used a HDPE different from the one used here, but a major difference in parameters is not expected, and his fitting parameters were used as initial estimates for this work.

2.2.1 The Tait Equation

Tait [28] proposed an empirical model of average isothermal compressibility for fresh and sea water as follows:

$$-\frac{1}{v(P_0,T)}\frac{v(P,T)-v(P_0,T)}{P}=\frac{C(T)}{B(T)+P} \tag{2.1}$$

or

$$v(P,T)=v(P_0,T)\left[\frac{B(T)+P-PC(T)}{B(T)+P}\right] \tag{2.2}$$

where P_0 is the initial pressure, and $v(P_0,T)$, $B(T)$, and $C(T)$ are functions of

temperature only. Wohl [1] used the right-hand side of Eq. 2.1 but used another definition of the compressibility as follows:

$$-\frac{1}{v(P_0, T)}\left[\frac{\partial v(P, T)}{\partial P}\right]_T = \frac{C(T)}{B(T)+P} \tag{2.3}$$

and integrated Eq. 2.3 as:

$$-\frac{1}{v(P_0, T)}\int_{v(P_0, T)}^{v(P, T)} dv(P, T) = \int_{P_0}^{P} \frac{C(T)}{B(T)+P} dP \tag{2.4}$$

to give Eq. 2.5:

$$v(P, T) = v(P_0, T)\left\{1 - C(T)\ln\left[1+\frac{P-P_0}{B(T)+P_0}\right]\right\} \tag{2.5}$$

By letting P_0 zero, Eq. 2.5 is reduced to Eq. 2.6 [1]:

$$v(P, T) = v(0, T)\left\{1 - C(T)\ln\left[1+\frac{P}{B(T)}\right]\right\} \tag{2.6}$$

where the zero-pressure isotherm is

$$v(0, T) = v_0 + v_1 T \tag{2.7}$$

where v_0 and v_1 are constants, and $B(T)$ is given by

$$B(T) = B_0 e^{-B_1 T} \tag{2.8}$$

where B_0 and B_1 are constants. Cutler *et al.* [29] found that $C(T)$ is a universal value of 0.0894 for high molecular weight hydrocarbons investigated and is independent of temperature. Equation 2.6 can thus be reduced to Eq. 2.9:

1) This equation is different from the original Tait model (Eq. 2.2). Strictly speaking, this is the Wohl model or the Tait-Wohl model, but it has been called the Tait model.

$$v(P,T)=v(0,T)\left\{1-0.0894\ln\left[1+\frac{P}{B(T)}\right]\right\} \tag{2.9}$$

and Eq. 2.9 has been very widely used to describe the *PVT* behavior of polymers. Its major advantage is its simplicity, which reduces calculation time. Equation 2.9 was used to describe the *PVT* behavior of pure HDPE for this study.

2.2.2 Sanchez-Lacombe Model

It has been found that the empirical Tait model makes better predictions than theoretical models. However, a theoretical model is required to predict the specific volume of a mixture to obtain the solubility of CO_2, because mixing rules for the parameters are available only for such models. For this study, the Sanchez-Lacombe (S-L) model was chosen, since it has a simple structure and has been used to describe the solubility of CO_2 [30-32].

The S-L model can be expressed as follows in terms of reduced variables:

$$\tilde{P}=-\tilde{\rho}^2-\tilde{T}\left[\ln(1-\tilde{\rho})+\left(1-\frac{1}{r}\tilde{\rho}\right)\right] \tag{2.10}$$

where $\tilde{T}\equiv T/T^*$, $\tilde{P}\equiv P/P^*$, and $\tilde{\rho}\equiv\rho/\rho^*$. The characteristic values are $T^*\equiv\epsilon^*/R$, $P^*\equiv\epsilon^*/v^*$, and $\rho^*\equiv M/(rv^*)$. The close-packed mer[2] volume is $v^*\equiv RT^*/P^*$, and ϵ^* is the interaction energy. The number of mers per molecule, *i.e.*, the number of lattice sites occupied by a molecule is $r=M/(v^*\rho^*)=MP^*/(RT^*\rho^*)$, where M is the molecular weight. Either (ϵ^*,r,v^*) or (T^*,P^*,ρ^*) is determined by curve fitting.

2.3 Experiments

2.3.1 *PVT* Apparatus

A Gnomix *PVT* apparatus [33] (Fig. 2.1) was used to determine the *PVT* behavior

2) In lattice fluid theory, a molecule occupying r-sites is called an r-mer, because the part occupying one site is called a mer.

of HDPE. This instrument is the most popular *PVT* apparatus for polymers. It has a high-pressure dilatometer with a bellows and a linear variable differential transformer (LVDT) and is used to measure the change in volume of a solid or molten sample in the temperature range from 30 to 400℃ and at pressures between 10 and 200 MPa. The volume change at a temperature lower than 30℃ or pressure lower than 10 MPa must be determined by extrapolation. This instrument consists of four parts: (1) temperature and pressure controllers, (2) heating and pressurizing elements, (3) a thermocouple, pressure transducers, and the LVDT, and (4) a piezometer cell and bellows.

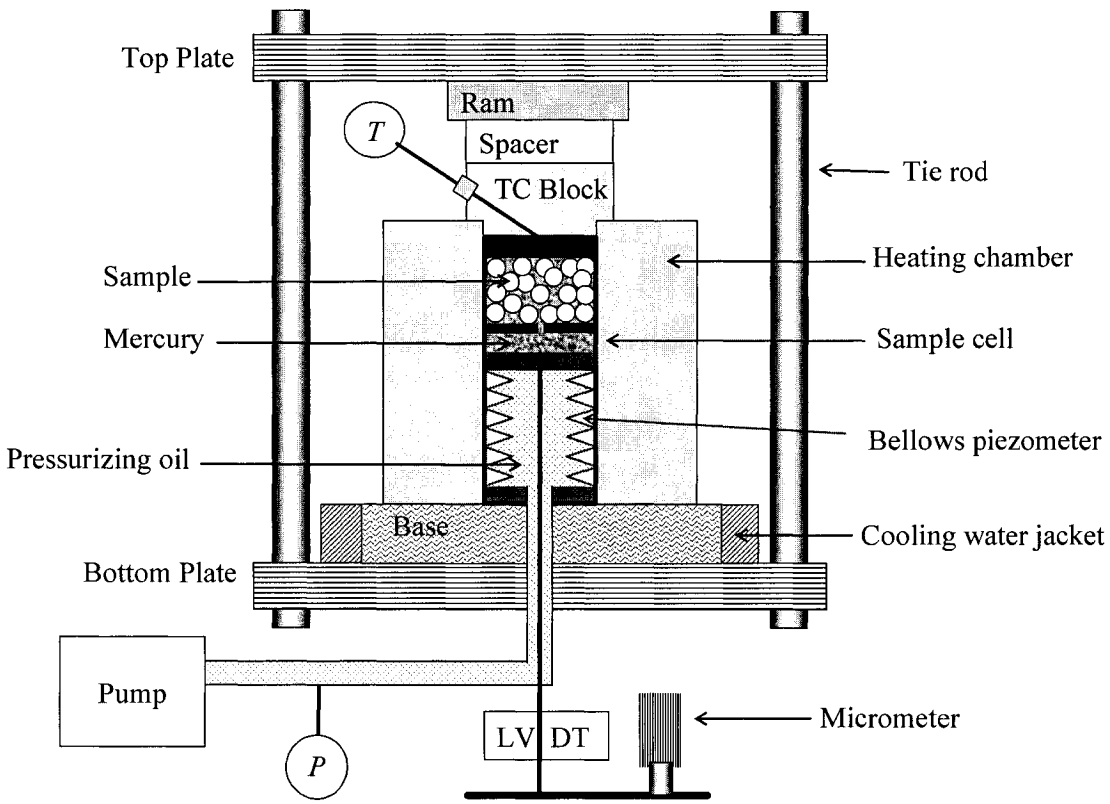

Figure 2.1. Schematic of the *PVT* apparatus (not to scale).

The Gnomix apparatus measures the volume change due to changes in temperature and pressure by use of the LVDT, of which resolution is 1 μm, representing a volume change of 10^{-4} cm^3/g. In the piezometer cell, the sample is surrounded by a

confining liquid, which was mercury for this study. The bellows in the cell allows for expansion or shrinkage of the sample, confining liquid, and sample cup, and such a change causes a linear displacement of the LVDT.

2.3.2 Calibration

A calibration must be carried out for each piezometer cell and confining liquid, because the changes in T and P influence the volume of the cell and fluid, and this affects the LVDT output. The calibration procedure is the same as a normal measurement except that no sample is present. The LVDT must also be calibrated for each experiment, because room temperature affects its response and is subject to fluctuation. The LVDT is calibrated by setting a value on the micrometer [Fig. 2.2-(e)] connected to the cell and setting the displacement value in the operating software.

2.3.3 Experimental Procedure

Prior to loading a sample, pellets received from the manufacturer are held in a vacuum oven at 50℃ for eight hours to reduce the level of O_2 and other small molecules. One to two grams of pellets are loaded into the sample cup, and the cup is loaded along with the bellows into the piezometer cell [Fig. 2.2-(b) left]. The cell is filled with mercury after evacuating it using a vacuuming and filling device [Fig. 2.2-(a)]. After loading the cell into the *PVT* system [Fig. 2.2-(d)], the system is heated or cooled by the heating and cooling elements around the cell [Fig. 2.2-(b) right] and pressurized by a hydraulic pump [Fig. 2.2-(f)]. Meanwhile, the change in volume is measured, and the temperature of the sample is determined by use of a high-pressure thermocouple [Fig. 2.2-(c)] on the cell. The pressure is determined by means of a pressure transducer installed between the system and the hydraulic pump. The temperature and pressure are changed by controllers [Fig. 2.2-(g)], and the schedule is programmed by the operating software. The change in the volume of the sample and mercury is transferred to the LVDT [Fig. 2.2-(e)].

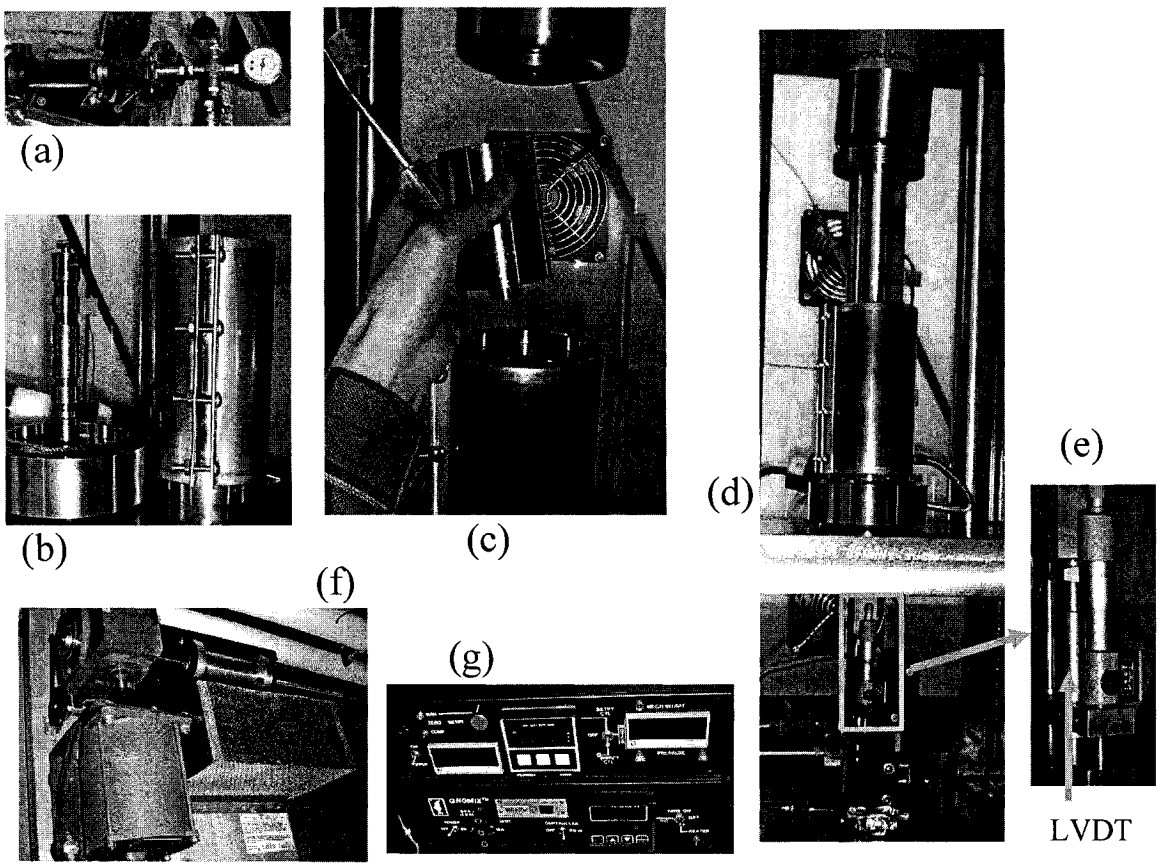

Figure 2.2. *PVT* apparatus: (a) vacuuming / filling device, (b) piezometer cell and heating/cooling element, (c) high-pressure thermocouple (TC) block, (d) setup of cell, LVDT, and micrometer, (e) LVDT and micrometer, (f) hydraulic pump, and (g) pressure and temperature controllers.

Two types of test can be performed: isothermal and isobaric. In an isothermal test the change in volume along isotherms at various pressures is recorded, and the results are used to determine the constants in the models. In an isobaric test the volume changes are recorded during heating or cooling at a constant rate at a given pressure. The heating/cooling rate and pressure dependence of the melting (T_m), crystallization (T_c), and glass transition (T_g) temperatures at a certain cooling or heating rate can be determined.

2.3.3.1 Isothermal *PVT* Measurement

An isothermal *PVT* run is performed at a fixed temperature and increasing pressure. The step-increase of pressure is 10 MPa. The volume change is recorded 10 min after the set pressure is achieved. After the system reaches the maximum set pressure, the system is vented to the atmosphere, and the temperature is increased to the next set temperature. The pressure sweep is repeated until the temperature reaches the maximum set temperature.

The major concern in an isothermal test is temperature measurement. The increase in pressure increases the temperature. The system is then cooled down to the set temperature, and then the pressure decreases. These fluctuations continue until the system reaches the set temperature and pressure. If the system is left alone for a very long time, the desired temperature and pressure will eventually be achieved, but the sample will degrade. To avoid this, a holding time of 10 min is inserted in the program. For all calculations, the feedback temperature is used for this work even though the feedback temperature is slightly different from the set temperature.

After one pressure-sweep at a temperature, measurements are carried out at another temperature. The temperature interval is five degrees near T_m ($110<T<150$℃) and ten degrees elsewhere. It requires 15 minutes to stabilize the temperature for the establishment of an isotherm. The command temperature ranges from 30 to 210℃, and the pressures are from 10 to 80 MPa. The specific volume change at 0 MPa for each isotherm is determined by extrapolation using the Tait model by an operating software for the *PVT* apparatus.

2.3.3.2 Isobaric *PVT* Measurement

An isobaric test is performed at heating and cooling rates of 2.5°C/min at a fixed pressure. The first temperature sweep is carried out at 10 MPa by heating, and the system is then cooled at the same rate after reaching the maximum set temperature. Meanwhile the volume change is recorded every 20 s. The next run is carried out at another pressure, and the pressure interval is 10 MPa; the temperature sweep is

repeated until the pressure reached 70 MPa. Temperature measurement in an isobaric test is much simpler than in an isothermal test, because the measured quantity is a transient temperature at each time of volume measurement.

2.4 Results and Discussion

2.4.1 Density

The density measurement results are given in Table 2.1. The method is described in detail in Appendix 1.

Table 2.1. Results of density determination.

Temperature	Water density	Polymer weight	Weight loss due to buoyancy	Polymer density	Polymer Spec. vol.
T (℃)	ρ_w (g/cm^3)	W_{pol} (g)	W_b (g)	ρ_{pol} (g/cm^3)	v_{pol} (cm^3/g)
24.5	0.9972 [34]	1.3216	1.3945	0.9451	1.0581

2.4.2 Effects of Temperature and Pressure on Specific Volume

Since the *PVT* apparatus measures only change of specific volume (Δv), the specific volume at a given temperature must be added to all data to obtain the absolute specific volume. However, the density is usually measured at room temperature, and this temperature is out of the range of the operating temperature, which must be above 30℃. Thus, two steps are required to obtain absolute volume. (1) To use an exponential equation

$$\Delta v = a\exp(bT) + c \tag{2.11}$$

where a, b, and c are fitting constants, and extrapolate Δv to 24.5℃, where the density of the sample was measured, to determine $\Delta v(24.5℃)$ (Fig. 2.3). (2) To add $[v_{pol}(24.5℃)\text{-}\Delta v(24.5℃)]$ to the data, where $v_{pol}(24.5℃) = 1/\rho_{pol}(24.5℃)$.

The effects of temperature and pressure on the specific volume of HDPE is shown in Fig. 2.4 where three regions can be observed. The specific volume decreases

smoothly with pressure in the melt and solid regions, while in the transition region there is a marked curvature change indicating a phase change caused by pressure increase at a fixed temperature. According to the slope, the volume change in the solid zone is smaller than that in the melt zone. On the other hand, at a fixed pressure, the large jumps in the transition zone indicate a phase transition due to the temperature increase.

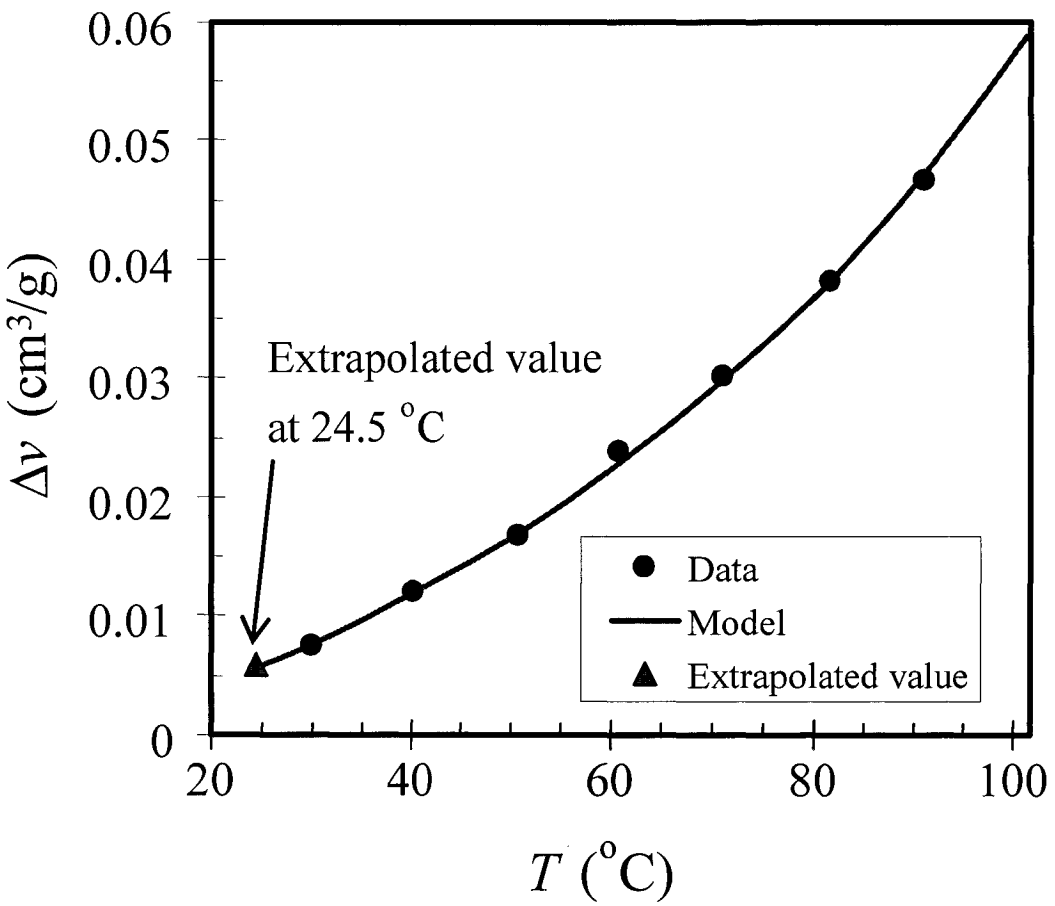

Figure 2.3. Extrapolation of volume change at 24.5℃

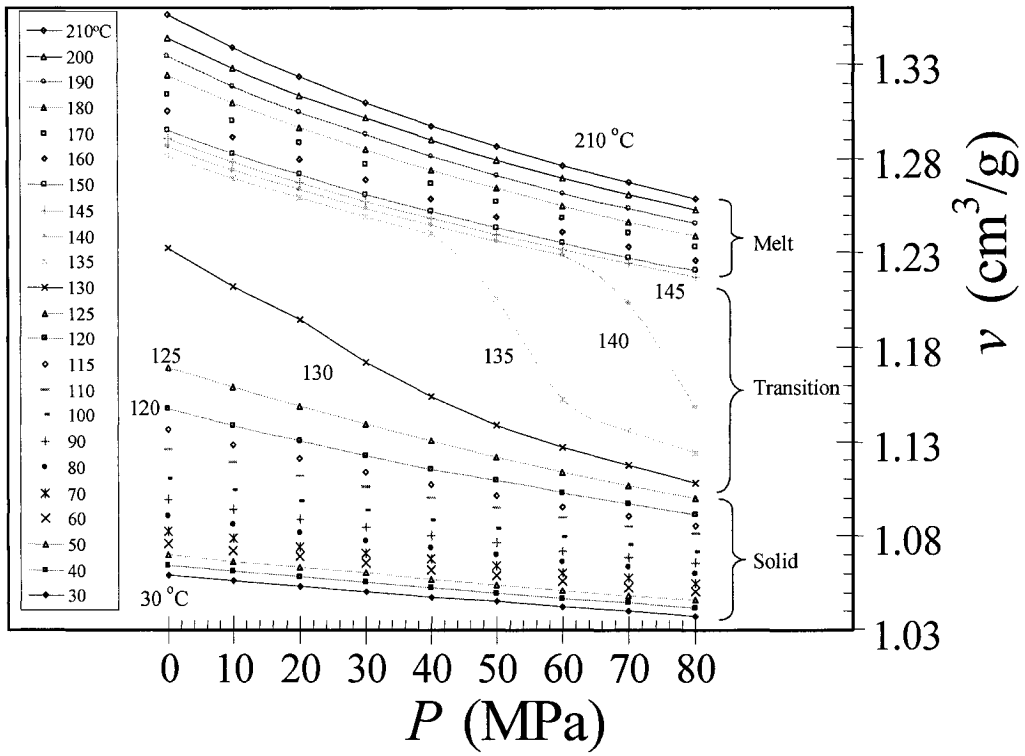

Figure 2.4. The effect of T and P on specific volume: Isothermal test. Numbers in legend indicate the set T in ℃. (Lines show trends only, not model predictions.)

From the curve indicating pressure-induced solidification, the temperature for rheological measurements can be determined. The curve at 135℃ shows a large volume decrease starting at 40 MPa, and the 140℃ isotherm shows a large decrease starting at 60 MPa. At 145℃, pressurizing up to 80 MPa cannot solidify the sample, but at temperatures below 145℃; a pressure increase can cause solidification. This implies that pressure increases the melting temperature, T_m. This means that rheological measurements at high pressures must be carried out at temperatures above the pressure-enhanced T_m. A temperature of 160℃ was chosen as the minimum temperature.

2.4.2.1 Effects of T and P on Vertical Shift Factors

Figure 2.5 shows that the effect of temperature on $b_T(T) \equiv \rho_{pol}(T)T/\rho_{pol}(T_0)T_0$ of HDPE at 0.1 MPa. Figure 2.6 shows that the effect of pressure on

$b_P(P) \equiv \rho_{pol}(P)/\rho_{pol}(P_0)$ of HDPE at 180℃. There are a 7% variation over 50 degrees and a 6% variation over 70 MPa, respectively. These dependencies will be discussed in Sections 5.4.4.5. and 6.7.4.

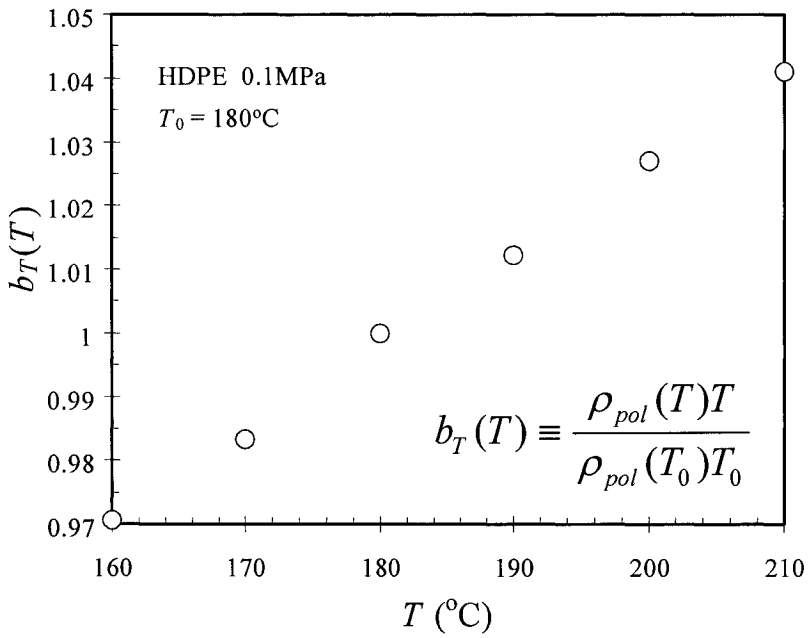

Figure 2.5. Effect of temperature on $b_T(T)$ of HDPE at 0.1 MPa.

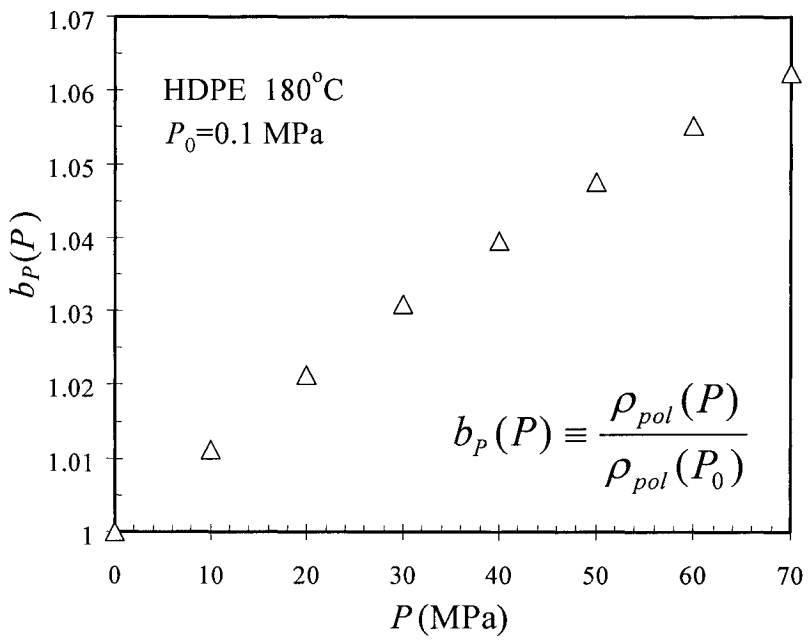

Figure 2.6. Effect of pressure on $b_P(P)$ of HDPE at 180℃.

2.4.2.2 Model Fitting: Tait Equation

Only the fully molten state is of interest here, so only data in the molten state were used for model fitting. Capt and Kamal [35] used two methods to fit *PVT* data to the Tait model (Eq. 2.6) and found that it is better to determine the four parameters in one non-linear regression than to determine them by separate regressions. The former method was used for this work. The fitting parameters were determined by the least square method, *i.e.* minimizing the following error sum:

$$S_1 \equiv \sum_i^N \left[v_i - v_{mp,i}(P_i, T_i, v_0, v_1, B_0, B_1) \right]^2 \tag{2.12}$$

where i is the index of data set of P and T, and N is the total number of data sets. The datum v is the specific volume corresponding to (P_i, T_i), and v_{mp} is the specific volume at (P_i, T_i) as predicted using the model and fitting parameters. The results and a comparison with data of Rodgers are given in Table 2.2. This model reasonably fits the data (Fig. 2.7). It has four adjustable parameters and can be expected to describe the *PVT* behavior better than other thermodynamic EOS's, which generally have only three parameters.

Table 2.2. Comparison between Tait model parameters of this work and those of Rodgers [26].

Parameter	Units	This work	Rodgers
v_0	cm^3/g	0.8867	1.1595
v_1	cm^3/gK	11.641×10^{-4}	8.0394×10^{-4}
B_0	MPa	180.0	179.9
B_1	1/K	2.713×10^{-3}	4.739×10^{-3}

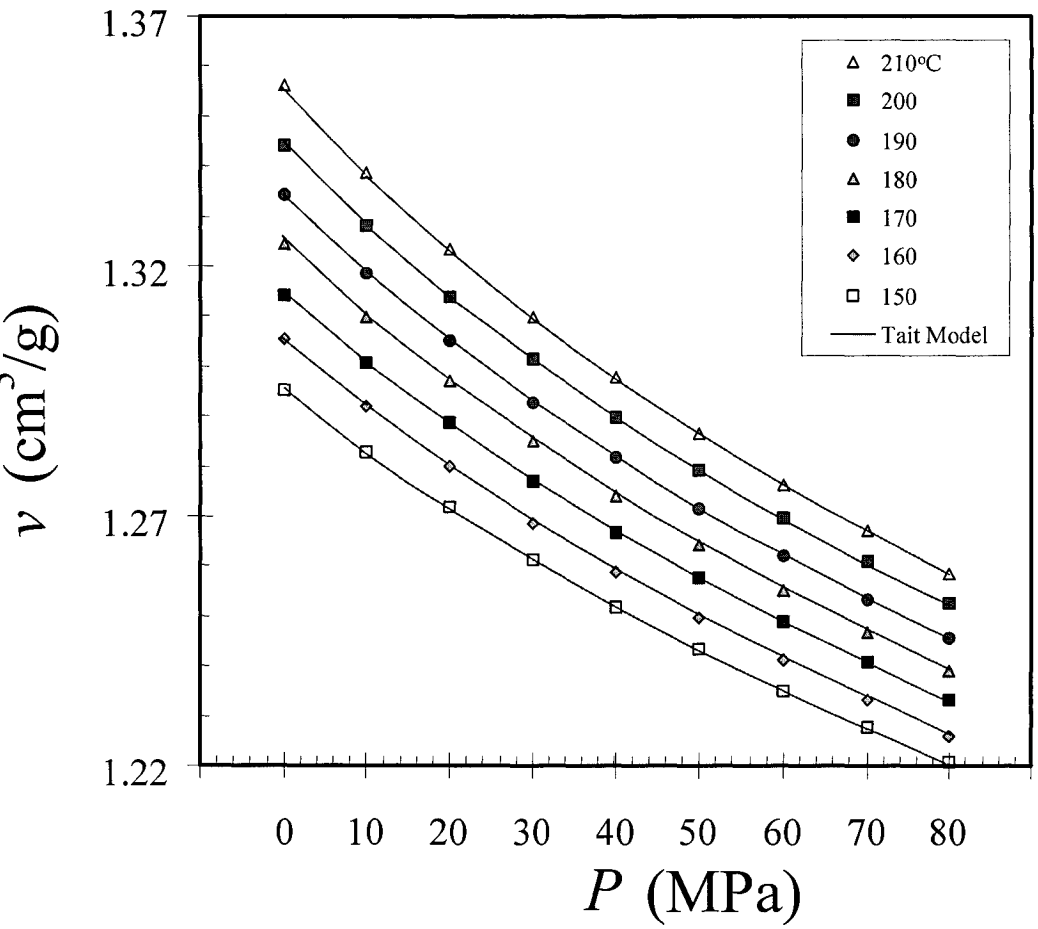

Figure 2.7. Comparison of data with Tait model predictions.

2.4.2.3 Model Fitting: Sanchez-Lacombe Equation

Unlike the Tait equation, the S-L equation does not give the volume explicitly. To calculate the specific volume, two steps are required using Eq. 2.10. First, model fitting is carried out by determining the parameters that minimize the S_2:

$$S_2 \equiv \sum_{i=1}^{N} \left\{ \tilde{P}_i + \tilde{\rho}_i^2 + \tilde{T}_i \left[\ln(1-\tilde{\rho}_i) + \left(1 - \frac{1}{r}\right)\tilde{\rho}_i \right] \right\}^2 \tag{2.13}$$

Second, using the data sets (P_i,T_i) and the parameters determined in the first step, reduced densities $\tilde{\rho}_{c,i}$ are calculated in the following equation by Newton's method:

$$\tilde{P}_i + \tilde{\rho}_{c,i}^{\,2} + \tilde{T}_i\left[\ln(1-\tilde{\rho}_{c,i}) + \left(1-\frac{1}{r}\right)\tilde{\rho}_{c,i}\right] = 0 \tag{2.14}$$

The parameters determined in the present study are compared with those of Rodgers [26] in Table 2.3. He fitted his data in two ranges: up to 50 and 200 MPa. He found that the first group gave a better fitting. The resulting parameters will be used to obtain the specific volume of HDPE/CO_2 mixture in the next chapter.

Table 2.3. Comparison of S-L parameters from this work with those of Rodgers [26].

Param.	Units	This work (~80MPa)	Rodgers (~50MPa)	Rodgers (~200MPa)
P^*	MPa	408.3	288.7	366.2
T^*	K	570	736	615
ρ^*	g/cm^3	0.8762	0.8670	0.9137

The predicted specific volumes for each set (P_i,T_i) were calculated from $\tilde{\rho}_{c,i}$ and are plotted along with the data in Fig. 2.8. The S-L model provides a less accurate description than the Tait model and over-estimates the volume at high and low pressures, and it significantly over-estimates the volume at high temperature and low pressure (circle in Fig. 2.8).

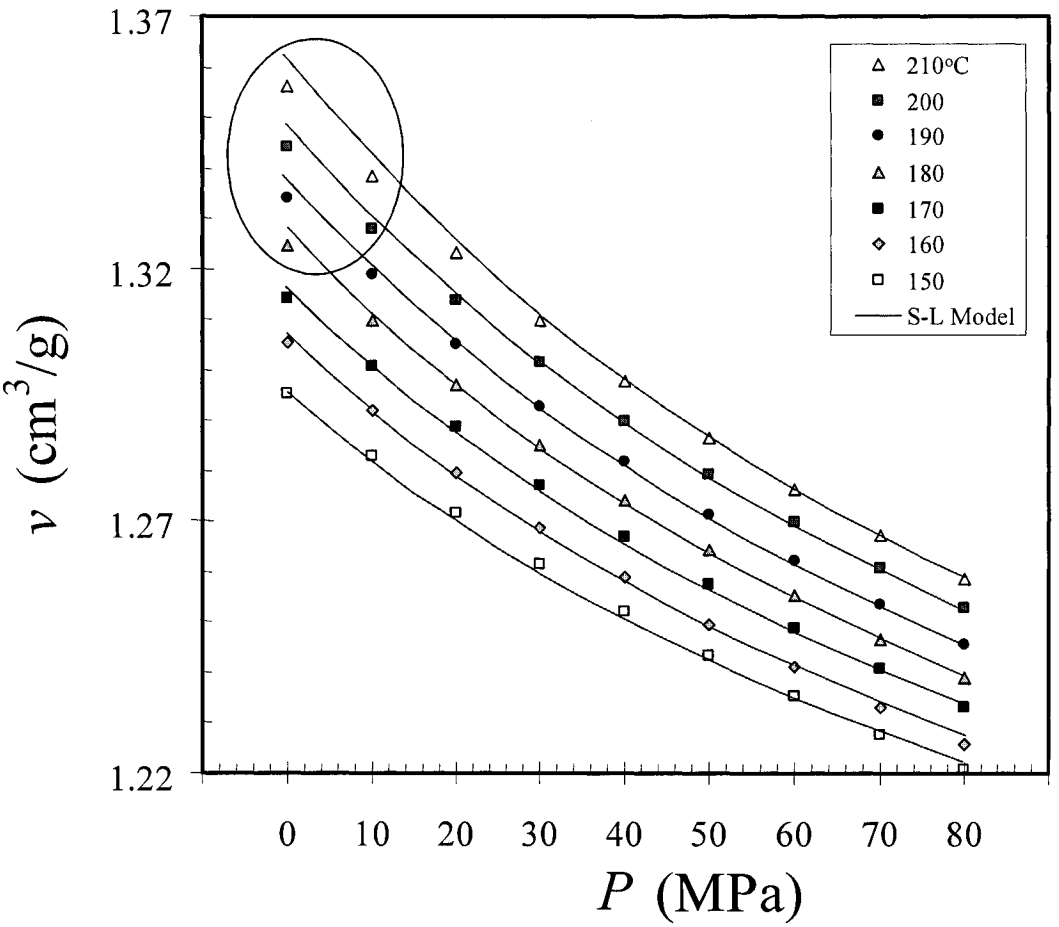

Figure 2.8. Comparison between data and S-L model prediction.

2.4.2.4 Compressibility

The isothermal compressibility is defined as:

$$\beta(P,T) \equiv \left[-\frac{1}{v(P,T)}\frac{\partial v(P,T)}{\partial P}\right]_T = \left\{-\frac{\partial \ln[v(P,T)]}{\partial P}\right\}_T \tag{2.15}$$

To obtain the compressibility, the logarithm of is used as shown in Fig. 2.9. Since $\ln v$ is nonlinear with pressure, a pressure-independent $\beta(P,T)$ cannot be achieved. Figure 2.9 shows that the slope of each curve $\beta(P,T)$ increases with temperature at a given pressure, and this implies that temperature increases the pressure sensitivity of volume.

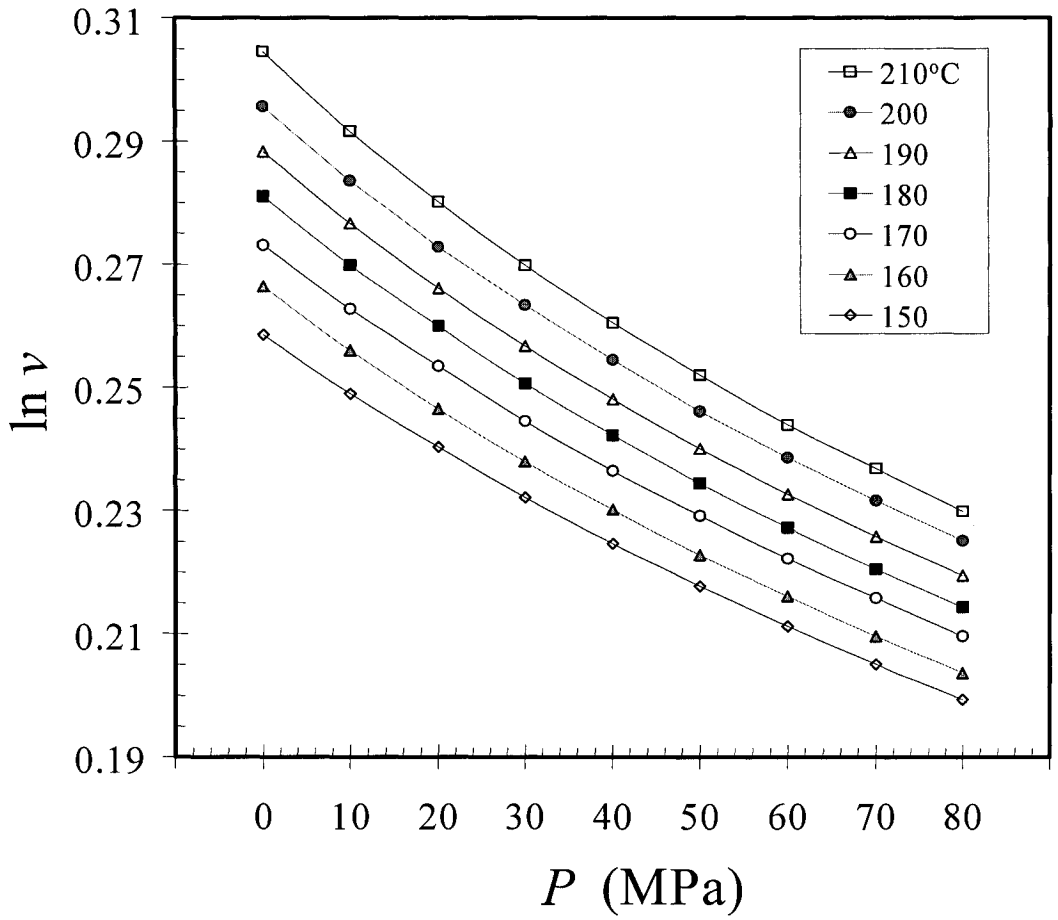

Figure 2.9. Effect of temperature and pressure on $\ln v$ as determined from isothermal *PVT* measurements. (Lines show trends only, not model predictions.)

2.4.3 Effect of Pressure on T_m and T_c

Isobaric *PVT* data were used to determine the effect of P on T_m and T_c at heating and cooling rates of 2.5℃/min. The results are plotted in Fig. 2.10 along with the results of the isothermal test. The isobaric test provides rate-dependent results: the same result as in an isothermal test cannot be expected, but the figure shows that the isobaric heating curve is similar to the isothermal curve at 10 MPa. The deviation between the two curves increases with pressure, and this indicates that pressure suppresses the rate of volume change with temperature and melting behavior. On the other hand, the deviation between the cooling and isothermal curves decreases with

pressure, and this implies that pressure accelerates the kinetic behavior of crystallization. This phenomenon can be considered for the study of effect of pressure on shear-induced crystallization.

The T_m and T_c values used in this study are defined as the temperatures where the tangent lines of the transition and melting zones cross. Figures 2.11 and 2.12 illustrate this method, the effect of P is shown in Fig. 2.13. Pressure increases both T_m and T_c linearly. The effect of pressure on these temperatures can be described by the following linear equations:

$$T_m(℃) = 0.27P(\mathrm{MPa}) + 140.1 \tag{2.16}$$

$$T_c(℃) = 0.28P(\mathrm{MPa}) + 121.2 \tag{2.17}$$

According to this, T_m at 70 MPa, which is the maximum operating pressure of the HPSPR, is 159℃. Even though this result is based on the transient behavior of specific volume, and $T_m(P)$ determined by an isobaric test is usually higher than that (145℃ for HDPE) determined by an isothermal test, the minimum operating temperature was chosen as 170℃, accounting for shear-induced crystallization in the high-pressure study.

The slopes in the melt zone in Figs. 2.11 and 2.12 show that pressure decreases the degree of thermal expansion, and this can be described by an isobaric thermal expansion coefficient:

$$\alpha(P,T) \equiv \left[\frac{1}{v(P,T)}\frac{\partial v(P,T)}{\partial T}\right]_P = \left\{\frac{\partial \ln[v(P,T)]}{\partial T}\right\}_P \tag{2.18}$$

Since $\ln v$ is linear with T (Fig. 2.14), α is independent of T. Figure 2.15 shows that it is a decreasing function of pressure, and this implies that pressure decreases the temperature sensitivity of volume.

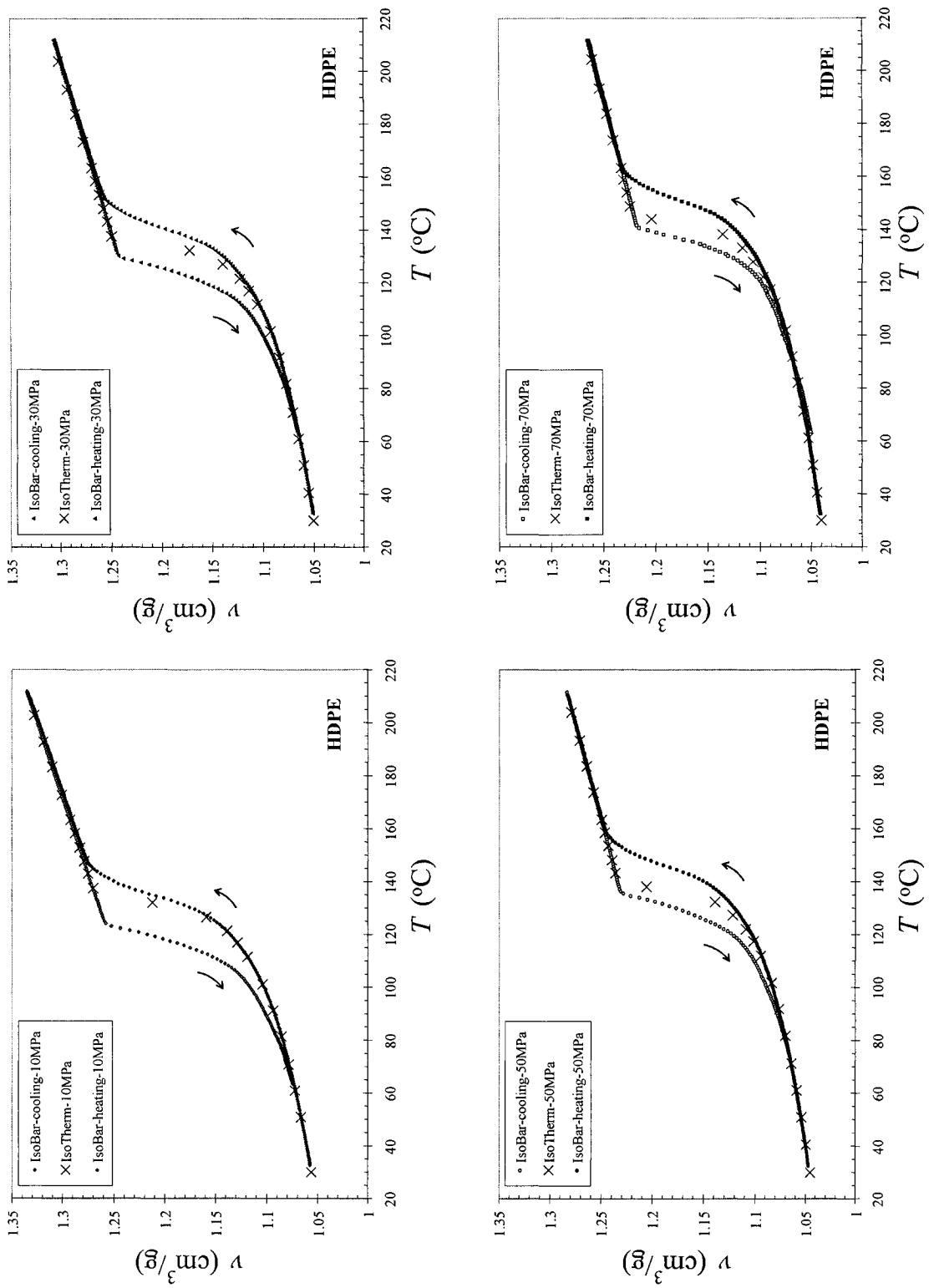

Figure 2.10. Comparison of isobaric tests with isothermal tests.

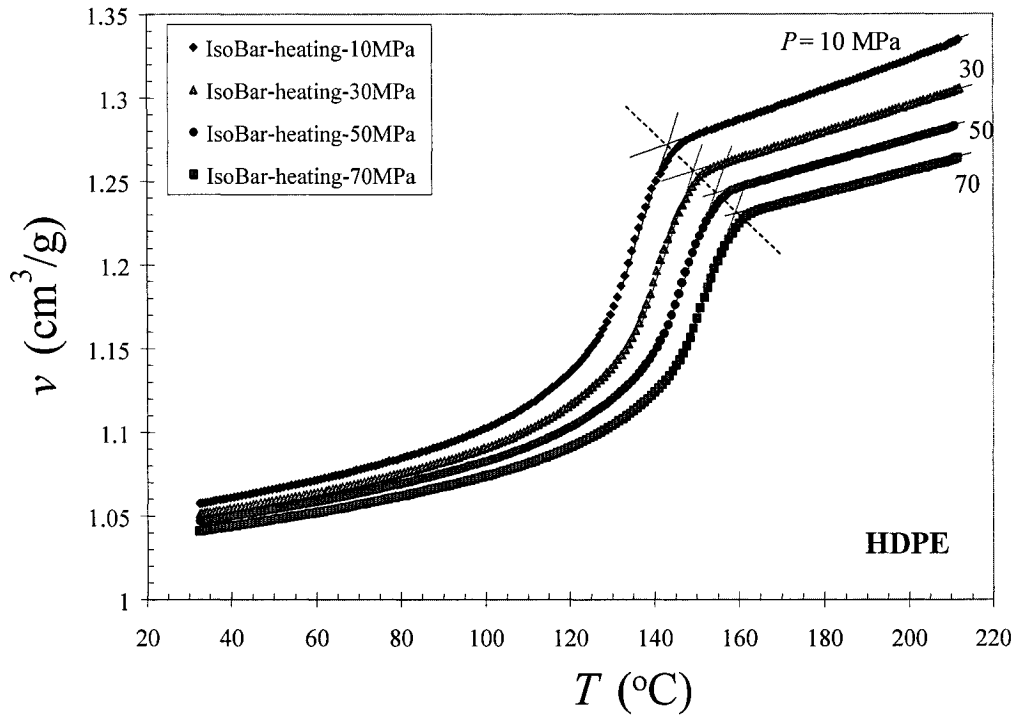

Figure 2.11. Isobaric heating curves at 2.5℃/min - determination of T_m.

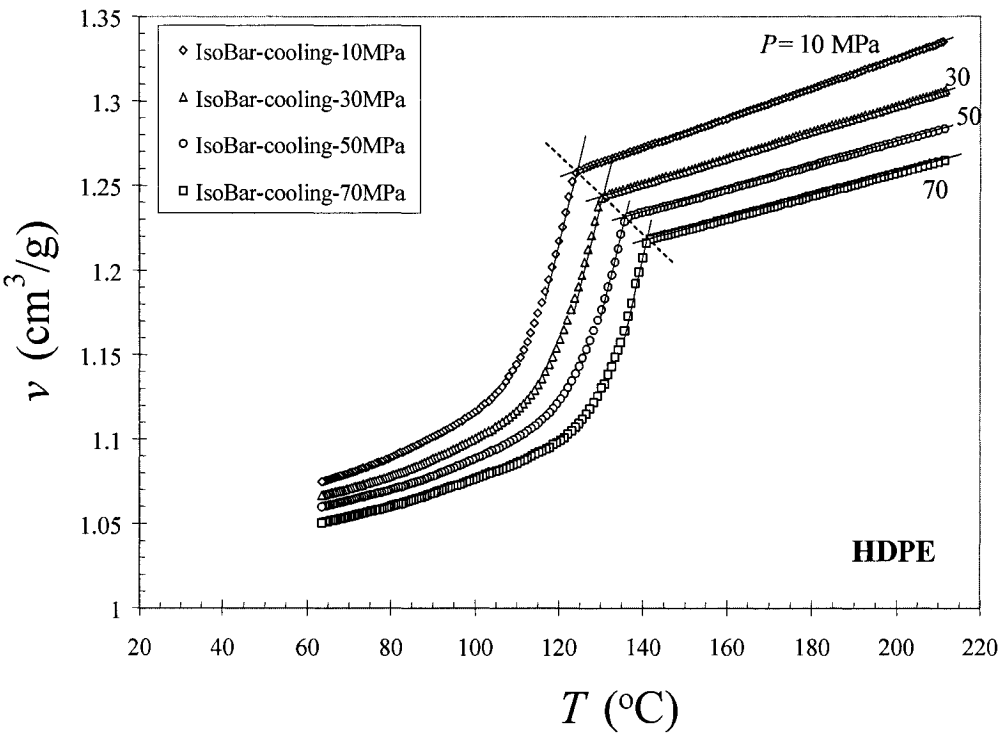

Figure 2.12. Isobaric cooling curves at -2.5℃/min - determination of T_c.

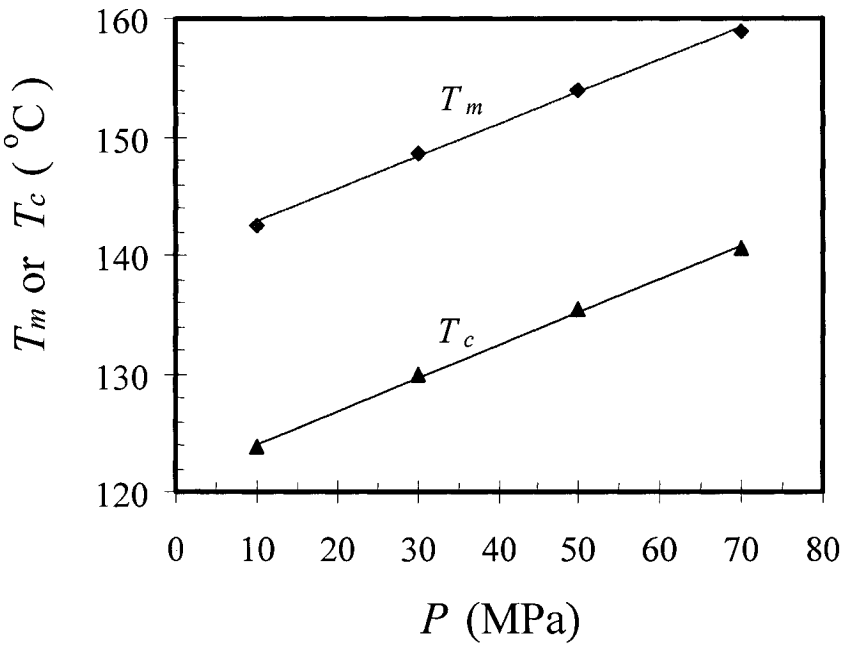

Figure 2.13. Effect of pressure on T_m and T_c.

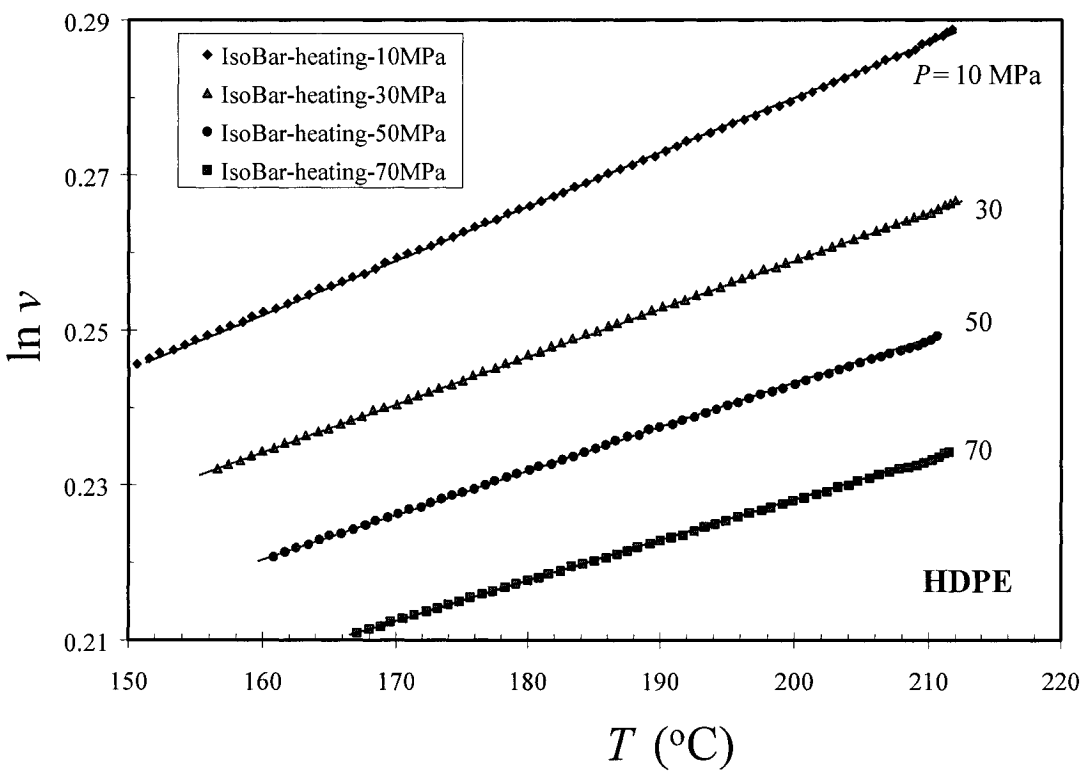

Figure 2.14. Effect of temperature and pressure on $\ln v$ as determined from isobaric *PVT* measurements.

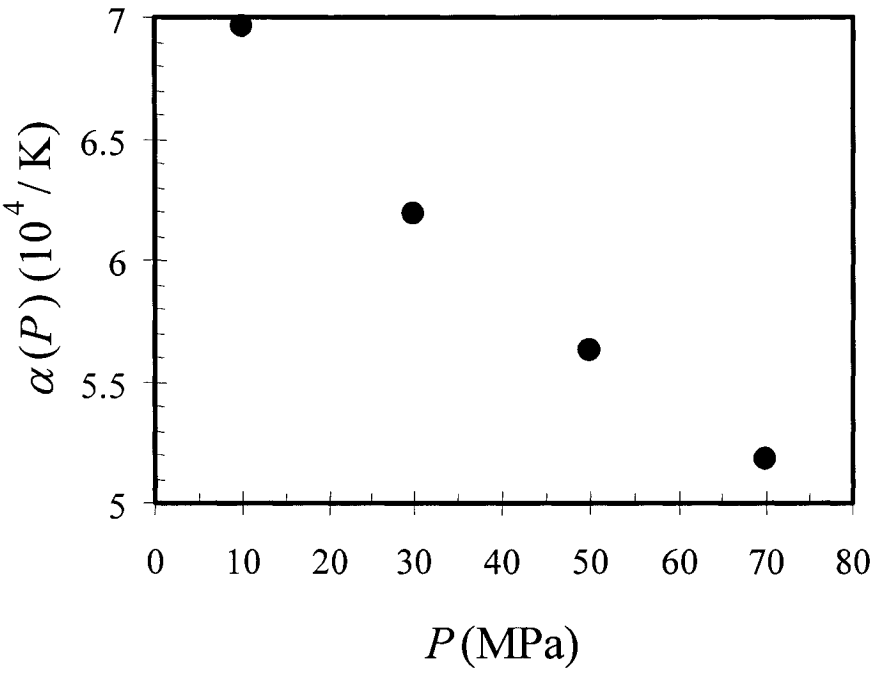

Figure 2.15. Effect of pressure on thermal expansion coefficient.

2.5 Conclusions

A Gnomix *PVT* apparatus was used to determine the *PVT* behavior of pure polymer, and the data were fitted to the Tait equation and the Sanchez-Lacombe equation. The Tait model fitted the data better. For CO_2 solubility determination, the parameters of the Tait equation will be used for the *PVT* values of pure polymer, and those of the S-L model will be used for the mixture of polymer and CO_2. The minimum temperature for rheological measurements at high pressures was 170℃, based on the effect of pressure on melting point. Pressure slows down melting behavior and accelerates crystallization of polymer. The *PVT* behavior of CO_2 and the mixture are discussed in the next chapter.

2.6 References

1. A. Wohl, "Untersuchungen über die Zustandsgleichung. IV. Die kompressionsgleichung der flüssigkeiten - Zustandsgleichung stark verdichteter stoffe (Investigations on the equation of state. IV. The compression equation of the liquids. - Equation of state of strongly consolidated materials.)," Zeitschrift für Physikalische Chemie, 99:234 (1921).
2. P.J. Flory, "Thermodynamics of high-polymer solutions," *J. Chem. Phys.* 10:51 (1942).
3. M.L. Huggins, "Thermodynamic properties of solutions of long-chain compounds," *Annals of New York Academy Science* 43:1 (1942).
4. I. Prigogine, N. Trappeniers, and V. Mathot, "Statistical thermodynamics of r-mers and r-mer solutions," *Discussion of the Faraday Society* 15:93 (1953).
5. I.C. Sanchez and R.H. Lacombe, "An elementary molecular theory of classical fluids. Pure fluids," *The Journal of Physical Chemistry* 80:2352 (1976).
6. I.C. Sanchez and R.H. Lacombe, "Statistical thermodynamics of polymer solutions," *Macromolecules,* 11:1145 (1978).
7. I.C. Sanchez and P.A. Rodgers, "Solubility of gases in polymers," *Pure & Appl. Chem.* 62:2107 (1990).
8. C. Panayiotou and J.H. Vera, "Statistical thermodynamics of r-mer fluids and their mixtures," *Polym. J.* 14:681 (1982).
9. G.T. Dee and D.J. Walsh, "Equations of state for polymer liquids," *Macromolecules* 21:811 (1988).
10. G.T. Dee and D.J. Walsh, "A modified cell model equation of state for polymer liquids," *Macromolecules* 21:815 (1988).
11. F. Doghieri and G.C. Sarti, "Nonequilibrium lattice fluids: a predictive model for the solubility in glassy polymers," *Macromolecules* 29:7885 (1996).
12. V.S. Parekh and R.P. Danner, "Prediction of polymer PVT behavior using the group contribution lattice-fluid EOS," *J. Polym. Sci., Part B* 33:395 (1995).
13. R. Simha and T. Somcynsky, "On the statistical thermodynamics of spherical and chain molecule fluids," *Macromolecules* 2:343 (1969).
14. R. Simha, "Configurational Thermodynamics of the liquid and glassy polymeric states," *Macromolecules*, 10:1025 (1977).
15. M.S. Wertheim, "Fluids with highly directional attractive forces: I. Statistical thermodynamics," *J. Stat. Phys.* 35:19 (1984).
16. M.S. Wertheim, "Fluids with highly directional attractive forces: II. Thermodynamic perturbation theory and integral equations," *J. Stat. Phys.* 35:35

(1984).

17. M.S. Wertheim, "Fluids with highly directional attractive forces: III. Multiple attraction sites," *J. Stat. Phys.* 42:459 (1986).

18. M.S. Wertheim, "Fluids with highly directional attractive forces: IV. Equilibrium polymerization," *J. Stat. Phys.* 42:477 (1986).

19. W.G. Chapman, K.E. Gubbins, G. Jackson, and M. Radosz, "SAFT: equation-of-state solution model for associating fluids," *Fluid Phase Equilibria* 52:31 (1989).

20. W.G. Chapman, K.G. Gubbins, G. Jackson, and M. Radosz, "New reference equation of state for associating liquids," *Ind. Eng. Chem. Res.* 29:1709 (1990).

21. S.H. Huang and M. Radosz, "Equation of state for small, large, polydisperse, and associating molecules," *Ind. Eng. Chem. Res.* 29:2284 (1990).

22. S.H. Huang and M. Radosz, "Equation of state for small, large, polydisperse, and associating molecules: extension to fluid mixtures," *Ind. Eng. Chem. Res.* 30;1994 (1991).

23. Y. Song, S.M. Lambert, and J.M. Prausnitz, "A perturbed hard-sphere-chain equation of state for normal fluids and polymers," *Ind. Eng. Chem. Res.* 33:1047 (1994).

24. P. Zoller, "*PVT* Relationships and Equation of State of Polymers," in *Polymer Handbook*, 3rd Edition, Edited by Brandrup and E.H. Immergut, p. VI475, Wiley, New York, 1989.

25. J. Cho and I.C. Sanchez, "*PVT* Relationships and Equation of State of Polymers" in *Polymer Handbook*, 4th Edition, Edited by J. Brandup, E.H. Immergut, and E. A. Grulke, p. VI591, Wiley, New York, 1999.

26. P.A. Rodgers, "Pressure-volume-temperature relationships for polymeric liquids: a review of equations of state and their characteristic parameters for 56 polymers," *J. of Applied Polymer Science* 48:1061 (1993).

27. K.-H. Hellwege, W. Knappe, and P. Lehmann, *Kolloid-Z.* "The isothermal compressibility of some amorphous and partly crystalline high polymers from 20 to 250 degrees and at pressures up to 2000 kg./sq. cm," *Z. Polym.* 183:110 (1962).

28. P.G. Tait, "Report on some of the physical properties of fresh water and sea-water," in *Report on the scientific results of the Voyage of H.M.S. Challenger during the years 1873-1876: Physics and Chemistry,* Vol. 2, Part IV, H.M. Stationery Office, London, 1888.

29. W.G. Cutler, R.H. McMickle, W. Webb, and R.W. Schiessler, "Study of the compressions of several high molecular weight hydrocarbons," *J. Chem. Phy.*, 29:727 (1958).

30. Y. Sato, K. Fujiwara, T. Takikawa, Sumarno, S. Takishima, H. Masuoka,

"Solubility and diffusion coefficients of carbon dioxide and nitrogen in polypropylene, high-density polyethylene, and polystyrene under high pressure and temperatures," *Fluid Phase Equilibria* 162:261 (1999).

31. G. Li, J. Wang, C.B. Park, P. Moulinie, and R. Simha, "Comparison of SS-based and SL-based estimation of gas solubility," 62nd *ANTEC* 2:2566 (2004).
32. E. Funami, K. Taki, S.-i. Kihara, and M. Ohshima, "Measurement of CO_2-induced polymer swelling and predictability of Sanchez-Lacombe equation of state for the density of polymer/CO_2 systems," The 10th Asian Pacific Confederation of Chemical Engineering (APCChE), Kitakyushu, Japan, Section 2H-10 (2004).
33. P. Zoller, P. Bolli, V. Pahud, and H. Ackermann, "Apparatus for measuring pressure-volume-temperature relationships of polymers to 350 degrees C and 2200kg/cm^2," *Review of Scientific Instruments* 47:948 (1976).
34. *CRC Handbook of Chemistry and Physics*, 66th Edition, CRC Press, Cleveland, p. F4-F5, 1985/1986.
35. L. Capt and M.R. Kamal, "The pressure-volume-temperature behavior polyethylene melts," *Intern. Polymer Processing* XV:83 (2000).

3. Solubility of CO_2 and Swollen Volume of HDPE

3.1 Introduction

Because the effect of CO_2 on the rheological properties will be shown as a function of CO_2 concentration, and the HPSPR for this work can operate only at the saturation concentration, the solubility of CO_2 must be known. A magnetic suspension balance (MSB) was used to determine the amount of dissolved CO_2. The buoyancy effect in a measurement cell changes the net weight of HDPE/CO_2 mixture. The *PVT* data described in the previous chapter, together with the CO_2 density determined using the MSB, were combined with data measured to account for this effect. To determine the solubility, the swollen volume of polymer is also required, and the Sanchez-Lacombe model was used to analyze the data because that could not be measured directly. The swollen volume of polymer obtained here was also used in the form of a vertical shift factor for Chap. 6.

3.2 Background Information

3.2.1 Chemical Potential and Saturation

Partial molar quantities of thermodynamic variables are used to describe components in a mixture, and the partial molar Gibbs free energy is called the chemical potential μ. For component i in a binary mixture with a component j this is defined as:

$$\mu_i \equiv \left(\frac{\partial G}{\partial N_i}\right)_{T,P,N_j} \tag{3.1}$$

where N_i and N_j are the number of moles of components i and j respectively, and the Gibbs free energy is defined as:

$$G \equiv H - TS \tag{3.2}$$

where H is the enthalpy, and S is the entropy at T and P. Net diffusion will take place from where the chemical potential is higher to where it is lower. For a two-phase system at equilibrium, the chemical potential of one species must be the same in both phases, and the concentration of component i in a mixture at equilibrium, *i.e.*, the mixture is saturated with i, is its solubility. The system of interest here is shown in Fig. 3.1. The polymeric liquid is assumed to be immobile due to its high molecular weight, so gas dissolves in the polymer, but the gas phase contains no polymer. At equilibrium, the chemical potential of gas in the gas phase μ_g^g is equal to that in the polymer/gas mixture phase μ_g^m, and the concentration of gas in the mixture is the solubility. The solubility of gas in a liquid increases with pressure, and elevated pressure is thus required to achieve a high solubility.

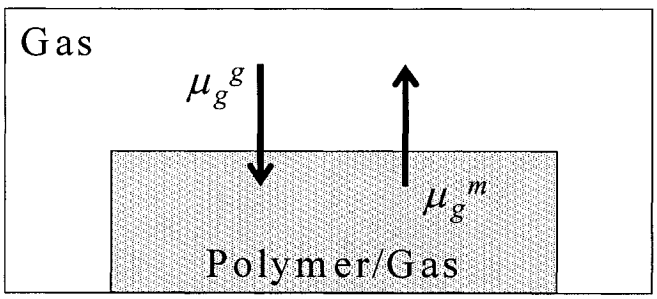

Figure 3.1. Gas dissolution and chemical potentials.

3.2.2 Equation of State and Mixing Rule

A theoretical model is required to calculate the volume of the HDPE/CO_2 mixture, which is required to account for buoyancy. Because the Sanchez-Lacombe model [1] is relatively easy to use, and previous researchers [2,3] found that this model predicts the *PVT* behavior of polymer/CO_2 mixture successfully, this model was chosen to describe the HDPE/CO_2 system:

$$\tilde{P}_m = -\tilde{\rho}_m^2 - \tilde{T}_m\left[\ln(1-\tilde{\rho}_m)+\left(1-\frac{1}{r}\tilde{\rho}_m\right)\right] \tag{3.3}$$

where the subscript m stands for the mixture, $\tilde{T}_m \equiv T/T^*$, $\tilde{P}_m \equiv P/P^*$, $\tilde{\rho}_m \equiv \rho_m/\rho^* = 1/\tilde{v}_m$, $T^* \equiv \epsilon^*/R$, $P^* \equiv \epsilon^*/v^*$, ϵ^* is the interaction energy, the close-packed mer volume is $v^* \equiv RT^*/P^*$, $\rho^* \equiv M_m/(rv^*)$, $r = M_m P^*/(RT^*\rho^*) = M_m/(\rho^* v^*)$, and M_m is the average molecular weight of the mixture. Each parameter for the mixture is related to those of the pure components by a mixing rule [1,4]. However, the mixing rule contains at least one interaction parameter, which cannot be predicted, and the equation of state is thus not predictive. The characteristic density of the mixture is:

$$\rho^* \equiv \frac{\overset{*}{\rho_1}\overset{*}{\rho_2}}{w_1\overset{*}{\rho_2} + w_2\overset{*}{\rho_1}} \tag{3.4}$$

where subscripts 1 and 2 refer to CO_2 and HDPE respectively, w_1 and w_2 are the weight fractions, and $w_1 + w_2 = 1$. The characteristic pressure for a mixture is defined as:

$$P^* \equiv \phi_1^2 P_1^* + \phi_2^2 P_2^* + 2\phi_1\phi_2 P_{12}^* \tag{3.5}$$

where ϕ_1 and ϕ_2 are volume fractions defined as:

$$\phi_1 = \left(\frac{w_1}{\overset{*}{\rho_1}}\right) \div \left(\frac{w_1}{\overset{*}{\rho_1}} + \frac{w_2}{\overset{*}{\rho_2}}\right) \tag{3.6}$$

$$\phi_2 = \left(\frac{w_2}{\overset{*}{\rho_2}}\right) \div \left(\frac{w_1}{\overset{*}{\rho_1}} + \frac{w_2}{\overset{*}{\rho_2}}\right) = 1 - \phi_1 \tag{3.7}$$

and P_{12}^* is defined as follows in terms of the interaction parameter, K_{12}:

$$P_{12}^* = (1 - K_{12})(P_1^* P_2^*)^{0.5} \tag{3.8}$$

Finally, the characteristic temperature for the mixture is:

$$T^* = P^*\left(\frac{\phi_1^0 T_1^*}{P_1^*} + \frac{\phi_2^0 T_2^*}{P_2^*}\right) \tag{3.9}$$

where

$$\phi_1^0 = \left(\frac{\phi_1 P_1^*}{T_1^*}\right) \div \left(\frac{\phi_1 P_1^*}{T_1^*} + \frac{\phi_2 P_2^*}{T_2^*}\right) \tag{3.10}$$

and

$$\phi_2^0 = \left(\frac{\phi_2 P_2^*}{T_2^*}\right) \div \left(\frac{\phi_1 P_1^*}{T_1^*} + \frac{\phi_2 P_2^*}{T_2^*}\right) = 1 - \phi_1^0 \tag{3.11}$$

There are three unknowns in the EOS for a binary mixture: $K_{12}(P,T)$, $\rho_m(P,T)$, which is related to swollen volume, and $\phi_1(P,T)$, which is related to the solubility.

At equilibrium:

$$\mu_1^1 = \mu_1^m \tag{3.12}$$

Sanchez and Lacombe [1] derived an expression for the Gibbs free energy of a binary mixture:

$$G_m = rN\epsilon^* \left\{ \tilde{T}_m \left[\frac{\phi_1}{r_1} \ln\phi_1 + \frac{\phi_2}{r_2} \ln\phi_2 \right] - \tilde{\rho}_m + \tilde{P}_m \tilde{v}_m + \tilde{T}_m \tilde{v}_m \left[(1-\tilde{\rho}_m)\ln(1-\tilde{\rho}_m) + \frac{\tilde{\rho}_m}{r} \ln\tilde{\rho}_m \right] \right\} \tag{3.13}$$

The chemical potential [1] of component 1 in the mixture can be obtained by differentiating the Gibbs free energy with respect to the number of moles of component 1, N_1:

$$\mu_1^m \equiv \left(\frac{\partial G_m}{\partial N_1}\right)_{T,P,N_2} \tag{3.14}$$

Sanchez and Lacombe [1] derived μ_1^m as:

$$\mu_1^m = RT\left[\ln\phi_1 + \left(1-\frac{r_1}{r_2}\right)\phi_2 + r_1^0\tilde{\rho}_m\frac{P_1^* + P_2^* - 2P_{12}^*}{P_1^*\tilde{T}_1}\phi_2^2\right] + r_1^0 RT\left[-\frac{\tilde{\rho}_m}{\tilde{T}_1} + \frac{\tilde{P}_1}{\tilde{\rho}_m\tilde{T}_1} + \left(\frac{1}{\tilde{\rho}_m}-1\right)\ln(1-\tilde{\rho}_m) + \frac{1}{r_1^0}\ln\tilde{\rho}_m\right] \tag{3.15}$$

where $\tilde{P}_1 \equiv P/P_1^*$, $\tilde{T}_1 \equiv T/T_1^*$, and two new parameters are defined for simplification:

$$r_1^0 = \frac{M_1 P_1^*}{RT_1^*\rho_1^*} \tag{3.16}$$

$$r_2^0 = \frac{M_2 P_2^*}{RT_2^*\rho_2^*} \tag{3.17}$$

The chemical potential of component 1 in a pure phase can be obtained from Eq. 3.15 by replacing $\tilde{\rho}_m$ with $\tilde{\rho}_1$ and letting $\phi_1 = 1$ and $\phi_2 = 0$:

$$\mu_1^1 = r_1^0 RT\left[-\frac{\tilde{\rho}_1}{\tilde{T}_1} + \frac{\tilde{P}_1}{\tilde{\rho}_1\tilde{T}_1} + \left(\frac{1}{\tilde{\rho}_1}-1\right)\ln(1-\tilde{\rho}_1) + \frac{1}{r_1^0}\ln\tilde{\rho}_1\right] \tag{3.18}$$

where $\tilde{\rho}_1 \equiv \rho/\rho_1^*$, and Eq. 3.12 can be expressed as:

$$r_1^0 RT\left[-\frac{\tilde{\rho}_1}{\tilde{T}_1} + \frac{\tilde{P}_1}{\tilde{\rho}_1\tilde{T}_1} + \left(\frac{1}{\tilde{\rho}_1}-1\right)\ln(1-\tilde{\rho}_1) + \frac{1}{r_1^0}\ln\tilde{\rho}_1\right] = RT\left[\ln\phi_1 + \left(1-\frac{r_1}{r_2}\right)\phi_2 + r_1^0\tilde{\rho}_m\frac{P_1{}^* + P_2{}^* - 2P_{12}{}^*}{P_1{}^*\tilde{T}_1}\phi_2^2\right] + r_1^0 RT\left[-\frac{\tilde{\rho}_m}{\tilde{T}_1} + \frac{\tilde{P}_1}{\tilde{\rho}_m\tilde{T}_1} + \left(\frac{1}{\tilde{\rho}_m}-1\right)\ln(1-\tilde{\rho}_m) + \frac{1}{r_1^0}\ln\tilde{\rho}_m\right] \tag{3.19}$$

Equations 3.3 through 3.11, 3.16, 3.17, and 3.19 together with experimental data were used to obtain the solubility of CO_2 and $\rho_m(P,T)$.

3.2.3 Methods of Solubility Measurement

Five methods have been proposed to determine the solubility of a gas in a polymer: barometric, gravimetric, spectroscopic, volumetric, and in-line. The first two of these are relevant to the present study. In the barometric (pressure decay) method [5-16], the initial weight of the sample is measured, and it is then exposed to the gas in a high-pressure vessel. The pressure will decrease due to the loss of CO_2 from the gas phase. The dissolved amount is inferred from the pressure decrease of the gas using an equation of state (EOS) for the gas. However, the volume of the gas phase decreases due to polymer swelling, and the solubility cannot be determined without knowing the swollen volume. In the gravimetric method, the sample is placed in a high-pressure vessel as in the case of the barometric method, but a pump keep the pressure constant by compensating for the dissolved gas. A balance monitors the weight of the sample until there is no further change with time, or the sample can be transferred to a balance outside of the vessel to measure the weight after a certain amount of time. Several methods were evaluated for measuring the weight of the sample: quartz crystal, quartz spring, microbalance, magnetic suspension balance [2,17-22], and electro-balance. As in the barometric method, the swollen volume must be known, as this affects the buoyancy and decreases the net weight. Tomasko *et al.* [23] summarized solubility data obtained using both barometric and gravimetric methods up to 2003.

3.2.4 Determination of Swollen Volume

An indirect method has been used to predict the swollen volume and gas solubility in the polymer [3,16,19,20,22,24]. Data alone cannot reveal the solubility if the swollen volume is unknown. Moreover, an EOS alone cannot predict solubility or swollen volume, since one or two parameters in the EOS must be determined

experimentally. However, combining an EOS with data can yield both the solubility and the swollen volume. The details of the procedure are described in Section 3.5.

Royer *et al.* [25] used a view cell to observe the swelling of Poly (dimethylsiloxane) (PDMS) by CO_2. A sapphire window in the high-pressure cell made it possible to use a digital camera to record images of the swelling sample. The amount of swell was determined from the height increase of the sample, and a 300% increase in volume at 27.6 MPa and 50℃ occurred during 10 hours. They also used the Sanchez-Lacombe (S-L) model to predict the swelling behavior and reported there was a close agreement between the prediction and the data. Nikitin *et al.* [26] employed a view cell of silica glass and reported a maximum 50% increase in volume for poly(butyl methacrylate) (PBMA) at 9 MPa and 38℃. Other research groups [27-30] have used similar methods. While a view cell allows direct measurement of swelling, the error can be large for a material that swells little, such as HDPE.

Recently, Funami *et al.* [2] developed a method to determine the density of a polymer/CO_2 mixture using a magnetic suspension balance (MSB). They immersed a platinum disk into a polymer sample fixed in the MSB and introduced CO_2 at high pressure and temperature. The disk was connected to a weight-measuring unit by a thin wire. The net weight of the disk in the sample is lower than that in the air due to buoyancy. While CO_2 was dissolving in the sample, the net weight of the disk increased, tracking the decrease of the sample density due to the decreased buoyancy. At equilibrium, the density of the mixture can be inferred from the total change of the weight. They measured the solubility of CO_2 in polymers up to 15 MPa and found that the agreement between the direct determination and indirect prediction using the S-L model was excellent even though it may take much time to reach the equilibrium net weight due to high melt viscosity of polymer. However, this method had not been developed yet when solubility measurements were made for this project, and the indirect method was used.

3.3 Apparatus: Magnetic Suspension Balance

A magnetic suspension balance (MSB) manufactured by Rubotherm and installed at the University of Toronto [22] was used to measure the density of CO_2 and the weight change of HDPE due to dissolved CO_2. Its principal components are: balance, magnets, sample holder, high-pressure and temperature chamber, and pressure and temperature transducers. Figure 3.2 is a photo and a schematic of this instrument.

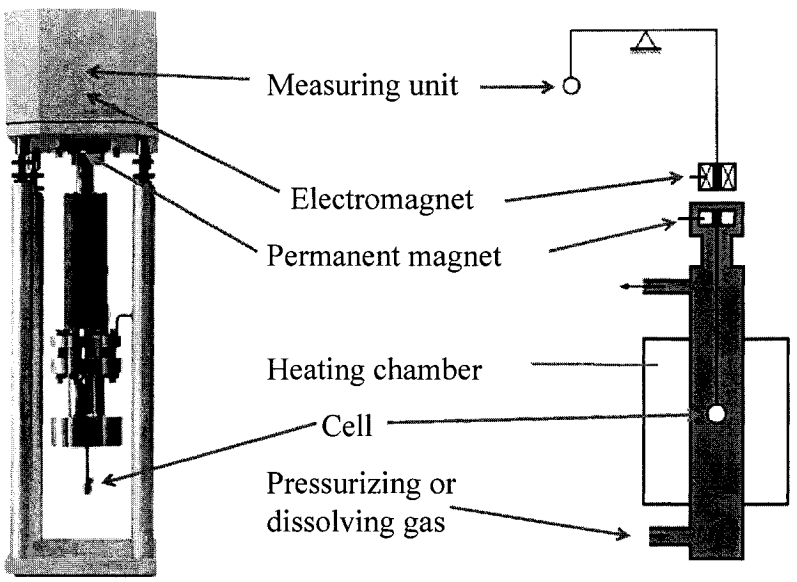

Figure 3.2. Photo and schematic of MSB. A high pressure chamber is not shown in the photo.

The MSB measures three types of weight. One (W_{R1}) is with no sample/sample holder and no sinker, which is a titanium weight used for determining the gas density. A second (W_{R2}) is with the sample/sample holder but no sinker, and the third (W_{R3}) is with the sample/sample holder and sinker. Figure 3.3 shows these situations. The measurements are performed in series by connecting or disconnecting the sample holder and sinker to or from the magnet. The weight of the sample/holder is determined using Eq. 3.20:

$$W_R(P,T) \equiv W_{R2}(P,T) - W_{R1}(P,T) \tag{3.20}$$

The weight of the sinker is necessary to obtain the gas density and is given by:

$$W_{sinker}(P,T) \equiv W_{R3}(P,T) - W_{R2}(P,T) \tag{3.21}$$

All measurements are carried out automatically by MessPro, the operating software for the MSB.

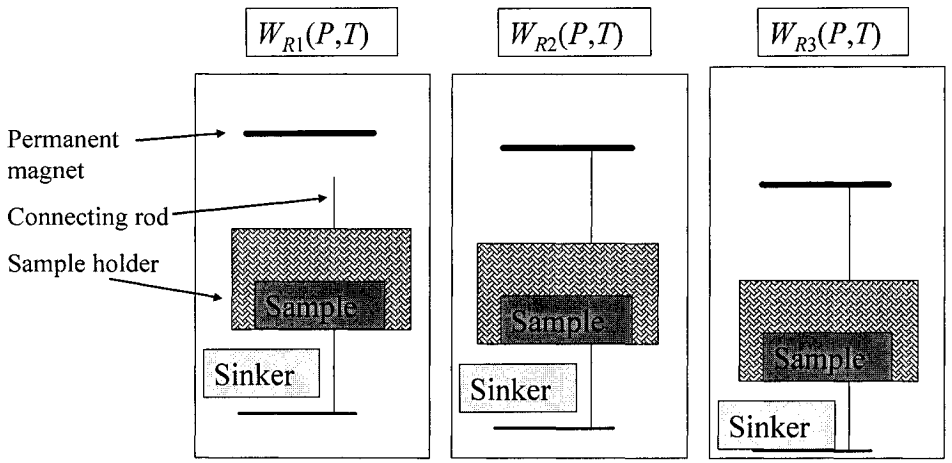

Figure 3.3. Illustration of three types of weight reading.

First, the weight of polymer W_{pol} is measured before introducing CO_2. Second, with the sample in the chamber, gas is introduced while a heater keeps the set temperature, and a syringe pump maintains the desired CO_2 pressure. The balance monitors the weight change of the sample. Diffusion of gas will continue until the system reaches equilibrium, *i.e.* until the chemical potentials of gas in the gas and mixture are the same. After this no further change in weight occurs, the solubility of gas in the sample can be obtained by:

$$S(P,T) = \Delta W(P,T) / W_{pol} \tag{3.22}$$

where W_{pol} is the initial weight of the sample, *i.e.*, the weight of the pure polymer, and $\Delta W(P,T)$ is the total weight change of the sample.

Because the sample is immersed in a fluid, buoyancy must be considered. This analysis is based on Archimedes' principle, which states that a body immersed in a fluid loses weight by an amount equal to the weight of the fluid it displaces:

$$W_R = W_{body} - \rho_g V_{body} \tag{3.23}$$

where W_R is the weight reading or net weight, W_{body} is the actual weight of the immersed body, and V_{body} is the volume of the body. Two quantities must be taken into account to compensate for the buoyancy: the density of the surrounding fluid ρ_g, and the volume of the immersed body. The procedure for analyzing the data is as follows. (1) The gas density is obtained using Archimedes' principle. Net weights are measured at different pressures:

$$W_R(P,T) = W_{sinker}(P,T) - \rho_g(P,T)\, V_{sinker}(T) \tag{3.24}$$

$$W_R(0,T) = W_{sinker}(0,T) - \rho_g(0,T)\, V_{sinker}(T) \tag{3.25}$$

where $\rho_g(0,T) = 0$, W_{sinker} is the weight of the sinker, $W_{sinker}(P,T) = W_{sinker}(0,T)$, and V_{sinker} is the volume of the sinker, which is assumed to be incompressible and thus equal to the value specified by the manufacturer (4.33094 cm^3). Subtracting Eq. 3.25 from Eq. 3.24 yields:

$$\rho_g(P,T) = \frac{-\Delta W_{sinker}(P,T)}{V_{sinker}(T)} \tag{3.26}$$

where $\Delta W_{sinker}(P,T) = W_{sinker}(P,T) - W_{sinker}(0,T)$. (2) The swollen volume of the sample $V_{sw}(P,T)$ can not be measured and is estimated using an EOS. A detailed analysis to obtain $V_{sw}(P,T)$ is presented in Section 3.5. The equation for the weight change, accounting for the buoyancy, is:

$$\Delta W(P,T) = \Delta W_R(P,T) + \rho_g(P,T)[V_{pol}(P,T) + V_{sw}(P,T) + V_{holder}(T)] \quad (3.27)$$

where $V_{pol}(P,T)$ is the volume of the pure polymer, determined by *PVT* measurements, and $V_{holder}(T)$ is the volume of the sample holder, as determine by a blank run as described in Section 3.4.2. The volume of the mixture is defined as:

$$V_m(P,T) \equiv V_{pol}(P,T) + V_{sw}(P,T) \quad (3.28)$$

Equation 3.29 summarizes the procedure for determining the weight change of the sample. Finally, the solubility of CO_2 in HDPE is obtained using Eqs. 3.22, 3.26 and 3.27.

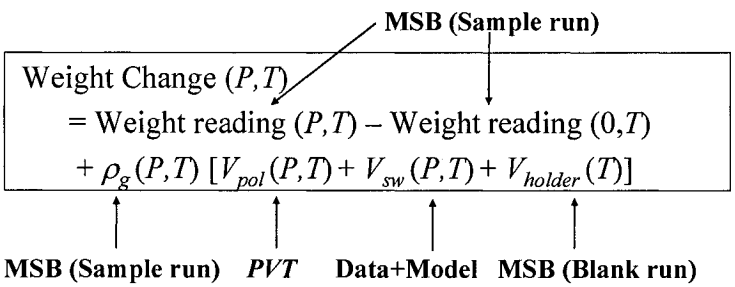

(3.29)

3.4 Experimental Procedure

3.4.1 Sample Preparation

The disk-shaped sample is prepared by compression molding at 165℃ and has a thickness of 3 mm and a diameter of 10 mm. It is kept in a vacuum oven at 50℃ for eight hours prior to a run to minimize the presence of volatiles.

3.4.2 Blank Run

The volume of the sample holder can be obtained by a blank test at 180℃. The system with no sample is heated, while a vacuum pump exhausts the chamber. When

no change in weight is observed, the vacuum pump is turned off. Carbon dioxide is then introduced at a pressure of 6.9 MPa (1000 psi) by use of an ISCO syringe pump, and values of W_{R1}, W_{R2}, and W_{R3} are recorded every three min for two hours. These steps are repeated until the pressure reaches 27.6 MPa (4,000 psi) with a pressure interval of 6.9 MPa. After W_{sinker} and W_R have been measured at each pressure, ΔW_{sinker} is used to calculate the gas density by using Eq. 3.26, and ΔW_R, the change in the weight reading for the sample holder, is used to calculate the volume of the sample holder using Eq. 3.30:

$$\rho_g(T,P) = \frac{-\Delta W_R(T,P)}{V_{holder}(T)} \tag{3.30}$$

The slope of a plot of $-\Delta W_R(T,P)$ versus $\rho_g(T,P)$ is $V_{holder}(T)$ and was found to be 1.2689 cm^3. Figure 3.4 shows that the slope is independent of pressure, and this confirms incompressibility of the sample holder.

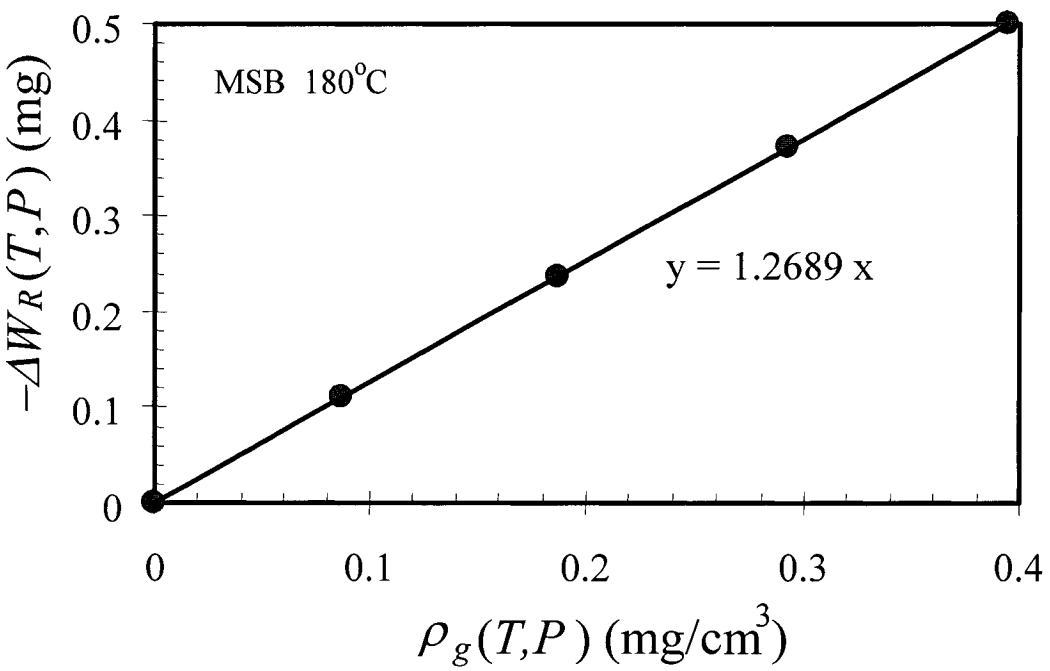

Figure 3.4. Determination of the volume of sample holder.

3.4.3 Sample Run

The procedure for a run with a sample is the same as for a blank run except that a sample is present. After the sample is loaded in the holder, its weight is measured, and the system is heated to the set temperature while a vacuum pump exhausts the chamber. The chamber is first pressurized to 3.4 MPa (500 psi) for two hours. The wait time was chosen after considering the diffusion time. Based on the diffusion study described in Chap. 6, two hours was found to be well above the saturation time for the thickness of 3 mm (Fig. 3.5). The absorption of gas causes a small pressure decrease, even though the syringe gas pump tries to maintain the set pressure, and this slight variation in pressure can cause a fluctuation in the weight reading. This problem can be solved by allowing the system to sit for a period well beyond the saturation time. The next step is to increase the pressure up to 6.9 MPa (1000 psi), and the system is again left for two hours. The pressure is further increased in steps until it reaches 34.5 MPa (5,000 psi).

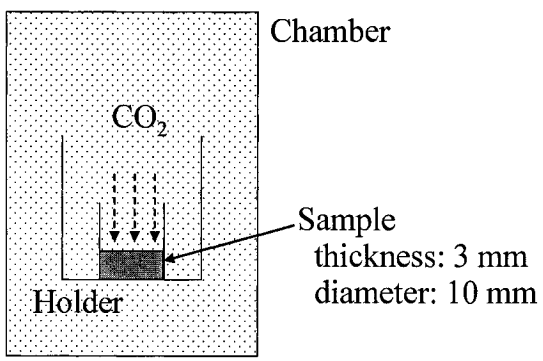

Figure 3.5. CO_2 diffusion into the sample.

3.5 Data Analysis

The swollen volume must be known to calculate the solubility, but it could not be measured. Nor could it be calculated from theory, because there are three unknowns (ρ_m, K_{12}, ϕ_1) but only two equations (Eqs. 3.3 and 3.19). A method used by other researchers [3,16,19,20,22,24] was employed to estimate the solubility, and the

computational scheme and procedure are summarized in Fig. 3.6. First, a value of the interaction parameter K_{12} is assumed and used in the EOS (Eq. 3.3) and the chemical potential equation (Eq. 3.19). By solving these equations simultaneously at P and T, the density of the mixture (ρ_m) and volume fraction of gas (ϕ_1) can be obtained. The swollen volume (V_{sw}) is then calculated using ρ_m and V_{pol}, and the theoretical solubility (S_T) is obtained from the relationship between solubility and weight fraction:

$$S = \frac{W_1}{1 - W_1} \ (\mathrm{g-CO_2/g-HDPE}) \tag{3.31}$$

where W_1 is the weight fraction of CO_2 obtained from Eq. 3.6. The subscript T is used to distinguish theoretical solubility from true solubility. The swollen volume is used in Eq. 3.27 with other experimental data to give the weight change (ΔW), accounting for the buoyancy effect. The solubility (S_{TE}) is calculated using Eq. 3.22. While S_T is a purely theoretical solubility based on the assumed K_{12}, S_{TE} is a half theoretical and half experimental quantity. The two values are compared, and the above procedure is repeated after revising K_{12}, until the difference is minimized. These steps are performed at each pressure using a Matlab code.

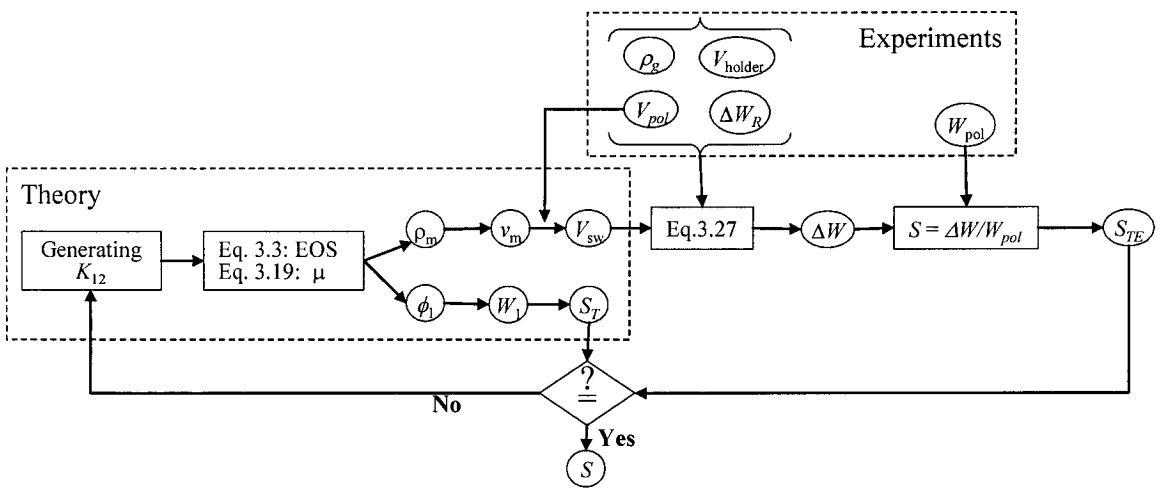

Figure 3.6. Flow chart for solubility calculation.

3.6 Results and Discussion

Figure 3.7 shows the effect of pressure on the density of CO_2 at 180℃ and pressures from 0.1 to 34 MPa. These data were used to obtain the parameters of the S-L model [1] for CO_2 and to determine the buoyancy effect. The parameters were determined by the least-square method using as initial guesses values reported by Areerat *et al.* [21] for an MSB system. The parameters for CO_2 are given in Table 3.1, and those for HDPE were determined by *PVT* measurements (Chap. 2). These were used to determine the parameters of the S-L model for the mixture by using the mixing rule.

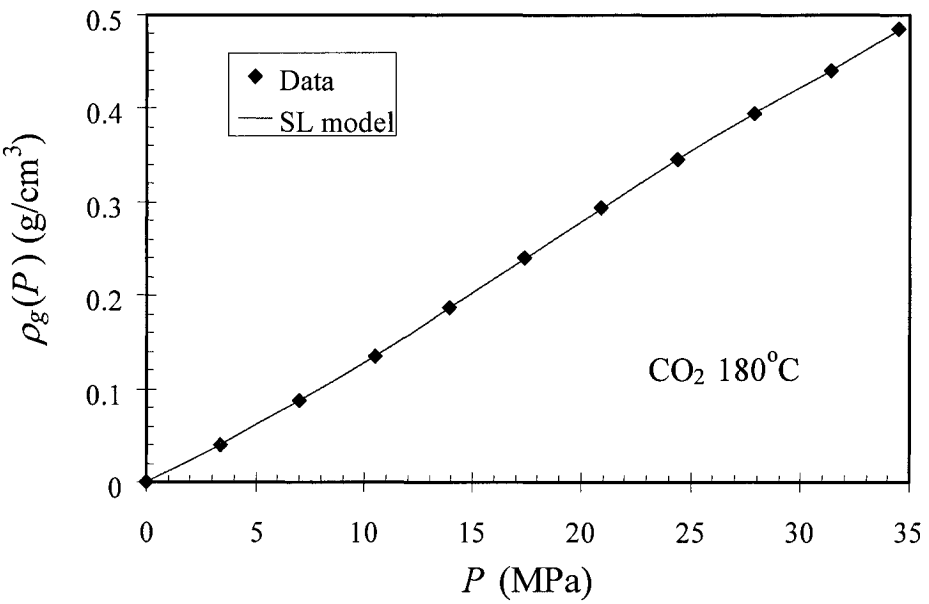

Figure 3.7. Effect of pressure on CO_2 density.

Table 3.1. Parameters for S-L model.

Material	ρ^*	P^*	T^*
	g/cm^3	MPa	K
CO_2	1.725	727.4	319
HDPE	0.876	408.3	570

Figure 3.8 shows the solubility increase with pressure. At 34 MPa, the solubility reaches 0.32 g-CO_2/g-HDPE and 24.5W% (100g-CO_2/g-mixture). Precise solubility data can only be obtained if the swollen volume is known. The solubilities obtained in this work were compared with those reported by Sato *et al.* [24], who used the pressure decay method and the same computational method as in this work. To estimate the swollen volume, they used literature values for the CO_2 parameters of the S-L model rather than determining them experimentally. Fig. 3.8 shows that there is an 8% difference between their data and those of this study.

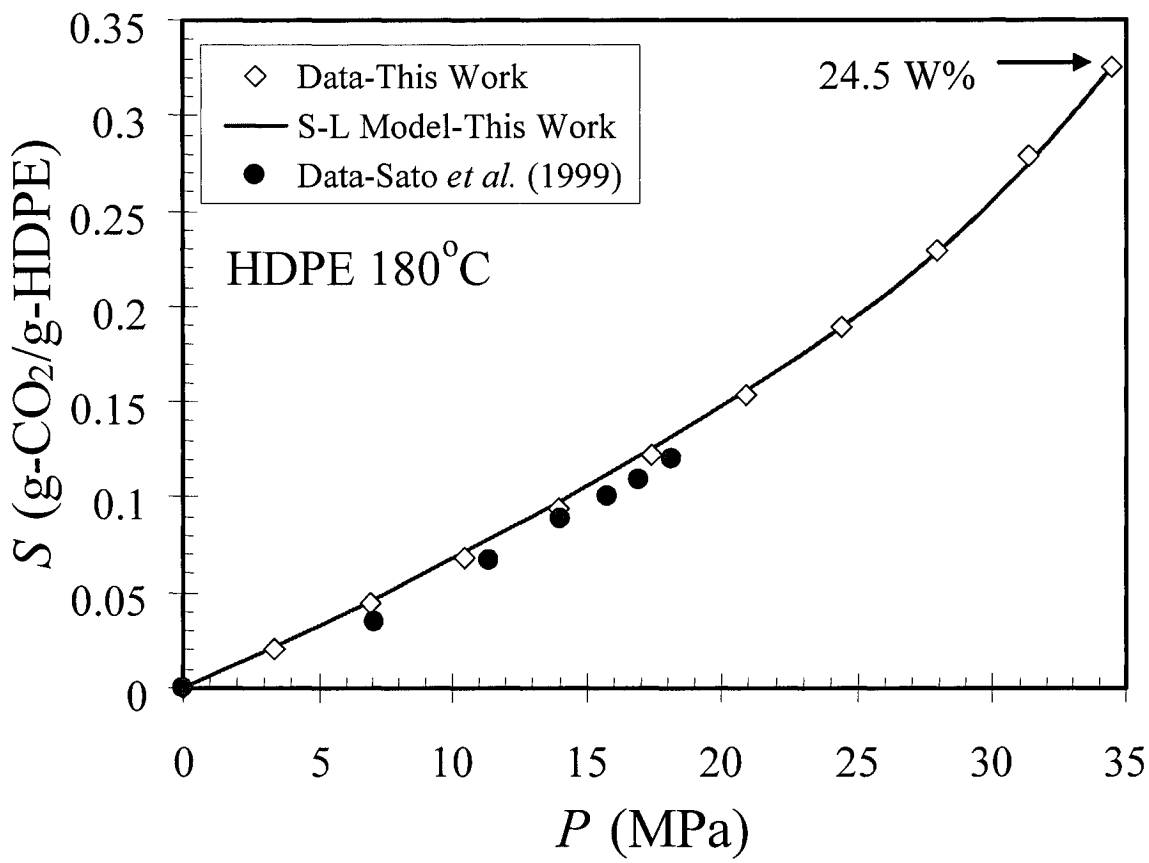

Figure 3.8. Effect of pressure on the CO_2 solubility in HDPE.

Figure 3.9 shows the mixture volume as a function of pressure. A 38% increase of the mixture volume was observed at 34 MPa. The linear swell factor k can be obtained from the mixture volume as:

$$k^2(P,C) \equiv V_m(P,C)/V_{pol}(P_0) \tag{3.32}$$

and is used in Section 6.6.2.4 to study the effect of the moving boundary. The power of two instead of three is used for the swell factor because a sample swells in only two directions in the HPSPR. For example, $k(18\,\mathrm{MPa}) = \sqrt{1.15} \cong 1.07$, and $k(34\,\mathrm{MPa}) = \sqrt{1.37} \cong 1.17$. At 18 and 34 MPa, 7 and 17% linear swells occur, respectively.

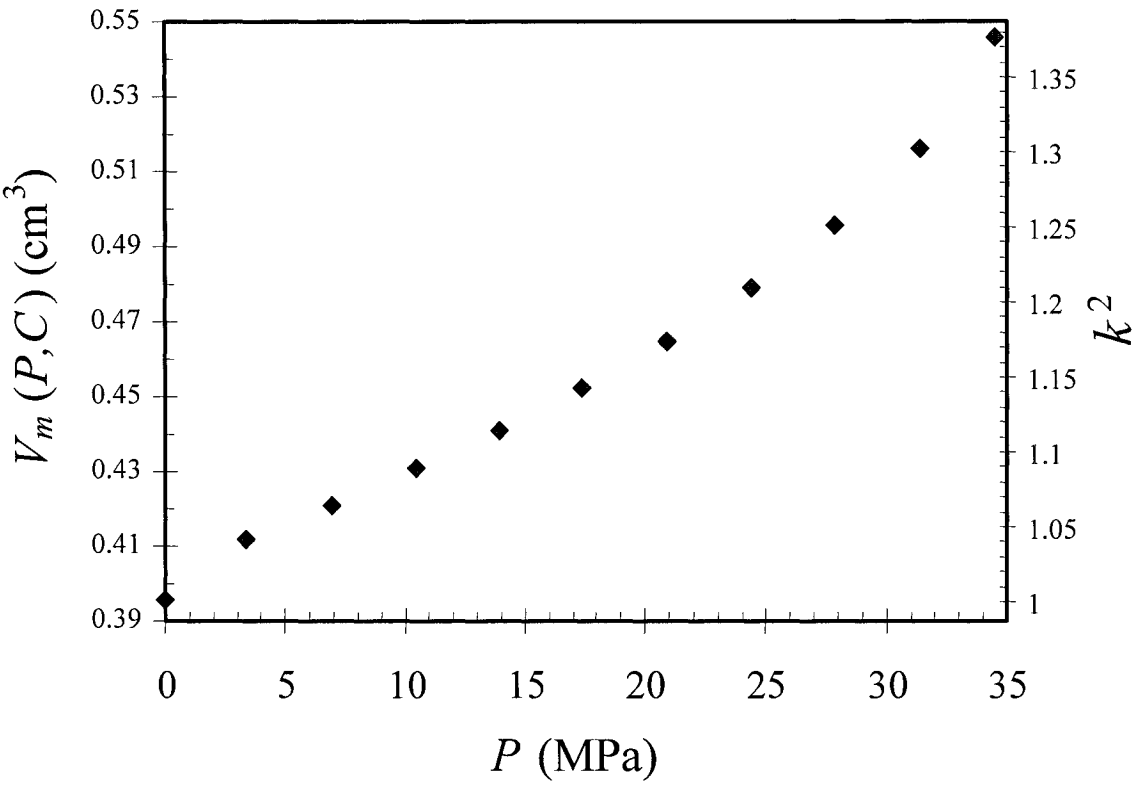

Figure 3.9. Volume of the mixture pressurized with CO_2 and the linear swell factor, W_{pol} = 0.3 g.

Figure 3.10 shows the effect of CO_2 pressure on the vertical shift factor [31]:

$$b_{P,C}(P,C) \equiv \frac{C_{pol}(P,C)}{\rho_{pol}(P_0)} = \frac{W_{pol}/V_m(P,C)}{W_{pol}/V_{pol}(P_0)} = \frac{V_{pol}(P_0)}{V_m(P,C)} = \frac{1}{k^2} \tag{3.33}$$

There is a 28% decrease of $b_{P,C}(P,C)$ at 34 MPa, and this is large enough to affect the rheological properties. This will be discussed in Chap. 4 and used for the study for the effect of CO_2 on viscosity in Chap. 6.

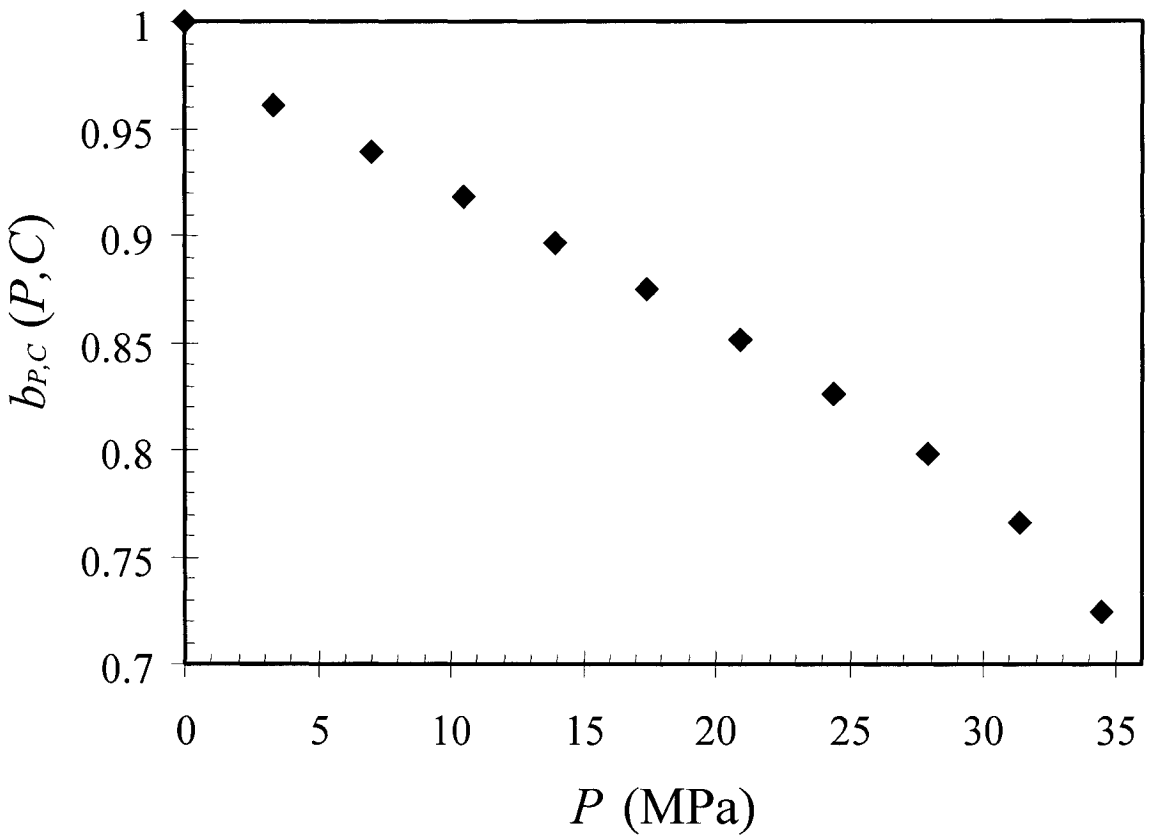

Figure 3.10. Effect of pressure on the concentration vertical shift factor, HDPE 180℃.

3.7 Conclusions

A magnetic suspension balance (MSB) was used to determine the solubility of CO_2 in HDPE and the volume of the HDPE/CO_2 mixture. To analyze the data, the Sanchez-Lacombe model and a mixing rule were used. The buoyancy effect arizing from CO_2 presence was accounted for by using the *PVT* data for HDPE and the CO_2 density. The solubility of CO_2 in HDPE at 34 MPa is 0.32 g-CO_2/g-HDPE, and the volume of the HDPE/CO_2 mixture at 34 MPa is 38% higher than that at 1 atm. The vertical shift factor of CO_2 concentration was also determined for use in making master curves of the rheological properties.

3.8 References

1. I.C. Sanchez and R.H. Lacombe, "Statistical thermodynamics of polymer solutions," *Macromolecules* 11:1145 (1978).
2. E. Funami, K. Taki, S.-i. Kihara, and M. Ohshima, "Measurement of CO_2-induced polymer swelling and predictability of Sanchez-Lacombe equation of state for the density of polymer/CO_2 systems," The 10th Asian Pacific Confederation of Chemical Engineering (APCChE), Kitakyushu, Japan, Section 2H-10 (2004).
3. S. Hilic, S.A.E. Boyer, A.A.H. Padua, and J.P.E. Grolier; "Simultaneous measurement of the solubility of nitrogen and carbon dioxide in polystyrene and of the associated polymer swelling," *J. Polym. Sci. Pol. Phys.*, 39:2063 (2001).
4. M.B. Kiszak, M.A. Meilchen, and M.A. McHugh, "Modeling high pressure gas-polymer mixtures the Sanchez-Lacombe equation of state," *J. Appli. Pol. Sci.* 36:583 (1998).
5. S.A. Stern and A.H. De Meringo, "Solubility of carbon dioxide in cellulose acetate at elevated pressures," *J. Pol. Sci.: Pol. Phys. Edi.* 16:735 (1978).
6. R.G. Wissinger and M.E. Paulaitis, "Swelling and sorption in polymer-CO_2 mixtures at elevated pressures," *J. Pol. Sci.: Part B: Pol. Phys.* 25:2497 (1987).
7. D.H. Rein, J. Csernica, R.F. Baddour, and R.E. Cohen, "CO_2 diffusion and solubility in a polystyrene-polybutadiene block copolymer with a highly oriented lamellar morphology," *Macromolecules* 23:4456 (1990).
8. Y. Sato, M. Yurugi, T. Yamabiki, S. Takishima, and H. Masuoka, "Solubility of propylene in semicrystalline polypropylene," *J. Appli. Pol. Sci.* 79:1134 (2001).
9. V.M. Shah, B.J. Hardy, and S.A. Stern, "Solubility of carbon dioxide, methane, and propane in silicone polymer. Effect of polymer side chains," *J. Pol. Sci.: Part B: Pol. Phys.* 24:2033 (1986).
10. G.K. Fleming and J.W. Koros, "Dilation of polymers by sorption of carbon dioxide at elevated pressures. 1. Silicone rubber and unconditioned polycarbonate," *Macromolecules* 19:2285 (1986).
11. G.K. Fleming and J.W. Koros, "Dilation of substituted polycarbonates caused by high-pressure carbon dioxide sorption," *J. Pol. Sci.: Part B: Pol. Phys.* 28:1137 (1990).
12. D.S. Pope, I.C. Sanchez, J.W. Koros, and G.K. Fleming, "Statistical thermodynamic interpretation of sorption/dilation behavior of gases in silicone rubber," *Macromolecules* 24:1779 (1991).
13. K.H. Brodt and G.C.J. Bart, "The Delft sorption set-up as an instrument to determine the intrinsic solubility and diffusion coefficient of gases in plastics," *J. Cellular Plastics* 26:478 (1993).

14. V.M. Shah, B.J. Hardy, and S.A. Stern, "Solubility of carbon dioxide, methane, and propane in silicone polymer. Effect of polymer backbone chains," *J. Pol. Sci.: Part B: Pol. Phys.* 31:313 (1993).

15. D.S. Pope and J.W. Koros, "Gas sorption-induced dilation of poly(4-methyl-1-pnetene)," *J. Pol. Sci.: Part B: Pol. Phys.* 34:1861 (1996).

16. Y. Sato, M. Yurugi, K. Fujiwara, S. Takishima, and H. Masuoka, "Solubility of carbon dioxide and nitrogen in polystyrene under high temperature and pressure," *Fluid Phase Equilibria.* 125:129 (1996).

17. J. von Schnitzler and R. Eggers, "Mass transfer in polymers in a supercritical CO_2-atmosphere," *J. Supercrit. Fluids* 16:81 (1999).

18. Y. Sato, T. Takikawa, A. Sorakubo, S. Takishima, and H. Masuoka, "Solubility and diffusion coefficient of carbon dioxide in biodegradable polymers," *Ind. Eng. Chem. Res.* 39:4813 (2000).

19. Y. Sato, T. Takikawa, S. Takishima, and H. Masuoka, "Solubility and diffusion coefficient of carbon dioxide in poly(vinyl acetate) and polystyrene," *J. Supercrit. Fluids* 19:187-198 (2001).

20. Y. Sato, T. Takikawa, M. Yamane, S. Takishima, and H. Masuoka, "Solubility and of carbon dioxide in PPO and PPO/PS blends," *Fluid Phase Equilibria* 194-197:847 (2002).

21. S. Areerat, Y. Hayata, R. Katsumoto, T. Kegasawa, H. Egami, and M. Ohshima, "Solubility of carbon dioxide in polyethylene/titanium dioxide composite under high pressure and temperature," *J. Appli. Pol. Sci.* 86:282 (2002).

22. G. Li, J. Wang, C.B. Park, P. Moulinie, and R. Simha, "Comparison of SS-based and SL-based estimation of gas solubility," 62nd *ANTEC* 2:2566 (2004).

23. D.L. Tomasko, H. Li, D. Liu, X. Han, M.J. Wingert, L.J. Lee, and K.W. Koelling, "A review of CO_2 applications in the processing of polymers," *Ind. Eng. Chem. Res.* 42:6431, (2003).

24. Y. Sato, K. Fujiwara, T. Takikawa, Sumarno, S. Takishima, H. Masuoka, "Solubility and diffusion coefficients of carbon dioxide and nitrogen in polypropylene, high-density polyethylene, and polystyrene under high pressure and temperatures," *Fluid Phase Equilibria* 162:261 (1999).

25. J.R. Royer, J.M. DeSimone, and S.A. Khan, "Carbon dioxide-induced swelling of poly(dimethylsiloxane)," *Macromolecules* 32:8965, (1999).

26. L.N. Nikitin, E.E. Said-Galiyev, R.A. Vinokur, A.R. Khokhlov, M.O. Gallyamov, and J. Schaumburg, "Poly(methyl methacrylate) and poly(butyl methacrylate) swelling in supercritical carbon dioxide," *Macromolecules* 35:934, (2002).

27. B.J. Briscoe and C.T. Kelly, "The effect of structure on gas solubility and gas induced dilation ain a series of poly(urethane) elastomers," *Polymer* 37:15, 3405,

(1996).

28. J. von Schnitzler and R. Eggers, "Mass transfer in polymers in a supercritical CO_2-atmosphere," *J. Supercrit. Fluids* 16:81 (1999).

29. H. Li, L.J. Lee, and D.L. Tomasko, "Effect of carbon dioxide on the interfacial tension of polymer melts," *Ind. Eng. Chem. Res.* 43:509 (2004).

30. Y.G. Li, H.B. Li, J. Wang, C.B. Park, H.S. Park, and P. Chen, "Measurement of swollen volume of polymer melt due to gas dissolution," The 62nd *SPE ANTEC* 2540 (2005).

31. J.D. Ferry, "Mechanical properties of substances of high molecular weight. VI. Dispersion in concentrated polymer solutions and its dependence on temperature and concentration," *J. of the Am. Chem. Soc.*, 72:3746 (1950).

4. Previous Work on the Effects of Temperature, Pressure, and Concentration

It is very important to know how rheological properties depend on the state variables in polymer processing. A number of theoretical and experimental approaches have been used to obtain these dependencies. Previous studies of the dependency of the viscosity on T, P, and concentration C of dissolved gas are discussed here.

4.1 Effect of Temperature, Pressure, and Concentration on Viscosity

In 1883 Barus [1] carried out high-pressure experiments with "marine glue" using an apparatus similar to a capillary rheometer (Section 6.3.1.1.1) and analyzed the data using Poiseuille's law. He suggested that the form of the relationship between the viscosity and pressure is that shown by Eq. 4.1:

$$\log[\eta_0(P)] = a + \beta P \tag{4.1}$$

where a and β are constants, and Eq. 4.1 can be rewritten in the following well-known form:

$$\ln\left[\frac{\eta_0(P)}{\eta_0(P_0)}\right] = \beta(P - P_0) \tag{4.2}$$

where P_0 is the reference pressure. In 1913 de Guzmán [2] proposed the following empirical relationship between viscosity and temperature:

$$\log[\eta_0(T)] = a' + B/T \tag{4.3}$$

where a and B are constants, and Eq. 4.3 can be rearranged to obtain the Arrhenius equation [1]:

$$\ln\left[\frac{\eta_0(T)}{\eta_0(T_0)}\right] = \frac{E_a}{R}\left(\frac{1}{T} - \frac{1}{T_0}\right) \tag{4.4}$$

where T_0 is the reference temperature. Only much later were these relationships derived theoretically.

Two theoretical approaches have been proposed to model the dependency of the viscosity on T and P. Both approaches involve the concept of free volume, but one, the absolute reaction rate theory, is associated with the change of reaction rate or activation energy with T and P, while the other, the free volume theory, is based on the change of free volume with T and P. Each approach considers the flow mechanism in a different way, and their predictions and applicable operating ranges are thus different. A detailed description of both approaches is given in Appendix 3.

4.1.1 Master Curves and Shift Factors

The method of reduced variables has been an essential tool for describing the dependency of rheological variables on the state variables (T,P,C), because using only the concept of shift factors, and reduced variables, the dependency can be described quantitatively. Materials whose behavior can be described in this manner are said to exhibit thermorheological or piezorheological simplicity or time-temperature [2] or time-pressure superposition. The origin of this concept is described in Appendix 4. A composite plot using reduced variables is called as a master curve.

In order to obtain a master curve that brings together data obtained at various temperatures and polymer concentrations, we need to make use of vertical and horizontal shift factors. Based on thermodynamic arguments, stresses should scale with the product of polymer density and temperature. For a pure polymer, therefore, the vertical [3] T shift factor b_T for stress quantities, *e.g.* $G(t)$ or $G'(\omega)$, should be:

---

1) Even though de Guzmán proposed Eq. 4.3 earlier than other researchers including Arrhenius [3], this equation is called "the Arrhenius equation" or "Arrhenius type equation" owing to the similarity to the Arrhenius equation for reaction rate constant: $k = A\exp(-E_a/RT)$ [4].

2) Considering a necessity of vertical shift factors (b_T, b_P, or b_C), which do not involve time, the phrase 'time-' does not express the whole aspect of building a master curve.

$$b_T(T) \equiv \frac{\rho_{pol}(T)T}{\rho_{pol}(T_0)T_0} \tag{4.5}$$

where ρ_{pol} is the density of polymer, and the subscript zero indicates the reference conditions. For a solution [5], the density is replaced by the polymer concentration C_{pol}, expressed in the same units as density (g/cm^3), and the factor becomes

$$b_{T,C}(T,C) \equiv \frac{C_{pol}(T,C)T}{\rho_{pol}(T_0,C_0)T_0} \tag{4.6}$$

where C is the solvent concentration, which is often used as the independent variable for a_C and b_C because it can be controlled directly, and C_{pol} is defined as Eq. 4.7:

$$C_{pol}(T,C) \equiv \frac{W_{pol}}{V_m(T,C)} \tag{4.7}$$

where W_{pol} is the weight of pure polymer in the solution, and V_m is the volume of the solution. There is no theory that suggests the form of a vertical pressure shift factor, but the approach is to use the $b_T(T)$ factor with $T = T_0$:

$$b_P(P) \equiv \frac{\rho_{pol}(P)}{\rho_{pol}(P_0)} \tag{4.8}$$

Finally, the vertical T, P, and C shift factor is

$$b_{T,P,C}(T,P,C) \equiv \frac{C_{pol}(T,P,C)T}{\rho_{pol}(T_0,P_0,C_0)T_0} \tag{4.9}$$

The horizontal [4] T shift factor a_T for frequency, shear rate, or time can be determined from the effect of temperature on the zero-shear viscosity if $\eta_0(T)$ is known:

3) A vertical shift factor is also called a stress or density shift factor.
4) A horizontal shift factor is also called a time, frequency, or shear rate shift factor.

$$a_T(T)b_T(T) \equiv \frac{\eta_0(T)}{\eta_0(T_0)} \tag{4.10}$$

or by shifting the stress curve at T onto that at T_0. The second method is used when $\eta_0(T)$ is not available, but $\eta_0(T)$ is naturally calculated by Eq. 4.10 while a_T is determined involving the least square method for the superposition. This method involves plots of stress versus shear rate, where the shift is carried out only along the shear rate axis, *i.e.*, horizontal shift on a stress-shear rate plot, rather than plots of viscosity versus shear rate, which require shifts along both axes. A temperature-independent viscosity plot is then constructed by plotting a master curve:

$$\frac{\eta(T)}{a_T(T)b_T(T)} \quad \text{versus } \dot{\gamma}a_T(T) \tag{4.11}$$

However, the vertical shift factor is often omitted, as it is rarely far from one, especially for crystallizable polymers, due to the limited range of temperatures that are experimentally accessible. When this is the case, the horizontal temperature shift factor is reduced to:

$$a_{1,T}(T) = \frac{\eta_0(T)}{\eta_0(T_0)} \tag{4.12}$$

where the subscript 1 is added in this thesis to distinguish this factor from a_T of the case considering b_T, because the horizontal temperature shift factor ignoring $b_T(T)$ will be different from that when $b_T(T)$ is used. A temperature-independent viscosity plot for this case is then constructed by plotting:

$$\frac{\eta(T)}{a_{1,T}(T)} \quad \text{versus } \dot{\gamma}a_{1,T}(T) \tag{4.13}$$

Since $a_{1,T}(T)$ is proportional to $\eta_0(T)$ for the same polymer *i.e.* the same $\eta_0(T_0)$, the above equation can be combined to show that a temperature-independent plot can be obtained by plotting:

$$\frac{\eta(T)}{\eta_0(T)} \quad \text{versus } \dot{\gamma}\eta_0(T) \tag{4.14}$$

if $\eta_0(T)$ is known.

In order to deal with the effect of pressure, the above equations are easily modified by replacing a_T with a_P, which can be determined from the effect of pressure on the zero-shear viscosity:

$$a_P(P)b_P(P) \equiv \frac{\eta_0(P)}{\eta_0(P_0)} \tag{4.15}$$

or by shifting the stress curve at P on to that at P_0 [6]. A pressure-independent viscosity plot is then constructed by plotting:

$$\frac{\eta(P)}{a_P(P)b_P(P)} \quad \text{versus } \dot{\gamma}a_P(P) \tag{4.16}$$

If the vertical temperature shift factor is omitted, *i.e.*, b_P becomes unity, the horizontal pressure shift factor is reduced to:

$$a_{1,P}(P) = \frac{\eta_0(P)}{\eta_0(P_0)} \tag{4.17}$$

A pressure-independent viscosity plot for this case is constructed by plotting:

$$\frac{\eta(P)}{a_{1,P}(P)} \quad \text{versus } \dot{\gamma}a_{1,P}(P) \tag{4.18}$$

Alternatively, a master-curve can be obtained by plotting:

$$\frac{\eta(P)}{\eta_0(P)} \quad \text{versus } \dot{\gamma}\eta_0(P) \tag{4.19}$$

In the case of a polymer solution at T, P, and C, the vertical shift factor $b_{T,P,C}$ is likely to be necessary because a solvent can have a much larger effect on polymer

density than temperature or pressure, Thus, to obtain a master curve of data taken at various values of T, P, and C, one should plot:

$$\frac{\eta(T,P,C)}{a_{T,P,C}(T,P,C)b_{T,P,C}(T,P,C)} \quad \text{versus} \quad \dot{\gamma}a_{T,P,C}(T,P,C) \tag{4.20}$$

Or, if the zero-shear viscosity is known, one can also obtain a master curve by plotting:

$$\frac{\eta(T,P,C)}{\eta_0(T,P,C)} \quad \text{versus} \quad \dot{\gamma}\eta_0(T,P,C)/b_{T,P,C}(T,P,C) \tag{4.21}$$

To study the dependency or sensitivity of rheological properties on state variables T, P, or C, it is necessary to see the slope of a shift factor versus a state variable plot instead of the absolute value of the shift factor, which is arbitrary since it changes regarding the reference condition.

4.1.2 Models for Temperature Dependency

As long as the temperature is at least 100℃ above the glass transition temperature (T_g), an exponential equation often called the Arrhenius equation [2], which can be derived using the absolute rate theory, can usually describe the temperature shift factor [5]:

$$\ln\left[\frac{\eta_0(T)}{\eta_0(T_0)}\right]=\ln\left[a_{1,T}(T)\right]=\frac{E_a}{R}\left(\frac{1}{T}-\frac{1}{T_0}\right) \tag{4.22}$$

where E_0 is the activation energy for flow. For $T_g < T < T_g + 100$℃, the WLF equation, based on the free volume theory, provides a better fit to data [7]:

$$\ln\left[a_{1,T}(T)\right]=\frac{-B_0(T-T_0)}{\frac{v_{f_0}}{v}\left[\frac{v_{f_0}}{v}\frac{1}{\alpha_0}+(T-T_0)\right]} \tag{4.23}$$

5) A vertical shift factor was usually omitted while models for T, P, or C dependency of viscosity were developed,

where v_{f0} is the free volume at T_0 (Section A.3.2). By using the fractional free volume, $f \equiv v_f/v$, Eq. 4.23 can be rewritten in the following well-known form:

$$\ln\left[a_{1,T}(T)\right] = \frac{-(B_0/f_{T_0})(T-T_0)}{f_{T_0}/\alpha_0 + (T-T_0)} \tag{4.24}$$

where B_0 is an empirical constant usually taken to be unity, f_{T_0} is the fractional free volume at T_0, and α_0 is the isobaric thermal expansion coefficient of the free volume, which equals $(1/v)(\partial v_f/\partial T)_P$.

4.1.3 Models for Pressure Dependency

Well above the melting temperature an exponential equation that is equivalent to Barus' relationship (Eq. 4.1) can often be used to describe the pressure shift factor:

$$\ln\left[\frac{\eta_0(P)}{\eta_0(P_0)}\right] = \ln\left[a_{1,P}(P)\right] = \beta(P-P_0) \tag{4.25}$$

where β is a constant often called the pressure coefficient and is defined as:

$$\beta \equiv \frac{1}{\eta_0}\left(\frac{\partial \eta_0}{\partial P}\right)_T \tag{4.26}$$

The pressure coefficient is a function of molecular structure but not of $\dot{\gamma}$, T, or P if the material is piezorheologically simple, and the Barus equation describes the pressure dependency. Ferry and Stratton [8] suggested an analog of Eq. 4.24 to describe the pressure shift factor at temperatures near T_g:

$$\ln\left[a_{1,P}(P)\right] = \frac{(B_0/f_{P_0})(P-P_0)}{f_{P_0}/\beta_f - (P-P_0)} \tag{4.27}$$

where f_{P_0} is the fractional free volume at P_0, and β_f is the isothermal compressibility

of the free volume, $(1/v)(\partial v_f/\partial P)_T$. Equation 4.27 can be rearranged as:

$$\frac{P-P_0}{\ln[a_{1,P}(P)]} = \frac{f_{P_0}/\beta_f - (P-P_0)}{B_0/f_{P_0}} \tag{4.28}$$

and if Eq. 4.28 is applicable, a plot of $(P-P_0)/\ln a_{1,P}$ against $(P-P_0)$ will be linear, and the parameters of Eq. 4.28 can be determined from the slope and intercept.

4.1.4 Models for Combined Dependency on Temperature and Pressure

For fully molten polymers the combined shift factor for time-temperature-pressure superposition (*t-T-P-S*) is often described by a combination of Eqs. 4.22 and 4.25 that arises from the absolute rate theory:

$$a_{1,T,P}(T,P) = \exp\left[\frac{E_0}{R}\left(\frac{1}{T}-\frac{1}{T_0}\right)\right]\exp[\beta(P-P_0)] \tag{4.29}$$

assuming the effects of T and P are separable. For other cases ($T_g < T < T_g + 100℃$), the Fillers-Moonan-Tschoegl equation [9,10], based on the free volume theory, was developed to describe *t-T-P-S*:

$$\ln[a_{1,T,P}(T,P)] = -\frac{B_0}{f_{T_0P_0}}\frac{\alpha_f(P)[T-T_0]-\beta_f(T)[P-P_0]}{f_{T_0P_0}+\alpha_f(P)[T-T_0]-\beta_f(T)[P-P_0]} \tag{4.30}$$

where f_{T_0,P_0} is the fractional free volume at T_0 and P_0, $\alpha_f(P)$ is the thermal expansion coefficient of the free volume at T_0, and $\beta_f(T)$ is the isothermal compressibility of the free volume at P_0. This equation can be used to predict the viscosity at given T and P and reduces to Eq. 4.24 at $P = P_0$ and to Eq. 4.27 at $T = T_0$. This equation takes into account simultaneously the effects of T and P on the free volume and unlike Eq. 4.29 is not separable.

However, O'Reilly [11] found that a plot of $\ln a_{T,P}$ versus P for polyvinyl acetate was linear as described by Barus equation (Eq. 4.25), while $\ln a_{T,P}$ versus T exhibited

considerable curvature, as indicated by the WLF equation (Eq. 4.24). He proposed the combined shift factor shown by Eq. 4.31, which is different from Eq. 4.30 in that pressure does not appear in the denominator:

$$\ln[\,a_{1,T,P}(T,P)] = -\frac{\alpha_f a[T-T_g]-bf_0[P-P_0]}{f_0[f_0+\alpha_f(T-T_g)]} \tag{4.31}$$

where a and b are fitting constants, and f_0 is the fractional free volume at the reference state. This equation reduces to the WLF equation, at $P=P_0$ and to the Barus equation, at $T=T_g$.

4.1.5 Models for Dependency on Concentration of Dissolved Gas

Late in the 1950s when the free volume theory was attracting interest, Fujita and Kishimoto [12] derived an equation to account for the effect of dissolved molecules on the viscosity of a polymer using the free volume theory. They used a relaxometer with a sorption unit to measure stress relaxation in polyvinyl accetate (PVAc) and polymethyl acrylate (PMA) films at a certain pressure of low molecular weight vapor. To account for the effect of a small amount of dissolved gas, *i.e.*, at low concentration C, they proposed an analog of the WLF equation based on the free volume theory:

$$\ln[\,a_C(C)] = \frac{(-1/f)C}{f/\theta+C} \tag{4.32}$$

where C is the gas concentration in g-gas/g-polymer, f is the fractional free volume, *i.e.*, the ratio of free volume to total volume, and θ is the contribution of the dissolved gas to the increase of free volume. Unlike WLF [7] and FS [8] equations, which model the ratio of zero-shear viscosity at two conditions, Fujita and Kishimoto used the zero-shear viscosity corrected for the density change of polymer and modeled only a horizontal shift factor a_C, which is defined as:

$$a_C(C) \equiv \frac{\eta_0(C)}{\eta_0(0)}\left[1+\frac{\rho_{pol}}{\rho_g}C\right] \tag{4.33}$$

where ρ_{pol} and ρ_g are densities of the pure polymer and the gas, respectively. If the volume of the mixture is simply additive as:

$$V_m(C) = V_{pol}(0) + V_g(0) \tag{4.34}$$

where $V_m(C)$ is the mixture volume of polymer and gas at the concentration C, $V_{pol}(0)$ is the volume of pure polymer, and $V_g(0)$ is the volume of pure gas, of which amount is relevant to that dissolved in the polymer at C, the last factor in Eq. 4.33 will be reduced to an inverse vertical shift factor $1/b_C$ as follows:

$$\begin{aligned} 1+\frac{\rho_{pol}}{\rho_g}C &= \frac{\rho_g+\rho_{pol}C}{\rho_g} = \frac{W_g/V_g(0)+[W_{pol}/V_{pol}(0)](W_g/W_{pol})}{W_g/V_g(0)} \\ &= \frac{V_m(C)}{V_{pol}(0)} = \frac{V_m(C)/W_{pol}}{V_{pol}(0)/W_{pol}} = \frac{\rho_{pol}(0)}{C_{pol}(C)} \equiv \frac{1}{b_C(C)} \end{aligned} \tag{4.35}$$

where W_{pol} and W_g are the weights of the pure polymer and the gas, respectively. Equation 4.33 is then reduced to:

$$a_C(C) \equiv \frac{\eta_0(C)}{\eta_0(0)}\frac{1}{b_C(C)} \tag{4.36}$$

However, if Eq. 4.34 is not valid, Eq. 4.33 cannot be reduced to Eq. 4.36. Only much later was such data made for polymers with SCFs.

Gerhardt *et al.* [13] used a capillary rheometer modified by back pressure control for high-pressure operation and a pressurized extrudate chamber to obtain approximate values of the viscosity for mixtures of poly dimethyl-siloxane (PDMS) with dissolved SC-CO_2. They used a concentration shift factor, a_c, to collapse the viscosity curves onto a master curve but did not consider the effect of pressure. They reported that the viscosity decreases with the weight fraction of CO_2 and obtained the shift factors a_c, needed to shift the viscosity curves with CO_2 onto that for pure

PDMS (Eq. 4.37):

$$\eta(a_C\dot{\gamma}) = \frac{\eta(C,\dot{\gamma})}{a_C} \tag{4.37}$$

where C is the CO_2 concentration. They also expressed the shift factor as the ratio of the zero-shear viscosities with and without CO_2:

$$a_C = \frac{\eta_0(C)}{\eta_0(0)} \tag{4.38}$$

They found that log a_C decreases linearly with concentration and proposed that there are two contributions to viscosity reduction due to dissolved CO_2: dilution of the polymer chain density and additional free volume. Gerhardt *et al.* [14] combined the free volume theory and equation of state theories of Sanchez-Lacombe [15-17] and Panayiotou-Vera [18,19] to model the CO_2 concentration dependency of the shift factor a_c. They suggested that the free volume mechanism plays a dominant role in the decrease of the melt viscosity. Kwag *et al.* [20] used the same instrument used by Gerhardt *et al.* [13] to study the effect of CO_2 on polystyrene (PS). They carried out experiments at two temperatures and several pressures and concentrations, and they used a separable shift factor $a \equiv a_T a_P a_C$ to construct a master curve. The apparent shear rate depended on the applied pressure, and they used a_p to isolate the concentration effect. They reported that a_c can be used to shift the viscosity curves obtained at various concentrations of CO_2. Kwag *et al.* [21] used the WLF equation and a_c measured by Kwag *et al.* [20] to estimate T_g, and they found that the estimated T_g values were in good agreement with T_g measured by Wissinger and Paulaitis [22] and Condo *et al.* [23].

Lee *et al.* [24] used a wedge die mounted on an extruder to measure the viscosity decrease of a PE/PS blend caused by SC-CO_2. Lee *et al.* [25] used a capillary die mounted on an extruder to study the effect of SC-CO_2 on PS viscosity. The apparent shear rate was dependent on the applied pressure, and to build a pressure corrected viscosity curve, they assumed that the effect of pressure on the viscosity of a PS/CO_2

solution is the same as that on pure PS. Ladin *et al.* [26] used a slit die rheometer to study the shear and extensional viscosities of a PBS/CO_2 solution. This group expressed the fractional free volume as a power series of T, P, and C as shown by Eq. 4.39:

$$\frac{1}{f}=\frac{a_1}{T-T_r}+a_2(P-P_r)+a_3(C-C_r)+a_4\frac{P-P_r}{T-T_r}+a_5(P-P_r)(C-C_r)+a_6\frac{C-C_r}{T-T_r}$$
$$+\frac{a_7}{(T-T_r)^2}+a_8(P-P_r)^2+a_9(C-C_r)^2+(\text{higher oder terms}) \tag{4.39}$$

where a_1 to a_9 are constants, and T_r, P_r, and C_r are reference conditions. They used the Doolittel equation as modified by Williams *et al.* [7]:

$$\eta=Ae^{1/f} \tag{4.40}$$

where A is a constant. They obtained the zero-shear viscosity as a function of T, P, and C by letting P_r and C_r be zero and neglecting the higher order terms to give:

$$\ln(\eta_0/A)=\frac{a_1}{T-T_r}+a_2P+a_3C+\frac{a_4P}{T-T_r}+a_5PC+\frac{a_6C}{T-T_r}+\frac{a_7}{(T-T_r)^2}+a_8P^2+a_9C^2 \tag{4.41}$$

which is not a WLF type equation. Taking only the first order terms leads to:

$$\ln(\eta_0/A)=\frac{a_1}{T-T_r}+a_2P+a_3C \tag{4.42}$$

which is a separable simple exponential equation. They built a master curve of the viscosity by plotting η/η_0 versus $\dot{\gamma}\eta_0$.

Royer *et al.* [27] used a high-pressure slit die rheometer to study the viscosity of PS melts plasticized by liquid and SC-CO_2. They also used the separable shift factor $a\equiv a_T a_P a_C$ to construct a master curve and proposed a predictive model for the separate effects of pressure and concentration on the viscosity, which is based on the free volume theory. They correlated the shift factors and the change in T_g due to the change in the free volume:

$$\log a_P = \frac{C_1(T - T_{g,mix,P_0})}{C_2 + T - T_{g,mix,P_0}} - \frac{C_1(T - T_{g,mix,P})}{C_2 + T - T_{g,mix,P}} \tag{4.43}$$

$$\log a_C = \frac{C_1(T - T_{g,P_0})}{C_2 + T - T_{g,P_0}} - \frac{C_1(T - T_{g,mix,P_0})}{C_2 + T - T_{g,mix,P_0}} \tag{4.44}$$

where P_0 is a reference pressure, T_{g,P_0} and T_{g,mix,P_0} are respectively the glass transition temperatures of the pure polymer and polymer/CO_2 solution at a reference pressure, and $T_{g,\mathrm{mix},P}$ is the glass transition temperature of polymer/CO_2 solution at P. They combined the above equations with a model [28] that predicts the depression of T_g by diluents.

Utracki and Simha [29] used three physical blowing agents including CO_2 to evaluate the relationship between the free volume and the viscosity of a polymer-compressed gas mixture during extrusion foaming. They used the relationship between the hole fraction h, $\eta(T,P)$, and (T,P) to describe the effects of T and P on the viscosity:

$$\ln [\eta(T,P)] = a_0 + a_1 \frac{1}{a_2 + h(T,P)} \tag{4.45}$$

The hole fraction was proposed as a correlating variable by Simha and Somcynsky [30] based on lattice-hole theory and can be obtained from PVT data. They evaluated the relationship between the viscosity and the volume fraction of the physical blowing agent to describe the effects of concentration of blowing agent on the viscosity:

$$\ln \eta = b_0 + b_1 \frac{1}{b_2 + \Phi} \tag{4.46}$$

where Φ is the volume fraction, which can be obtained from PVT data.

Yeo and Kiran [31,32] used a falling-cylinder viscometer to measure the zero-shear viscosity of the PS/Toluene/CO_2 system at elevated pressures. They used a

simple exponential equation to describe the effect of dissolved CO_2:

$$\eta = A\exp(-BW_1) \tag{4.47}$$

where A and B are constants, and W_1 is the weight fraction of CO_2.

Oh and Lindt [33] used a high-pressure Couette viscometer to study the effect of SCF on the viscosity. The operating temperature ranges from 130 to 200℃ and pressure up to 20 MPa (3000 psi). The shear rates were around 0.1 s^{-1}. They showed a master curve but gave no analysis of the shift factors.

4.1.6 Viscosity Model Incorporating Shift Factors

A shift factor can be incorporated into a viscosity model to derive an equation for the master curve. For example, the Cross model can be written in master-curve form as follows:

$$\frac{\eta(\dot{\gamma},T,P,C)}{a_{T,P,C}(T,P,C)b_{T,P,C}(T,P,C)} = \frac{\eta_0(T_0,P_0,C_0)}{1+\left|\lambda(T_0,P_0,C_0)\dot{\gamma}\,a_{T,P,C}(T,P,C)\right|^{m(T_0,P_0,C_0)}} \tag{4.48}$$

The reference parameters, $\eta_0(T_0,P_0,C_0)$, $\lambda(T_0,P_0,C_0)$, and $m(T_0,P_0,C_0)$ are determined by fitting data at the reference condition (T_0,P_0,C_0). If $\eta/(a_{T,P,C}b_{T,P,C})$ is plotted as a function of $\dot{\gamma}\,a_{T,P,C}$ the resulting master curve should be independent of T, P, and C. To generate master curves for other rheological properties, the same shift factor should be valid.

4.2 Effect of Temperature, Pressure, and Concentration on Creep Compliance

The creep compliance increases with increasing temperature [34], but the steady-state compliance of a monodisperse, linear polymer decreases with a product of temperature and density. The steady-state compliance of a linear, monodisperse, unentangled melt as a function of M and ρT is predicted by the Rouse theory [35]

to be:

$$J_s^0 = \frac{0.4M}{R\rho(T)T} \quad \text{for } M < M_c' \tag{4.49}$$

where M_c' is a critical molecular weight. The steady-state compliance of a highly entangled monodisperse polymer is found to be a function of only ρT [35]:

$$J_s^0 = \frac{0.4M_c'}{R\rho(T)T} \quad \text{for } M > M_c' \tag{4.50}$$

Wagner and Laun [36] reported that creep compliance and creep recovery curves at various temperatures can be superposed onto a single curve by a horizontal shift along the time axis using a_T, the temperature shift factor from viscosity experiments:

$$J(t/a_T, \sigma, T) = J(t, \sigma, T_0) \tag{4.51}$$

Park [6] carried out high-pressure creep experiments at a constant stress of 3 kPa at four pressures and 170℃ for a branched metallocene polyethylene (BmPE) (Fig. 4.1). The viscosity values were obtained from the reciprocal of the final slope of the creep compliance. Based on these viscosities, pressure shift factors a_p were obtained and compared with those obtained in steady-shear rate experiments for the same polymer. The difference between the shift factors from the two experiments at a given pressure was not deemed significant. Figure 4.2 shows the shifted creep curves, and these reveal that pressure retards creep:

$$J(t/a_P, \sigma, P) = J(t, \sigma, P_0) \tag{4.52}$$

Since it is known that the effect of increasing pressure is opposite to that of increasing CO_2 concentration, the same analysis as was used for high-pressure data will be used. However, no experimental data for the effect of C on creep have been reported.

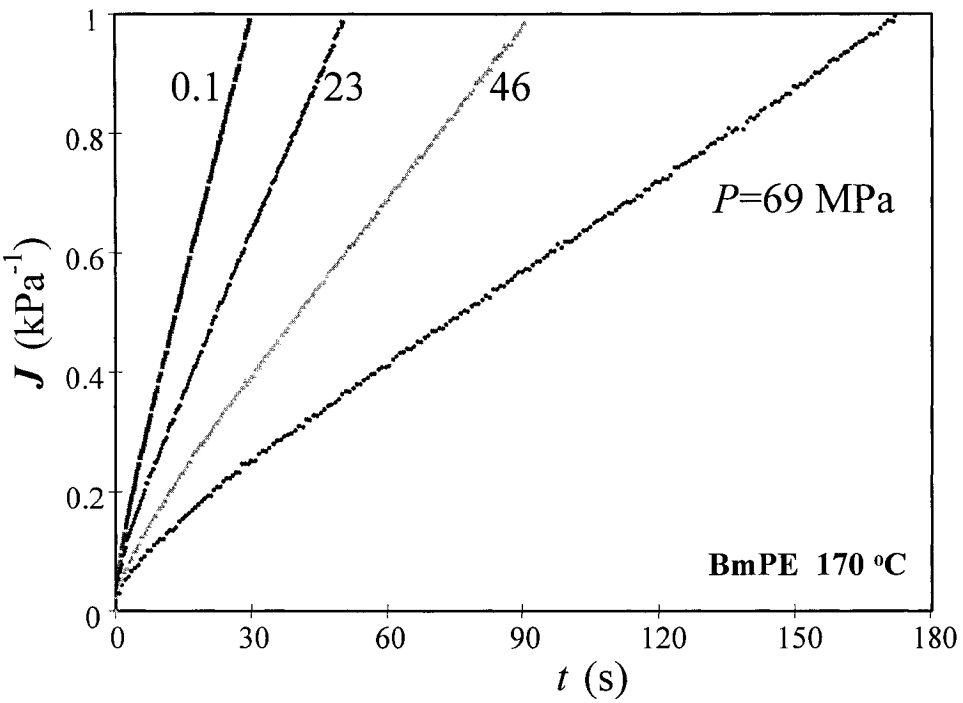

Figure 4.1. Pressure dependence of the creep of BmPE at 170℃.

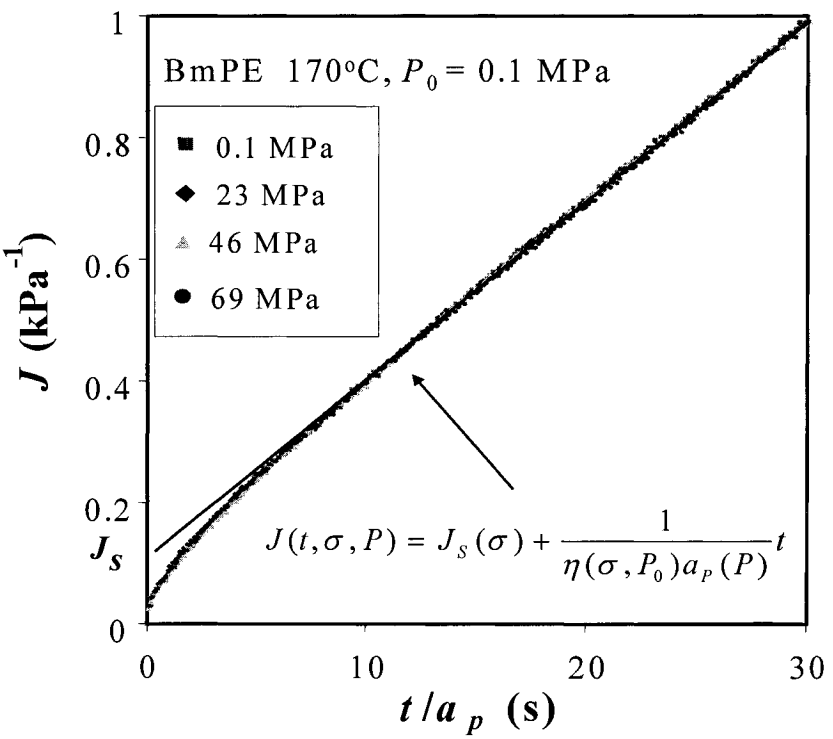

Figure 4.2. Master curve of creep compliance of BmPE at 170℃.

4.3 References

1. C. Barus, "Isothermals, isopiestics and isometrics relative to viscosity, "*American J. Science* XLV:87 (1883).
2. J. de Guzmán, "Relación entre la fluidez y el calor de fusión (Relation between the fluidity and the heat of fusion)," *Anales de la Sociedad Espanola de Fisica Y Quimica* 11:353 (1913).
3. S. Arrhenius, "Die theoretische deutung von viskositäts-messungen kolloidaler lösungen (The theoretical interpretation of viscosity measurements of colloidal solutions)," *Meddelanden Från K. Vetenskapsakademiens Nobelinstitut* 3:1 (1916).
4. S. Arrhenius, "Über die reaktionsgeschwindigkeit bei der inversion von rohrzucker durch säuren (On the reaction rate of the inversion of sucrose by acids)," *Zeitschrift für Physickalische Chemie* 226 (1889).
5. J.D. Ferry, "Mechanical properties of substances of high molecular weight. VI. Dispersion in concentrated polymer solutions and its dependence on temperature and concentration," *J. of the Am. Chem. Soc.* 72:3746 (1950).
6. H.E. Park, "Effect of pressure on the rheological properties of three polyethylenes," Master's Thesis, McGill University, Montreal, 2001.
7. M.L. Williams, R.F. Landel, and J.D. Ferry, "The temperature dependence of relaxation mechanisms in amorphous polymers and other glass-forming liquids," *J. American Chemical Society* 77:3701 (1955).
8. J.D. Ferry and R.A. Stratton, "The free volume interpretation of the dependence of viscosities and viscoelastic relaxation times on concentration, pressure, and tensile strain," *Kolloid-Zeitschrift* 171:107 (1960).
9. R.W. Fillers and N.W. Tschoegl, "The effect of pressure on the mechanical properties of polymers," *Trans. Society of Rheology* 21:51 (1977).
10. W.K. Moonan and N.W. Tschoegl, "Effect of pressure on the mechanical properties of polymers. 2. Expansivity and compressibility measurements," *Macromolecules* 16:55 (1983).
11. J.M. O'Reilly, "The effect of pressure on glass temperature and dielectric relaxation time of poly(vinyl acetate)," *J. Polymer Science* 57:429 (1962).
12. H. Fujita and A. Kishimoto, "Diffusion-controlled stress relaxation in polymers. II. Stress relaxation in swollen polymers," *J. Polym. Sci.* 28, 547 (1958).
13. L.J. Gerhardt, C.W. Manke, and E. Gulary, "Rheology of polydimethylsiloxane swollen with supercritical carbon dioxide," *J. Polym. Sci.: Part B: Polym. Phys.* 35:523 (1997).
14. L.J. Gerhardt, A. Garg, C.W. Manke, and E. Gulary, "Concentration-dependent viscoelastic scaling models for polydimethylsiloxane melts with dissolved carbon

dioxide," *J. Polym. Sci.: Part B: Polym. Phys.* 33:1911 (1998).

15. I.C. Sanchez and R.H. Lacombe, "An elementary molecular theory of classical fluids. Pure fluids," *J. of Physical Chemistry* 80:2352 (1976).
16. R.H. Lacombe and I.C. Sanchez, "Statistical thermodynamics of fluid mixtures," *J. of Physical Chemistry* 80:2568 (1976).
17. I.C. Sanchez and R.H. Lacombe, "Statistical thermodynamics of polymer solutions," *Macromolecules* 11:1145 (1978).
18. C. Panayiotou and J.H. Vera, "Local compositions and local surface area fractions: a theoretical discussion," *Canadian J. of Chem. Eng.* 59:501 (1981).
19. C. Panayiotou and J.H. Vera, "Statistical thermodynamics of r-mer fluids and their mixtures," *Polymer Journal* 14:681 (1982).
20. C. Kwag, C.W. Manke, and E. Gulari, "Rheology of molten polystyrene with dissolved supercritical and near-critical gases," *J. Polym. Sci.: Part B: Polym. Phys.* 37:2771 (1999).
21. C. Kwag, C.W. Manke, and E. Gulari, "Effects of dissolved gas on viscoelastic scaling and glass transition temperature of Polystyrene Melts," *Ind. Eng. Chem. Res.* 40:3048 (2001).
22. R.G. Wissinger and M.E. Paulaitis, "Glass transitions in polymer/carbon dioxide mixtures at elevated pressures," *J. Polym. Sci. B: Poly. Phys.* 29:631 (1991).
23. P.D. Condo, D.R. Paul, and K.P. Johnston, "Glass transitions of polymers with compressed fluid diluents: type II and III behavior," *Macromolecules* 27:365 (1994).
24. M.H. Lee, C. Tzoganakis, and C.B. Park, "Extrusion of PE/PS blends with supercritical carbon dioxide," *Polym. Eng. and Sci.* 28:1112 (1998).
25. M.H. Lee, C.B. Park, and C. Tzoganakis, "Measurements and modeling of PS/supercritical CO_2 solution viscosities," *Polym. Eng. and Sci.* 39:99 (1999).
26. D. Ladin, C.B. Park, S.S. Park, and H.E. Naguib, "Measurements and modeling of rheological properties of biodegradable PBS/CO_2 solutions," 58th *SPE ANTEC* (Vol.2) 46:1955 (2000).
27. J.R. Royer, Y.J. Gay, J.M. Desimone, S.A. Khan, "High-pressure rheology of polystyrene melts plasticized with CO_2: experimental measurement and predictive scaling relationships," *J. Polym. Sci.: Part B: Polym. Phys.* 28:3168 (2000).
28. T. Chow, "Molecular Interpretation of the glass transition temperature of polymer-diluent systems," *Macromolecules* 13:362 (1980).
29. L.A. Utracki and R. Simha, " Free volume and viscosity of polymer-compressed gas mixtures during extrusion foaming," *J. of Polym. Sci.: Part B: Polymer Physics*, 39:342 (2001).

30. R. Simha and T. Somcynsky, "On the statistical thermodynamics of spherical and chain molecule fluids," *Macromolecules* 2:342 (1969).

31. S.-D. Yeo and E. Kiran, "Viscosity reduction of polystyrene solutions in toluene with supercritical carbon dioxide," *Macromolecules* 32:7325 (1999).

32. S.-D. Yeo and E. Kiran, "High-pressure viscosity of polystyrene solutions in toluene + carbon dioxide binary mixtures," *J. of Applied Polymer Science* 75:306 (2000).

33. J.-H. Oh and J.T. Lindt, "A novel Couette viscometer for polymer solutions in supercritical fluids," 60th *SPE ANTEC* (Vol. 2) 2:1920 (2002).

34. P.E. Tomlins, B.E. Read, and G.D. Dean, "The effect of temperature on creep and physical aging of poly(vinyl chloride)," *Polymer* 35:4376 (1994).

35. J.M. Dealy and K.F. Wissbrun, *Melt Rheology and Its Role in Plastics Processing*, Chapman and Hall, London, 1995.

36. M.H. Wagner and H.M. Laun, "Nonlinear shear creep and constrained elastic recovery of a LDPE melt," *Rheol. Acta* 17:138 (1978).

5. Rotational Rheometry

5.1 Introduction

Rotational rheometry is widely used to determine rheological properties due to its simplicity. One of its applications is to determine linear viscoelastic (LVE) behavior, which is the simplest type of viscoelastic behavior. Within the linear regime, the Boltzmann superposition principle governs all rheological behavior. Linear behavior can be studied using deformations that are either very small, very slow, or in the early stage of a large or fast deformation. The LVE properties provide valuable information regarding molecular structure. Another application of rotational rheometry is to carry out creep tests, which can provide the shear viscosity at very low shear rates.

Experiments were carried out to determine (1) fixture geometry and gap dependency of data, (2) thermal stability of sample, (3) zero-shear viscosity, (4) strain limit for LVE behavior, and (5) temperature dependency of the complex viscosity. For these tests, time sweeps, strain sweeps, and frequency sweeps were performed in strain-controlled mode. Creep tests were carried out in stress-controlled mode.

5.1.1 Small Amplitude Oscillatory Shear

Small amplitude oscillatory shear (SAOS) is the method generally used to determine the LVE properties of molten polymers. This type of test can be done in either strain- or stress-controlled mode. For SAOS in strain-controlled mode, a sinusoidal strain is imposed on the sample:

$$\gamma(t) = \gamma_0 \sin(\omega t) \tag{5.1}$$

where γ_0 is the strain amplitude, and ω is the frequency. If γ_0 is sufficiently small,

the resulting stress is also sinusoidal with a phase angle δ:

$$\sigma(t) = \sigma_0 \sin(\omega t + \delta) \tag{5.2}$$

where σ_0 is the stress amplitude. Figure 5.1 shows the essential features of SAOS. The amplitude ratio is defined as

$$G_d \equiv \sigma_0 / \gamma_0 \tag{5.3}$$

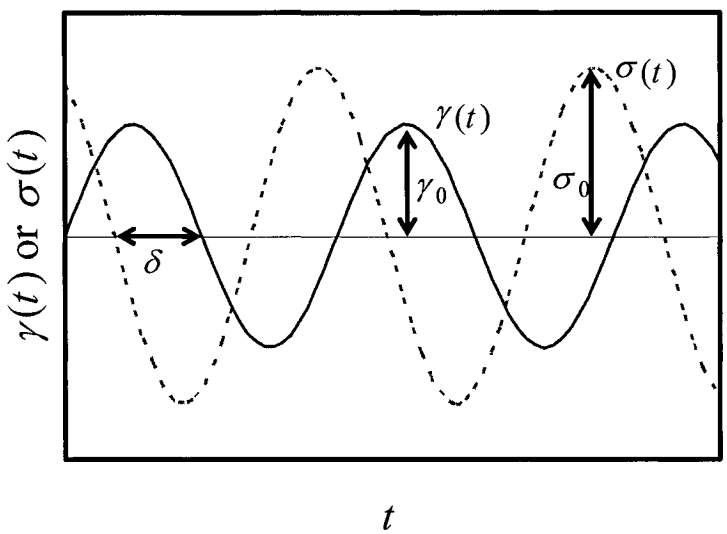

Figure 5.1. Essential features of an SAOS experiment.

The absolute value of the complex viscosity is:

$$|\eta^*(\omega)| = \sqrt{[\eta'(\omega)]^2 + [\eta''(\omega)]^2} \tag{5.4}$$

and can be obtained from the storage (G') and loss (G'') moduli:

$$G' \equiv G_d \cos\delta \tag{5.5}$$

$$G'' \equiv G_d \sin\delta \tag{5.6}$$

$$\eta' \equiv G''/\omega = (G_d \cos\delta)/\omega \tag{5.7}$$

$$\eta'' \equiv G'/\omega = (G_d \sin\delta)/\omega \tag{5.8}$$

In this thesis the term "complex viscosity" is used to mean the absolute value of the complex viscosity.

Time sweep tests are used to determine the rate of thermal degradation. A polymer exposed to heat and/or oxygen over a period of time will be degraded either by chain scission or cross-linking [1]. At relatively low temperatures, or at the beginning of degradation, polyethylene (PE) undergoes branching, which causes an increase in the viscosity, while polypropylene (PP) undergoes chain scission, which results in a decrease in the viscosity. By measuring the change in a rheological property such as G' with time, the degree of degradation can be monitored. Since degradation affects rheological properties, the experimental time must be kept within a strict limit. Strain sweep tests are performed to determine the maximum strain at which the behavior is linear and torque values are still within instrumental range. Frequency sweep tests are then performed to determine $G'(\omega)$, $G''(\omega)$, and $|\eta^*(\omega)|$.

Several empirical relationships between the viscosity function $\eta(\dot{\gamma})$ and the complex viscosity as a function of frequency have been proposed. For example, Cox and Merz [2] noted that there was a close relationship between the complex viscosity and the apparent viscosity measured using a capillary rheometer for two polystyrenes. The curve of apparent viscosity η_A versus apparent shear rate at the wall $\dot{\gamma}_A$ on a log plot appeared to be a continuation of the curve of $|\eta^*(\omega)|$ versus ω, implying that:

$$|\eta^*(\omega)| \approx \eta_A(\dot{\gamma}_A) \quad \text{where } \omega = \dot{\gamma}_A \tag{5.9}$$

In the next chapter, the following slightly different and more commonly used relationship between nonlinear and dynamic behavior will be evaluated (Section 6.7.2):

$$|\eta^*(\omega)| \approx \eta(\dot{\gamma}) \quad \text{where } \omega = \dot{\gamma} \tag{5.10}$$

5.1.2 Creep Compliance

In a creep experiment the stress is increased suddenly from 0 to σ_0 at $t = 0$, and the strain is recorded as a function of time. Polymeric liquids continue to deform as long as the stress is applied, approaching a steady rate of strain. Data are usually expressed in terms of $J(t)$, the creep compliance, which is independent of stress in the region of linear viscoelasticity:

$$J(t) \equiv \frac{\gamma(t)}{\sigma_0} \tag{5.11}$$

At long times the compliance of a melt becomes linear with time:

$$J(t) = J_s^0 + \frac{t}{\eta_0} \tag{5.12}$$

where J_s^0 is the steady-state compliance, which is determined by the extrapolation of the limiting long-time slope back to $t = 0$. Compliance has the dimension of reciprocal modulus, but it is not equal to the reciprocal of the relaxation modulus, which is defined as $G(t) \equiv \sigma(t)/\gamma_0$ in a step-strain experiment.

In the nonlinear region, *i.e.*, at sufficiently high stresses, the creep compliance depends on stress:

$$J(t,\sigma) \equiv \frac{\gamma(t)}{\sigma} \tag{5.13}$$

and at long times:

$$J(t,\sigma) = J_s(\sigma) + \frac{1}{\eta(\sigma)}t \tag{5.14}$$

where $J_s(\sigma)$ is the steady-state compliance for nonlinear viscoelastic behavior. With increasing stress, $J(t,\sigma)$ increases, and $J_s(\sigma)$ decreases [3]. To obtain linear creep data, the limiting stress for linear behavior must be determined by making measurements at several stresses. Ye [4] has reported that the limiting stress for linear behavior is

about 10 Pa for a long-chain branched metallocene polyethylene with a polydispersity of 2.3 and a level of long-chain branching of $0.053/10^3$ backbone carbon atoms. Dynamic stress sweep, *i.e.* SAOS in stress-controlled mode, was not considered to determine the onset stress for the linear regime because dynamic stress sweep results in the frequency-dependent behavior of a sample.

5.2 Apparatus

A rotational rheometer generates torsional flow in a sample loaded between upper and lower fixtures, one of which is rotated. In strain-controlled mode, a displacement is applied to the rotating fixture, and the resulting torque is recorded as a function of time. In stress-controlled mode, a specified torque is applied, and the resulting rotary motion is recorded.

Two rotational rheometers (Fig. 5.2) manufactured by Rheometric Scientific were used for this study. An Advanced Rheometric Expansion System (ARES) was used for strain-control tests, and a Stress Rheometer 5000 (SR5000) was used for stress-control tests. The ARES can operate at higher frequencies and torque and generates more reliable data at high frequencies than the SR5000, whereas the SR5000 is advantageous for low-frequency and torque experiments. The operating ranges of the two rheometers used are given in Table 5.1. The tests performed using each instrument for this study are summarized in Table 5.2.

Because the transducers of both rheometers are sensitive to noise and spikes in the power supply, a Tripp-Lite model SU6K uninterrupted power supply (UPS) system supplies electricity to the rheometers to ensure stable power. The SR5000, whose response is very sensitive to vibration, is mounted on an air table.

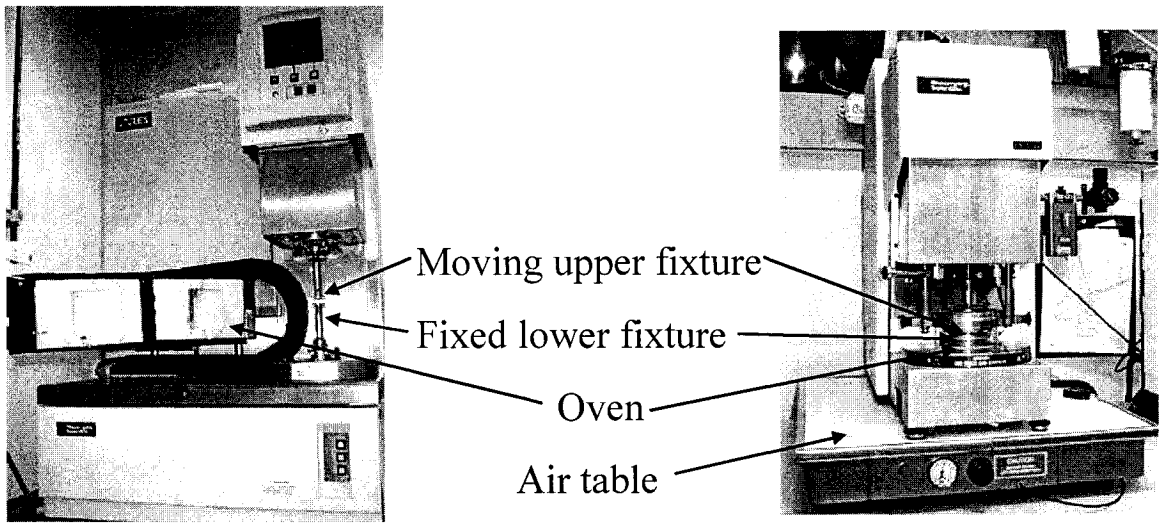

Figure 5.2. ARES (left) and SR5000 (right).

Table 5.1. Operating ranges of SR5000 and ARES.

Measurement variables	SR5000	ARES	Related property
Torque ($g_f$cm = 9.81×10^{-5} Nm)	0.01 - 500	2 - 2000	Shear stress (Pa)
Angular velocity (rad/s ≈ 9.54 rpm): steady	10^{-3} - 100	10^{-3} - 100	Shear rate (s^{-1})
Angular frequency (rad/s = 0.16 Hz): dynamic	10^{-5} - 100	10^{-5} - 500	Frequency (rad/s)
Normal force (g_f = 9.81×10^{-3} N)	2 - 2000	2 - 2000	Normal stress (Pa)

Table 5.2. Tests used for LVE studies (PD=parallel-disks; CP=cone-plate).

Type of test	Application	Geo-metry	Mode	Control	Rheometer	Section
$\lvert\eta^*\rvert(t)$: Time sweep	Thermal stability	PD	Dynamic	Strain	ARES	5.4.1
$\lvert\eta^*\rvert(\omega,h)$: Frequency sweep	Gap (h) dependency	PD/ CP				5.4.2
$J(t,\sigma)$: Creep	Viscosity	CP	Steady	Stress	SR5000	5.4.3
$\lvert\eta^*\rvert(\gamma)$: Strain sweep	LVE range	CP	Dynamic	Strain	ARES	5.4.4.1
$\lvert\eta^*\rvert(\omega,T)$: Frequency sweep	Temp. shift factor	PD				5.4.4.5

5.2.1 Fixture Geometry

To select a geometry type (cone-plate or parallel-disks, Fig. 5.3) and size (cone angle, diameter, or gap), the ranges of viscosity and deformation rate must be known. The lower the viscosity, the larger the diameter needs to be. According to the operating manual, 25 mm diameter fixtures are good for most polymer melts.

Cone-plate geometry (Fig. 5.4) has the advantage of a uniform deformation rate, which is given by Eq. 5.15:

$$\dot{\gamma} = \frac{\Omega}{\Theta} \tag{5.15}$$

where Ω is the angular velocity in rad/s, and Θ is the cone angle in radians. The uniform strain is important specially in the study of nonlinear behavior. The tip of the cone is an obtuse surface rather than a sharp apex, so there must be a gap to compensate for the missing cone tip (Fig. 5.4). Data using this geometry are very sensitive to the gap setting. The cone available has a diameter (ϕ) of 25 mm, a cone angle (Θ) of 0.0997 rad, and a gap setting of 0.0457mm. The sample thickness at the rim is $(\phi/2)\tan(\Theta) = 1.2504\,\text{mm}$. The center of a sample is severely squeezed during sample loading, and a high normal force results. Another difficulty arising from sample squeezing is shown in Section 5.3.3.1. These difficulties are serious in loading a highly viscous material. To avoid such problems, the sample should be squeezed very slowly. In spite of such difficulties, this geometry is preferred for the study of nonlinear viscoelastic (NLVE) behavior because of the homogeneity of the deformation. Thus, cone-plate fixtures are used only when essential, and this geometry was used here for creep tests and strain sweeps, which involve NLVE behavior.

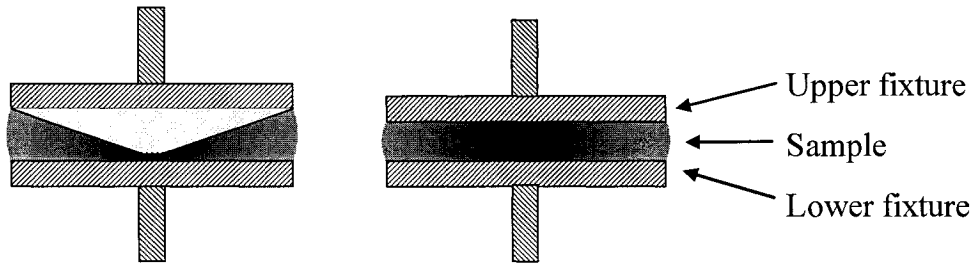

(a) Cone-plate (b) Parallel-disks

Figure 5.3. Fixtures with sample loaded.

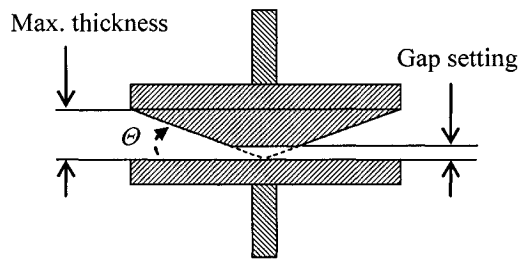

Figure 5.4. Geometry of cone-plate.

In parallel-disks geometry, it is much easier to load a sample and the gap between the two disks can be varied. Although the strain and shear rate vary with radius, this is not a problem in making LVE measurements, because the stress is always proportional to the deformation, and if the deformation on the rim is in linear regime, that in the rest parts must also be linear. Thus, dynamic data for the determination of $G'(\omega)$ and $G''(\omega)$ were obtained using parallel-disks. The advantages of cone-plate and parallel-disks are summarized in Table 5.3. The ellipses indicate factors favoring the selection of each geometry. The rheometric equations [5, Chap. 5; 6, Chap. 9] are summarized in Table 5.4 for each geometry.

Table 5.3. Advantages of each geometry.

Geometry	Is easy to use?	Can be used for	
		LVE ?	NLVE ?
Cone-plate	No	Yes	(Yes)
Parallel-disk	(Yes)	(Yes)	No

Table 5.4. Comparison between cone-plate and parallel-disks.

Geometry	Cone-Plate	Parallel Disk
Advantages	Homogeneous deformation and rate Simple working equations	Variable gap Simple sample loading
Disadvantages	Sensitive to zeroing gap Difficult sample loading	Inhomogeneous strain and rate
Gap		h
Cone angle	Θ	
Torque Max. torque Steady-state torque	$M(t)$ M_0 (oscillatory shear) M_{ss} (steady shear)	
Angular displacement Max. angular disp.	$\phi(t)$ ϕ_0	
Angular velocity	$\Omega = \frac{d\phi(t)}{dt}$	
Shear stress	$\sigma(t) = \frac{3M(t)}{2\pi R^3}$	$\sigma(t) = \frac{2M(t)}{\pi R^3}$ (on edge)
Shear strain	$\gamma(t) = \frac{\phi(t)}{\tan\Theta} \cong \frac{\phi(t)}{\Theta}$	$\gamma(t) = \frac{\phi(t)R}{h}$ (on edge)
Shear rate (steady)	$\dot{\gamma} = \frac{\Omega}{\tan\Theta} \cong \frac{\Omega}{\Theta}$	$\dot{\gamma} = \frac{\Omega R}{h}$ (on edge)
η (steady)	$\eta \equiv \frac{\sigma}{\dot{\gamma}} = \frac{3M_{ss}\Theta}{2\pi R^3\Omega}$	$\eta = \frac{2M_{ss}h}{\pi R^4\Omega}$ (on edge)
Frequency (oscillatory)	ω	
Phase angle (oscillatory)	δ	
Max. σ (oscillatory)	$\sigma_0 = \frac{3M_0}{2\pi R^3}$	$\sigma_0 = \frac{2M_0}{\pi R^3}$ (on edge)
Max. γ (oscillatory)	$\gamma_0 = \frac{\phi_0}{\tan\Theta} \cong \frac{\phi_0}{\Theta}$	$\gamma_0 = \frac{\phi_0 R}{h}$ (on edge)
$G' \equiv \frac{\sigma_0\cos\delta}{\gamma_0}$	$G' = \frac{3M_0\Theta\cos\delta}{2\pi R^3\phi_0}$	$G' = \frac{2M_0h\cos\delta}{\pi R^4\phi_0}$
$G'' \equiv \frac{\sigma_0\sin\delta}{\gamma_0}$	$G'' = \frac{3M_0\Theta\sin\delta}{2\pi R^3\phi_0}$	$G'' = \frac{2M_0h\sin\delta}{\pi R^4\phi_0}$
Method to change $\dot{\gamma}$	Changing Ω	Changing Ω or h
Method to delay edge failure at high $\dot{\gamma}$	Changing Θ	Decreasing h

5.3 Experimental Procedure

5.3.1 Sample Preparation

The most convenient method of sample-disk preparation is compression molding and using this method minimizes the strain and thermal histories. The sample was molded at 165℃ using a mold of stainless steel plate having nine holes with a diameter of 25 mm. The thickness of the mold is important, because the sample must be slightly thicker than the rheometer gap but thin enough to avoid a large normal force during sample loading. Mold plates with thicknesses of 1.19 and 1.50 mm were available. The thickness was measured by a Starrett 734XFL micrometer with a resolution of 0.001 mm. In setting the thickness of a mold, it must be taken into account that the sample thickness at room temperature will be smaller than the mold thickness, which governs the sample thickness in the molten state at a high temperature. However, the diameter of a sample changes very little on heating and cooling.

All samples were kept in a vacuum oven at 50℃ for eight hours to minimize the levels of oxygen, unreacted monomer, and other volatile molecules. All tests were carried out in a nitrogen environment to delay the oxidative degradation of samples.

5.3.2 Calibration

The torque transducer is calibrated by hanging weights on the calibration fixture connected to the torque head anvil (Fig. 5.5). The torque is first tared without a weight in the Orchestrator, which is the operating software for the ARES and SR5000. After suspending the weight, the appropriate torque value is assigned in Orchestrator. Since the weight generates a force in one direction, the bending of the torque shaft affects the transducer output. However, Orchestrator takes this into account, if the weight is hung in the specified direction.

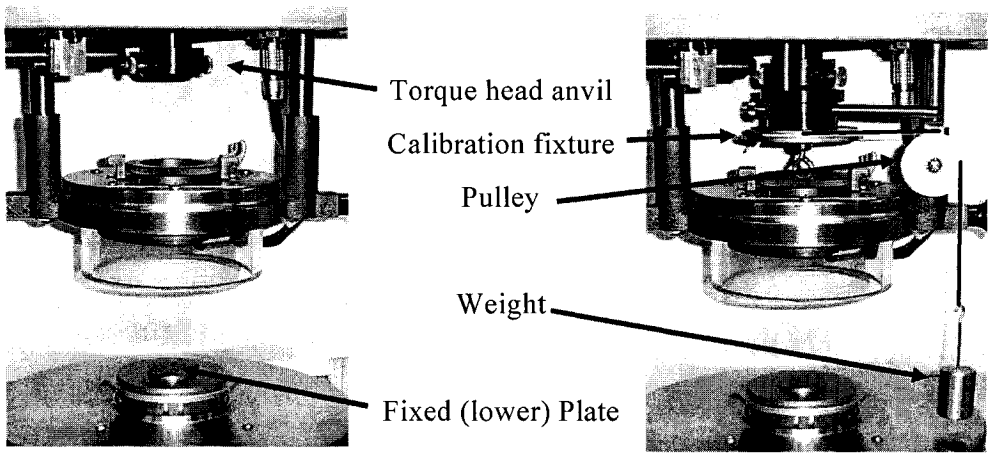

Figure 5.5. Before and after loading calibration fixture and weight on SR5000.

5.3.3 Zeroing the Gap and Loading a Sample

Variations in temperature and removal of the fixture can change the zero position of the upper plate, so the gap must be corrected for each experiment and at each temperature. Both the fixtures and the instrument frame will expand until they reach thermal equilibrium, and this affects the gap. To avoid problems arising from non-equilibrium thermal behavior, the chamber is also preheated to the experimental temperature for several hours prior to zeroing the gap. The ARES and SR5000 require gas flow to heat up the system, and air is used instead of nitrogen during preheating to reduce operating cost.

Initial zeroing is carried out by setting the gap to zero after lowering the upper fixture until it touches the bottom plate. Touching is confirmed by monitoring the normal force. A particular value of normal force is always used to confirm a zero gap. For this study, one Newton was selected.

A sample must be loaded carefully to avoid air bubbles between the sample and the lower plate. After placing the sample on the plate, it is pushed down in the center, and a spatula is used to sweep the bubbles from the center to the rim. Before setting the desired gap, the edge of the sample is trimmed with the gap set slightly larger than its final value. The step-by-step procedure for sample loading and gap zeroing is as follows:

5.3.3.1 Procedure for Cone-plate

1. Lower the cone until it touches the plate.
2. Set the gap to zero.
3. Raise the cone until the gap is 20 mm.
4. Load a sample on the plate.
5. Lower the cone until the gap is 0.08 mm.
6. Trim the sample flush with the edge of the fixtures.
7. Lower the cone until the desired gap setting (0.046 mm) is reached and the sample edge is round [Figs. 5.3 (a) and 5.6]. Make sure that the normal stress does not exceed the prescribed maximum value. The cone must be lowered very carefully to avoid the phenomenon shown in Fig. 5.7.

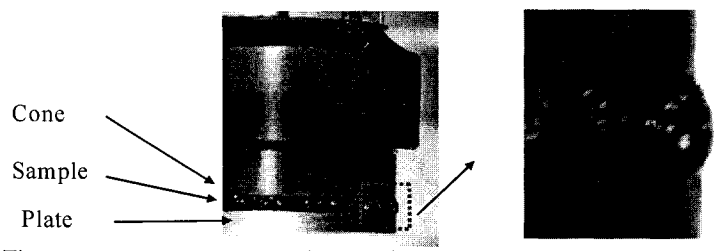

Figure 5.6. Proper sample loading between cone and plate.

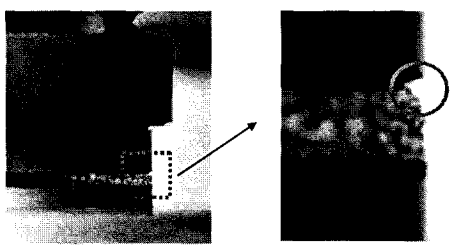
Figure 5.7. Failure in sample loading between cone and plate.

5.3.3.2 Procedure for Parallel-disks

1. Lower the upper plate until it touches the bottom plate.
2. Set the gap to zero.

3. Raise the upper plate until the gap is 20 mm.

4. Load the sample on the bottom plate.

5. Lower the upper plate until the gap is 102 % of the desired gap value.

6. Trim the sample flush with the edge of the disks.

7. Lower the upper plate until the gap is the desired value and the sample edge is round [Fig. 5.3 (b)].

5.3.4 Dynamic Time Sweep for Thermal Stability Determination

To determine the effect of degradation on the sample, oscillatory-shear, time-sweep experiments were carried out at the highest test temperature using the ARES. The test was carried out in a nitrogen environment. A time-sweep experiment does not need to be limited to the LVE regime, because only the variation with time is of interest. The strain and frequency must be small enough to avoid breaking the sample but large enough to provide a satisfactory signal-to-noise ratio. Since time-sweep tests are carried out for a long time, the number of measurements should be minimized to avoid breaking the sample due to strain history. Measurements were made every ten minutes over ten hours, which was the maximum time for any test made.

5.3.5 Creep Experiments

The SR5000 is used to determine the viscosity at very low shear rates and 180℃ by a measurement of the creep compliance. At $t = 0$, a stress is imposed, and the resulting strain is recorded as a function of time and divided by the stress to obtain the creep compliance.

5.3.6 Dynamic Strain Sweep

Since the maximum strain for linear viscoelastic behavior varies with frequency, temperature and polymer, to determine the linear regime strain sweep experiments

must be carried out prior to each frequency sweep. For this purpose the frequency range was divided into decades. At each test temperature and at the highest frequency of each decade, SAOS is carried out over a range of strains. When the moduli and complex viscosity begin to decrease with strain, the sample is exhibiting nonlinear viscoelasticity. The strain for subsequent frequency sweeps in each decade must be lower than the limiting value for LVE.

5.3.7 Dynamic Frequency Sweep

At each test temperature SAOS is performed at the strain amplitudes determined by strain sweep for each decade of frequency: 500-100, 100-10, 10-1, 1-0.1, and 0.1-0.01 rad/s, working down from high to low frequencies. If the complex viscosities at two strains are not the same at 100, 10, 1, and 0.1 rad/s, NLVE behavior has occurred, and the strain values must be revised. This is one method to confirm that the result of a strain-sweep test is correct, and that frequency-sweep data are in the linear regime.

5.4 Results and Discussion

5.4.1 Thermal Stability

Figure 5.8 shows the changes in the storage and loss moduli with time at 210℃ with $\gamma_0 = 3\%$ and $\omega = 1\,\mathrm{rad/s}$ over ten hours. The loss modulus decreases by 1.5% over the first four hours and then increases by 1% over the next six hours. The storage modulus increases steadily by 3.7% over ten hours. These variations are acceptable for rheological measurements. The temperature of 210℃ was the maximum test temperature, and thermal stability at lower temperatures is expected to be better than that at 210℃. The HDPE sample is a commercial grade, which is assumed to contain a stabilizer, and it shows good thermal stability. Drying in a vacuum oven also improves thermal stability.

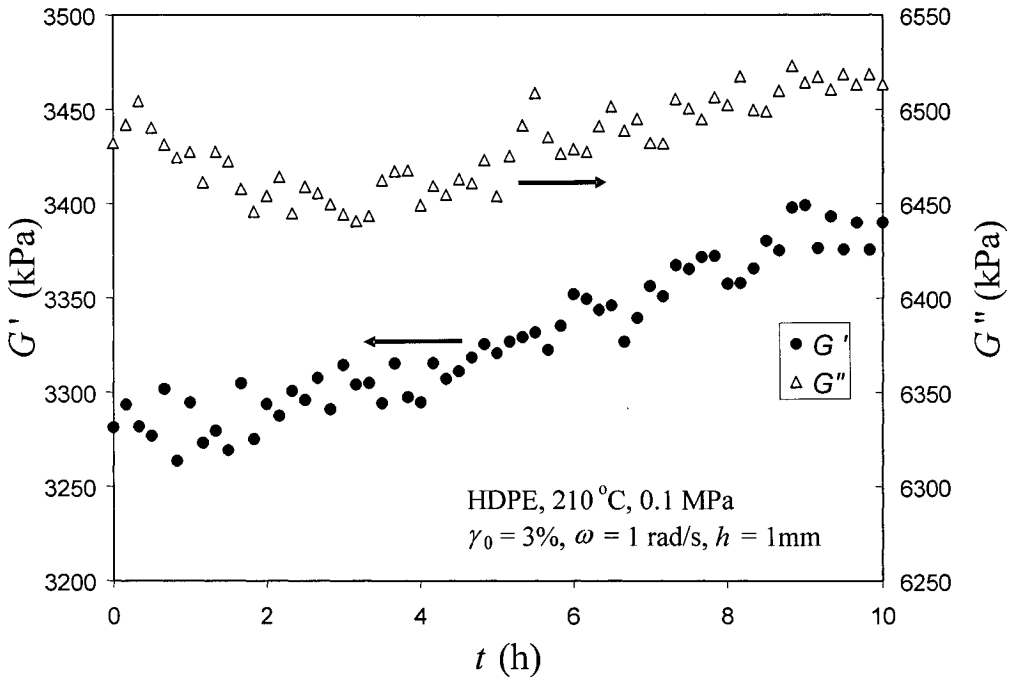

Figure 5.8. Dynamic time sweep for HDPE at 210℃ and h=1mm for ten hours.

5.4.2 Gap and Geometry Dependency

The gap between the parallel-disks must be large enough to validate the continuum assumption [3, p. 38], but increasing the gap raises the angular speed and displacement to obtain the same shear rate and strain. There is thus an optimum gap. Moreover, both parallel-disks and cone-plate geometries should generate the same data in the linear regime. In response to the above concerns, SAOS experiments were performed using both cone-and-plate and parallel-disks fixtures for five gap values. Figure 5.9 shows results for $\gamma_0 = 8\%$ at 180℃. A plot for a gap of 0.95 mm, which is the gap in the HPSPR, was also made but is not shown in Fig. 5.9 because it showed the same result as that for 1.0 mm. Data for cone-plate and parallel-disks with gaps of 1.0 and 1.2 mm are in good agreement, but those for parallel-disks with gaps of 1.5 and 0.6 mm are lower. Datum at 0.14 rad/s with a gap of 0.6 mm is 4% lower than that with a gap of 1.0 mm. Considering all the factors discussed earlier, parallel-disks fixture with a gap of 1.0 mm were selected for LVE measurements,

i.e., frequency sweep, and the cone-plate geometry was used for creep and strain sweep tests that involved NLVE behavior.

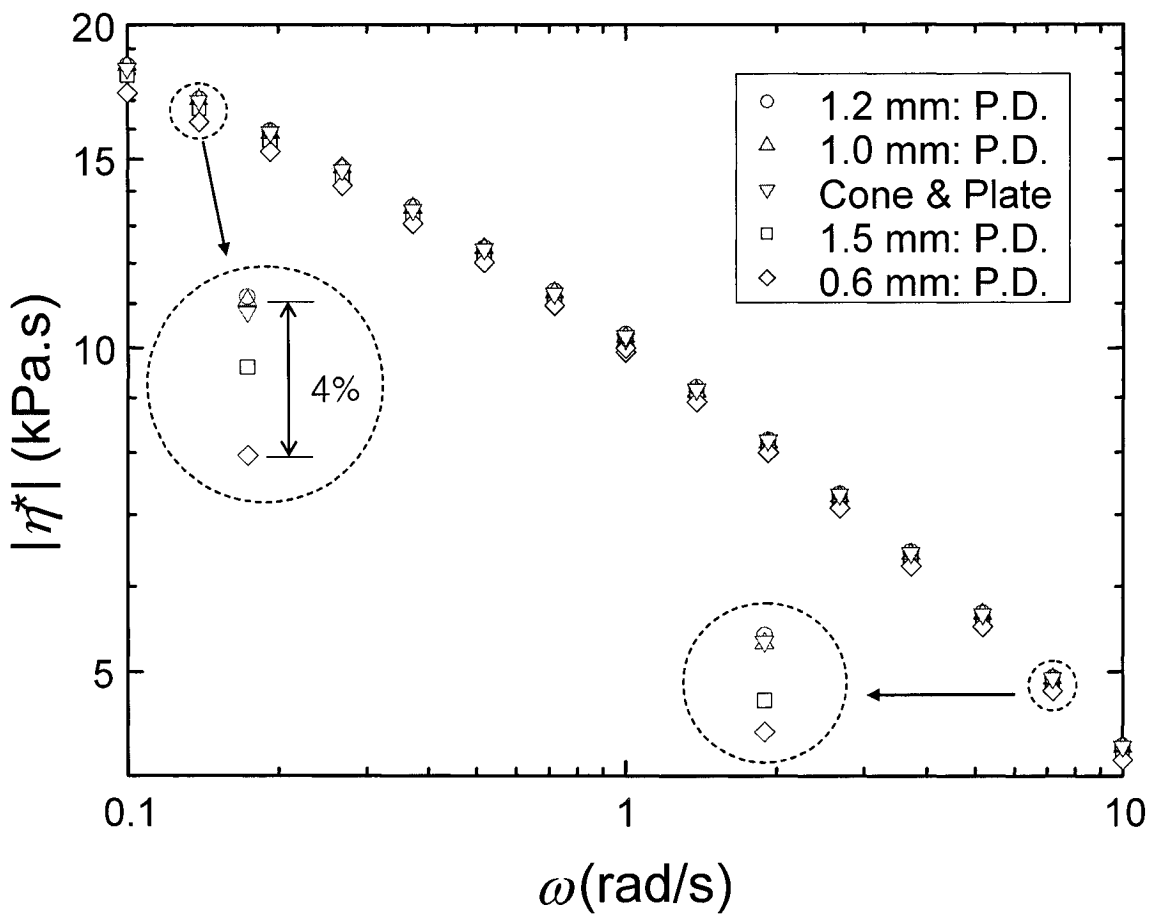

Figure 5.9. Effect of gap and geometry on SAOS for HDPE at 180℃ (P.D.=parallel-disks).

5.4.3 Creep

The SR5000 has two options for data sampling: linear and logarithmic. Linear sampling takes data at equal time intervals, while logarithmic sampling takes data at equal intervals of log time. Creep experiments were carried out at 5 Pa and 180℃, generating 350 sampling points. As can be seen in Fig. 5.10, which shows data obtained using linear sampling, and Fig. 5.11, which is for logarithmic sampling, the linearly sampled data have a much higher noise level (noise/signal=±3.2%) in

$[dJ(t)/dt]^{-1}$ than the logarithmically sampled data. The slope was calculated using a 2-point difference equation:

$$\frac{dJ(t)}{dt} = \frac{\Delta J(t)}{\Delta t} \equiv \frac{J(t_i) - J(t_{i-1})}{t_i - t_{i-1}} \tag{5.16}$$

where i is the time index. If $[dJ(t)/dt]^{-1}$ is noisy, it is difficult to determine the viscosity by linear regression of $J(t)$ of long times. Even though the logarithmically sampled data showed fluctuation at short times, this fluctuation is not a concern, because only data at long times are used to obtain the viscosity. All other creep experiments were carried out using logarithmic sampling.

The zero-shear viscosity η_0 should be independent of stress, and the effect of stress on the slope is thus of interest. Figure 5.12 shows creep compliance curves at several stresses for HDPE at 180℃. The inset has expanded scales to show the short-time linear behavior.

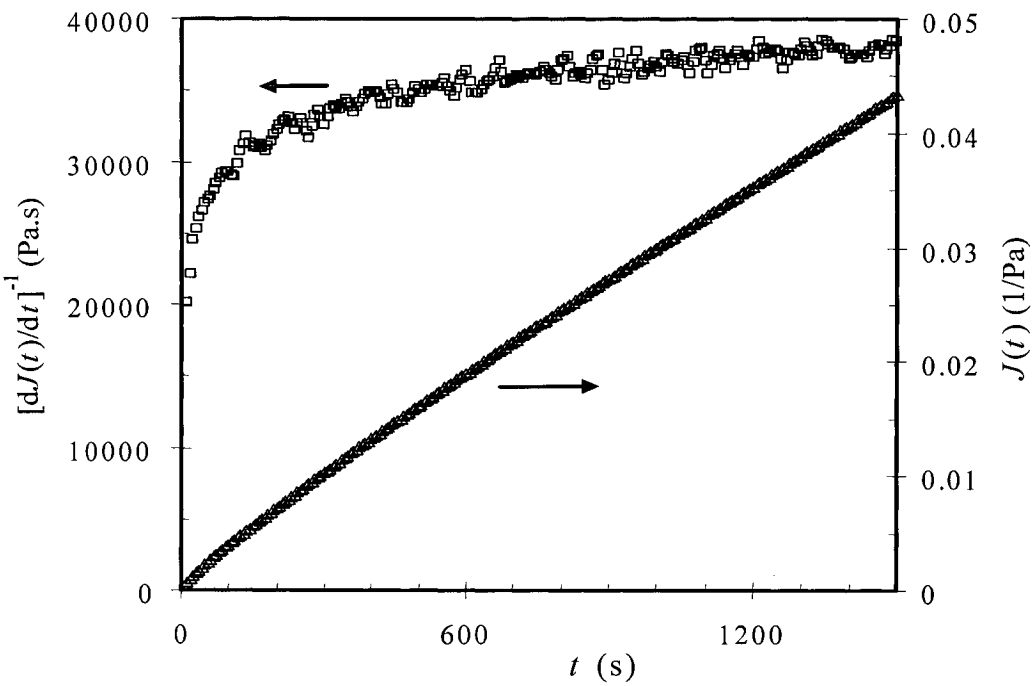

Figure 5.10. Creep compliance of linear sampling for HDPE with 5 Pa at 180℃.

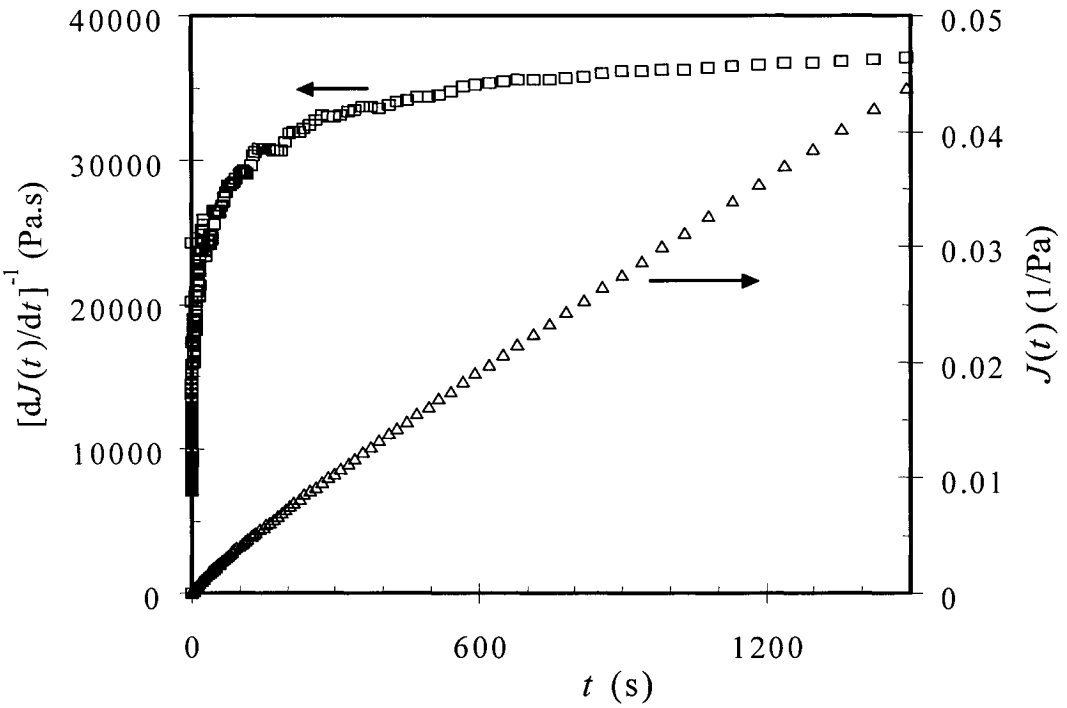

Figure 5.11. Creep compliance of logarithmic sampling for HDPE with 5 Pa at 180℃.

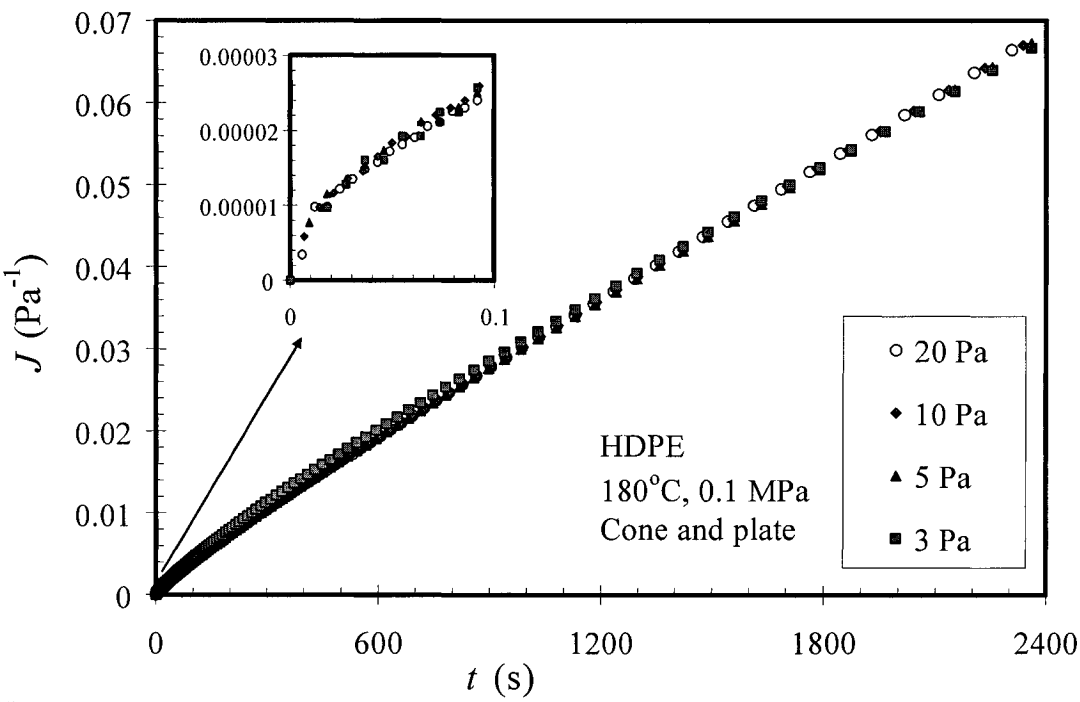

Figure 5.12. Dependency of creep compliance on stress for HDPE at 180℃. Applied stress values are given in legend.

Figure 5.13 shows the resulting viscosity as a function of shear stress, and Fig. 5.14 shows it as a function of shear rate, which was calculated from the slope of the creep compliance. Even at these very low shear stresses and rates, the viscosity is not at its Newtonian plateau. Wagner and Wissbrun [7] have noted that for polymers with broad molecular weight distributions, the viscosity continues to change with shear rate even at very low shear rates. The polydispersity index (PDI) of this HDPE is 13.6, which is fairly high, and as a result this sample does not reveal its zero-shear viscosity within the experimental window. Reducing the stress below 3 Pa to find the linear range is not practical, because this would involve a torque below 0.01 $g_f$cm, the lower limit of the instrument. Thus the zero-shear viscosity for this material could not be obtained by means of creep experiments. However, the viscosity values inferred from creep data were used with $\eta(\dot{\gamma})$ data obtained by use of the HPSPR to fit a model and estimate η_0. The highest viscosity from creep data was used as the initial estimate for the model fitting of the steady shear data from the HPSPR (Section 6.7.3).

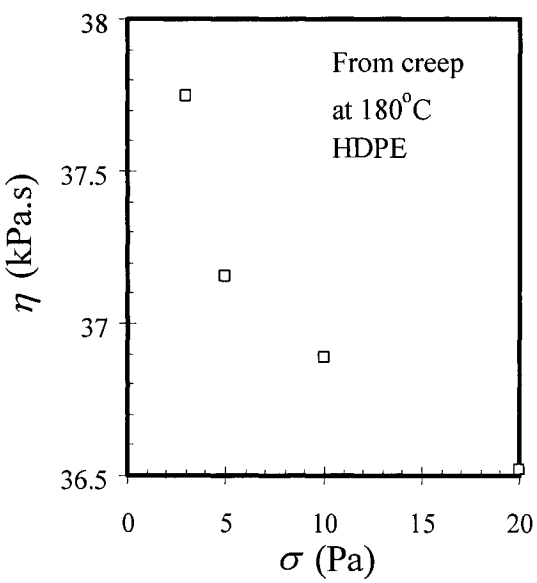

Figure 5.13. Viscosity as a function of stress for HDPE at 180℃.

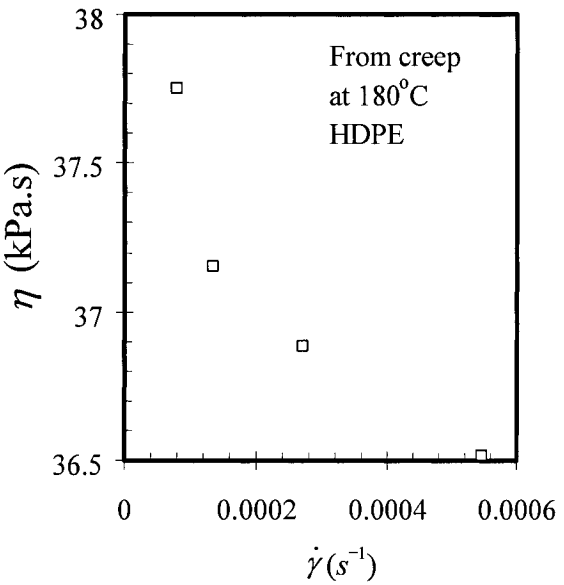

Figure 5.14. Viscosity as a function of shear rate for HDPE at 180℃.

5.4.4 Complex Viscosity versus Frequency

5.4.4.1 Strain Sweep

The frequency range was divided into five zones, and strain sweep tests were performed at 0.1, 1, 10, 100, and 500 rad/s at various strain amplitudes. Figure 5.15 shows data at 100 rad/s and 180℃ for strains from 2 to 10%. The data start decreasing at strains above 5%. Strains lower than 5% can also generate linear data at 100 rad/s, but the torque may fall below the resolution of the torque transducer at the lower frequencies in the decade. A strain of 5% is thus used as the strain amplitude γ_0 for frequencies between 10 and 100 rad/s in the frequency sweep tests. Table 5.5 shows the strain amplitudes used for each frequency range and temperature.

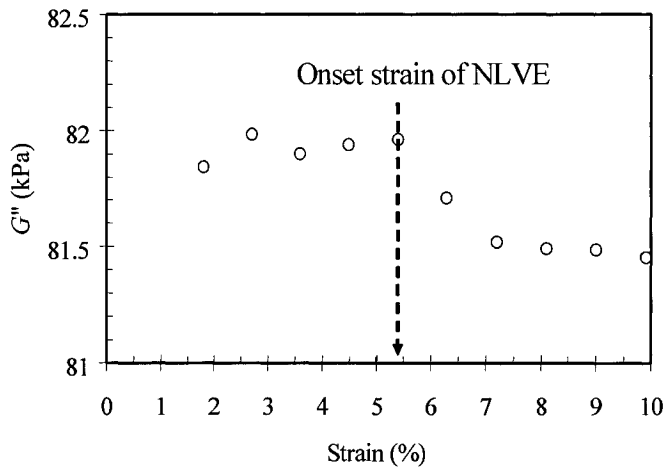

Figure 5.15. Strain sweep test at 100 rad/s.

Table 5.5. Strain amplitude (%) for each frequency range and temperature.

T (℃)	Frequency range (rad/s)				
	500-100	100-10	10-1	1-0.1	0.1-0.01
160	1	2	4	8	10
170	1.5	4	5	9	15
180	3	5	6	10	20
190	4	6	7	10	30
200	4	7	8	10	40
210	4	8	9	10	50

5.4.4.2 Frequency Sweep

Figure 5.16 shows the effect of frequency on the moduli and complex viscosity at 180℃. Five strain amplitudes were used in each decade of frequency. Two data points fall on each grid line where two strain amplitudes overlapped, but these cannot be distinguished because of the LVE behavior. The complex viscosity data exhibit neither a power-law region at high frequencies nor a Newtonian plateau at low frequencies.

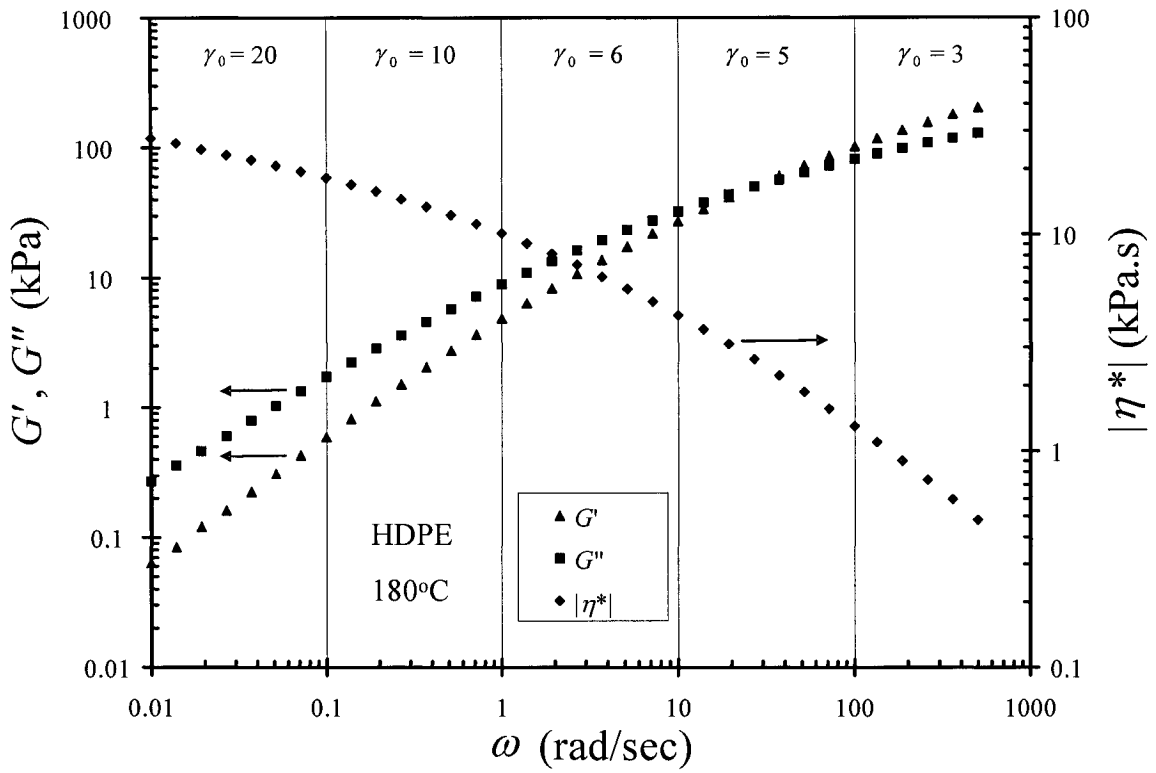

Figure 5.16. Dependency of moduli and complex viscosity on frequency for HDPE at 180℃.

5.4.4.3 Model Fitting

Before studying the effect of temperature on the LVE behavior, the data at the reference temperature ($T_0 = 180°C$) were fitted to a model by the least square method using 'Solver' in Microsoft Excel to describe the effect of frequency on the complex viscosity. To determine $\eta_0(T_0)$, the viscosity data obtained from creep tests

and those obtained from steady simple shear tests (Chapter 6) were used, and the detailed procedure is described in Section 6.7.3. Nonlinear regression was carried out to determine two or three parameters (characteristic time and power) at the reference temperature and one additional parameter $a_T(T)$ for the other temperatures. The regression was repeated until the following sum was minimized:

$$S=\sum_{i=1}^{N}\left(\frac{|\eta_i^*|-|\eta_{mp,i}^*|}{|\eta_i^*|}\right)^2 \tag{5.17}$$

where i is the frequency index, $|\eta^*|$ is a complex viscosity datum, $|\eta_{mp}^*|$ is a model-predicted complex viscosity value, and N is the number of data.

Three models (Section 6.2.2.1) for $\eta(\dot{\gamma})$ were used to describe $|\eta(\omega)|$: the Carreau [8] (Eq. 5.18), Cross [9] (Eq. 5.19), and Yasuda [10] (Eq. 5.20) models as follows:

$$|\eta^*(\omega)|=\frac{\eta_0(T_0)}{[1+(\lambda(T_0)\omega)^2]^{r(T_0)}} \tag{5.18}$$

$$|\eta^*(\omega)|=\frac{\eta_0(T_0)}{1+|\lambda(T_0)\omega|^{m(T_0)}} \tag{5.19}$$

$$|\eta^*(\omega)|=\frac{\eta_0(T_0)}{\left\{1+\left[\lambda(T_0)\omega\right]^{a(T_0)}\right\}^{[1-n(T_0)]/a(T_0)}} \tag{5.20}$$

where $\eta_0(T_0)$ is the zero-shear viscosity, $\lambda(T_0)$ is a time constant, and $a(T_0)$, $m(T_0)$, $n(T_0)$, and $r(T_0)$ are fitting parameters at T_0. The Carreau model cannot match the observed curvature (Fig. 5.17), as the model quickly approaches a power-law model as the frequency increases (Eq. 5.21). The model also approaches a zero-shear viscosity too fast as the frequency decreases (Eq. 5.22).

$$\eta=\frac{\eta_0}{[1+(\lambda\omega)^2]^p}\approx\frac{\eta_0}{(\lambda\omega)^{2p}}:\ \omega>1 \text{ and } (\lambda\omega)^2\gg 1 \tag{5.21}$$

$$\eta = \frac{\eta_0}{[1+(\lambda\omega)^2]^p} \approx \eta_0 : \ \omega < 1 \text{ and } (\lambda\omega)^2 \ll 1 \tag{5.22}$$

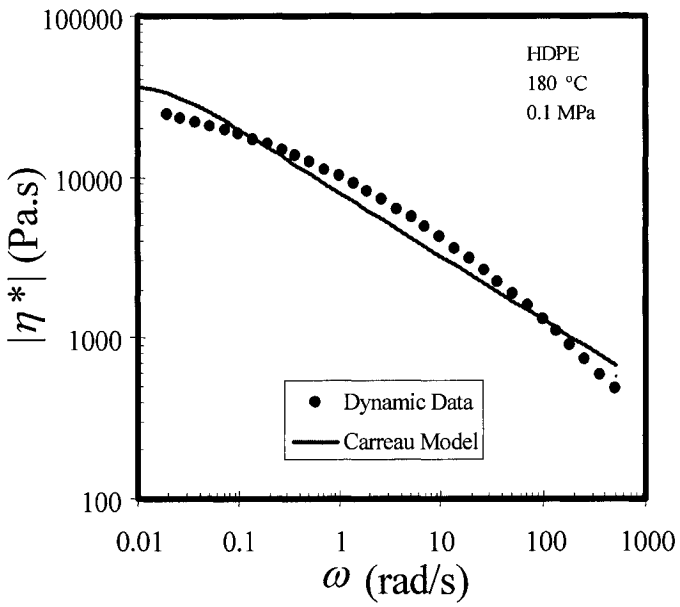

Figure 5.17. The Carreau model fitting.

The Cross model (Fig. 5.18) described the data better than the Carreau model, but

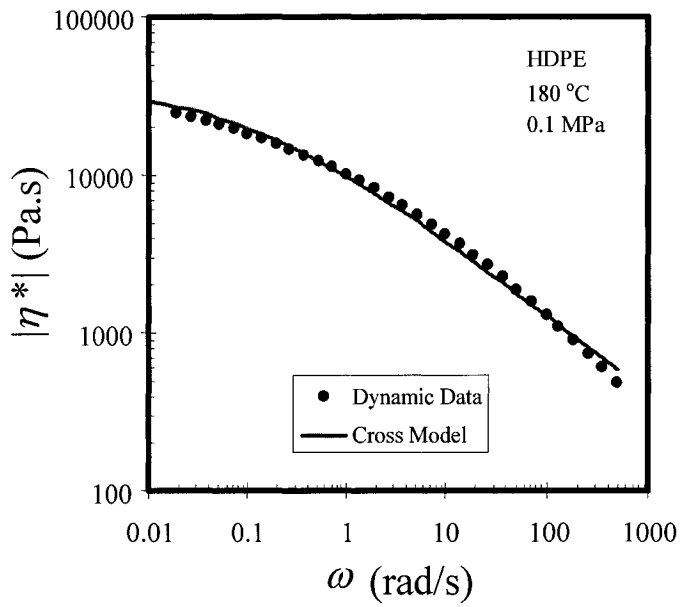

Figure 5.18. The Cross model fitting.

there is still some discrepancy. The Yasuda model has an additional parameter and provides a good fit of the data (Fig. 5.19); this model was therefore used for the complex viscosity.

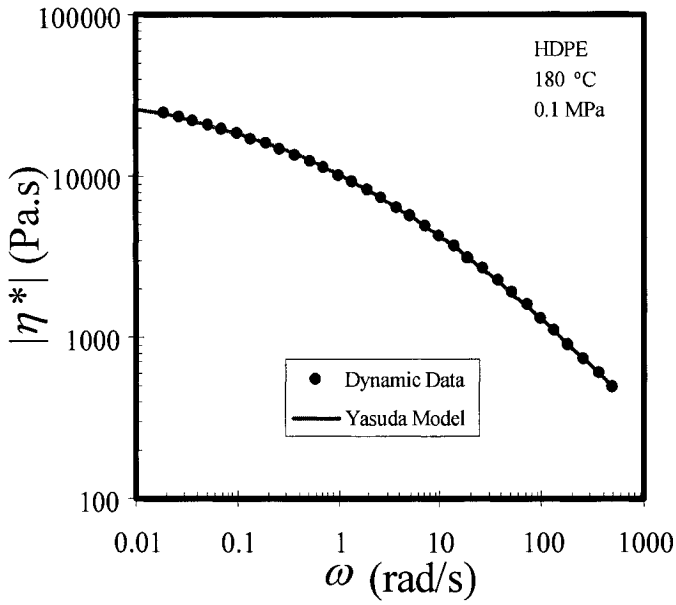

Figure 5.19. The Yasuda model fitting.

5.4.4.4 Shear-Rate Range for NLVE Measurements

In SAOS tests, torque values can be kept within the transducer's operating range by changing the strain amplitude. However, in steady simple shear experiments with the HPSPR, which was used for the NLVE measurements, the operational stress range can be altered only by changing the shear-rate range, if the gap is fixed. The shear-rate range is thus governed by the instrumental and material stress ranges. Rather than determining the shear-rate range by trial and error, it is advantageous to estimate the range in advance using the results of SAOS experiments.

Park [11] reported that the shear stress must be above 2 kPa, which is ten times the noise level of the stress transducer of the HPSPR, to obtain reliable data. He also found that polyethylenes exhibited a flow instability at around 100 kPa, beyond which it was impossible to determine a steady-state stress. Thus, the expected stress

range for PE is between 2 and 100 kPa.

To correlate SAOS data with the viscosity, the frequency for the stress range is associated with the shear rate. There is no theory that relates $|\eta^*(\omega)|$ with $\eta(\dot{\gamma})$ at $\omega = \dot{\gamma}$, but experimental results have shown that the two curves are very similar [11]. Figure 5.20 shows the shear stress σ (the stress amplitude), which is estimated as $|\eta^*(\omega)|\omega$, versus ω. The shear-rate range for stresses of 2-100 kPa is indicated to be 0.1-50 s^{-1}. The validity and usefulness of this method is discussed in the next chapter. Since the stress depends on temperature, so will the shear-rate range, and temperature shift factors (Section 5.4.4.5) can be used at other temperatures.

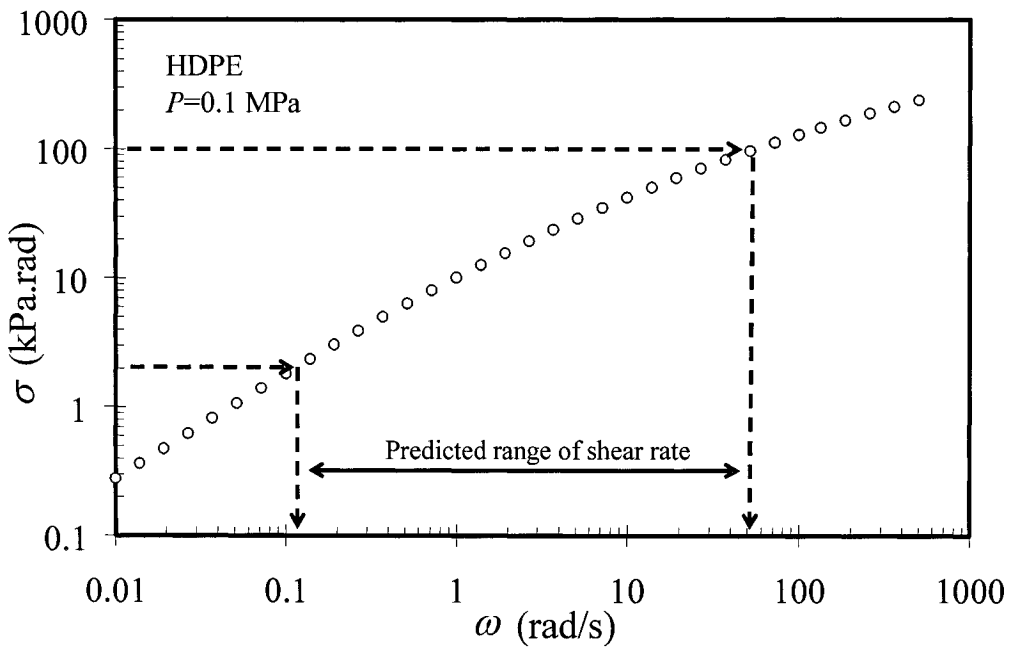

Figure 5.20. Prediction of shear-rate range from the stress values of SAOS test at 180℃.

5.4.4.5 Effect of Temperature on LVE Behavior and Temperature Shift Factors

The effect of temperature on the complex viscosity is shown in Fig. 5.21. Temperature shift factors were used to describe this effect quantitatively and construct a master curve. Figure 5.22 shows stress amplitude as a function of

frequency at several temperatures. To build a master curve, The stress versus frequency curve was first shifted along the vertical stress axis by a factor of $b_T(T)$, which is defined as:

$$b_T(T) \equiv \frac{T\rho(T)}{T_0\rho(T_0)} \tag{5.23}$$

where ρ is density obtained from *PVT* data, and then this curve was shifted along the horizontal axis onto that at T_0, to determine the factor $a_T(T)$. The zero-shear viscosity at T is then given by:

$$\eta_0(T) = a_T(T)b_T(T)\eta_0(T_0) \tag{5.24}$$

While $b_T(T)$ is usually assumed to be unity, this is not strictly true, as described in Section 2.4.2.1 (Fig. 2.5) there is an 7% variation over 50 degrees. In order to evaluate the validity of assuming $b_T(T)$ to be unity, since *PVT* data were available, the effect of ignoring $b_T(T)$ could be determined. The zero-shear viscosity ignoring $b_T(T)$ at T can be calculated by:

$$\eta_0(T) = a_{1,T}(T)\eta_0(T_0) \tag{5.25}$$

The determination of a_T is based on the following expression:

$$\sigma[\omega a_T(T), T]/b_T(T) = \sigma(\omega, T_0) \tag{5.26}$$

where $b_T(T) \neq 1$. The master-curve form of the Yasuda model of stress (Fig. 5.23) using $a_T(T)$ for horizontal shift and $b_T(T)$ for vertical shift is as follows:

$$\frac{\sigma(\omega, T)}{b_T(T)} = \frac{\eta_0 \omega a_T(T)}{\left\{1 + [\lambda\omega a_T(T)]^a\right\}^{(1-n)/a}} \tag{5.27}$$

where η_0, n, a, and λ are the fitting parameters determined at T_0, 180℃. The determination of $a_{1,T}(T)$ is based on Eq. 5.28:

$$\sigma[\omega a_{1,T}(T), T] = \sigma(w, T_0) \tag{5.28}$$

The master-curve form of the Yasuda model (Fig. 5.24) for Eq. 5.28 is given by Eq. 5.29:

$$\sigma(\omega, T) = \frac{\eta_0 a_{1,T}(T)\omega}{\left\{1 + [\lambda\omega a_{1,T}(T)]^a\right\}^{(1-n)/a}} \tag{5.29}$$

The regression for determining $a_T(T)$ or $a_{1,T}(T)$ was repeated until the following sum was minimized:

$$S = \sum_{i=1}^{N}\left(\frac{\sigma_i - \sigma_{mp,i}}{\sigma_i}\right)^2 \tag{5.30}$$

where i is the frequency index, σ is a stress datum, σ_{mp} is a model-predicted stress value, and N is the number of data. Both shifted results show equally good superposition, and this implies that: (1) this material shows thermorheological simplicity, and the temperature shift factor at each temperature is independent of frequency, and (2) the shift factor $b_T(T)$ is not necessary to build a master curve. Assuming $b_T(T)$ to be unity is thus a valid procedure. However, if this factor is a strong function of temperature, and strong shear thinning occurs, $b_T(T)$ will be required. This is illustrated in Appendix 5. A case similar to the former is that gas is dissolved in polymer, *i.e.* a shift factor is a strong function of concentration (Section 6.7.7).

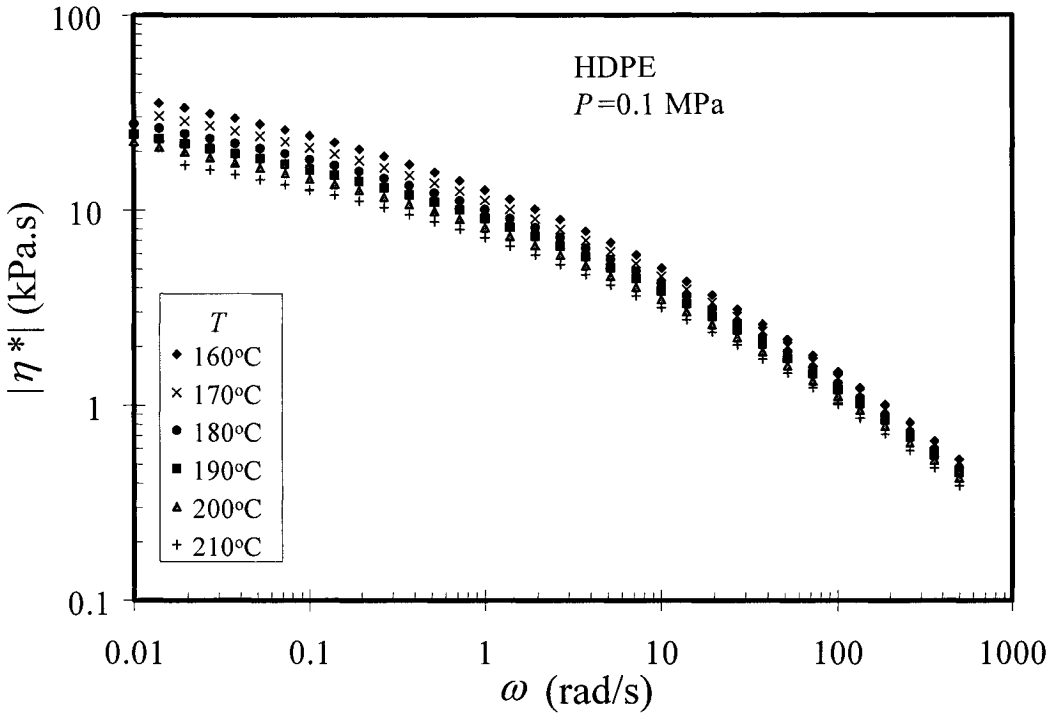

Figure 5.21. The effect of temperature and frequency on the complex viscosity.

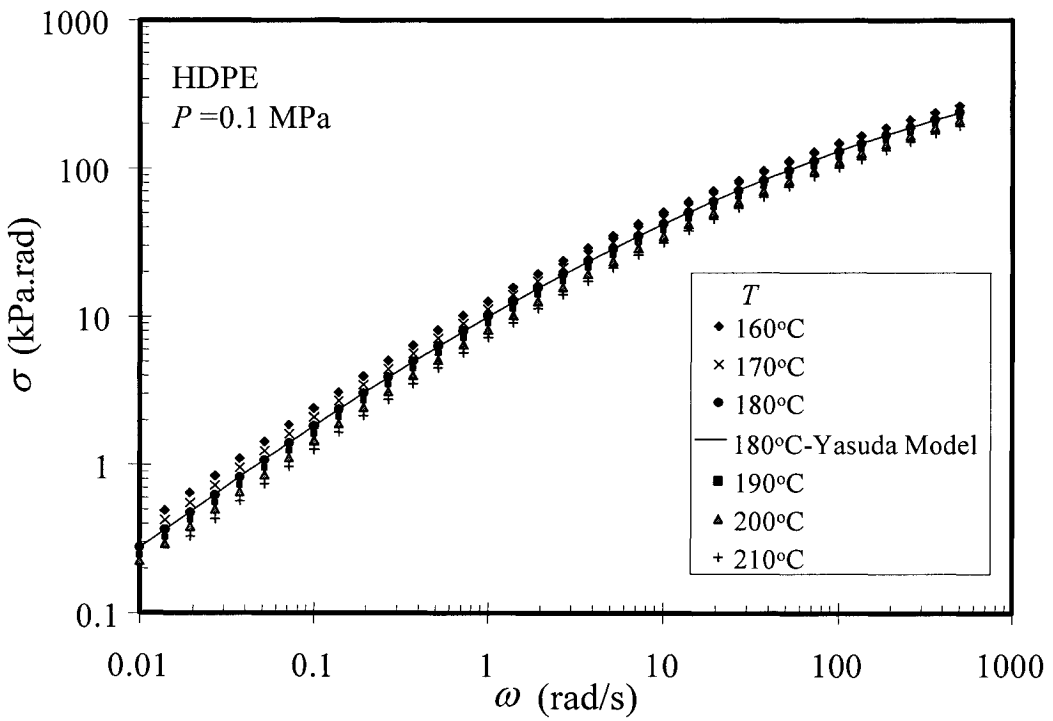

Figure 5.22. The effect of temperature and frequency on the stress from SAOS.

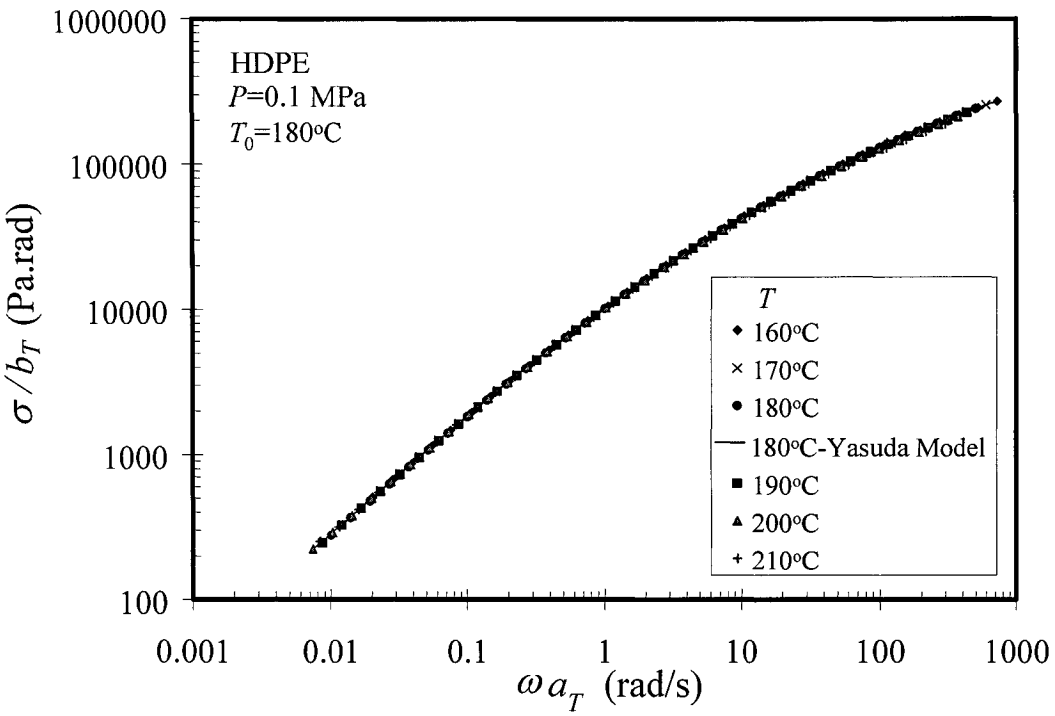

Figure 5.23. Shifted curves of stress using both a_T and b_T.

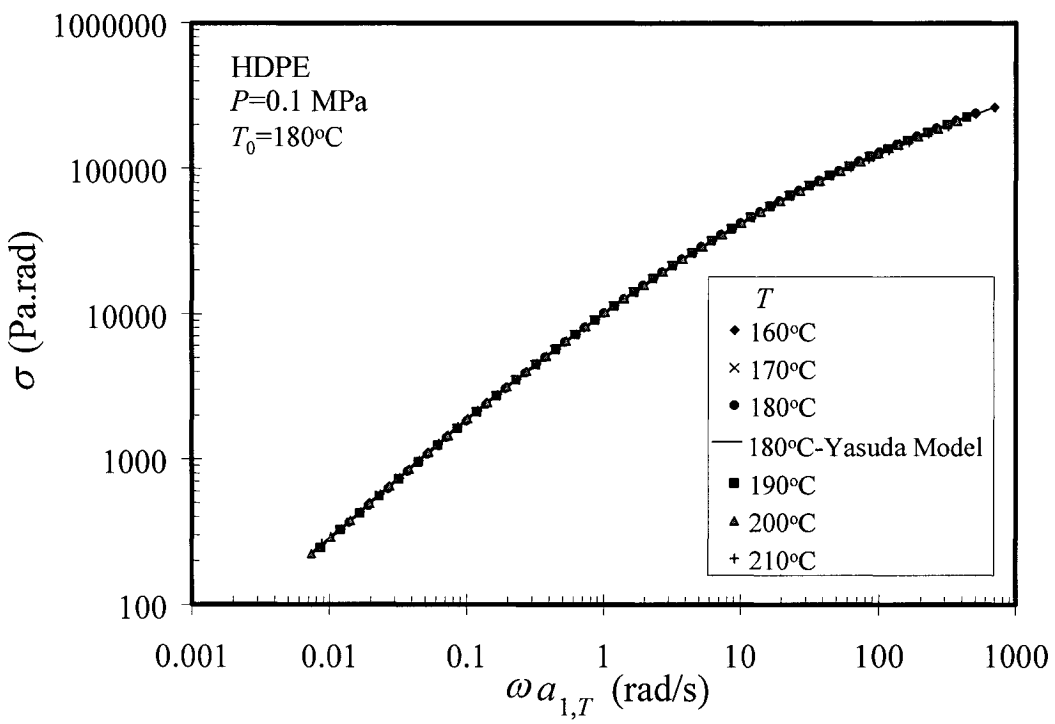

Figure 5.24. Shifted curves of stress using $a_{1,T}$ and assuming b_T to be one.

To compare the various shift factors, they are plotted in Fig. 5.25 as functions of the inverse temperature. Each factor can be modeled using an Arrhenius equation as follows:

$$\ln[a_{1,T}(T)] = \frac{E_{a,a_1}}{R}\left(\frac{1}{T} - \frac{1}{T_0}\right) \tag{5.31}$$

$$\ln[a_T(T)] = \frac{E_{a,a}}{R}\left(\frac{1}{T} - \frac{1}{T_0}\right) \tag{5.32}$$

$$\ln[b_T(T)] = -\frac{E_{a,b}}{R}\left(\frac{1}{T} - \frac{1}{T_0}\right) \tag{5.33}$$

$$\ln[a_T(T)b_T(T)] = \frac{E_a}{R}\left(\frac{1}{T} - \frac{1}{T_0}\right) = \frac{E_{a,a} - E_{a,b}}{R}\left(\frac{1}{T} - \frac{1}{T_0}\right) \tag{5.34}$$

A linear relationship between ln (shift factor) and $1/T$ indicates that the activation energy is independent of temperature. Values of the activation energy are given in Table 5.6. It should be noted that:

$$a_{1,T}(T) \neq a_T(T)b_T(T) \tag{5.35}$$

even though both sides are the ratio of zero-shear viscosity at two temperatures, and this implies that the zero-shear viscosity calculated at T depends on whether $b_T(T)$ is ignored. This occurs when a shift factor was obtained by shifting the stress curve instead of using the zero-shear viscosity. However, the difference in activation energies based on $a_{1,T}(T)$ and $a_T(T)b_T(T)$ is 4%, and this is at the level of the uncertainty in the data. The temperature shift factors, $a_{1,T}(T)$ obtained here will be expressed as $a_T(T)$ in the remainder of this thesis and compared with those obtained in steady simple shear tests using the HPSPR in the next chapter (Section 6.7.5). This will reveal whether the effect of temperature on LVE is the same as its effect on NLVE.

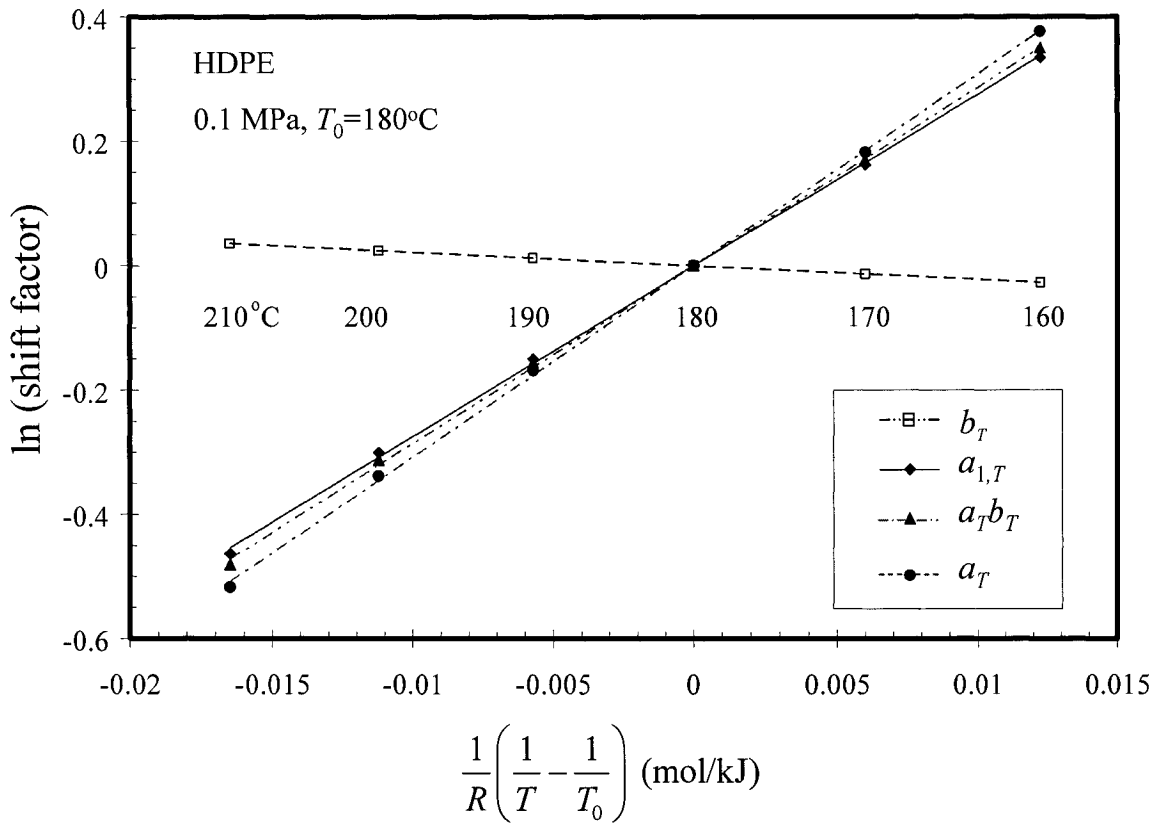

Figure 5.25. Effect of temperature on the temperature shift factors.

Table 5.6. Activation energy for shift factors.

Shift factor	E_a (kJ/mol)
$b_T(T)$	2.2
$a_{1,T}(T)$	27.5
$a_T(T)b_T(T)$	28.6
$a_T(T)$	30.8

5.5 Conclusions

Two rotational rheometers were used for this study. The optimal gap was found to be 1 mm for the parallel-disk geometry. The thermal stability of the HDPE was found to be satisfactory for this study. The zero-shear viscosity could not be determined using creep tests due to the high PDI of HDPE. The four-parameter Yasuda model describes the complex viscosity versus frequency data very well. The

effect of temperature on LVE behavior was studied by using temperature shift factors. The simple exponential Arrhenius equation successfully describes the temperature dependency of the shift factors. The validity of using a vertical shift factor $b_T(T)$ based on *PVT* density data was tested, and it was found that this factor could be taken to be unity to build a master curve of the complex viscosity. The comparison of LVE and NLVE behaviors is presented in the next chapter.

5.6 References

1. C.H. Bamford and C.F.H. Tipper, *Degradation of Polymers*, Elsevier, New York, 1975.
2. W.P. Cox and E.H. Merz, "Correlation of dynamic and steady flow viscosities," *J. Polym. Sci.* 28:619 (1958).
3. J.M. Dealy and K.F. Wissbrun, *Melt Rheology and Its Role in Plastics Processing*, Chapman & Hall, London, 1995.
4. Y. Ye, "The study of long time relaxation behavior of metallocene polyethylene," Master's Thesis, McGill University, Montreal, 2001.
5. J.M. Dealy, *Rheometers for Molten Plastics*, Van Nostrand Reinhold Company, New York, 1982.
6. R.L. Powell, "Rotational Viscometry," in *Rheological Measurement*, Second Edition, Edited by A.A. Collyer and D.W. Clegg, Chapman and Hall, London, 1998.
7. H.L. Wagner and K.F. Wissbrun, "Molecular weight and rheology of acetal copolymers," *Makromol. Chemie* 81:14 (1965).
8. P.J. Carreau, "Rheological equations from molecular network theories," Doctoral Thesis, University of Wisconsin, Wisconsin, 1969.
9. M.M. Cross, "Deformation and Flow," in *Polymer Systems*, Edited by Wetton and Whorlow, Macmillan, London, 1968.
10. K.Y. Yasuda, R.C. Armstrong, and R.E. Cohen, "Shear flow properties of concentrated solutions of linear and star branched polystyrenes," *Rheol. Acta* 20:163 (1981).
11. H.E. Park, "Effect of pressure on the rheological properties of three polyethylenes," Master's Thesis, McGill University, Montreal, 2001.

6. Effects of Pressure, Temperature, and Concentration on Rheological Properties

6.1 Introduction

Even though elevated pressures are involved in several important polymer processing operations, such as high-speed extrusion and injection molding, the pressure dependence of rheological properties such as viscosity has not been well studied due to the difficulty of carrying out experiments at a uniform, high pressure. The effect of pressure on rheological properties is in many ways the reverse of that of temperature, and knowledge of temperature effects is useful in understanding the effects of pressure.

The effect of SC-CO_2 on rheological properties is attracting growing interest, because of potential applications of SC-CO_2 in plastics processing. Until now, only modified capillary rheometers have been used to determine approximate viscosities at elevated pressures with dissolved SC-CO_2 (Chap. 4). These instruments are not useful for the determination of viscoelastic properties such as the creep compliance.

It is necessary to apply a constant and uniform stress to determine the creep compliance, which is an important viscoelastic property. Creep tests are also useful for the study of wall slip. The slip velocity increases with shear stress above a critical value of around 0.1 MPa, depending on the nature of the polymer, and it is also of interest to study the pressure dependence of slip as well as the effect of dissolved SC-CO_2. However, due to the difficulty of making measurements at high pressure, no creep or slip measurements at elevated pressures with SC-CO_2 have been reported.

The high-pressure sliding plate rheometer developed at McGill University is well suited to such measurements, because the shear strain and pressure are uniform throughout the sample, and it can be easily programmed to generate any desired shear strain as a function of time. By replacing the inert pressurizing medium with CO_2, the effect of dissolved CO_2 on the rheological properties of a molten polymer

can be determined. For the purpose of comparison, the effect of dissolved nitrogen (N_2) was also determine.

Another application of the apparatus is the study of plastic foams, since the HPSPR can be used to simulate the foaming process by releasing the pressure suddenly. The HPSPR can be used to study the effect of strain history on foam formation, the effects of P, T, and C on foam structure, and the effect of foam structure on melt viscosity. The last mentioned type of study is of interest for a process in which foaming and flow in a mold occur simultaneously. The rheological properties of foamed polymeric liquids have been studied by applying pressure driven flow, but the pressure and temperature are not uniform in this situation, and bubbles are not fully formed in the capillary or slit in which pressure is measured. Han [1, p.325] pointed out that elaborate theoretical analysis is required to interpret the data obtained. However, data analysis is quite straightforward in the case of the HPSPR.

6.2 Rheological Properties of Interest

6.2.1 Viscosity

The viscosity of a molten polymer is very important, as it is directly related to processability; it depends on temperature T, pressure P, shear rate $\dot{\gamma}$, molecular structure, and additives. Reliable viscosity data taking into account these factors are required for the simulation and design of polymer processes and for the development of new polymers. It is clear that viscosity data obtained at atmospheric pressure or without accounting for dissolved SC-CO_2 can be quite misleading if applied to a high-pressure process with or without dissolved SC-CO_2.

6.2.1.1 Shear Rate Dependence of Viscosity

For Newtonian fluids the viscosity is independent of shear rate, but most polymer melts are non-Newtonian fluids in which the viscosity is a strong function of shear

rate. The curve of viscosity versus shear rate shows three regions: Newtonian (constant viscosity), transition, and power law. The limiting value of the viscosity at low shear rates is called the zero-shear or Newtonian viscosity, which is given the symbol η_0. In the transition region the viscosity decreases with increasing shear rate, finally approaching power-law behavior. Plots using linear scales do not show the three regions clearly, so η versus $\dot{\gamma}$ data are usually plotted using logarithmic scales.

An equation to describe the dependence of viscosity on shear rate is required to determine the effect of P, T, and C on rheological properties by use of shift factors. A number of equations have been proposed. One example is the power-law model that often describes the viscosity at high shear rates:

$$\eta = \eta_0 |\lambda\dot{\gamma}|^{n-1} \tag{6.1}$$

where n is the power-law index, and λ is a characteristic time of the material. This time constant usually has the same temperature dependence as the viscosity and can thus be expressed in terms of a material constant, τ, having units of stress:

$$\lambda \equiv \eta_0/\tau \tag{6.2}$$

Since η_0 is a function of T and P, λ is also a function of T and P.

To describe the viscosity over a broad range of shear rates, several generalized power law equations have been proposed. An example is the Cross model [2], which is shown as Eq. 6.3:

$$\eta = \frac{\eta_0}{1+|\lambda\dot{\gamma}|^m} \tag{6.3}$$

At low shear rates, the viscosity approaches η_0, and at high shear rates, the viscosity shows power law behavior with $m = 1-n$. The characteristic time, λ, is the inverse of the shear rate at which the viscosity is half the zero-shear viscosity. The Carreau model [3, p.78] is given by:

$$\eta = \frac{\eta_0}{[1+(\lambda\dot{\gamma})^2]^p} \tag{6.4}$$

where p is a material constant, and the viscosity shows power law behavior with $p=(1-n)/2$ at high shear rates. Yasuda [4] added another constant, a, to facilitate curve fitting, to give Eq. 6.5:

$$\eta = \frac{\eta_0}{[1+(\lambda\dot{\gamma})^a]^{(1-n)/a}} \tag{6.5}$$

where n is the traditional power-law constant.

6.2.2 Stress Growth Function

While modified capillary rheometers have been used to determine approximate values of the viscosity at elevated pressures, these instruments are not useful for the determination of viscoelastic properties. The sliding-plate rheometer is well-suited to such measurements, because the shear strain is uniform throughout the sample, and it can be easily programmed to generate any desired shear strain as a function of time.

Figure 6.1 shows the essential features of the transient stress during start-up of shearing. The stress curve exhibits an overshoot, with the maximum stress σ_S occurring at a time, t_S, and a plateau, which starts at t_{SS} where the stress reaches its steady-state value σ_{SS}.

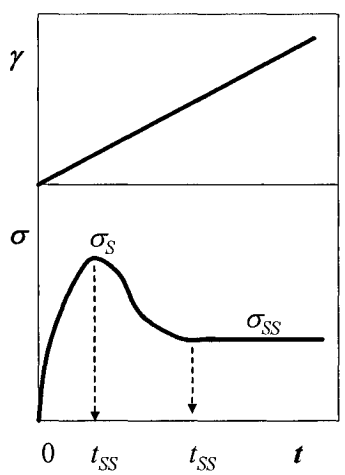

Figure 6.1. Stress profile for start-up shearing at a constant shear rate.

6.2.3 Creep and Steady-State Compliances

By use of feedback-control based on the signal from the shear stress transducer, it is possible to carry out experiments in which the shear stress is the controlled variable. In particular, creep experiments can be carried out in this way. The effects of pressure and dissolved CO_2 on the creep compliance $J(t,\sigma,P,C)$ and the steady-state compliance $J_S(t,\sigma,P,C)$ will be determined.

6.3 Previous High-Pressure Rheometers

There are many kinds of rheometer for atmospheric pressure measurements but only a few that are capable of operation at high pressure. Two types of rheometer have been used for high-pressure studies: pressure-driven rheometers, in which flow is generated by a pressure drop, and drag flow rheometers, in which one bounding wall moves relative to another to generate the shearing deformation. A pressure-driven rheometer forces the sample through a capillary or slit, and the resulting pressure drop is measured. Such an instrument can be used to measure the approximate viscosity at high shear rates, but because the pressure and shear rate are neither uniform nor independent, these instruments are not useful for viscoelasticity studies and are not ideal for the study of the effect of pressure on viscosity. A drag flow rheometer, on the other hand, such as a concentric cylinder rheometer, generates a deformation that is independent of the applied pressure. However, seal friction, end effects, and flow instability limit its usefulness at high pressures and shear rates. Figure 6.2 shows the velocity and the stress profiles in the two types of instrument.

The stress profiles in both types of rheometer are material-independent and can be derived from Cauchy's equations:

$$\rho\frac{D\vec{v}}{Dt}=-\rho g\nabla h-\nabla P+\nabla\cdot\underline{\tau} \tag{6.6}$$

For steady-state, fully-developed flow, Eq. 6.6 can be reduced to the following

equations for pressure driven flow in a slit and for simple shear (drag) flow:

$$0 = -\frac{\partial P}{\partial x} + \frac{\tau_{yx}}{\partial y} \qquad \text{Slit flow} \qquad (6.7)$$

$$0 = \frac{\tau_{yx}}{\partial y} \qquad \text{Simple shear flow} \qquad (6.8)$$

where τ_{yx} is the shear stress, σ. The above equations show that the shear stress in a slit flow is a linear function of y, while that in a simple shear flow is constant. However, the velocity profile for pressure flow depends on the properties of the sample, while in simple shear flow it is independent of fluid properties. Park [5] reviewed high-pressure rheometers in detail.

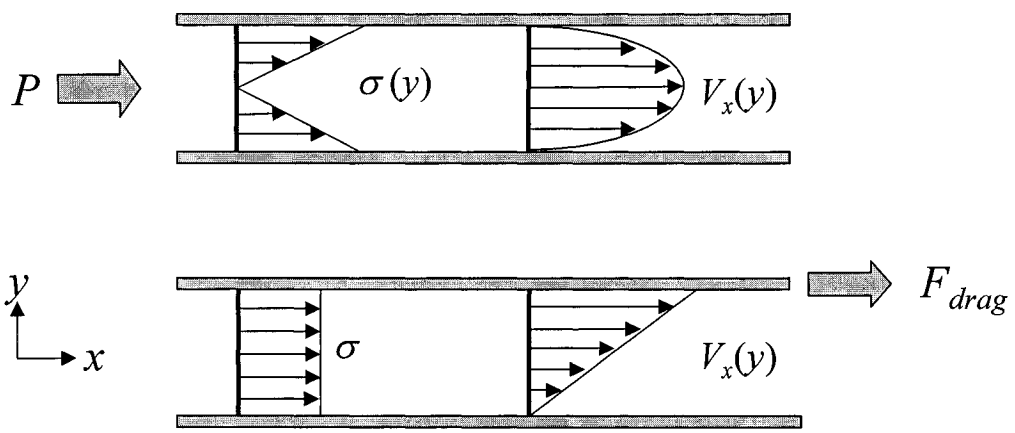

Figure 6.2. The stress and the velocity profiles of pressure-driven flow and drag flow.

6.3.1 Pressure-Driven Rheometers

A rheometer based on pressure-driven flow consists of a heated barrel, a piston or pressurization system, and a die. A capillary rheometer (Fig. 6.3) has a circular die, and in a slit rheometer (Fig. 6.4) it is a thin rectangular slit. A moving piston generates flow in the die, and the resulting pressure drop is measured or, if a pressurization system is used, the driving pressure is set, and the flow-rate is measured.

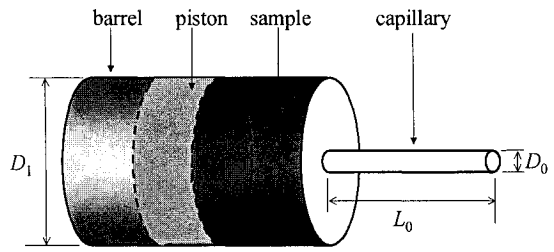

Figure 6.3. Geometry of a capillary rheometer.

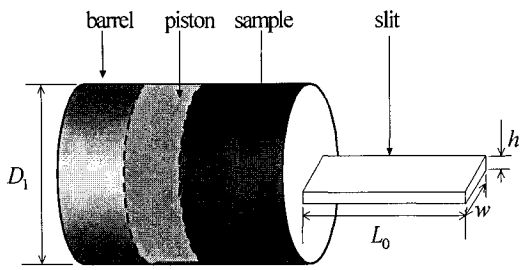

Figure 6.4. Geometry of a slit rheometer.

Capillary and slit rheometers are popular for measurements at high shear rates, and they simulate to some degree flows occurring in plastics processing. However, the shear stress and the shear rate must be inferred indirectly from the driving pressure and volumetric flow rate. Since the pressure and shear rate are inhomogeneous, the molecules in a sample will have various pressure and deformation histories.

6.3.1.1.1 High-Pressure Capillary Rheometer

A capillary rheometer consists of a barrel, a piston, and a capillary. Data from a capillary rheometer are usually reported in terms of the wall shear stress, σ_w, and the wall shear rate, $\dot{\gamma}_w$. However, since these quantities can only be inferred from the measured pressure drop and flow rate, several assumptions must be made in the treatment of the raw data. The Bagley end correction [6] is often used to obtain σ_w, and the Rabinowitch correction [7] is used to estimate $\dot{\gamma}_w$. Figure 6.5 [8] shows the pressure distribution in a capillary rheometer, where P_d is the driving pressure, P_a is the environmental pressure, ΔP_{ent} is the entrance pressure drop, ΔP_{cap} is the pressure drop in the capillary, and ΔP_{ex} is the exit pressure drop. The two excess pressure drops, ΔP_{ent} and ΔP_{ex}, are related to the elasticity of the melt [9].

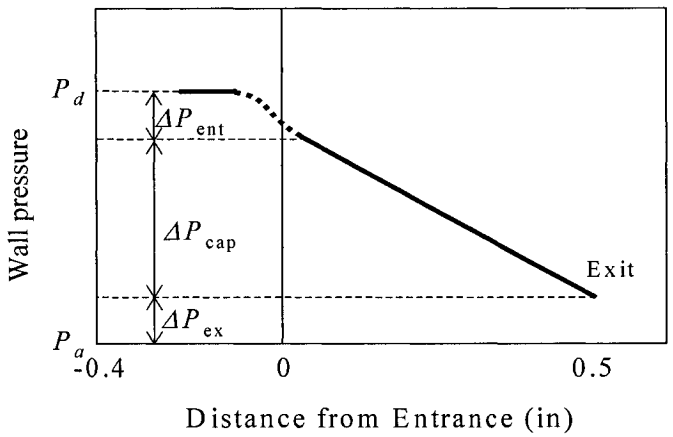

Figure 6.5. Pressure distribution in a capillary rheometer.

The Bagley end correction is used to correct for the excess pressure drops, and the true wall shear stress is given by:

$$\sigma_w = \frac{P_d}{2(L_0/R+e)} \tag{6.9}$$

where L_0 is the length of the capillary, R is $D_0/2$, and e is the Bagley end correction, which is the intercept on the L_0/R axis of a P_d versus L_0/R plot, *i.e.*, a Bagley plot. The wall shear rate can be obtained from the apparent shear rate by use of the Rabinowitch correction. The apparent shear rate is the shear rate that would obtain for a Newtonian fluid:

$$\dot{\gamma}_A \equiv \left(\frac{4Q}{\pi R^3}\right) \tag{6.10}$$

where Q is the volumetric flow rate. The Rabinowitch correction takes into account the shear rate dependence of the viscosity and gives the true wall shear rate, $\dot{\gamma}_w$:

$$\dot{\gamma}_w = \left(\frac{3+b}{4}\right)\dot{\gamma}_A \tag{6.11}$$

where

$$b \equiv \frac{d(\log\dot{\gamma}_A)}{d(\log\sigma_w)} \tag{6.12}$$

High-pressure capillary rheometers are similar in basic design to standard instruments but do not exhaust to the atmosphere. Rheometers of this type were developed by Westover [10], Kamal and Nyun [11,12], Karl [13], Driscoll and Bogue [14], Baker and Thomas [15], Mackley *et al.* [16], Chakravorty *et al.* [17], and Binding *et al.* [18].

6.3.1.1.2 High-Pressure Slit Rheometer

The hydrostatic pressure varies along the length of a capillary die, but it is difficult to measure the local pressure gradient, which is necessary for the determination of the viscosity. If a slit die is used, pressure transducers can be installed directly in the wall of the slit, and the pressure distribution in the die can be determined. However, a correction for the wall shear rate is still required.

The wall shear stress in a slit is given by:

$$\sigma_w = \left(\frac{-\Delta P}{L}\right)\frac{h}{2} \tag{6.13}$$

where ΔP is the pressure drop for a slit of length L. The wall shear rate [19] is given by:

$$\dot{\gamma}_w = \left(\frac{6Q}{h^2 w}\right)\left(\frac{2+\beta}{3}\right) \tag{6.14}$$

where:

$$\beta \equiv \frac{d[\log(6Q/wh^2)]}{d[\log(\sigma_w)]} \tag{6.15}$$

High-pressure slit die rheometers have been used by Laun [20], Kadijk and Van den Brule [21], and Langelaan *et al.* [22].

6.3.2 Drag Flow Rheometers

The advantage of drag flow rheometers is that the hydrostatic pressure is independent of the force driving the deformation, and the shear rate and hydrostatic pressure can thus be controlled independently. The pressure is uniform throughout the sample, but shear rate corrections are required for some geometries.

6.3.2.1 High-Pressure Couette-Flow Rheometer

A concentric cylinder (Couette) rheometer consists of two concentric cylinders, a rotational drive, and a torque measuring device. The sample fills the gap between the two cylinders, and one cylinder is rotated. The shear rate is obtained from the rotational speed, while the torque is used to calculate the shear stress. Stress relaxation experiments can also be carried out.

Mooney [23] used a concentric cylinder (Couette) plastometer. Semjonow [24] and Cogswell [25], Bair *et al.* [26,27], Khandare *et al.* [28] used pressurized Couette rheometers. Highgate and Whorlow [29] have shown that end effects make a substantial contribution to the measured torque in such a device.

6.3.2.2 High-Pressure Falling Sphere Viscometer

Falling sphere viscometers have been used for the measurement of the pressure dependence of the zero-shear viscosity, which is determined by measuring the terminal velocity of a sphere falling in pressurized melt. No dynamic seals are required, and the apparatus is easy to construct and operate. A falling sphere viscometer is not suitable for the study of viscoelasticity, but it can be used to determine the important rheological property η_0 at high pressure. This type of rheometer was used by Foltz *et al.* [30] and Sobczak *et al.* [31-35].

6.4 High-Pressure Sliding Plate Rheometer

Giacomin *et al.* [36,37] developed a sliding-plate rheometer (SPR) incorporating a shear stress transducer, which has significant advantages over other types of rheometer. The parallel-plate geometry and drag flow allow the generation of simple shear flow, and the shear stress transducer measures stress with no end or edge effects. Giacomin [36] describes the SPR in detail in his doctoral thesis.

The high-pressure sliding plate rheometer (HPSPR) [38,39] developed at McGill University can generate controlled, homogeneous, shearing deformations at a uniform pressure in either strain- or stress-controlled modes. The HPSPR is similar in basic design to the earlier, ambient-pressure SPR but requires a special housing and SST due to the high-pressures involved. This rheometer can be used to determine the effects of pressure, temperature and shear history on the rheological behavior of elastomers and molten thermoplastics.

6.4.1 Sliding-Plate Rheometer

Figure 6.6 shows the basic principle of an SPR. The rheometer generates a shear deformation by moving one plate relative to the other. The basic rheological quantities, stress and strain, are related to the measured quantities as follows:

$$\sigma = F/A \tag{6.16}$$

$$\gamma = X/h \tag{6.17}$$

$$\dot{\gamma} \equiv \frac{d\gamma}{dt} = V/h \tag{6.18}$$

where F is the shear force, X is the displacement of the moving plate, V is its velocity, and h is the gap between the two plates.

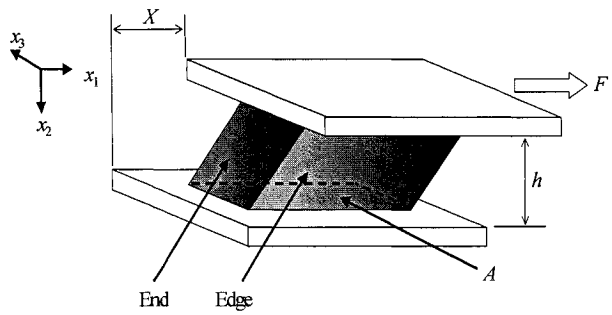

Figure 6.6. Basic principle of sliding-plate flow. An edge is a free surface parallel to the moving direction, and an end is normal to the direction.

An SPR has some limitations. The length of the rheometer limits the total strain and shear rate, and edge and end effects induce inhomogeneity in the deformation of elastic materials. These effects arise from a stress mismatch at the free surfaces [40]. Sample degradation is much less severe than that in a parallel disk or cone-plate rheometer, since the maximum torque is obtained at the edge in the latter instruments where the sample is exposed to the environment. Secondary flow in the sliding-plate rheometer arises from the normal stress differences [41]:

$$N_1 \equiv \sigma_{11} - \sigma_{22} \tag{6.19}$$

$$N_2 \equiv \sigma_{22} - \sigma_{33} \tag{6.20}$$

Since the shape of the wetted area of an SPR is not precisely controlled, it is difficult to establish this area. It is thus difficult to obtain the true stress by measuring the total force on one of the plates. To eliminate the surface area problem and edge/end effects, the shear stress transducer (SST) was developed by Dealy [42] and used by Giacomin *et al.* [36,37] in the SPR. Figure 6.7 [43] shows the essential features of the SPR. The stress is measured in the center of the sample by means of the SST, and the stress measurement is not affected by the free-surface phenomena and degradation at the edges of the sample. The area over which the shear force is measured is equal to that of the SST active face, and it is not necessary to know the wetted area. Figure 6.8 shows the SST and the beam that deflects in response to a shear force on the active face. This SST is called a "disc-spring transducer", because the elastic member is a steel diaphragm [44]. Figure 6.9 shows the basic dimensions of the SST.

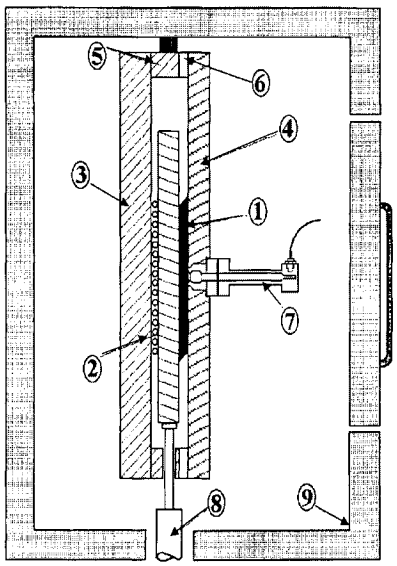

Figure 6.7. Cross section showing the essential elements of the SPR incorporating a disk-spring-type shear stress transducer. 1 sample; 2 moving plate; 3 back support; 4 stationary plate; 5 end frame; 6 gap spacer; 7 shear stress transducer incorporating a rigid beam supported by a steel diaphragm disk spring; 8 linear actuator; and 9 oven.

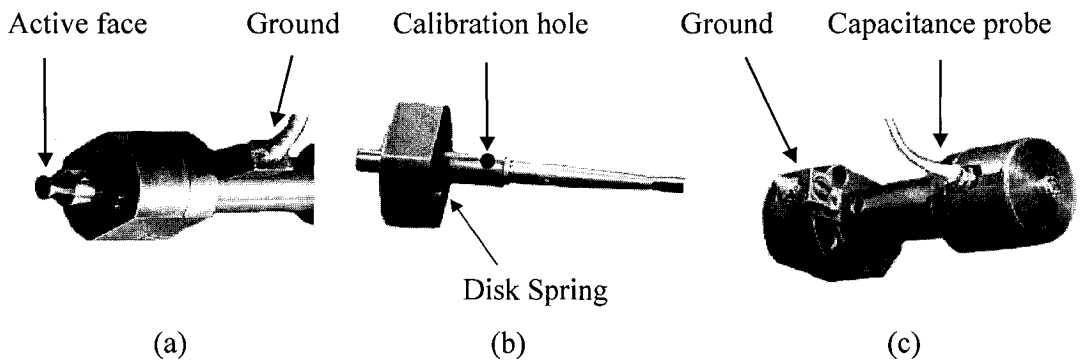

Figure 6.8. SST and beam (a) Left-top view of the SST. (b) Cantilever beam in the SST. (c) Right-top view.

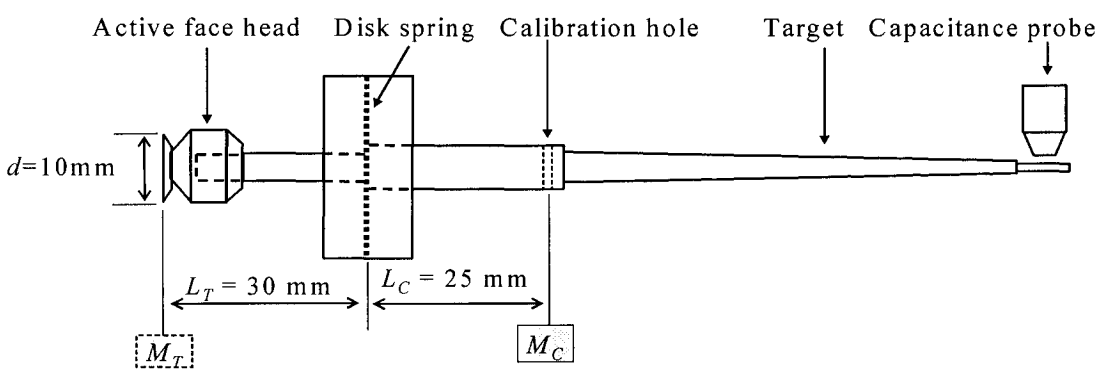

Figure 6.9. Dimensions of the SST of the SPR.

The capacitance proximity probe provides a signal related to the distance between the probe tip and the target. A shear stress causes deflection of the beam and a change in the probe signal. A Capacitec signal conditioner and amplifier (Fig. 6.10) provide a signal that is proportional to stress, and an analog to digital (A/D) convertor provides a digital output.

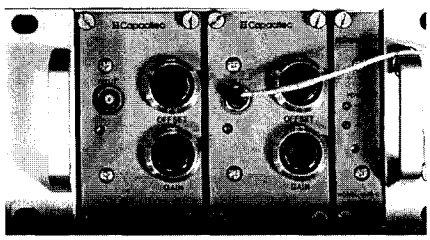

Figure 6.10. Capacitec amplifiers.

User-defined deformation histories can be generated by means of the servohydraulic linear actuator with computer control. It is possible, for example, to generate the following histories: steady shear, single or multi step strains, start-up and cessation of steady shear, interrupted shear, large amplitude oscillatory shear, exponential shear, and creep and creep recovery. A precision linear bearing table supports the movement of the moving plate. High-temperature lubricant is required in the bearing system to keep the movement smooth.

In controlled strain experiments, the command displacement is compared with the actual displacement of the moving plate, and a feedback loop controls the displacement of the moving plate. In controlled stress experiments, a command stress is compared with the stress sensed by the SST, and a feedback loop controls the displacement of the moving plate. This latter type of experiment requires very careful tuning of the controller.

6.4.2 High-Pressure Sliding Plate Rheometer

The high-pressure sliding plate rheometer (HPSPR) developed at McGill University can generate controlled, homogeneous, shearing deformations at uniform pressure. This rheometer can be used to determine the effects of pressure, temperature and shear deformations on the rheological behavior of elastomers and molten thermoplastics. Koran [38] and Park [5] describe this rheometer in detail in their theses.

6.4.2.1 Basic Features

The HPSPR has been used to study several materials, and its capabilities and limitations have been explored. Figures 6.11 to 6.14 show the HPSPR system. It operates over a temperature range from 25 to 225℃, and under a vacuum or at pressures up to 70 MPa. It can generate shear rates of 10^{-3} to 500 s^{-1} and can measure shear stresses over a range from 0.146 to 300 kPa. A vessel able to withstand an operating pressure of 70 MPa at a temperature of 225℃ encases the two parallel plates and most parts of the shear stress transducer. One part of the vessel consists of the cover plate, which swings open for sample loading. It is fixed to the main body of the pressure vessel by sixteen, 7/8-in bolts, which are tightened by an air-powered torque wrench. Openings at the top and bottom of the rheometer allow actuation rods to translate, so that the volume inside the vessel remains constant.

The rheometer is pressurized by a hand pump made by Enerpac. The pressurizing medium is Krytox™ General Purpose Oil 107 made by Dupont. This oil is thermally stable, nonflammable, non-volatile, a good lubricant and does not swell either polar or nonpolar materials. Koran [38] found that there was no rheological effect of this oil on Dowlex™ 2049 linear low density polyethylene. After filling the HPSPR with Krytox oil, the approximate desired pressure is generated by means of the hand pump. The pressure is then adjusted precisely by the piston pump. A Dynisco pressure transducer is used to determine the pressure in the HPSPR. The transducer

is calibrated by means of a dead weight tester. The most convenient method of sample preparation is by compression molding, which produces a rectangular sheet. Using this method the sample can be prepared quickly in order to minimize strain and thermal history.

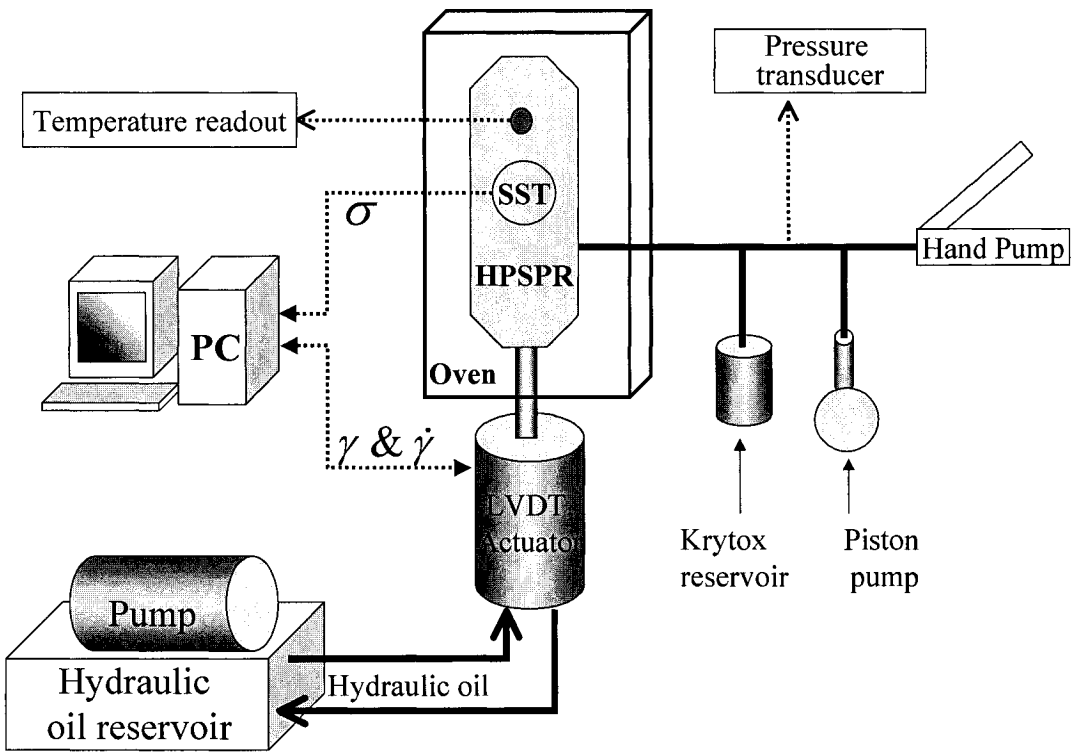

Figure 6.11. Auxiliary components of the HPSPR.

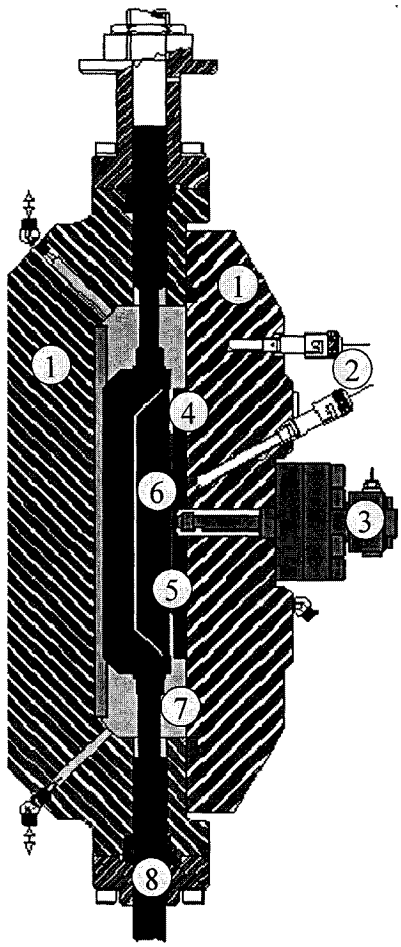

Figure 6.12. Side view of HPSPR [38]:
1. High-pressure vessel
2. Thermocouple
3. Shear stress transducer
4. Fixed plate
5. Sample (red strip)
6. Moving plate
7. Pressurizing medium
   (Krytox oil or gas)
8. Actuating rod

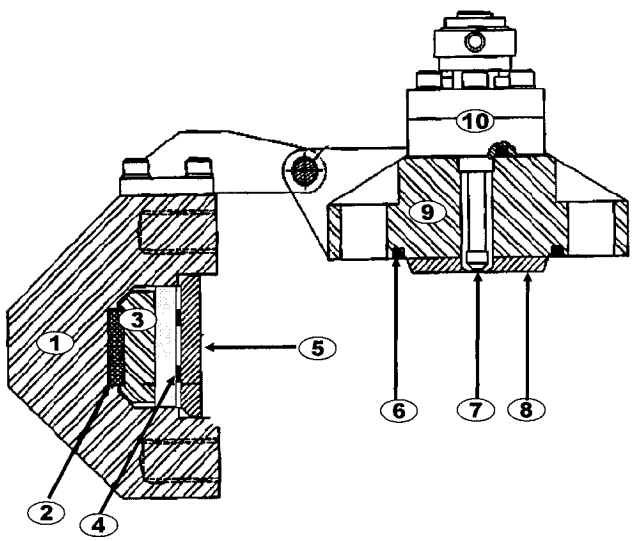

Figure 6.13. Top view of the HPSPR [38]: 1. main body of pressure vessel; 2. bearing plate; 3. moving plate carriage; 4. spacers; 5. moving plate; 6. O-ring; 7. SST active face head; 8. fixed plate; 9. cover plate of pressure vessel; and 10. SST.

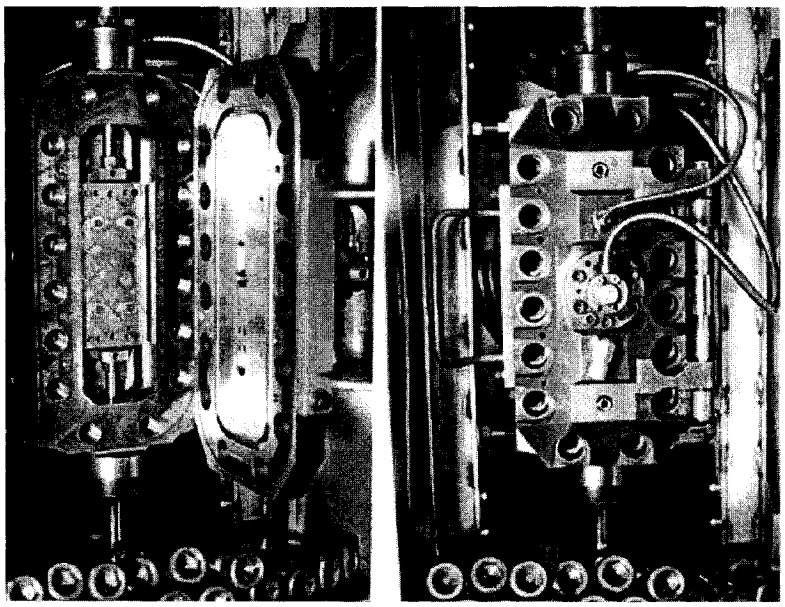

(a) (b)

Figure 6.14. Photo of HPSPR in oven (a) Cover plate open (b) Cover plate closed.

6.4.2.2 Shear Stress Transducer

Figures 6.15 and 6.16 show the details and method of installation of the SST. Torsion bars are used instead of the diaphragm used in the SPR.

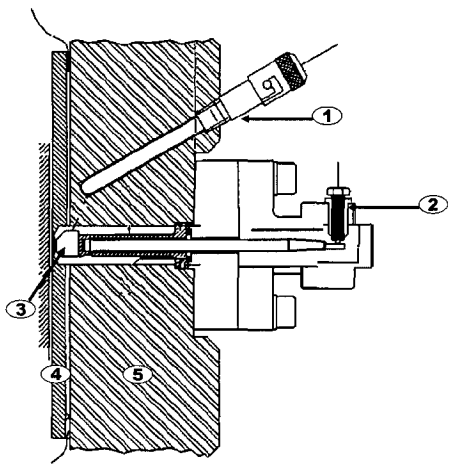

Figure 6.15. Schematic of SST in the HPSPR [38]: 1. thermocouple; 2. Capacitance probe; 3. SST active face head; 4. fixed plate; and 5. Cover plate of pressure vessel.

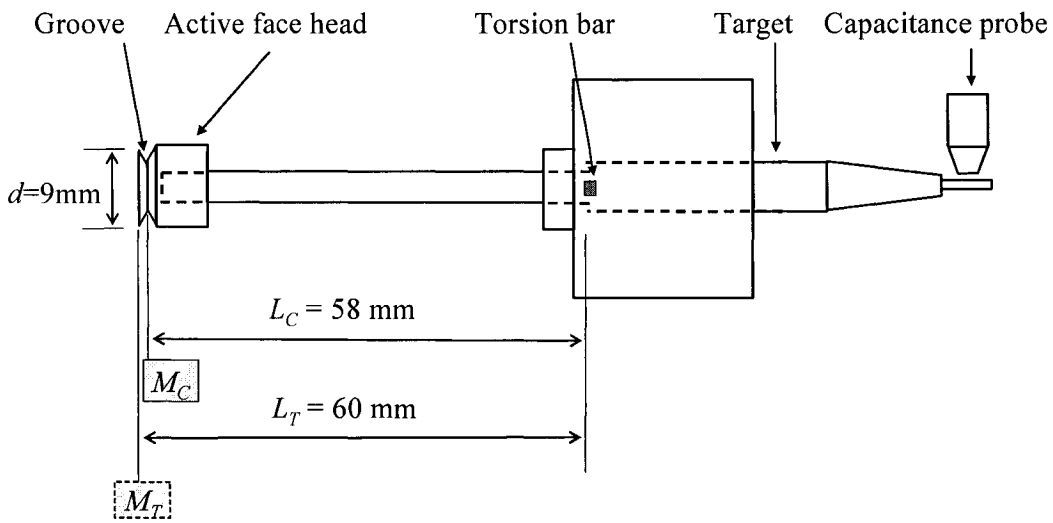

Figure 6.16. Dimensions of SST of HPSPR.

6.4.2.2.1 Calibration of SST

Calibration is performed by suspending masses from the SST active face head (Fig. 6.17). The linearity of the calibration is confirmed by use of a series of masses (Fig. 6.18). This calibration can be performed at any temperature but only at atmospheric pressure, since the cover plate of the pressure vessel must be open for calibration.

Because a mass cannot be suspended from the actual surface of the active face, it is hung instead from a groove in the head by a length of wire. This groove is located 2.5 mm from the active face (Fig. 6.16). The effective stress on the active force σ corresponding to a mass M_C is:

$$\sigma \equiv \frac{F}{A} = \frac{\left(M_C \frac{L_C}{L_T} g\right)}{\pi (d/2)^2} \tag{6.21}$$

where F is the applied force, A is the surface area of the active face, M_C is the mass on the groove, M_T is the imaginary mass on the active face, L_C is the distance from the torsion bar to the groove, L_T is that between the torsion bar and the active face, d is the diameter of the active face, and g is the acceleration of gravity.

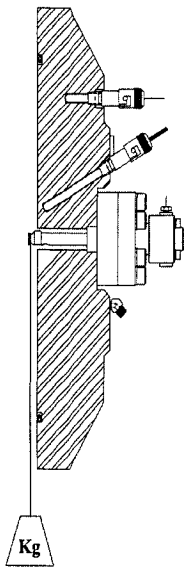

Figure 6.17. Suspended mass calibration at atmospheric pressure [38].

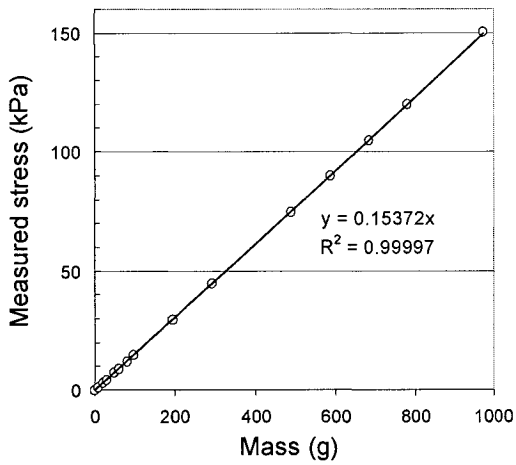

Figure 6.18. Confirmation of the linearity of the calibration line.

6.4.2.3 Sealing

Both dynamic and static seals are required. Cup-seals prevent oil leaks around the actuating rods during their linear motion, and an O-ring prevents oil leaks through the gap between the two plates of the pressure vessel.

6.4.2.3.1 Cup-seals

Polytetrafluoroethylene (PTFE) [45] is used for many dynamic seals due to its chemical inertness, non-adhesive properties, very low friction coefficient, and excellent heat resistance. The material of the dynamic cup-seal (Shamban-Busak Variseal) of the rheometer is PTFE , which is filled with graphite to increase heat, chemical, and wear resistance.

A cup-seal consists of two parts: a graphite-filled PTFE cup and a metal spring. Figure 6.19 shows how cup-seals work. When there is no pressure, there is a small gap between the cup-seal and the actuating rod. Pressure, which is applied by means of the pressurizing oil, pushes the cup wall outward, closing the gap and sealing the rod.

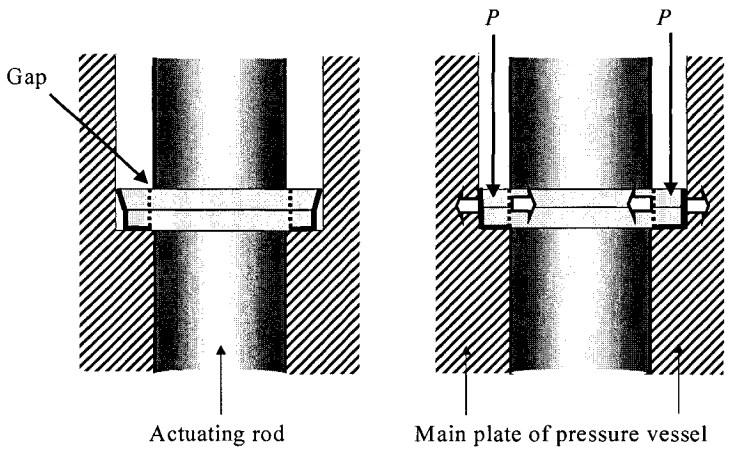

Figure 6.19. Sealing mechanism of a cup-seal around the actuating rod at the bottom.

6.4.2.3.2 O-ring

There is a groove on the inner surface of the cover plate of the pressure vessel to take the Viton™(flouroelastormer) O-ring that prevents oil leakage through the gap between the main body and cover plate of the pressure vessel. Viton™ is used for the O-ring, since it has excellent chemical resistance, non-stick features, can be injection molded (unlike PTFE), and is less tough than PTFE. However, if the sixteen, 7/8-inch bolts are not tightened sufficiently, the O-ring will be damaged by extrusion as shown in Fig. 6.20, even if the pressure holds. The torque on the tightening bolts is controlled by adjusting the air pressure on the Qix Modular FRL combination regulator (Fig. 6.21). Table 6.1 shows the values used at various test pressures.

It was found that the 7/8-inch bolts cannot be loosened if the HPSPR system stays at high T and P for too long a time. In this case a bolt can be loosened by increasing the air pressure of the regulator. When a bolt is tightened, the air pressure should not exceed 500 kPa, so that there is still room to increase this pressure further. (The pressure of the lab compressed air is 700 kPa.)

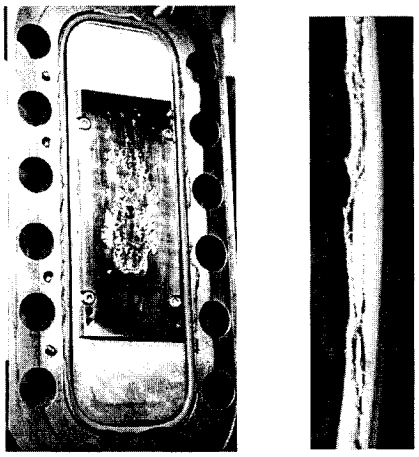

(a) (b)

Figure 6.20. Defective O-ring due to weak tightening. (a) the defective O-ring on the cover plate (b) enlarged extruded segment.

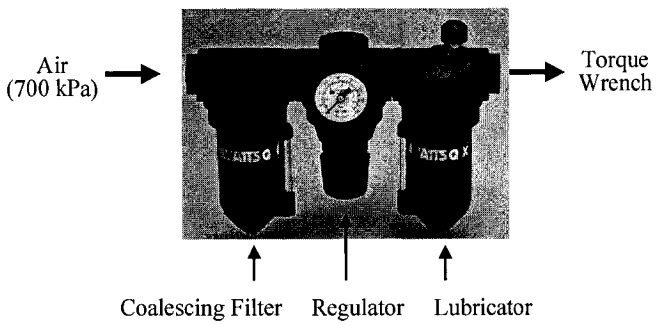

Figure 6.21. Regulator combination.

Table 6.1. Torques for bolt-tightening.

Test Pressure (MPa)	Required torque for the wrench (Nm)	Air Pressure of the regulator	
		(psi)	(kPa)
~ 35	310	33	230
~ 52	465	52	360
~ 69	615	69	480

6.4.3 Pressurizing System

The pressure inside the HPSPR is increased by a hand pump after filling the rheometer with Krytox oil, which is stored in a reservoir. Fine tuning of the pressure level is carried out by a piston pump, and the resulting pressure is measured by the Dynisco pressure transducer.

6.4.3.1 Pressure Transducer

A Dynisco pressure transducer Model 830 (Fig. 6.22) was used to measure the pressure inside the HPSPR. The operating range of this transducer is -54 to 120℃ and 0 to 70 MPa. The specified effect of temperature on span is ±0.036% full scale per ℃, and the nominal accuracy is ±0.5%. A Dynisco Model 1290 Strain Gauge Input Indicator is used to display the pressure value. The indicator was calibrated at the factory, but the calibration was verified by use of a dead weight tester (Fig. 6.23). The calibration line (Fig. 6.24) was obtained by recording the indicated pressure values for the weights on the tester, and it exhibited good linearity but a -1.15% deviation from the applied pressure. Table 6.2 shows the indicated pressure values for various applied pressures.

Figure 6.22. Pressure transducer.

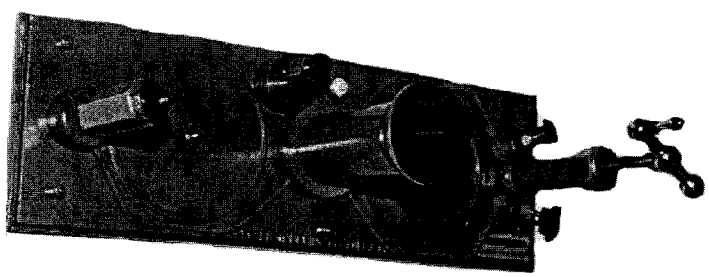

Figure 6.23. Dead weight tester.

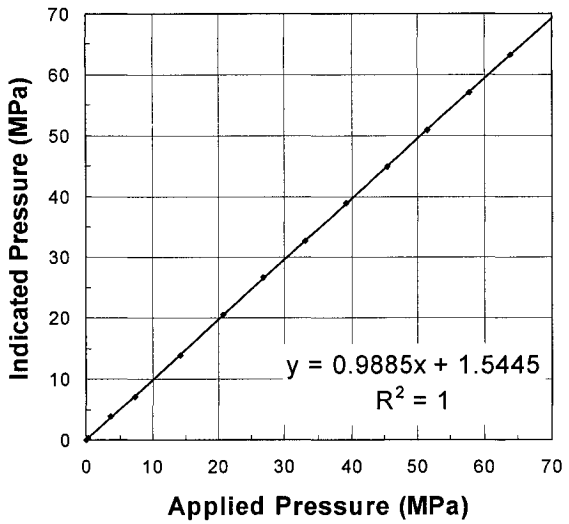

Figure 6.24. Calibration line of the pressure transducer.

Table 6.2. Indicated pressures at various applied pressures.

Applied Pressure		Indicated Pressure
(MPa)	(psia)	(psig)
0.1	15	0
23.0	3330	3280
45.9	6660	6570
68.9	10000	9870

6.4.3.2 Hand Pump

The pump used to pressurize the HPSPR was an Enerpac P-2282 hand pump (Fig. 6.25), which can generate pressures up to 275 MPa. The hand pump provides two-speed operation for faster filling. It takes about 30 minutes to increase the pressure to 70 MPa. Table 6.3 shows the specifications of the hand pump. When the high pressure is released, the release valve must be opened a little. If the valve is

turned by more than 30° at 70 MPa, the sealing system of the pump will be damaged. It is recommended that the valve be opened initially by 5° and increased gradually with decreasing pressure.

Table 6.3. Basic features of the Enerpac hand pump P-2282.

Oil Capacity (ℓ)	Pressure Rating (MPa)		Oil Displacement per Stroke (mℓ)		Piston Stroke (cm)
	1st Stage	2nd Stage	1st Stage	2nd Stage	
1	1.4	275	16	0.6	2.54

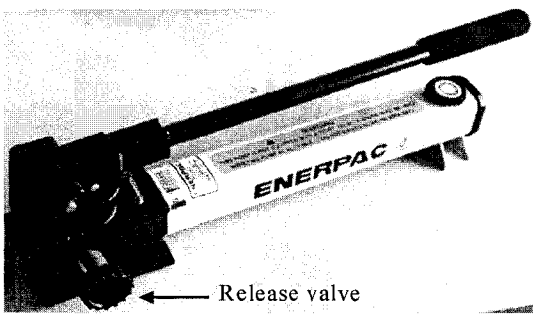

Figure 6.25. Enerpac hand pump P-2282.

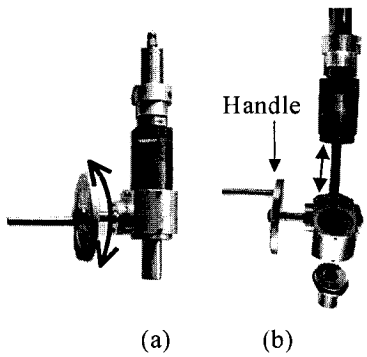

Figure 6.26. Worm-drive piston pump. (a) whole pump and (b) disassembled pump.

6.4.3.3 Piston Pump

Since one stroke of the hand pump increases the pressure by 2 to 7 MPa, an additional system was required to set the desired pressure. A worm-drive piston pump (Fig. 6.26) makes it possible to increase the pressure by 0.02 MPa for each revolution of the pump handle. Revolving the handle causes a linear displacement of the piston in the pump housing.

6.4.4 Modification of the HPSPR

As mentioned in the previous section, the pressurizing medium for the HPSPR was originally an inert oil, and the system needed to be modified to allow for pressurization with SC-CO_2. The modification posed several challenges. First, the high-pressure seals, fittings, and tubing system had to be re-designed to accommodate SC-CO_2. In addition, a device for pressurizing the CO_2, a safety valve, and CO_2 ventilation system were installed. Lubricating the sliding motion of the moving plate was a problem, as the Krytox oil previously used had also served as the lubricant.

6.4.4.1 Tubing System, Compressor, and Vacuum Pump

The first modification was the addition of a tubing and valving system to make it possible to use either pressurization medium. Figure 6.27 is a schematic of the modified pressurizing system. The lower tubing system is used for studies of the effect of P alone using Krytox oil, and the upper part is for studying the combined effect of P and C when a gas is used.

For use with SC-CO_2, an additional pressurizing unit is required. The vapor pressure of CO_2 at room temperature is 5.8 MPa (838 psi) as can be seen in Fig.1.3. Unlike nonliquefied gases, such as N_2, He, O_2, which have very high vapor pressures at room temperature, *i.e.*, room temperature is well above the critical temperature, the pressure in a cylinder of pure CO_2 cannot be greater than its vapor pressure at room temperature as long as two phases exist in the gas cylinder, which is well below the critical pressure of 7.4 MPa (1070 psi). There are two ways to achieve a higher pressure than the vapor pressure. One is to add a high-pressure nonliquefied gas into the cylinder and to use a dip tube to take out the liquid, high-pressure CO_2 (Fig. 6.28). The second method is to use a compressor or liquid pump to increase the pressure (Fig. 6.29). Since the first method uses equipment that can be supplied by a compressed gas company, it will be simpler to use. However, it has some

limitations: a maximum pressure of 41 MPa (6000 psi) and possible contamination by the added gas. For this reason, the pressure of CO_2 was increased by an external device, and an ISCO syringe pump was chosen.

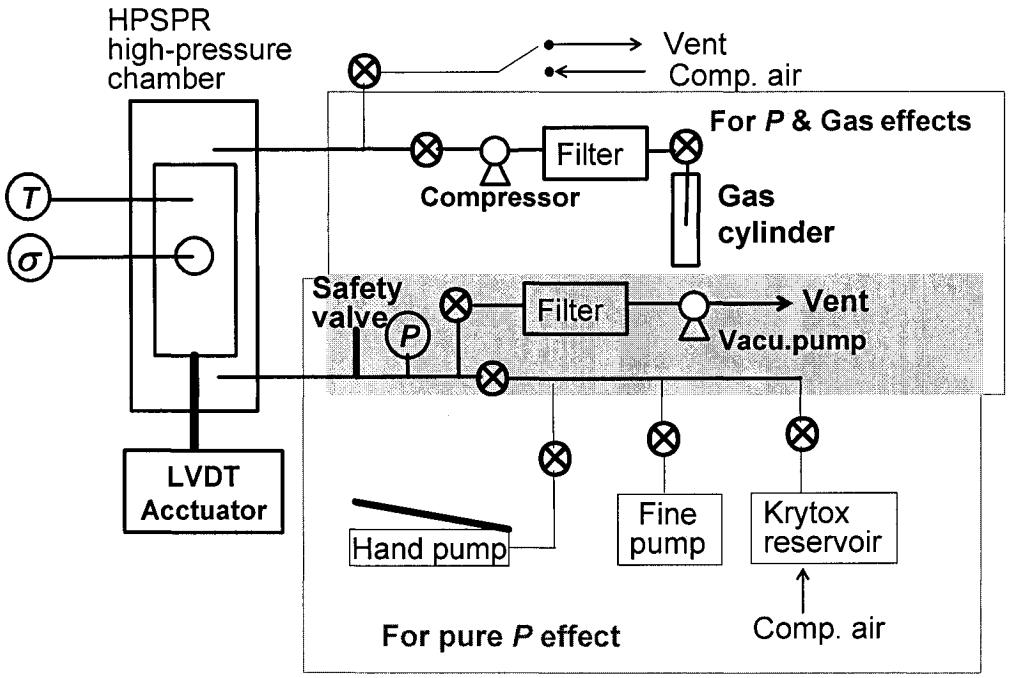

Figure 6.27. Schematic of pressurizing system.

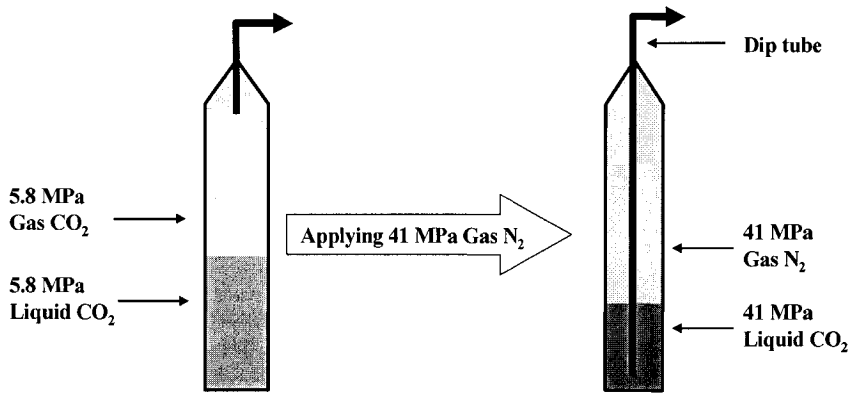

Figure 6.28. Increasing pressure above the vapor pressure by adding high- pressure N_2.

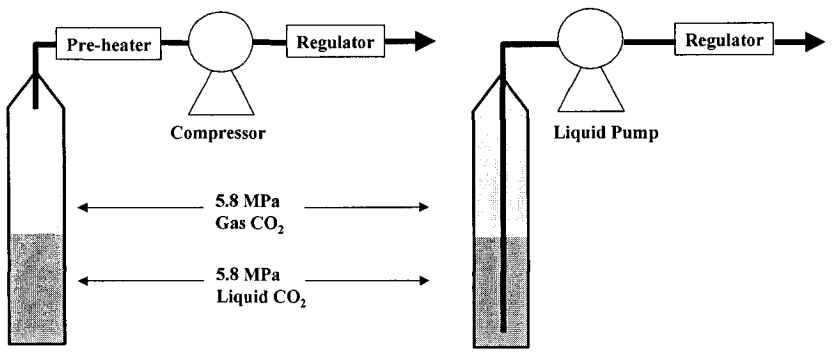

Figure 6.29. Increasing the pressure above the vapor pressure by using a compressor or pump.

The ISCO 100DM syringe pump system is a positive displacement pump and consists of a controller and pump module. The piston-driven pump module uses a single-speed gear train. The controller offers either flow controlled or pressure controlled modes, but the latter is required to keep the system pressure constant. The maximum pressure is 69 MPa (10,000 psi), and the detailed specifications are given in Table 6.4. This pump has little pulsation, and this feature is very important, since the shear stress transducer of the HPSPR is sensitive to pressure. However, this pump cannot pressurize and be refilled at the same time and has a little reservoir volume, so several refilling actions may be required to increase the pressure in the HPSPR to the desired level. It takes three minutes to refill the pump cylinder. During an experiment, the line between the pump cylinder and the rheometer is left open to replace CO_2 lost by absorption into the sample or small leaks, and this is closed during refilling. In the cylinder, a cup seal like that in the HPSPR, of graphite-impregnated Teflon™, is used, and this material is known to be inert to SC-CO_2. To avoid contamination, CO_2 is not recycled.

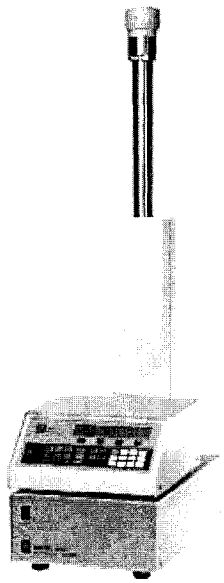

Figure 6.30. ISCO 100DM pump and its controller.

Table 6.4. Specifications of ISCO 100DM pump.

Pressure Range	10-10,000 psi
Pressure Resolution	10 psi
Operating Temperature	0-200°C
Capacity	103 ml
Flow Range	0.00001-30 ml/min
Flow Accuracy	0.5% of setpoint
Displacement Resolution	4.8 nl
Motor Stability	± 0.001% per year
Plumbing Ports	1/8" Valco

A vacuum pump is used to remove air from the rheometer and the sample prior to pressurization with CO_2. A diaphragm vacuum pump (Gast DAA-V175, Fig. 6.31) was used. This pump can generate a vacuum up to 28 in.Hg.

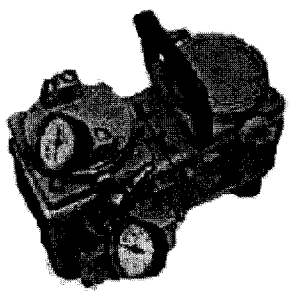

Figure 6.31. Gast vacuum pump.

6.4.4.2 Tubes

The original pressure tubes for the HPSPR were 9/16" O.D. inside the oven and 1/4" outside the oven. The 9/16" tubes generated unnecessary volume and required more refillings of the syringe pump to keep the set pressure. The large tube caused

another problem. A high torque must be applied to tighten the fittings, and this can damage the fittings on the backside of the HPSPR. The tube size was thus reduced to 1/4". However, the smaller tubes can cause a problem when the HPSPR is being filled with Kytox oil, which is very viscous, before pressurizing with the hand pump. It used to take four minutes to fill the rheometer with Krytox oil, but it takes 18 min with the new tubes at 180℃.

6.4.4.3 Seals

A potential problem is posed by the interactions between SC-CO_2 and the O-ring and cup seals. Even though Viton™ (flouroelastormer) has excellent chemical resistance, SC-CO_2 is a good solvent for some fluoropolymers, and even if fillers are used, the SC-CO_2 may cause swelling. Moreover, SC-CO_2 can dissolve or extract small molecules such as monomer, plasticizer, and other additives [46], and this may eventually cause a leak. Changes in the pressure will affect the rheological properties of the polymer and the response of the shear stress transducer (SST) and should thus be minimized. Choosing the proper O-ring was a major challenge. Finally, Teflon™ was chosen for the O-ring after testing a number of candidates. Appendix 6 describes how Teflon™ was chosen and how the shape of the O-ring was modified. A graphite-filled PTFE, which is the material for the cup seals, is known to have good resistance to SC-CO_2, and the cup seals were not replaced.

Two types of test were carried out to determine the effect of SC-CO_2 on the seals. First, after applying pressure to the CO_2 using the ISCO gas pump at 180℃, without a plastic sample in place, all valves were closed. A pressure decrease was observed, but the leak was too slow to be detected by soap water. The pressure decrease continued for a long time. A severe drop of pressure would indicate that the seals do not work. The other method is to measure the flow rate of gas when CO_2 is supplied by the gas pump to keep the set pressure. The pump controller displays the flow rate of gas, and this indicates the rate of gas leak. A cupseal of graphite-filled (PTFE) and a Teflon™ O-ring were found to be good seals.

6.4.4.4 Safety valve

Since the whole experimental procedure involves not only high pressure and temperature but also phase transitions of CO_2, over-pressure may develop. This could cause serious injury to people near the instrument and damage of the equipment. One way to prevent such an excess pressure is to install a pressure relieving device. The most probable cause of a sudden over-pressure is an abrupt phase change, and the device should thus accomplish instant opening by bursting to relieve the pressure. A safety valve or a safety-relief valve can be used rather than a relief valve, which provides only a non-bursting, bleeding action. A HiP safety head (Figs. 6.32 and 6.34) with a rupture disk (Fig. 6.33) was chosen. If the system pressure exceeds the burst pressure of the rupture disk, this disk will be broken to release the pressure. This safety head is connected to the HPSPR directly without any valve. Because the values of standard burst pressure are given at room temperature, the temperature correction factor must be known to select an appropriate disk. For example, the factor is 0.81 for 200℃, so that a disk with a burst pressure of 87 MPa must be used for the system at 70 MPa. The effective area of a disk must match the tubing system, and thus the proper disk has an 87 MPa burst pressure and a 1/4" effective area, which is the outer diameter of the HPSPR tubing system.

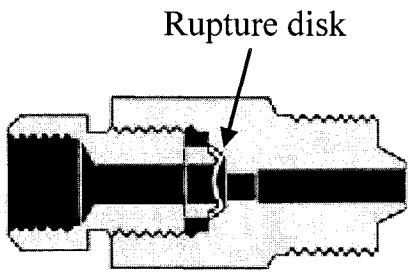

Figure 6.32. Safety head with a rupture disk.

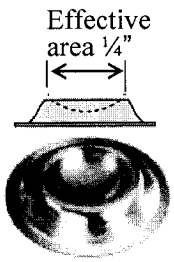

Figure 6.33. Rupture disk.

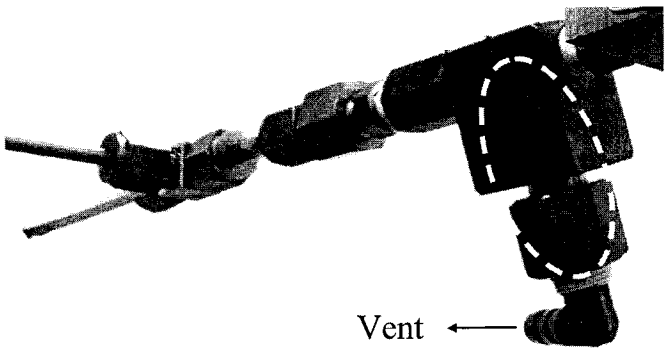

Figure 6.34. Safety head (in ellipse) in tubing system.

6.4.4.5 CO_2 Ventilation

Because the human respiratory system is regulated by the CO_2 concentration in the lungs, the amount of this gas in the lab must be kept within the proper range. However, there is a possibility that a large amount of CO_2 might leak during or after an experiment. Due to higher density of CO_2 compared to air, it falls, and it is hard to remove it by ventilation at the ceiling. To remove CO_2 after an experiment or during a sudden release of CO_2 during foaming studies, a bellows pipe was installed. One end is connected to one port of the HPSPR [Fig. 6.35 (a)], and the other is connected to the ventilation system of the laboratory [Fig. 6.35 (b)].

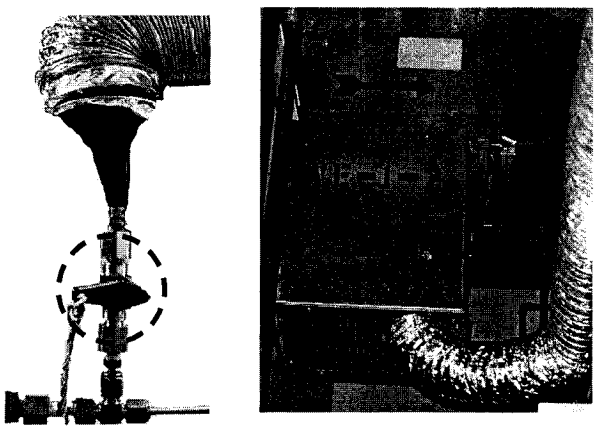

Figure 6.35. Bellows pipe. (a) connection to rheometer; (b) connection to ventilation.

The on-off valve in the circle in Fig. 6.35 can release CO_2 gradually, or suddenly for foaming experiments. Such a sudden release of pressure could cause a large expansion of gas, and the bellows type of duct was chosen to accommodate the expansion. The valve is operated by pulling a string attached to a knob and extends outside the lab to avoid possible harm to the operator. Figure 6.36 shows this operation: (a) is the valve knob, (b) is the bellows when the valve is closed. (c) is the valve opened by pulling the string far from the system, and (d) shows the expanded pipe due to sudden expansion of CO_2. Meanwhile the CO_2 in the pipe is removed by ventilation at the other end [Fig. 6.35 (b)].

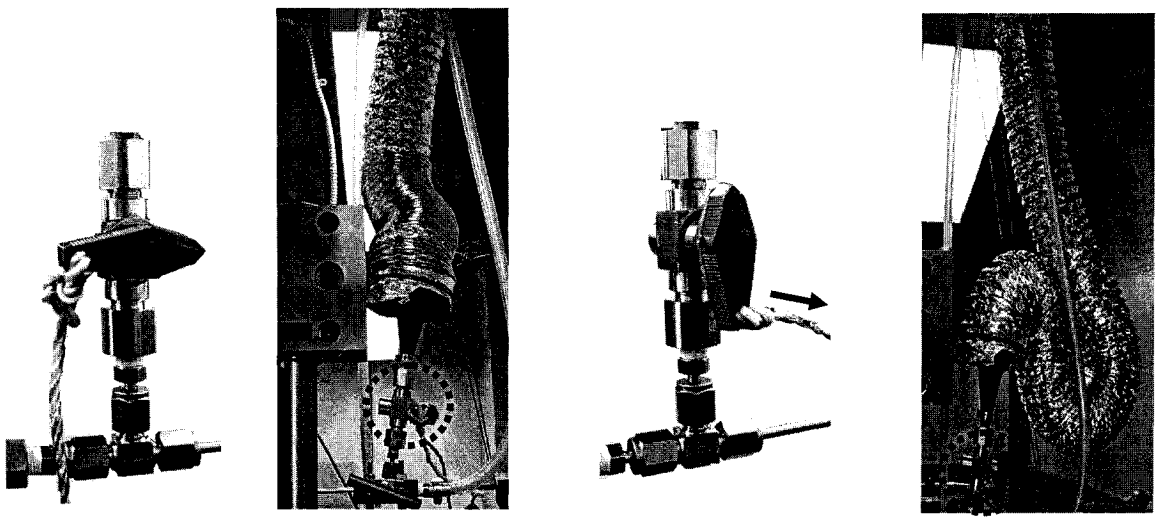

Figure 6.36. Sudden release of pressure. (a) and (b) before release; (c) and (d) after release.

6.4.4.6 Bearing Plate

There is no ball bearing system to support the sliding motion of the rheometer. Instead, dynamic seals around the actuating rod and the bearing plate support the actuating rod, and the bearing plate (Fig. 6.37) is a brass slab supporting the moving carriage.

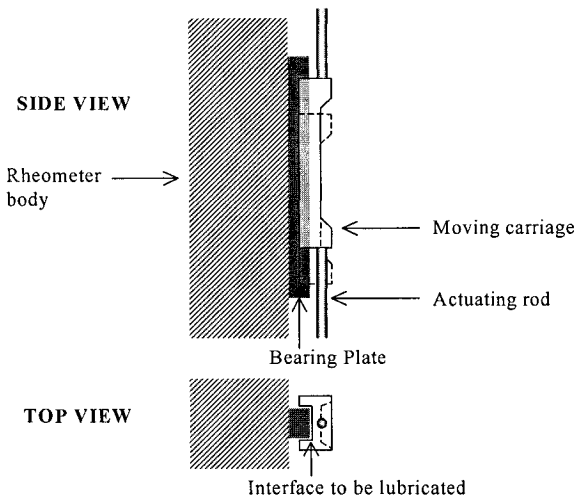

Figure 6.37. Interface between the bearing plate and moving carriage.

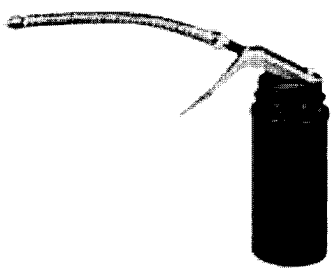

Figure 6.38. A pistol oiler.

When Krytox oil is used as the pressurizing medium, the interface between the plate and carriage is lubricated automatically by the oil. However, when CO_2 is used to pressurize, an independent lubrication system must be provided. One way to lubricate prior to an experiment with CO_2 is to make a sinusoidal movement of the moving carriage in Krytox oil to let the oil flow into the gap between the carriage and the bearing plate. However, it is laborious work to do the lubrication after filling the whole rheometer. Instead, Krytox is applied on the top part of the gap between the moving carriage and bearing plate using a pistol oiler (Fig. 6.38), and the sinusoidal movement is then used to spread the oil.

6.4.4.7 Operating Software

The original operating software for the SPR was QuikTest™, developed by EnduraTEC. QuikTest™ works in Dos™ environment and has 12-bit data acquisition; for example, the resolution of stress, which ranges from -300 to +300 kPa, is 600 kPa / 2^{12}=0.146 kPa. In the middle of the present study the operating software was upgraded to WinTest™ to obtain higher data resolution. WinTest™ works in

Windows™, has 15-bit data acquisition, and the resolution of stress is 600 kPa / 2^{15}=0.018 kPa. The resolution of displacement of Wintest™ is also eight times that of QuickTest™.

6.4.4.8 SST Housing with a Probe Positioner

To obtain an initial stress of zero at the experimental temperature and pressure, the stress was tared in the operating software, but a large amount of taring was found to cause a change in the gain and a loss of input range. For example, taring 100 kPa of stress decreases the calibration slope by 2% and the maximum stress from 300 to 200 kPa. This problem arises from the fact that the capacitance probe (Fig. 6.16) is fixed to the SST housing, so thermal expansion of the SST cannot be compensated for. To eliminate this problem, a new SST housing with a probe positioner was designed (Fig. 6.39). This housing allows one to adjust the position of the probe by turning a screw adjustor, which is connected to the capacitance probe by several gears and joints in the new housing. The screw adjustor is turned by use of a screw driver that is extended (Fig. 6.40-b) to the outside of the oven through a hole (Fig. 6.40-a) in the oven so as not to disturb the temperature in the oven. Clockwise revolution moves the probe away from the SST target and increases the stress reading. The screw adjustor is turned until a stress reading close to zero is obtained, and then the stress is tared in the operating software. While the SST is calibrated the cover plate of HPSPR must be open to allow the weight-hanging cable access to the SST head (Fig. 6.17). This changes the access angle to the screw adjustor, so that the straight screw driver cannot thus go through the hole. Rather than making another hole in the oven wall, a universal joint is used to extend the screw driver through the same hole (Fig. 6.41).

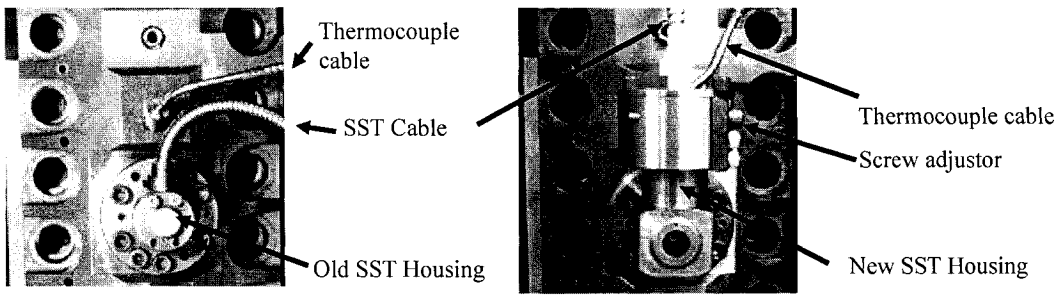

Figure 6.39. Old and new SST housings.

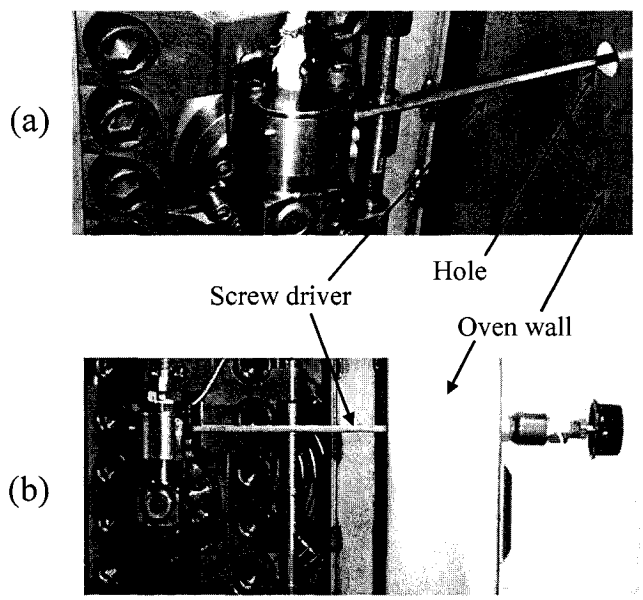

Figure 6.40. Extension of screw driver through hole to outside.

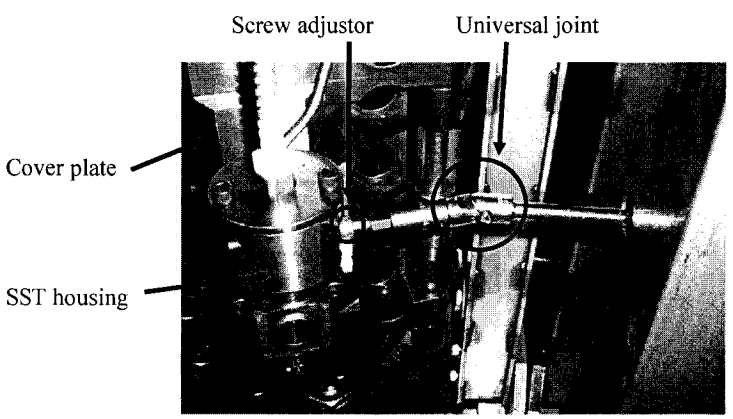

Figure 6.41. Universal joint is used while calibrating SST.

6.5 Experiments

Samples are prepared by compression molding of a sheet at 165℃. The sample mold is an aluminum plate with a rectangular hole 10cm×18cm in size. The thickness of the mold is 1.66mm. A sample is cut to be a strip of 1.5cm×8cm for pure pressure studies or 0.8cm×8cm for a study at elevated pressure and with CO_2.

The experimental procedure varies with the pressurizing medium and the type of control. For pressure only Krytox is used (Appendix 7 describes the detailed experimental procedures.), and for the combined effect of pressure and concentration, CO_2 is used as the pressurizing medium. The strain-controlled mode is used for steady-state measurements, and stress control is used for creep measurements.

6.5.1 Steady-shear Test

First, experiments are performed in a Krytox environment to determine the stress as a function of shear rate at a given temperature and pressure, and the viscosity is calculated. The shift factors are obtained by shifting the stress curves onto the curve at the reference state.

Second, experiments are performed in an SC-CO_2 environment. To confirm saturation of CO_2 in the sample, time sweep experiments are performed at each pressure prior to the shear-rate experiments. The saturation time obtained experimentally is compared with that estimated from diffusion coefficient data. After confirming the saturation time experimentally, a shear-rate sweep is performed at the same conditions as those used with Krytox as the pressurizing fluid. This confirming step is described in the section on diffusion. The shift factors are obtained in the same manner as in the previous case.

6.5.2 Creep Test

Using the controlled stress mode, a constant stress is applied, the resulting displacement is monitored, and the creep compliance is calculated. The experimental temperature and pressure for creep were the same as those for the steady-simple shear tests. Experiments with Krytox are followed by measurements of the effect of dissolved gas on the viscoelastic properties.

6.5.3 Foaming Studies

Foam is formed by suddenly relieving the pressure on the system following shear deformation. The rheometer is then cooled and the resulting foamed structure inspected and characterized, for example by scanning electron microscopy (SEM). Since a proper method to collect the sample without disturbing the foamed structure has not been developed, this topic was not investigated as part of this study.

One possible application is to study the effects of P, T, C on foam structure. A plastic sample could be placed not between the two plates but in the rheometer (Fig. 6.42) and saturated with CO_2. After saturating samples with CO_2, the pressure was suddenly released ($-\Delta P/\Delta t = 1\,\mathrm{MPa/s}$), and the samples were then removed as quickly as possible. A foamed structure could be analyzed.

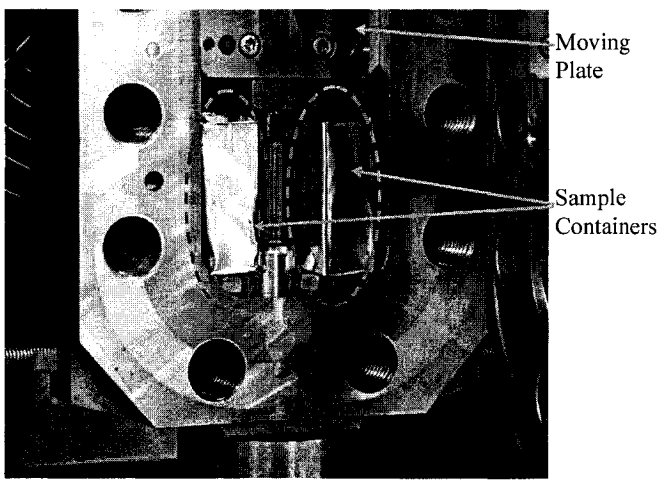

Figure 6.42. Sample loading for study of foam structure.

Another application is to study the effect of foamed structure on viscosity. First a sample between the two plate was saturated with CO_2, then the pressure was suddenly released, and finally the viscosity was measured. The effect of foaming or gas bubbles on the viscosity could be determined by comparing viscosity data at 1 atm without CO_2, those at 1 atm after foaming, and those at an elevated pressure with dissolved CO_2.

6.6 Diffusion of Supercritical Fluid in Polymer

To obtain reliable results, experiments must be carried out while the sample is saturated with CO_2 at each pressure, as the rheometer does not have independent control of pressure and gas concentration. The saturation process takes a long time, as diffusion occurs only from the thin edges of the sample. The saturation time needs to be estimated, and diffusion theory was used to make this estimate. The estimated saturation time can also be used to select suitable polymers for experiments involving dissolved gas. A polymer with too long a saturation time cannot be used because of thermal degradation.

6.6.1 Diffusion Theory

When a diffusant permeates a polymer, the diffusion problem is modeled as follows: the diffusant is first sorbed at the entering face and dissolves there, and equilibrium is established between the two components until the gradient in the chemical potential of the dissolving gas μ_g vanishes as discussed in Chapter 3.

6.6.2 Fick's Law of Diffusion

Fick's first law [47] states that the flux is proportional to the concentration gradient at steady state:

$$\vec{F} = -D\nabla C \tag{6.22}$$

where $\vec{F}$ is the flux vector that gives the amount of substance diffusing across a unit area in unit time, C is the concentration of diffusing substance, and D is the diffusion coefficient. The x-component of the flux vector can be expressed as:

$$F_x = -D(\partial C/\partial x) \tag{6.24}$$

Fick's second law [47] describes unsteady-state diffusion:

$$\frac{\partial C}{\partial t} = -\left(\frac{\partial F_x}{\partial x} + \frac{\partial F_y}{\partial y} + \frac{\partial F_z}{\partial z}\right) = \frac{\partial(D\partial C)}{\partial x^2} + \frac{\partial(D\partial C)}{\partial y^2} + \frac{\partial(D\partial C)}{\partial z^2} \tag{6.25}$$

where C is a function of x, y, z, and t. This equation is similar to the heat conduction equation, and Carslaw and Jaeger [48] describe its application to thermal conduction. Crank and Park [49], Crank [50], and Hines and Maddox [51] cover diffusion for many special cases.

It is sometime reported that D is a function of C, and this renders Eq. 6.25 solvable only by numerical methods. In practice, average values of D are tabulated for use over given ranges of composition. If D is assumed to be independent of C, Eq. 6.25 becomes

$$\frac{\partial C(x,y,z,t)}{\partial t} = D\left[\frac{\partial^2 C(x,y,z,t)}{\partial x^2} + \frac{\partial^2 C(x,y,z,t)}{\partial y^2} + \frac{\partial^2 C(x,y,z,t)}{\partial z^2}\right] \tag{6.26}$$

for which analytical solutions are available. For the present application diffusion in the z-direction does not occur because the thin sample is sandwiched between steel plates.

6.6.2.1 Solution of the 1-D Fick's Equation

The analytical solution of Fick's equation in one-dimension (1-D) is discussed prior to that in two-dimension (2-D), which is more general, because the solution in 1-D must be known to obtain that in 2-D. Since the width of the sample is less than

its length (Fig. 6.43), diffusion is assumed to take place only in the x-direction, and Eq. 6.26 simplifies to:

$$\frac{\partial C(x,t)}{\partial t} = D\left[\frac{\partial^2 C(x,t)}{\partial x^2}\right] \tag{6.27}$$

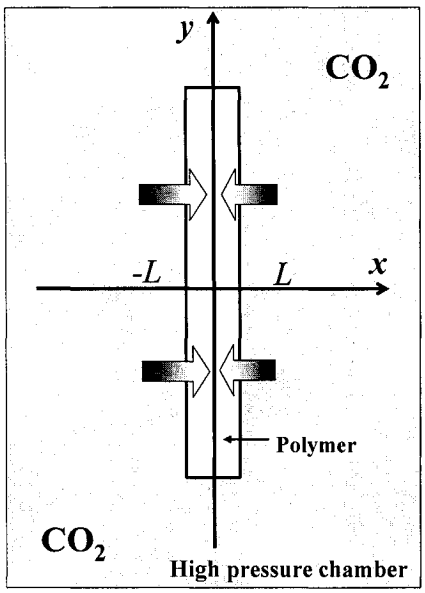

Figure 6.43. Diffusion in x-direction.

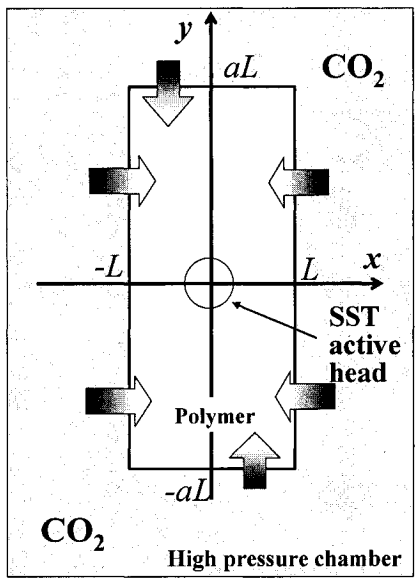

Figure 6.44. Diffusion in x and y directions.

The region $-L < x < L$ is initially at a uniform concentration: $C(x,0) = C_0$, There is no net diffusion in the center: $\partial C(x)/\partial x = 0$ at $x = 0$, and the surfaces are kept at a constant concentration: $C[\pm L(t),t] = C_1$. This is in fact a moving boundary problem due to swelling, but the boundary is assumed to be fixed for simplification of the solution: $C(\pm L,t) = C_1$. This will be examined further in section 6.6.2.4. Using the intial and boundary conditions, the concentration at any point in the slab at time t is given by Eq. 6.28 [51]:

$$\frac{C(x,t) - C_1}{C_0 - C_1} = \frac{4}{\pi}\sum_{n=0}^{\infty}\frac{(-1)^n}{2n+1}\exp\left[\frac{-D(2n+1)^2\pi^2 t}{4L^2}\right]\cos\frac{(2n+1)\pi x}{2L} \tag{6.28}$$

This equation can be rearranged to obtain the degree of saturation:

$$\frac{C(x,t)-C_0}{C_1-C_0}=1-\frac{4}{\pi}\sum_{n=0}^{\infty}\frac{(-1)^n}{2n+1}\exp\left[\frac{-D(2n+1)^2\pi^2t}{4L^2}\right]\cos\frac{(2n+1)\pi x}{2L} \tag{6.29}$$

This quantity has the following properties:

$$\lim_{t\to 0}\frac{C(x,t)-C_0}{C_1-C_0}=0 \tag{6.30}$$

$$\lim_{t\to \infty}\frac{C(x,t)-C_0}{C_1-C_0}=1 \tag{6.31}$$

For the problem of interest C_0 is zero, and C_1 is the solubility S of the diffusant in the polymer assuming instant local equilibrium at the interface. Then, Eq. 6.29 reduces to:

$$\frac{C(x,t)}{S}=1-\frac{4}{\pi}\sum_{n=0}^{\infty}\frac{(-1)^n}{2n+1}\exp\left[\frac{-D(2n+1)^2\pi^2t}{4L^2}\right]\cos\frac{(2n+1)\pi x}{2L} \tag{6.32}$$

The concentration in the center of the sample, $C(0, t)$ can be used to indicate the saturation time, because the center will be saturated last:

$$\frac{C(0,t)}{S}=1-\frac{4}{\pi}\sum_{n=0}^{\infty}\frac{(-1)^n}{2n+1}\exp\left[\frac{-D(2n+1)^2\pi^2t}{4L^2}\right] \tag{6.33}$$

The quantity $C(0, t)/S$ is a measure of the level of saturation at time t. If $M(t)$ is the total amount of diffusing substance absorbed by the sheet at time t, and $M(\infty)$ is the corresponding quantity after infinite time, these quantities can be obtained by integrating the concentration over the width as follows:

$$M(t) \equiv \int_{-L}^{L} C(x,t)dx = 2\int_{0}^{L} C(x,t)dx$$
$$= 2S\int_{0}^{L}\left\{1-\frac{4}{\pi}\sum_{n=0}^{\infty}\frac{(-1)^n}{2n+1}\exp\left[-\frac{D(2n+1)^2\pi^2 t}{4L^2}\right]\cos\frac{(2n+1)\pi x}{2L}\right\}dx$$
$$= 2SL - 2SL\sum_{n=0}^{\infty}\frac{8}{(2n+1)^2\pi^2}\exp\left[-\frac{D(2n+1)^2\pi^2 t}{4L^2}\right] \tag{6.34}$$

$$M(\infty) = \lim_{t\to\infty} M(t) = 2SL \tag{6.35}$$

The quantity $M(t)/M(\infty)$ is another measure of the level of saturation at time t and is given by Eq. 6.36:

$$\frac{M(t)}{M(\infty)} = 1 - \sum_{n=0}^{\infty}\frac{8}{(2n+1)^2\pi^2}\exp\left[\frac{-D(2n+1)^2\pi^2 t}{4L^2}\right] \tag{6.36}$$

Thus, the time required to reach a given saturation level in terms of $C(0,t)$ or $M(t)$ can be estimated if D is known. However, the actual system (Fig. 6.44) is two dimensional (2-D) and should not be reduced to 1-D problem without justification.

6.6.2.2 Solution of the 2-D Fick's Equation

The analytical solution of Fick's equation in 2-D is also known. Equation 6.26 for 2-D can be written as:

$$\frac{\partial C(x,y,t)}{\partial t} = D\left[\frac{\partial^2 C(x,y,t)}{\partial x^2} + \frac{\partial^2 C(x,y,t)}{\partial y^2}\right] \tag{6.37}$$

and the boundary and intial conditions are:

$$\text{B.C.1: } C(\pm L,y,t) = C_1, \quad t > 0 \tag{6.38}$$

$$\text{B.C.2: } C(x,\pm aL,t) = C_1, \quad t > 0 \tag{6.39}$$

$$\text{B.C.3: } \frac{\partial C(x,y,t)}{\partial x} = 0 \quad \text{at } x = 0 \tag{6.40}$$

$$\text{B.C.4: } \frac{\partial C(x,y,t)}{\partial y} = 0 \quad \text{at } y = 0 \tag{6.41}$$

$$\text{I.C.: } C(x,y,0) = C_0 \tag{6.42}$$

The solution of this type of problem is the product of the solutions of two, one-variable equations [48, p.33]. Equations 6.28 and 6.32 through 6.36 with $C_1 = S$ and $C_0 = 0$ for 2-D are given by Eqs. 6.43 through 6.48:

$$\begin{aligned}\frac{C(x,y,t) - C_1}{C_0 - C_1} = &\left\{\frac{4}{\pi}\sum_{n=0}^{\infty}\frac{(-1)^n}{2n+1}\exp\left[\frac{-D(2n+1)^2\pi^2 t}{4L^2}\right]\cos\frac{(2n+1)\pi x}{2L}\right\} \\ &\times\left\{\frac{4}{\pi}\sum_{m=0}^{\infty}\frac{(-1)^m}{2m+1}\exp\left[\frac{-D(2m+1)^2\pi^2 t}{4(aL)^2}\right]\cos\frac{(2m+1)\pi y}{2aL}\right\}\end{aligned} \tag{6.43}$$

where a is the length to width ratio.

$$\begin{aligned}\frac{C(x,y,t)}{S} = 1 - &\left\{\frac{4}{\pi}\sum_{n=0}^{\infty}\frac{(-1)^n}{2n+1}\exp\left[\frac{-D(2n+1)^2\pi^2 t}{4L^2}\right]\cos\frac{(2n+1)\pi x}{2L}\right\} \\ &\times\left\{\frac{4}{\pi}\sum_{m=0}^{\infty}\frac{(-1)^m}{2m+1}\exp\left[\frac{-D(2m+1)^2\pi^2 t}{4(aL)^2}\right]\cos\frac{(2m+1)\pi y}{2aL}\right\}\end{aligned} \tag{6.44}$$

$$\begin{aligned}\frac{C(0,0,t)}{S} = 1 - &\left\{\frac{4}{\pi}\sum_{n=0}^{\infty}\frac{(-1)^n}{2n+1}\exp\left[\frac{-D(2n+1)^2\pi^2 t}{4L^2}\right]\right\} \\ &\times\left\{\frac{4}{\pi}\sum_{m=0}^{\infty}\frac{(-1)^m}{2m+1}\exp\left[\frac{-D(2m+1)^2\pi^2 t}{4(aL)^2}\right]\right\}\end{aligned} \tag{6.45}$$

$$M(t) \equiv \int_{-aL}^{aL}\int_{-L}^{L} C(x,y,t)dxdy = 4\int_{0}^{aL}\int_{0}^{L} C(x,y,t)dxdy$$
$$= 4SaL^2 - 4SaL^2\left\{\sum_{n=0}^{\infty}\frac{8}{(2n+1)^2\pi^2}\exp\left[-\frac{D(2n+1)^2\pi^2 t}{4L^2}\right]\right\}$$
$$\times\left\{\sum_{m=0}^{\infty}\frac{8}{(2m+1)^2\pi^2}\exp\left[-\frac{D(2m+1)^2\pi^2 t}{4(aL)^2}\right]\right\} \tag{6.46}$$

$$M(\infty) = \lim_{t\to\infty} M(t) = 4SaL^2 \tag{6.47}$$

$$\frac{M(t)}{M(\infty)} = 1 - \left\{\sum_{n=0}^{\infty}\frac{8}{(2n+1)^2\pi^2}\exp\left[\frac{-D(2n+1)^2\pi^2 t}{4L^2}\right]\right\}$$
$$\times\left\{\sum_{m=0}^{\infty}\frac{8}{(2m+1)^2\pi^2}\exp\left[\frac{-D(2m+1)^2\pi^2 t}{4(aL)^2}\right]\right\} \tag{6.48}$$

The solutions of Eqs. 6.45 and 6.48 can be represented by plots of $C(0,0,t)/S$ or $M(t)/M(\infty)$ versus dimensionless diffusion time, Dt/L^2, and this plot can be used for samples having any values of D, a, and L. From this chart, the time for a certain level of saturation can be easily calculated for given D, a, and L. Figures 6.45 and 6.46 show these plots for various values of a. The increase of $C(0,0,t)/S$ delays in the beginning (circle in Fig. 6.45), because it takes time for molecules to reach the center.

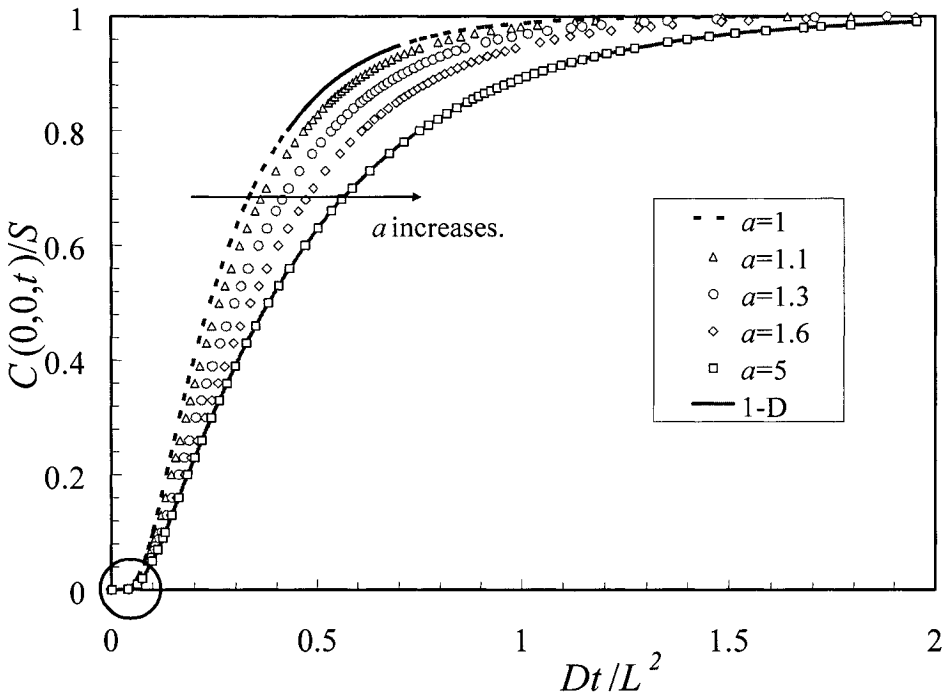

Figure 6.45. Relative concentration in the center of the polymer sheet.

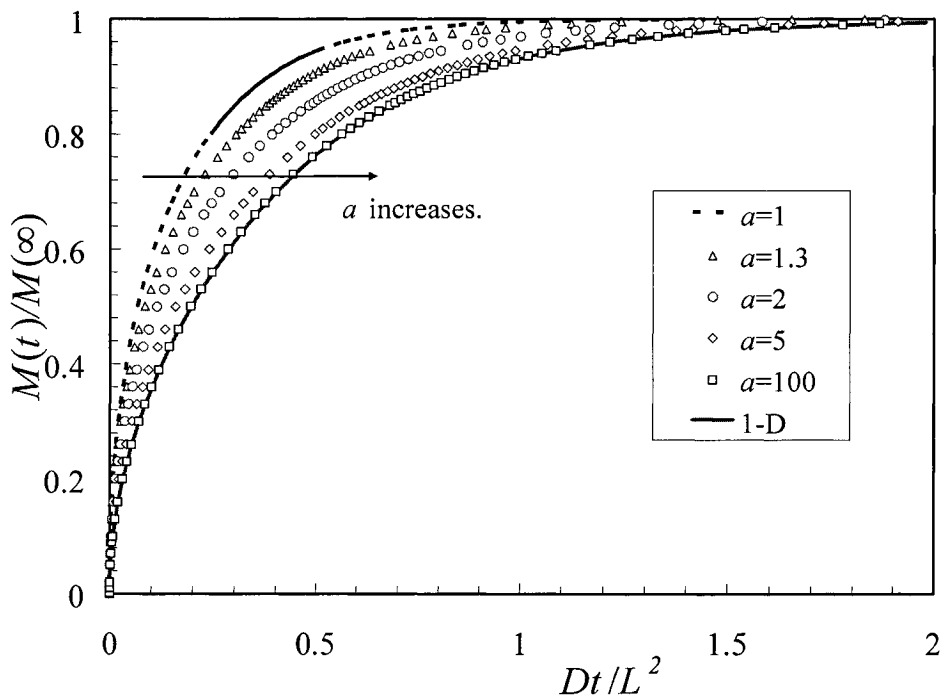

Figure 6.46. Relative quantity absorbed by the polymer sheet.

6.6.2.3 Effect of Length to Width Ratio on Saturation Time

Figure 6.45 shows that the curve of $C(0,0,t)/S$ with a=5 is almost the same as the solution of the 1-D problem ($a \rightarrow \infty$), while Fig. 6.46 shows that this is not the case for $M(t)/M(\infty)$. The time for a certain level of saturation and Dt/L^2 for the 2-D case, where diffusion occurs in two directions, will always be less than that for 1-D, where diffusion takes place only in one direction. Thus, to treat the problem as 1-D for the case of $M(t)/M(\infty)$, the sample must be very narrow. However, for the center plane concentration, the diffusion from nearer edge will be dominant, and when a is only five, the problem can be reduced to 1-D. It is clearly shown in Fig. 6.47, which shows $[Dt/L^2(a)]/[Dt/L^2(\infty)]$ versus a for 99% saturation, where $Dt/L^2(a)$ is the dimensionless diffusion time as a function of a, and $Dt/L^2(\infty)$ is that for the case of 1-D. The ratio $[Dt/L^2(a)]/[Dt/L^2(\infty)]$ shows how close to the 1-D problem the actual system is. For $a \geq 5$, this ratio does not change significantly for concentration (dashed curve), but it does change for the absorbed amount (solid curve). This indicates that samples with $a \geq 5$ can be treated as 1-D, considering

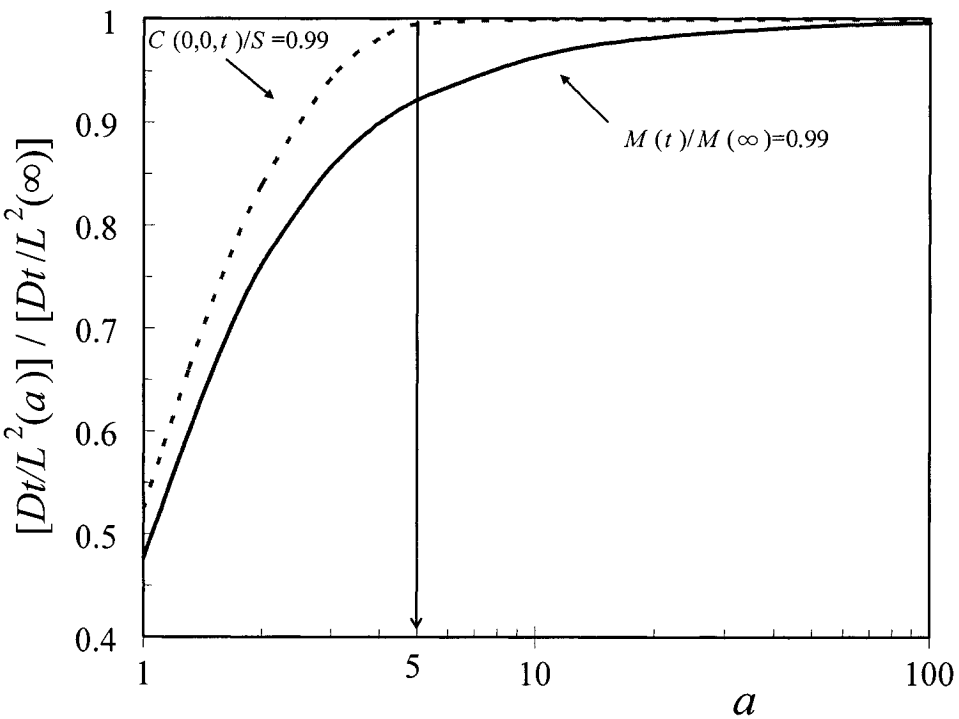

Figure 6.47. Effect of a on 99% saturation time; Comparison of 1-D and 2-D solutions.

saturation in terms of concentration, but only samples of $a \geq 100$ can be considered to be 1-D in terms of absorbed amount.

6.6.2.4 Moving Boundary

The boundaries for this problem were assumed to be fixed, but the actual boundaries, which are then edges of the sample, move outward with time due to swelling, and L thus increases with t. Equation 6.37 with moving boundaries will predict a longer saturation time than that with fixed boundaries. A moving boundary problem requires time-consuming numerical analysis, but it can be estimated from solutions to problems with an unswollen fixed boundary and a totally swollen, fixed boundary. The unswollen sample has dimension $(L)(aL)(H)$, and for the totally swollen sample these are $(L')(aL')(H)$, where H is the height, *i.e.*, the gap between the steel plates of the rheometer, L is the initial width of pure polymer sample, $L' = \lim_{t \to \infty} L(t)$, V_{pol} is the volume of pure polymer, and that of the swollen polymer/CO_2 mixture is $V_m = \lim_{t \to \infty} [L(t)aL(t)H(t)]$. The linear swell factor $k \equiv L'/L$ can be obtained from the following relationships: $V_{pol} = (L)(aL)(H)$, and $V_m = (L')(aL')(H) = (kL)(akL)(H) = k^2 V_{pol}$. The equilibrium edge location after swelling will be at:

$$L' = kL = \sqrt{\frac{V_m}{V_{pol}}} L \tag{6.49}$$

The time response of fully swollen sample is slower than that unswollen by a factor of k^2 since time is proportional to L^2 times the dimensionless diffusion time. As shown in Chap. 3, $V_m / V_{pol} = 1.15$ and $k = \sqrt{1.15} \cong 1.07$ at 18 MPa, *i.e.* 7% linear swell occurs. Using the above values Fig. 6.48 shows the results. The solution with moving boundary will be between the solid (unswollen) and dashed (fully swollen) curves, but there is no significant difference between the two solutions. The solution to the unswollen problem was thus used for this study. Obviously, if the swelling is severe, the moving boundary must be taken into account.

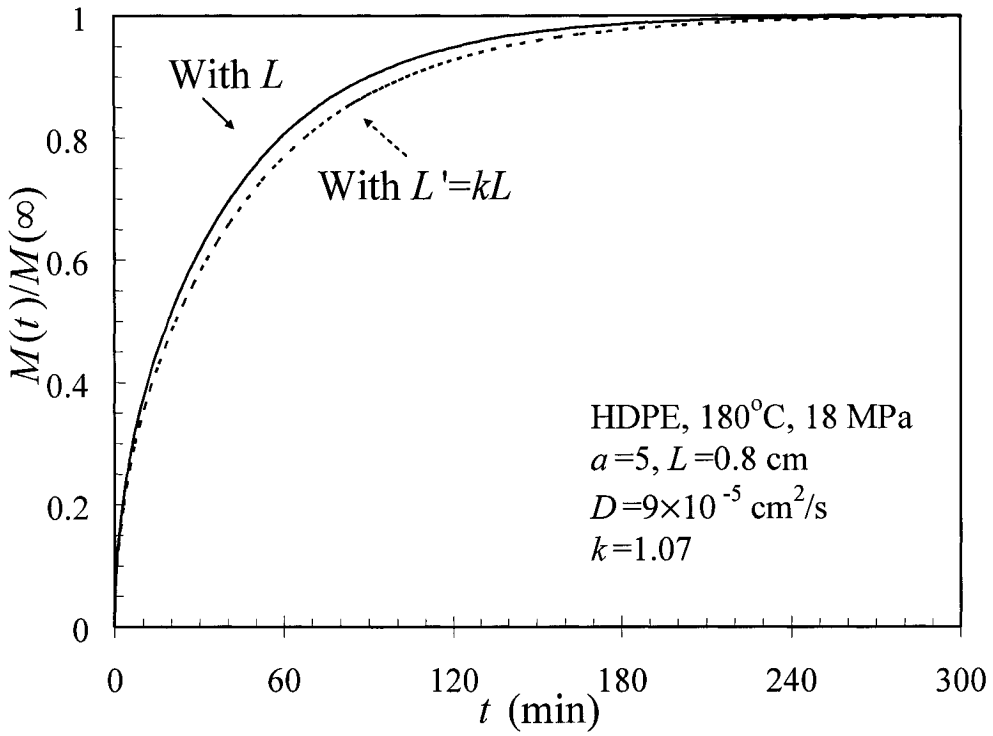

Figure 6.48. Effect of swollen boundary on the solutions of Fick's equation.

6.6.2.5 Estimate of the Saturation Time

One of the objectives of the diffusion study was to estimated the saturation time to select suitable polymers for this study. Sato [52] reported that D for the HDPE is around 9×10^{-5} (cm^2/s) at 180℃ and only a weak function of P. The sample dimension is 1.6 cm × 8.0 cm, so that a=5, and L (half the sample width) is 0.8 cm. Figure 6.49 shows that Dt/L^2 is 1.64 for $M(t)/M(\infty)=0.99$ and 1.96 for $C(0,0,t)/S$=0.99. The corresponding times for 99% saturation are then 3.3 and 3.7 h, respectively. Based on the estimated saturation time, HDPE was selected for the CO_2 study. Polystyrene (PS) would require two days, because D of PS [53] is one tenth that of HDPE. This polymer was not studied, despite its foaming applications, because such a long period at high temperature would result in thermal degradation.

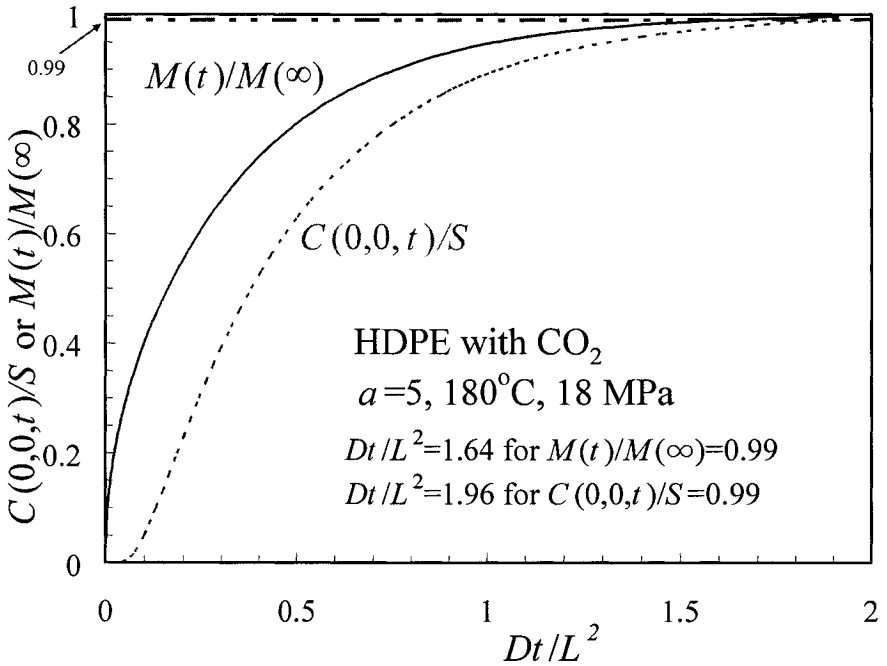

Figure 6.49. Values of Dt/L^2 for 99% saturation with a=5 for HDPE.

6.6.3 Saturation Measurement Using the HPSPR

Another objective of the diffusion study was to estimate the saturation time before starting shear experiments. The saturation time estimated by the model can be compared with experimental viscosity data obtained using the HPSPR. Once a sample is loaded, the viscosity near the center of the sample is measured by the SST as a function of time after pressurization with CO_2. Due to plasticization, the viscosity decreases until the polymer is saturated with gas, and the viscosity change thus indicates the level of saturation.

The viscosity (■) was measured every 20 min at 180℃, 18 MPa with CO_2, and $\dot{\gamma}=0.63s^{-1}$. The first datum with CO_2 was measured at t=30 min, because after loading a sample it takes this long for the system temperature to reach the set-point temperature. The steady viscosity (●) was also measured at the same condition without CO_2 in another experiment. Figure 6.50 shows the data, which show that there is no significant viscosity decrease after four hours. This implies that the viscosity measurements can safely begin four hours after loading a sample.

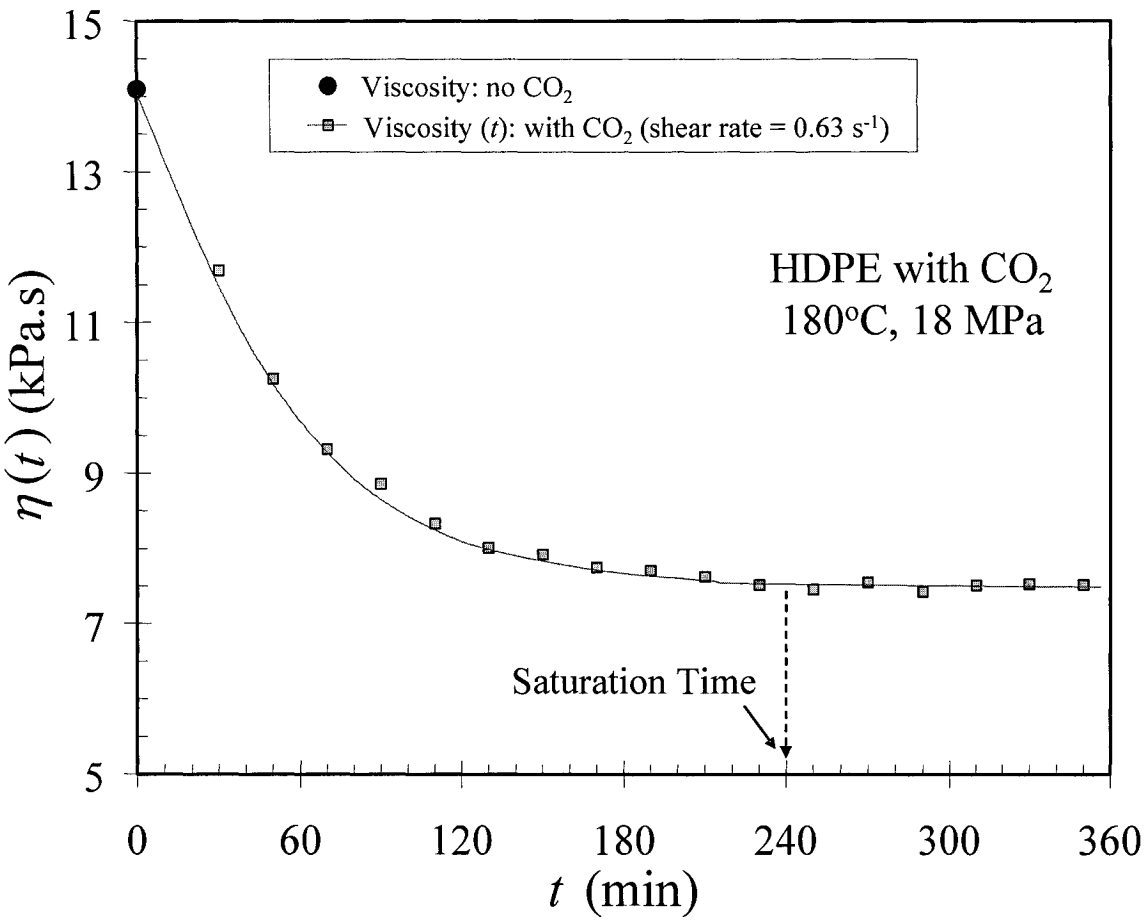

Figure 6.50. Viscosity decrease with time.

The experimental viscosity saturation time and the predicted diffusion time should be similar. To make this comparison, a relative viscosity is defined as:

$$\eta_R(t) \equiv \frac{\eta(t)-\eta(0)}{\eta(\infty)-\eta(0)} \tag{6.50}$$

where $\eta(\infty)$ is the viscosity at saturation. This measure of the level of saturation is qualitatively similar to $C(0,0,t)/S$ and $M(t)/M(\infty)$ and has the following limiting values:

$$\lim_{t\to 0}\eta_R(t)=0 \tag{6.51}$$

$$\lim_{t\to \infty}\eta_R(t)=1 \tag{6.52}$$

The concentration $C(0,0,t)$ is an absolute measure of the saturation level, because it is at the point that is saturated last, while the absorbed amount $M(t)$ shows the average level of saturation in the whole sample. The shear stress transducer of the HPSPR measures the stress in the neighborhood of sample center. The behavior of $\eta(t)$ is thus expected to be between $C(0,0,t)$ and $M(t)$. The three measures of saturation level are compared in Fig. 6.51. The approach of η_R to its limiting value is a little slower than that of $C(0,0,t)/S$ but otherwise quite similar. This discordance can be explained by the uncertainty in the value of D and moving boundary. The measurement of D is very difficult, and its value is more uncertain than those of the other parameters, such as the solubility of the gas. If a lower value of D is used, the predicted saturation will be slower, and the viscosity data will be between $C(0,0,t)$ and $M(t)$. For example, Fig. 6.52 shows the relationship between model and data when D is set equal to $8\times10^{-5}\ \mathrm{cm^2/s}$. This shows that the HPSPR can actually be used to estimate the diffusion coefficient of a gas in molten polymer.

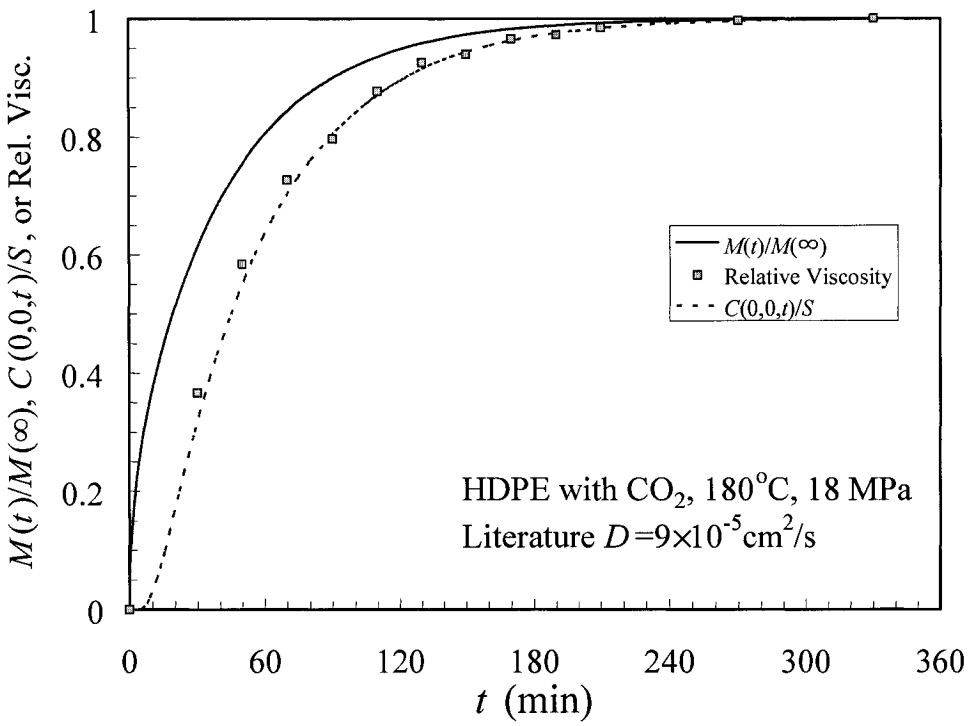

Figure 6.51. Comparison between experimental data and model prediction using a literature D: HDPE, 180℃.

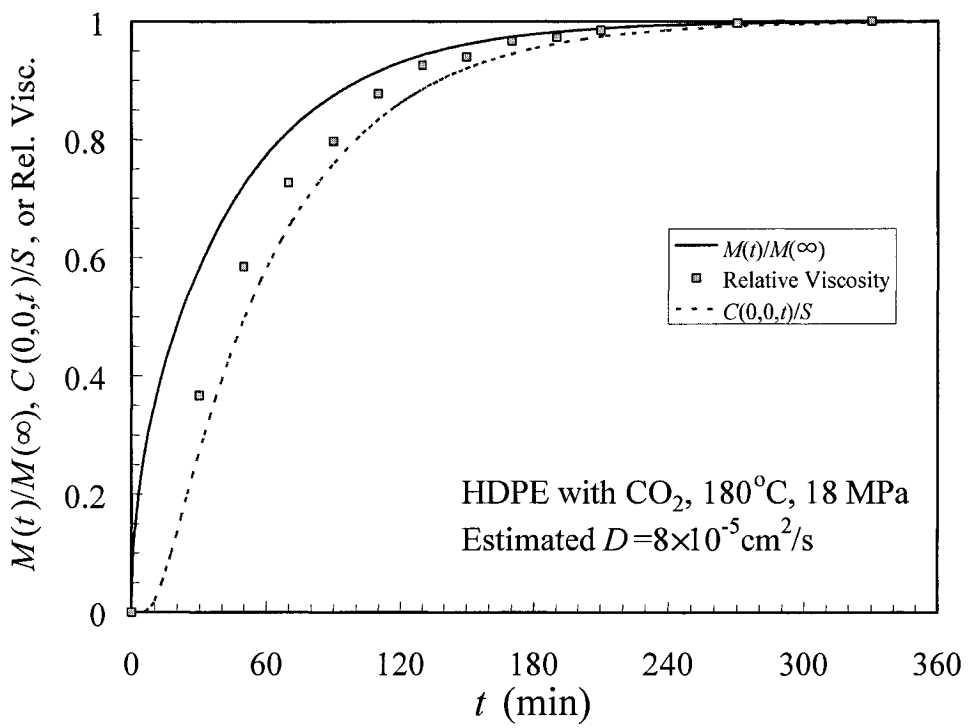

Figure 6.52. Effect of changing D on model prediction: HDPE, 180℃.

6.6.4 Acceleration of Diffusion

To overcome the limitation of sample selection, a method to accelerate diffusion was studied. The use of porous plates was considered to provide diffusion in the z-direction, where the sample has its largest surface area, but the pores would be clogged by polymer, and the saturation time could vary from one experiment to another if the pores were not cleaned properly.

Another method that was discovered is to shear the sample while CO_2 is dissolving. It was observed that the diffusion was enhanced by continuous sinusoidal shearing (△) at 0.01 Hz with an amplitude of 0.1 mm (Fig. 6.53). The viscosity was measured every 30 min, while the sample was continuously sheared. The viscosity became constant after two hours, which is half the saturation time for the no shearing case. The system is a creeping flow with $Re \sim 0$, which is reversible, and CO_2 molecules in the polymer are not expected to convect due to the shearing motion. Moreover, shearing occurs in the y-direction, and diffusion takes place primarily in the x-direction. The small rearrangement of polymer chains by oscillatory shearing may enhance the diffusion of CO_2 molecules. Using this procedure it might be possible to study polystyrene. This phenomenon is very beneficial to extrusion foaming, which has a very short residence time of gas. Figure 6.53 also shows that shearing (▲) at 0.06 Hz with a 0.1 mm amplitude initially enhances diffusion, but the viscosity then falls steadily starting at t=180 min. This implies that faster shearing may rupture the sample or cause cavitation.

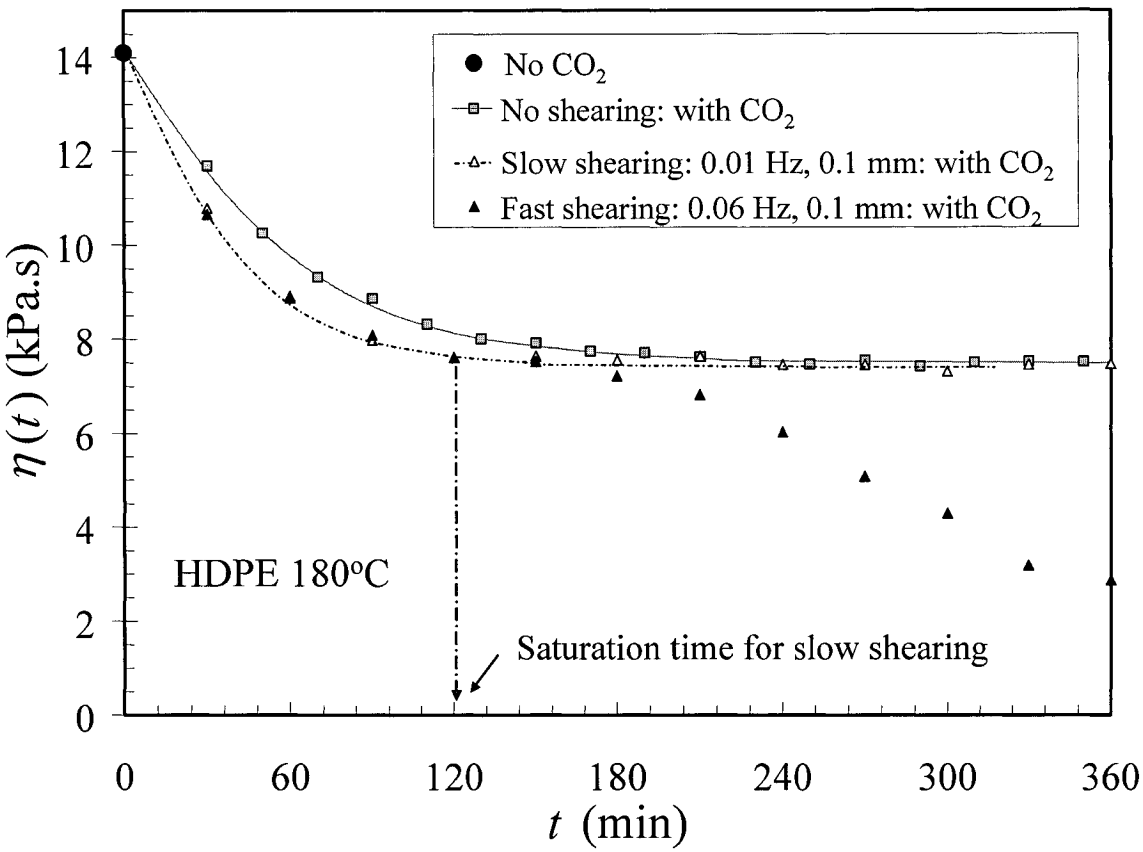

Figure 6.53. Effect of oscillatory shearing on the viscosity decrease during absorption of CO_2.

6.7 Results and Discussion

6.7.1 Reproducibility

In order to ensure the precision of data, all sensors were calibrated periodically. In particular, the calibration of the stress transducer was verified regularly, but adjustment was rarely required. In the middle of the study, the operating software was upgraded from QuikTest™ to WinTest™. It was necessary to verify that the results using both systems were in accord. As can be seen in Fig. 6.54, the reproducibility of data obtained using both is satisfactory. Figure 6.55 shows the reproducibility of data obtained at various times after applying CO_2 at set P for samples assumed to be saturated with CO_2. The data confirm that the samples were

indeed saturated and that the viscosity had not changed five hours after pressurizing with CO_2.

At the reference temperature of 180℃ shear-rate sweep tests were repeated four times at atmospheric pressure. The maximum relative standard deviation was 5%. At the other conditions, tests were repeated one to three times, and there was a maximum 6% relative difference (*RD*):

$$RD \equiv \left(\frac{highest - lowest}{lowest} \right)_{\dot{\gamma}} \times 100 \tag{6.53}$$

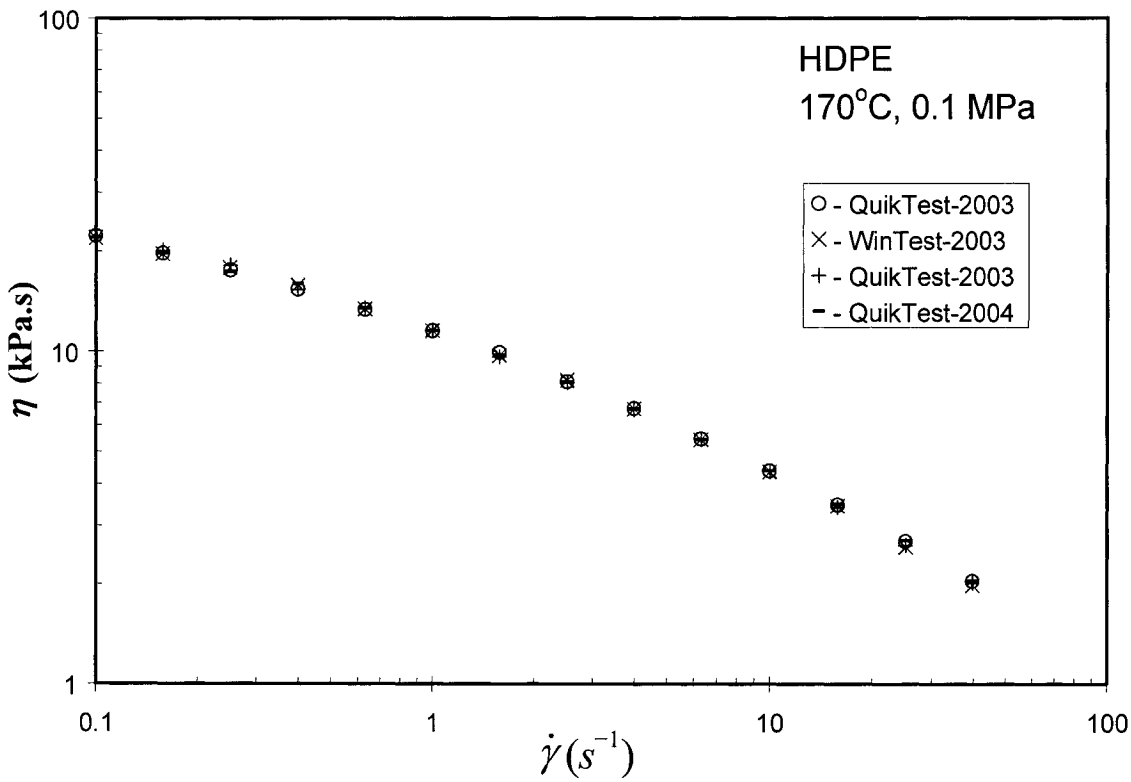

Figure 6.54. Reproducibility before and after software change.

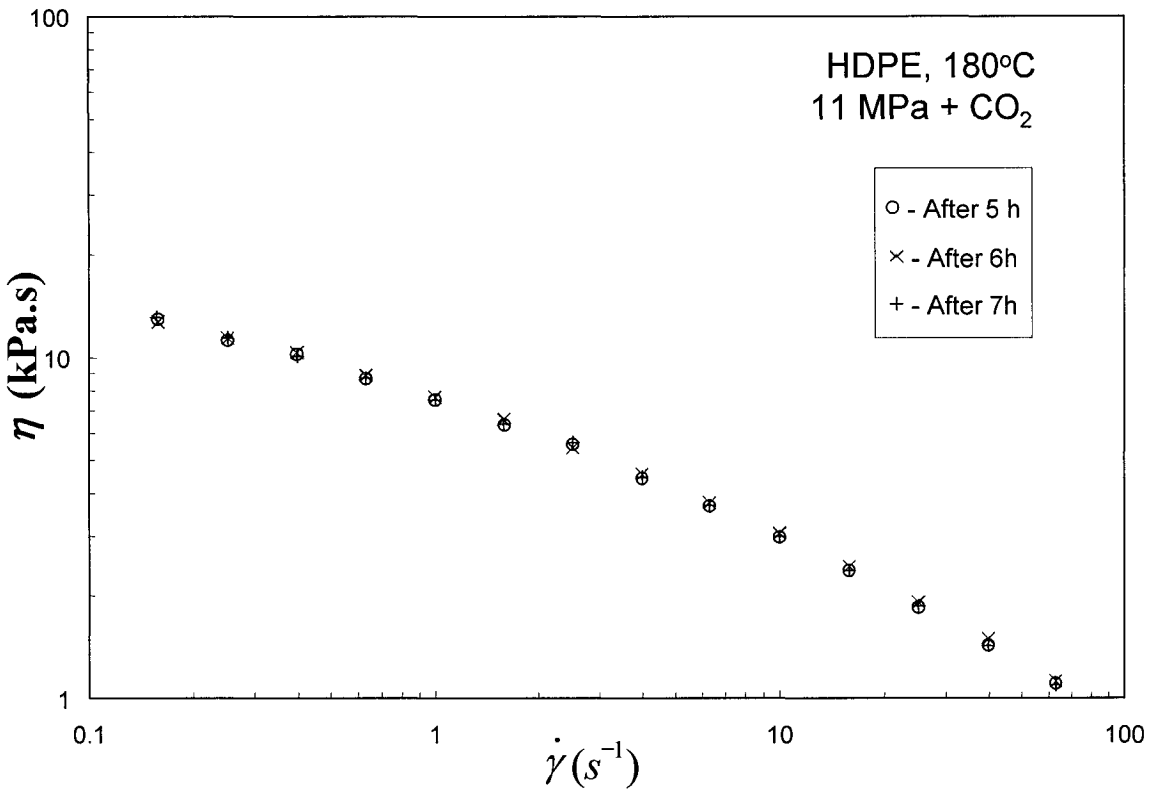

Figure 6.55. Variation of η with time after applying CO_2.

6.7.2 Comparison between the Viscosity and Complex Viscosity

About half a century ago, Cox and Merz [54] compared viscosity data with complex viscosity data for two polystyrenes. They reported that the apparent viscosity η_A measured in a capillary rheometer was nearly the same as the complex viscosity. Specifically they found that the curve of η_A versus apparent shear $\dot{\gamma}_A$ seemed to be a smooth continuation of the $|\eta^*|$ versus ω data on a double logarithmic plot. As can be seen in Fig. 6.56, the ranges for the two data sets did not overlap and are separated by a decade of shear rate or frequency. The often used "Cox-Merz rule" is not what Cox and Merz originally suggested. Instead, it is:

$$|\eta^*(\omega = \dot{\gamma})| = \eta(\dot{\gamma}) \tag{6.54}$$

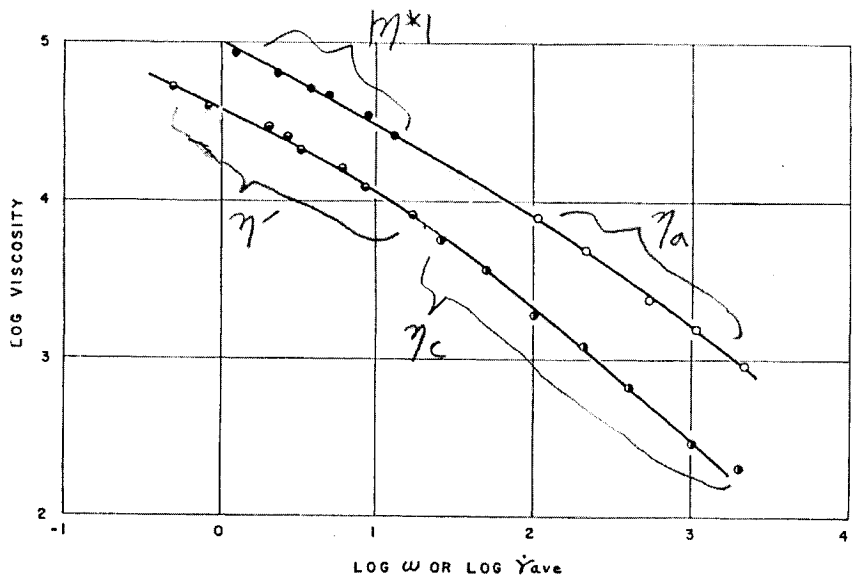

Typical flow data for polystyrene B. Complex dynamic viscosity, $|\eta^*|$ (●), compared to steady flow apparent viscosity, η_a(O); and dynamic viscosity, η'(◒) compared to steady flow consistency, η_c(◑).

Figure 6.56. The original Cox-Merz observation [54].

Kim [55] compared the complex viscosity at low frequencies with viscosity data obtained using a capillary rheometer at high shear rates. He found that the relative locations of the two curves varied with the polymer, but the order of magnitude was the same. Smillo [56] and Xu [57] used the Schümmer approximation [58] and the original Cox-Merz idea to obtain no-slip viscosity curve for polybutadiene (PBD) samples. The Schümmer approximation is a procedure for determining the true viscosity function from apparent viscosity data without the Rabinowitch correction:

$$|\eta^*(\omega = \dot{\gamma}_A)| = \eta_A(\dot{\gamma}_A) = \eta(x^*\dot{\gamma}) \tag{6.55}$$

where η_A and $\dot{\gamma}_A$ are the apparent viscosity and shear rate obtained using a capillary rheometer, and x^* is the shift factor. The first equality in Eq. 6.55 is the original Cox-Melz relationship. Based on the above relationships, they found that they could shift the viscosity versus shear-rate curve onto the complex viscosity versus frequency curve by use of a constant shift factor of 0.83.

A similar analysis was performed for this study. Figure 6.57 compares viscosity

versus shear-rate data with complex viscosity versus frequency data. The values of viscosity (■) and complex viscosity (◆) do not agree perfectly, but the order of magnitude and shape of the two curves are very similar. The viscosity shows slightly more shear thinning than the complex viscosity, and the two curves cross each other at 1 s^{-1}. The shift factor of 0.83 was used, but the agreement between shifted viscosity curve (▲) and complex viscosity (◆) was worse rather than better. Indeed, the curvature of each data set is different, so it cannot be expected that the viscosity curve will superpose onto the complex viscosity curve by shifting the entire curve on a double logarithmic plot.

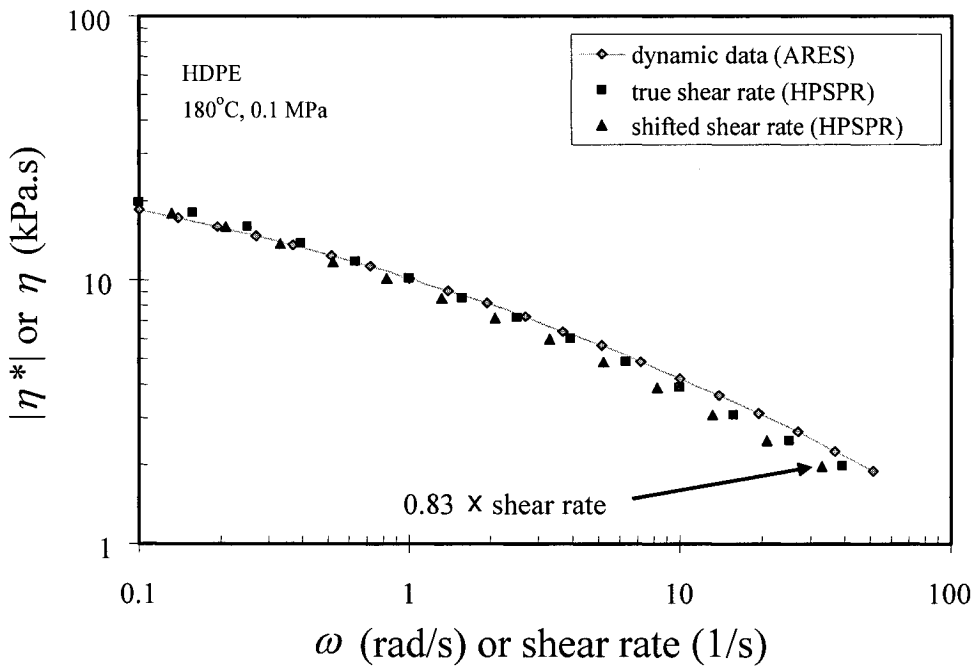

Figure 6.57. Comparison of viscosity with complex viscosity.

However, since the agreement between the viscosity (■) and complex viscosity (◆) is fairly good, the "rule" was found to be quite useful. For example, the shear-rate range for the viscosity measurements was experimentally found to be 0.1-40 s^{-1} at 180℃ and 0.1 MPa, while the range, estimated using the dynamic data in section 5.4.4.4, was 0.1-50 s^{-1}. For other temperatures, the predicted range was shifted by the temperature shift factor, which was obtained from dynamic data, and

found to work well. However, at elevated pressures with CO_2, no prediction was possible, because no shift factor was available *a priori*.

6.7.3 Model Fitting and Zero-Shear Viscosity

The Cross model was chosen to describe the viscosity data:

$$\eta(\dot{\gamma}) = \frac{\eta_0}{1+|\lambda\dot{\gamma}|^m} \tag{6.56}$$

As mentioned in the previous chapter, the zero-shear viscosity could not be determined directly from creep data, and an initial trial value was taken to be that at the lowest attainable shear stress from the creep tests (Section 5.4.3). The characteristic time λ is the inverse of the shear rate at which the viscosity is half its zero-shear value. Viscosity values from both creep and steady shear tests were fitted to Eq. 6.56, and the result is shown in Fig. 6.58 for tests at 1 atm. The zero-shear viscosity resulting from the curve fit was 38.0 kPa.s at 180℃.

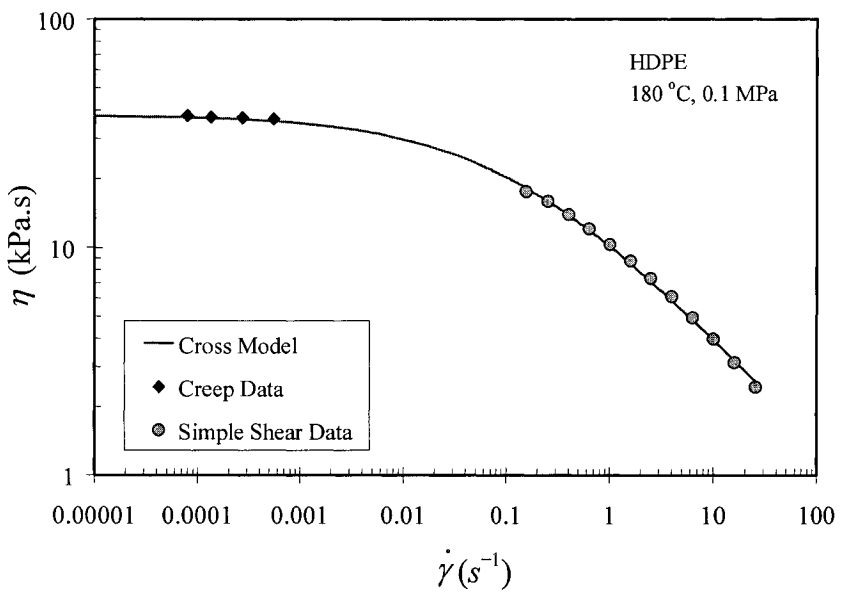

Figure 6.58. Cross model fitting using data from creep and simple shear tests.

6.7.4 Effect of Pressure on Viscosity

Figure 6.59 shows the results of shear-rate sweep tests at 180℃ and at seven pressures from 0.1 to 69 MPa. Data at 14 MPa are not shown to avoid confusion. As is well known, the viscosity increases with pressure.

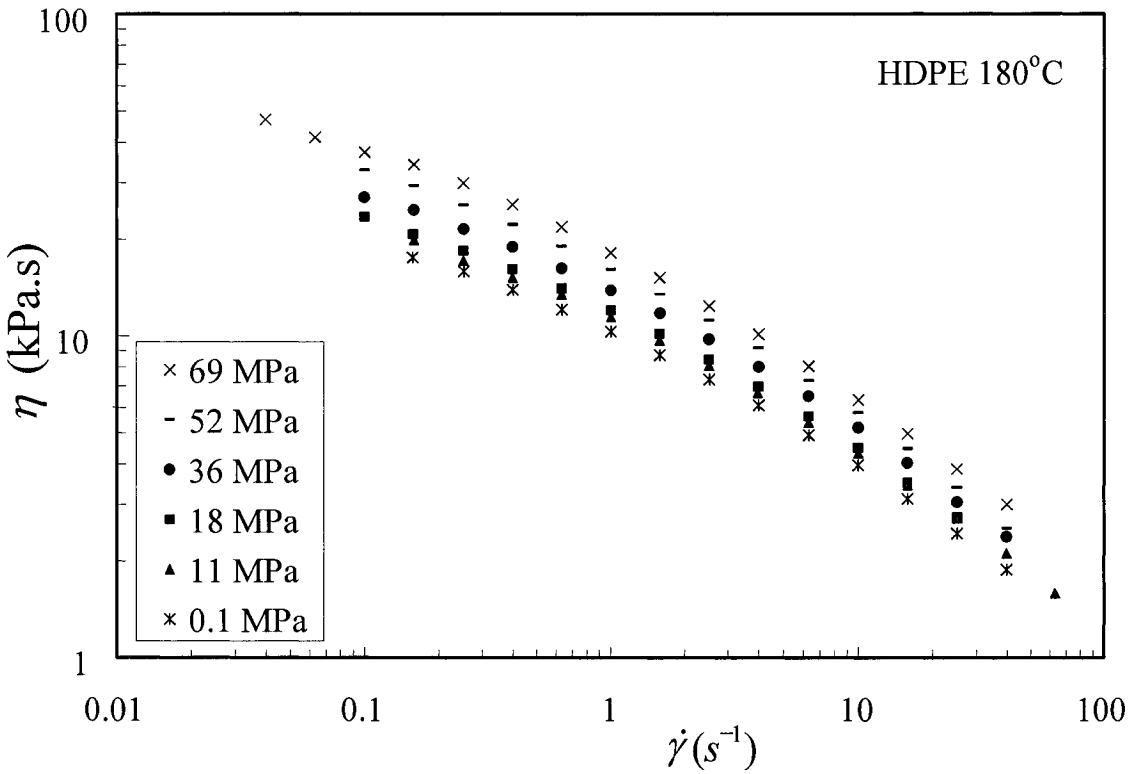

Figure 6.59. Effect of pressure on the viscosity at 180℃.

Pressure shift factors were determined in the same manner as for temperature. The vertical shift factor, $\rho T/\rho_0 T_0$ simplifies to $\rho(P)/\rho_0(P_0)$ at a constant temperature, but since pressure has little effect on density (6% deviation over 70 MPa, Section 2.4.2.1), the vertical shift factor for pressure was neglected in this study. (The 7% deviation over 50 degrees showed $b_T(T)$ is not necessary in Section 5.4.4.5.) The horizontal pressure shift factor $a_{1,P}(P)$ will be represented as $a_P(P)$ in the rest of this thesis. Taking as reference values at P_0 (1 atm) the three parameters (η_0, λ, m) determined from the atmospheric curve, stress versus shear-rate curves were shifted along the horizontal, shear-rate axis by the factor $a_p(P)$, leading to a stress master

curve:

$$\sigma\left[\dot{\gamma}a_p(P),P\right]=\sigma(\dot{\gamma},P_0) \tag{6.57}$$

The viscosity master curve version of the Cross model is Eq. 6.58:

$$\frac{\eta(\dot{\gamma},P)}{a_p(P)}=\frac{\eta_0(P_0)}{1+\left|\lambda(P_0)\dot{\gamma}a_p(P)\right|^{m(P_0)}} \tag{6.58}$$

The zero-shear viscosity at P is then given by:

$$\eta_0(P)=\eta_0(P_0)a_p(P) \tag{6.59}$$

Figure 6.60 shows the shifted result, and we see that the superposition was good. This implies that HDPE exhibits piezorheological simplicity, *i.e.* that the pressure shift factor is independent of shear rate.

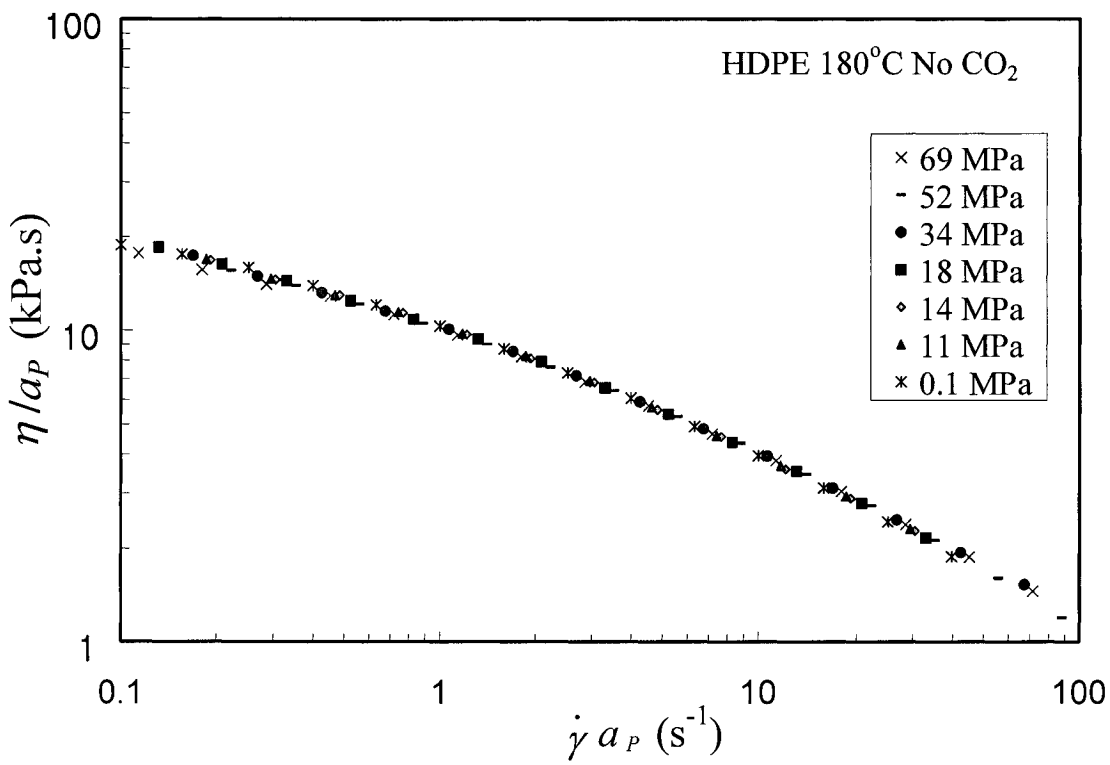

Figure 6.60. Shifted viscosity using $a_P(P)$, P_0=0.1 MPa.

Figure 6.61 shows the pressure shift factors versus pressure as well as the line fitted to the Barus model:

$$\ln[a_P(P)] = \beta(P - P_0) \tag{6.60}$$

where β is the slope of $\ln[a_P(P)]$ versus $(P\text{-}P_0)$, of which physical meaning is pressure sensitivity of the viscosity and whose value is shown in Fig. 6.61.

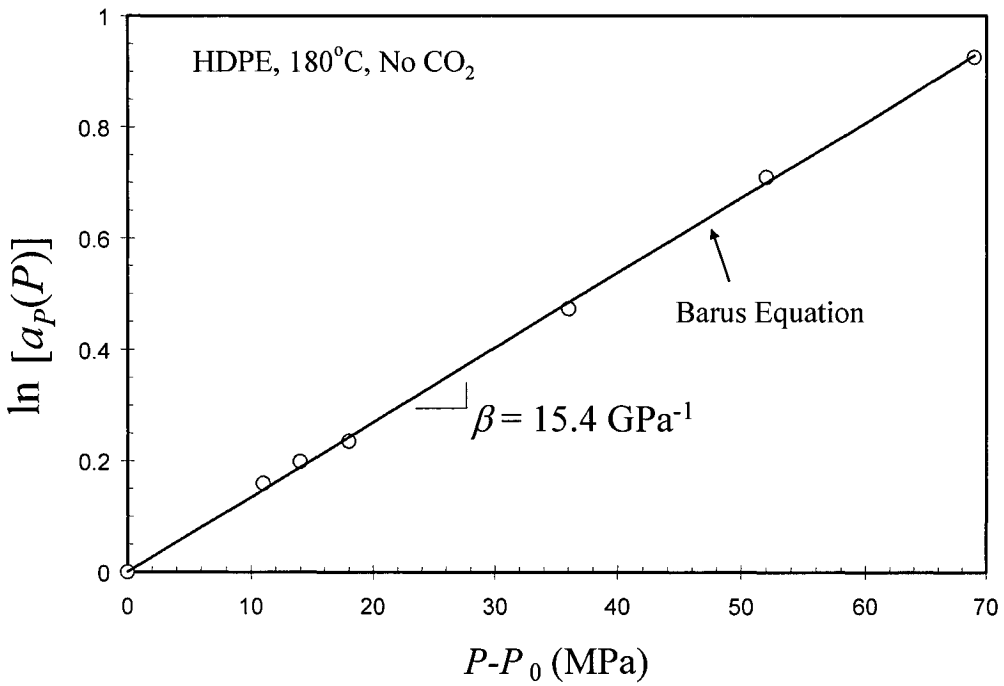

Figure 6.61. Effect of pressure on pressure shift factor, P_0=0.1 MPa.

6.7.5 Effect of Temperature on Viscosity and Comparison with Linear Viscoelasticity Data

To obtain the temperature shift factor $a_T(T)$ for steady simple shear, shear-rate sweep tests were performed at three temperatures from 170 to 200℃, at atmospheric pressure. Figure 6.62 shows the shifted result, and Fig. 6.63 shows the effect of temperature on a_T. The slope of the line in Fig. 6.63 is the activation energy (E_a)

and was found to be 25.2 kJ/mol. Theoretically, the shift factor should agree with that from SAOS data (Section 5.4.4.5). The shift factor from SAOS is 1.8% larger than that from the simple shear tests at 200℃. This deviation is within the experimental error range of 6% (Section 6.7.1). Considering that quite different apparatuses and fitting models (the Cross and the Yasuda models) were used, the deviation is deemed to be negligible.

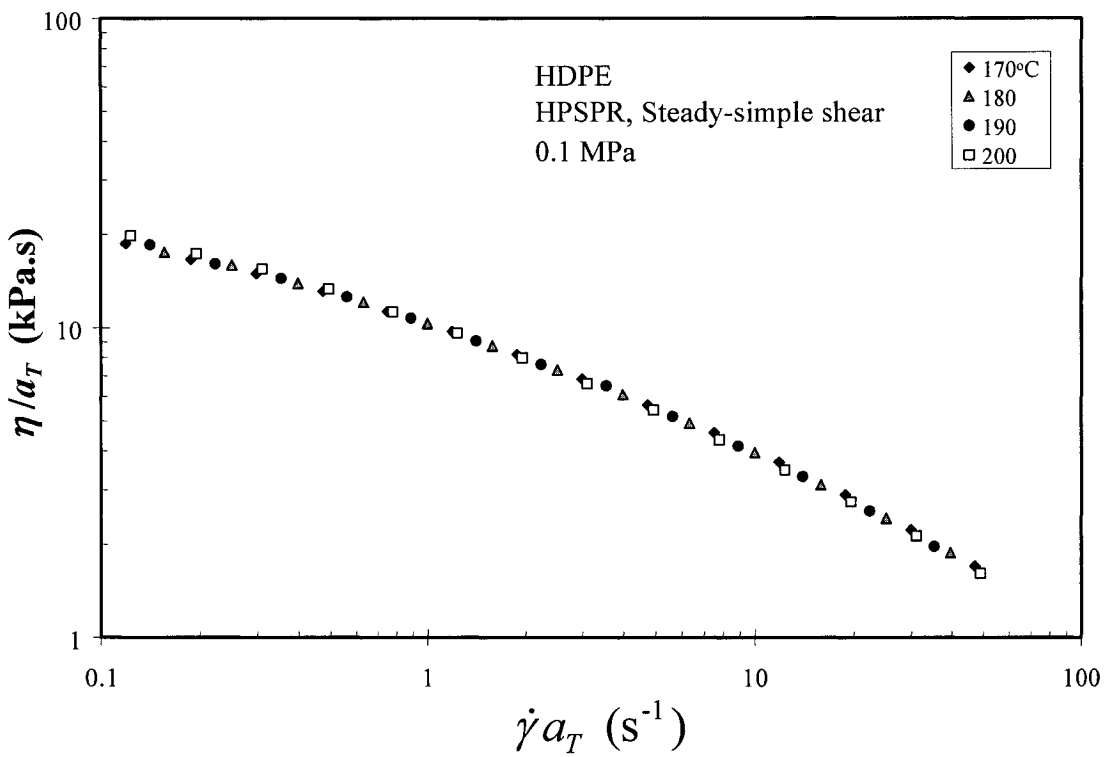

Figure 6.62. Shifted viscosity data using a_T, T_0=180℃.

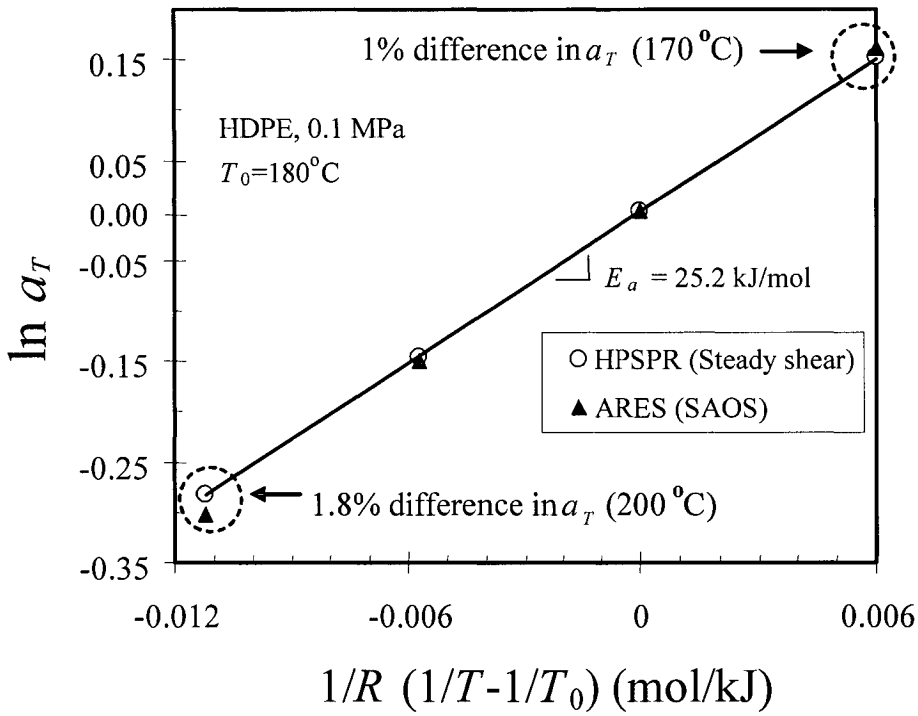

Figure 6.63. Comparison of the temperature shift factors from steady shear and dynamic tests at 1 atm, T_0=180℃.

6.7.6 Relative Influence of *T* and *P*

The effect of temperature on the viscosity is similar to that of pressure but in the opposite direction, and the relative influence of the two variables can be described by noting the change in temperature required to change the viscosity by the same amount as a prescribed change in pressure:

$$\left(\frac{\partial T}{\partial P}\right)_{\eta_0} \tag{6.61}$$

The effects of pressure and temperature on viscosity can be modeled using the simple Barus and Arrhenius exponential equations. If these two effects are assumed to be separable:

$$\eta_0(T,P)=\eta_0(T_0,P_0)e^{\frac{E_a}{R}\left(\frac{1}{T}-\frac{1}{T_0}\right)}e^{\beta(P-P_0)} \tag{6.62}$$

By taking the derivative of both sides of Eq. 6.62, the following expressions are obtained:

$$\left[\frac{\partial\eta_0(T,P)}{\partial P}\right]_T=\eta_0(T_0,P_0)\beta e^{\frac{E_a}{R}\left(\frac{1}{T}-\frac{1}{T_0}\right)}e^{\beta(P-P_0)} \tag{6.63}$$

$$\left[\frac{\partial\eta_0(T,P)}{\partial T}\right]_P=-\frac{\eta_0(T_0,P_0)E_a}{RT^2}e^{\frac{E_a}{R}\left(\frac{1}{T}-\frac{1}{T_0}\right)}e^{\beta(P-P_0)} \tag{6.64}$$

The zero-shear viscosity (Eq. 6.62) is a function of temperature and pressure as follows:

$$d\eta_0=\left(\frac{\partial\eta_0}{\partial T}\right)_P dT+\left(\frac{\partial\eta_0}{\partial P}\right)_T dP \tag{6.65}$$

To give no change in the viscosity as:

$$d\eta_0=0 \tag{6.66}$$

Eq. 6.65 is reduced to:

$$\left(\frac{\partial\eta_0}{\partial T}\right)_P dT+\left(\frac{\partial\eta_0}{\partial P}\right)_T dP=0 \tag{6.67}$$

and

$$\left(\frac{\partial T}{\partial P}\right)_{\eta_0}=-\left(\frac{\partial\eta_0}{\partial P}\right)_T\Big/\left(\frac{\partial\eta_0}{\partial T}\right)_P \tag{6.68}$$

The final equation can be obtained by combining Eqs. 6.63, 6.64, and 6.68 as:

$$\left(\frac{\partial T}{\partial P}\right)_{\eta_0} = \frac{R\beta}{E_a} T^2 \text{ (K/MPa)} \tag{6.69}$$

which shows that the relative influence depends only on temperature (Fig. 6.64). The function $(\partial T/\partial P)_{\eta_0}$ [1] implies how much temperature should increase for an increase of pressure to keep the same viscosity, and the higher the value of this function, the greater the sensitivity to pressure. Figure 6.64 shows that the relative sensitivity of the viscosity on pressure increases with temperature with $\beta = 15.4\,\text{GPa}^{-1}$ and $E_a = 27.5\,\text{kJ/mol}$. For example, the value at 170℃ is 0.91℃/MPa, and that at 190℃ is 1.00℃/MPa. This implies that an increase in pressure of 1 MPa has the same effect on the viscosity as a reduction in temperature of 0.91℃ around 170℃, and 1.00℃ around 190℃, respectively. Cogswell [59, p.45] reported the following for HDPE:

$$\left(\frac{\Delta T}{\Delta P}\right)_{\eta} = 0.42\ ℃/\text{MPa} \tag{6.70}$$

which is about one half the value from this work.

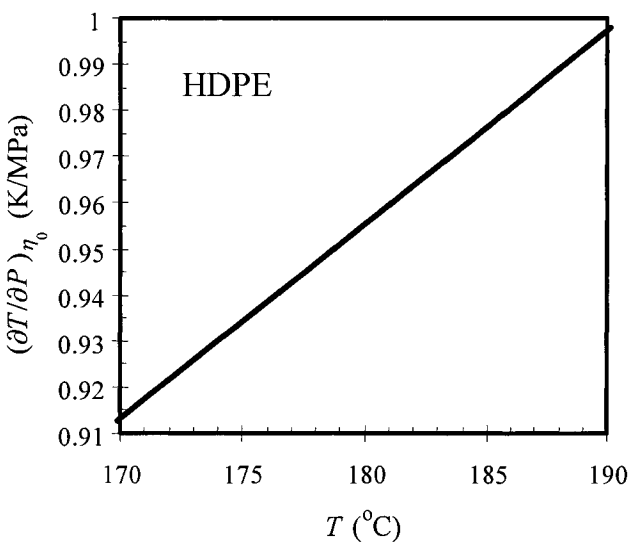

Figure 6.64. Relative influence of temperature and pressure on the viscosity as a function of temperature.

1) Since pressure and temperature affect the viscosity in the opposite direction, this function seems to be negative. However, to compensate the effect of one variable on the viscosity, the other must change in the same direction, and this function is thus positive.

6.7.7 Combined Effects of Pressure and CO_2 on viscosity

Shear-rate sweeps were carried out at five pressures under CO_2 at 180℃. Saturation was confirmed by the constancy of the viscosity with time. The viscosity versus shear-rate data are shown in Fig. 6.65. Data without CO_2 are also shown for comparison, but data for 14 MPa are omitted to avoid confusion. Open symbols are for samples saturated with CO_2. While pressure alone increases the viscosity, pressure plus dissolved CO_2 has the opposite effect even at a given pressure. This results from plasticization by the CO_2. For example, the data at 11 MPa (▲) are slightly higher than those at 1 atm (*), while these with CO_2 at 11 MPa (△) are well below the atmospheric pressure points. The effect of CO_2 is clearly very large, because it not only compensates for the increase of viscosity due to pressure, but also decreases the viscosity below its value at atmospheric pressure. One aspect that should be noted is that the curve at 52 MPa with CO_2 (+) and that at 36 MPa (×) are very

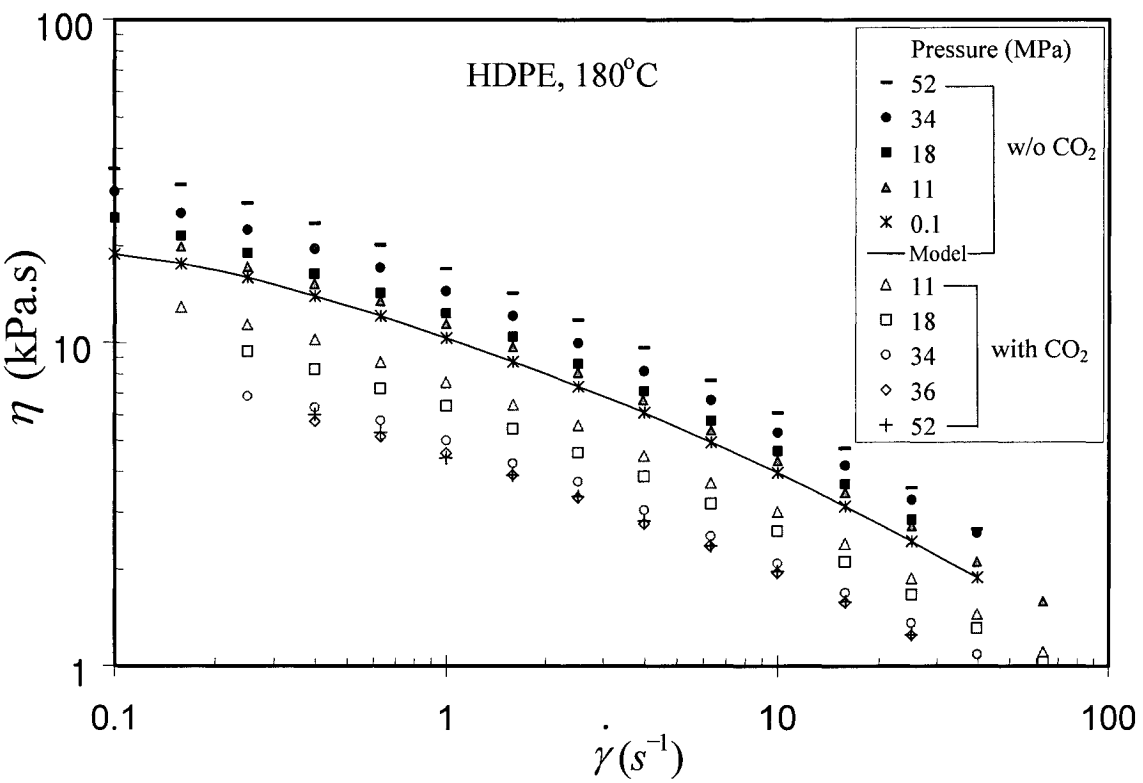

Figure 6.65. Effects of pressure and CO_2 on the viscosity versus shear rate curve.

similar. This implies that the effect of increasing the pressure from 36 to 52 MPa is exactly balanced by the plasticization effect of the CO_2, and the viscosity cannot be decreased further by increasing the CO_2 pressure above 36 MPa. However, it is not clear to see if the viscosity at 52 MPa remains the same, *i.e.*, the saturated viscosity, at higher pressures, or if the viscosity would increase at pressure higher than 52 MPa.

The data were shifted to form a master curve. While the vertical shift for pressure was not used, the vertical shift for concentration must be taken into account, as it was shown to be a strong function of concentration in Chapter 3. Figure 3.10 shows there is a 28% decrease over 34 MPa. Equation 6.71 defines this shift factor:

$$b_{P,C}(P,C) \equiv \frac{C_{pol}(P,C)}{\rho_{pol}(P_0)} \tag{6.71}$$

where $C_{pol}(P,C) \equiv W_{pol}/V_m(P,C)$, and $\rho_{pol}(P_0) \equiv W_{pol}/V_{pol}(P_0)$. The effect of the vertical factor was shown by comparing two cases with and without the vertical shift factor.

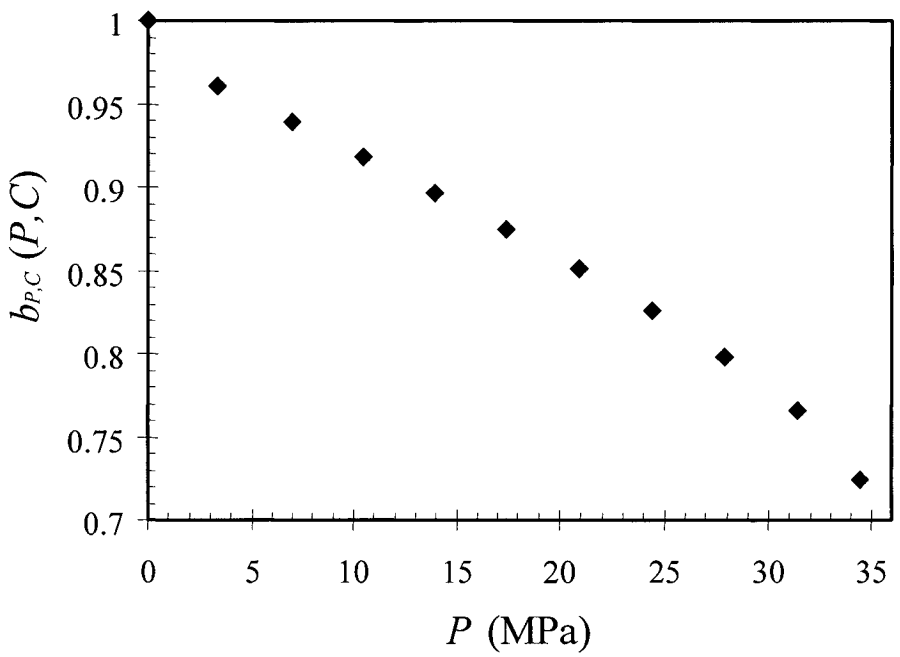

Figure 3.10. Effect of pressure on the concentration vertical shift factor HDPE 180℃.

To obtain pressure and concentration shift factor, the Cross model of stress was used. The master curve of the model with both horizontal and vertical shift factors is:

$$\frac{\sigma(\dot{\gamma},P,C)}{a_{P,C}(P,C)b_{P,C}(P,C)}=\frac{\eta_0(P_0)\dot{\gamma}}{1+|\lambda(P_0)a_{P,C}(P,C)\dot{\gamma}|^{m(P_0)}} \tag{6.72}$$

where $a_{P,C}(P,C)$ is the combined pressure and concentration shift factor not ignoring $b_{P,C}(P,C)$, which is assumed to be $b_C(C)$ due to little effect of P on density, while the master curve equation with only a horizontal shift factor is:

$$\frac{\sigma(\dot{\gamma},P,C)}{a_{1,P,C}(P,C)}=\frac{\eta_0(P_0)\dot{\gamma}}{1+|\lambda(P_0)a_{1,P,C}(P,C)\dot{\gamma}|^{m(P_0)}} \tag{6.73}$$

where $a_{1,P,C}(P,C)$ is the combined pressure and CO_2 concentration shift factor ignoring the vertical shift factor. The concentration C is the solubility of CO_2 at P for the data of this project. Figure 6.66 shows the shifting procedure for the case with $b_C(C)$. The original stress data (▲) were shifted (■) vertically by $b_C(C)$, and then shifted (●) horizontally determining $a_{P,C}(P,C)$.

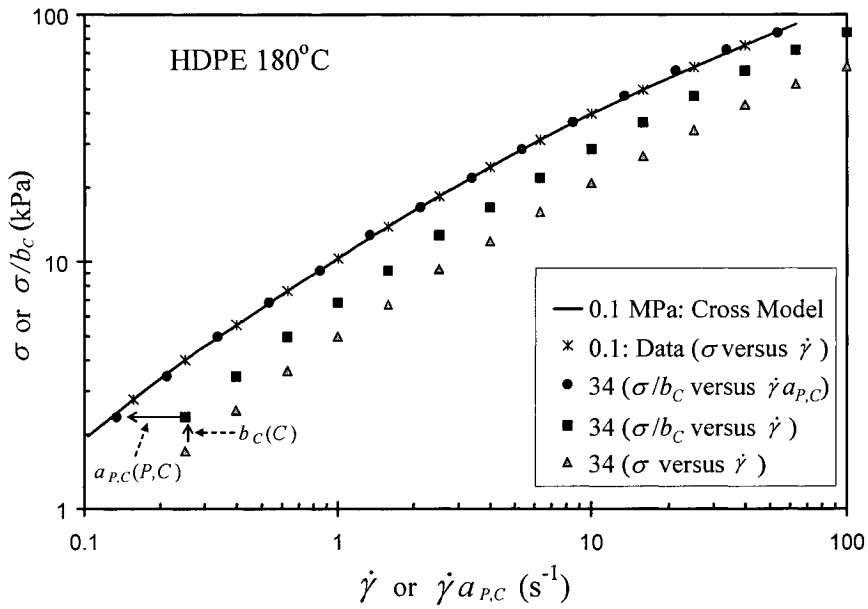

Figure 6.66. Procedure of vertical and horizontal shift of stress data.

The viscosity master curve of the Cross model with both horizontal and vertical shift factors is:

$$\frac{\eta(\dot{\gamma},P,C)}{a_{P,C}(P,C)b_{P,C}(P,C)}=\frac{\eta_0(P_0)}{1+|\lambda(P_0)a_{P,C}(P,C)\dot{\gamma}|^{m(P_0)}} \tag{6.74}$$

while the viscosity master curve equation with only a horizontal shift factor is:

$$\frac{\eta(\dot{\gamma},P,C)}{a_{1,P,C}(P,C)}=\frac{\eta_0(P_0)}{1+|\lambda(P_0)a_{1,P,C}(P,C)\dot{\gamma}|^{m(P_0)}} \tag{6.75}$$

Figures 6.67 and 6.68 show the shifted results of the viscosity, and it can be observed that the shifted data with the vertical shift factor (Fig. 6.67) is slightly better than those without the vertical shift factor in Fig. 6.68, which shows that data (ellipses in Fig. 6.68) at low and high shear rates are more scattered than those in Fig. 6.67. This difference can be studied by analyzing the error sum for the regression, which is defined as:

$$S=\sum_{j=1}^{M}\left[\sum_{i=1}^{N}\left(\frac{\sigma_i-\sigma_{mp,i}}{\sigma_i}\right)^2\right]_j \tag{6.76}$$

where σ is a datum of stress, σ_{mp} is a model-predicted stress, i is the shear-rate index, j is the pressure and concentration index, N is the number of data sets of one shear-rate sweep, and M is the number of conditions (P_j,C_j). The sum S for the case with $b_C(C)$ is 11.1, and that ignoring $b_C(C)$ is 12.2. Thus, the shift with $b_C(C)$ shows a 10% better shifted result than that without $b_C(C)$. Further analysis was carried out only with $a_{P,C}(P,C)$ and $b_C(C)$.

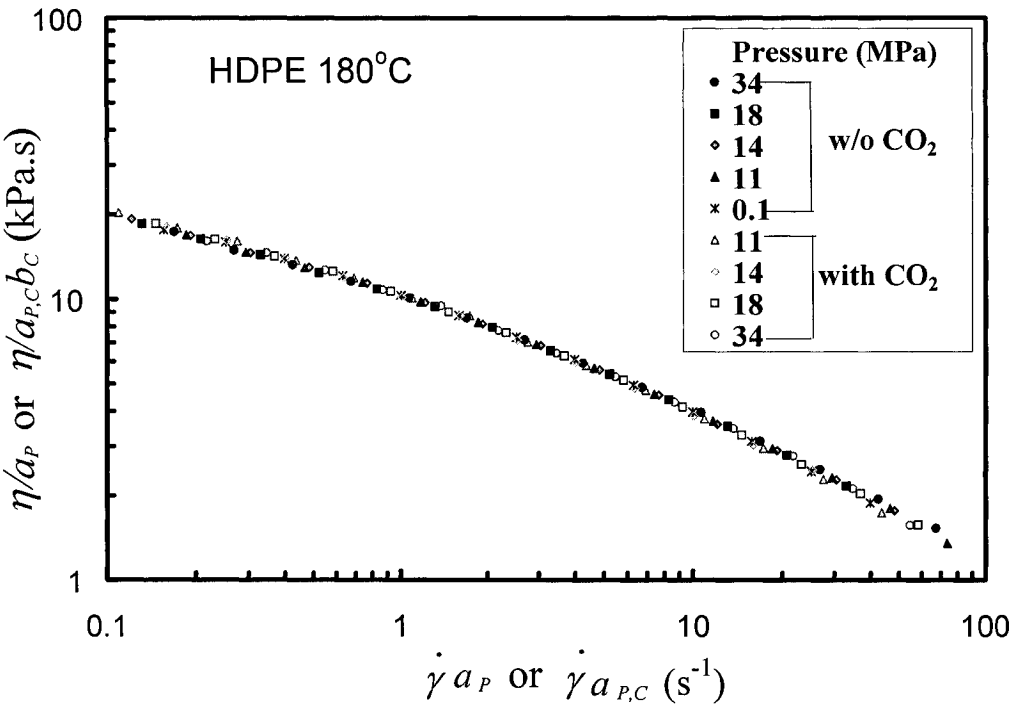

Figure 6.67. Viscosity shifted using both horizontal and vertical shift factors for CO_2 concentration. No vertical shift was used for the pure pressure effect.

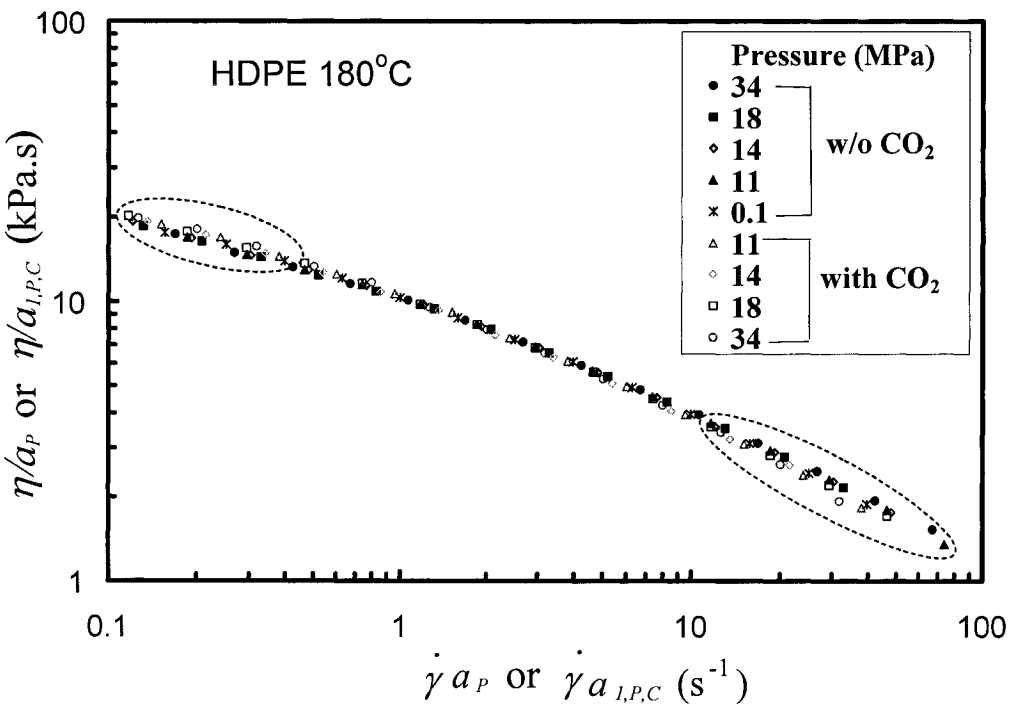

Figure 6.68. Viscosity shifted using only a horizontal shift factor for CO_2 concentration. No vertical shift was used for the pure pressure effect.

Figure 6.69 shows the two shift factors as functions of pressure. As mentioned before, to study the effect of CO_2 at constant pressure, it is assumed that effects of pressure and CO_2 are separable, *i.e.* $a_{P,C}(P,C) = a_P(P)a_C(C)$:

$$\frac{\eta_0(P,C)}{\eta_0(P_0,0)} = a_{P,C}(P,C)b_C(C) = a_P(P)a_C(C)b_C(C) \tag{6.77}$$

where $a_C(C)$ is a horizontal concentration shift factor and assumed to be calculated from $a_{P,C}(P,C)$:

$$a_C(C) = a_{P,C}(P,C)/a_P(P) \tag{6.78}$$

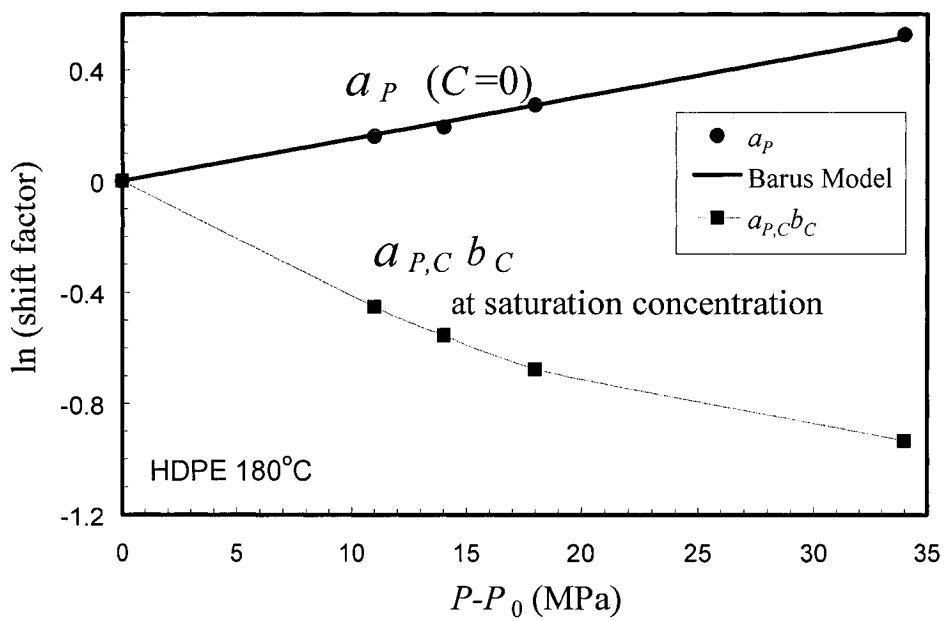

Figure 6.69. Shift factors as functions of pressure.

The concentration shift factor $a_C(C)b_C(C)$ can thus be obtained as:

$$a_C(C)b_C(C) = a_{P,C}(P,C)b_C(C)/a_P(P) \tag{6.79}$$

where all terms on the right hand side are data, and $a_P(P)$ is the shift factor ignoring $b_P(P)$. The quantity $a_C(C)b_C(C)$ represents a pressure-independent ratio of zero-shear

viscosity at C and C_0:

$$a_C(C)b_C(C) = \frac{\eta_0(C)}{\eta_0(C_0)} \tag{6.80}$$

where C_0 is zero for this study. The Fujita-Kishimoto (F-K) model [60] was used to describe the effect of CO_2 concentration alone. This model is an analog of the WLF equation based on the free volume theory:

$$\ln\left[\frac{\eta_0(C)}{\eta_0(C_0)}\right] = \ln a_C(C) = \frac{-AC}{B+C} \tag{6.81}$$

where C_0 is the reference concentration, and A in the units of reciprocal concentration and B in the units of concentration are fitting constants. However, they did not include b_C explicitly in the model (Section 4.1.5).

Since the free volume theory models the ratio of the viscosity, b_C was included in the following model in this study:

$$\ln\left[\frac{\eta_0(C)}{\eta_0(C_0)}\right] = \ln\left[a_C(C)b_C(C)\right] = \frac{-A'C}{B'+C} \tag{6.82}$$

where C_0 is zero. Equation 6.82 can be rewritten as:

$$\frac{1}{\ln\left[a_C(C)b_C(C)\right]} = -\frac{B'}{A'}\frac{1}{C} - \frac{1}{A'} \tag{6.83}$$

where A' and B' are fitting constants. According to Eq. 6.83 a plot of $1/\ln\left[a_C(C)b_C(C)\right]$ versus $1/C$ should be a straight line with a slope of $-B'/A'$ and an intercept of $-1/A'$, and such a plot is shown in Fig. 6.70. Figure 6.71 shows the two shift factors as functions of concentration along with the prediction of Eq. 6.82 with $A' = 2.35$ and $B' = 0.23$. It is clear that the free volume model can describe the effect of concentration. From this, it may be inferred that CO_2 molecules increase the

free volume of the polymer. In plastics processing, the polymer is generally not saturated, so for practical applications independent shift factors for pressure and concentration are required.

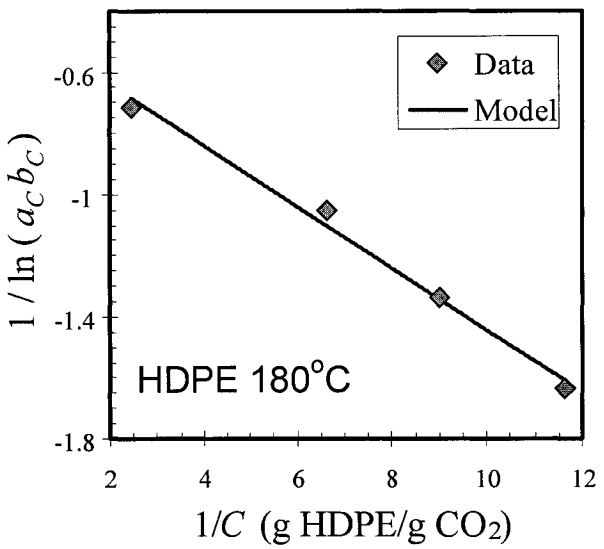

Figure 6.70. Effect of concentration on the concentration shift factor.

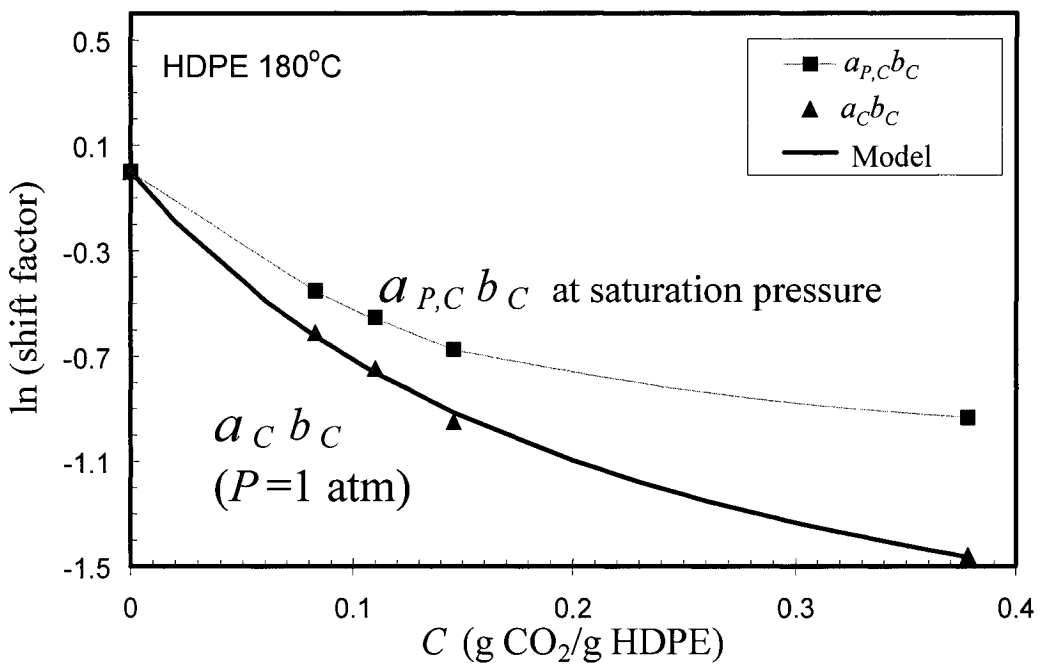

Figure 6.71. Shift factors as functions of concentration.

6.7.8 Comparison between Effects of CO_2 and N_2 on Viscosity

Figure 6.72 shows a comparison between effects of CO_2 and N_2 on the viscosity at 18 MPa. The decrease of the viscosity due to N_2 (◆) doubles the increase due to pure pressure (▲), and the data with N_2 (◆) are slightly lower than those at 1 atm (□) while these with CO_2 (●) are much below the atmospheric pressure points. The effect of N_2 is clearly much less than that of CO_2, because the solubility of N_2 is only one tenth that of CO_2 [52]. Figure 6.73 shows the differences between effects of CO_2 and N_2 at 34 MPa. Unlike results at 18 MPa, the data with N_2 (◆) are the same as those at 1 atm (□) while these with CO_2 (●) are well below the atmospheric data. The increase of the viscosity due to pure pressure can be exactly compensated by the plasticization effect of N_2 at 34 MPa, and the relative effect of N_2 to pressure at 34 MPa is less than that at 18 MPa. Further increase of N_2 pressure may bring the viscosity curve above the atmospheric curve, *i.e.*, the plasticization effect of N_2 cannot fully compensate the effect of pressure. Nitrogen has not only a much less effect on the viscosity than CO_2 but also a different effect relative to pressure.

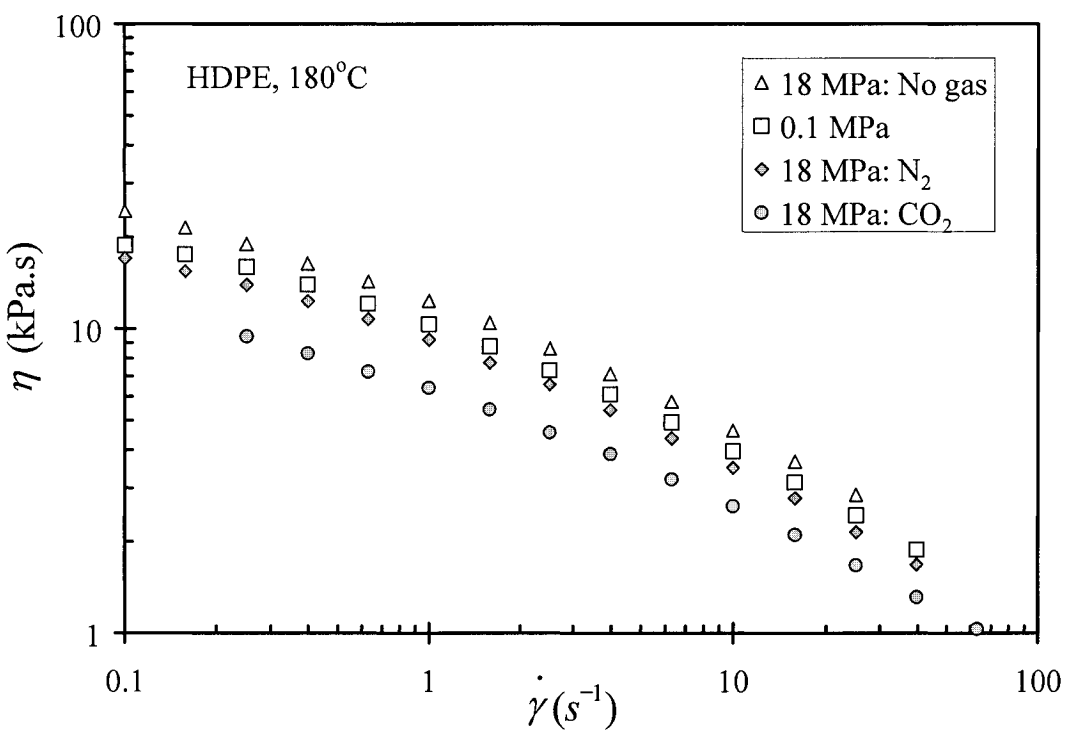

Figure 6.72. Comparison between effects of CO_2 and N_2 on viscosity at 18 MPa.

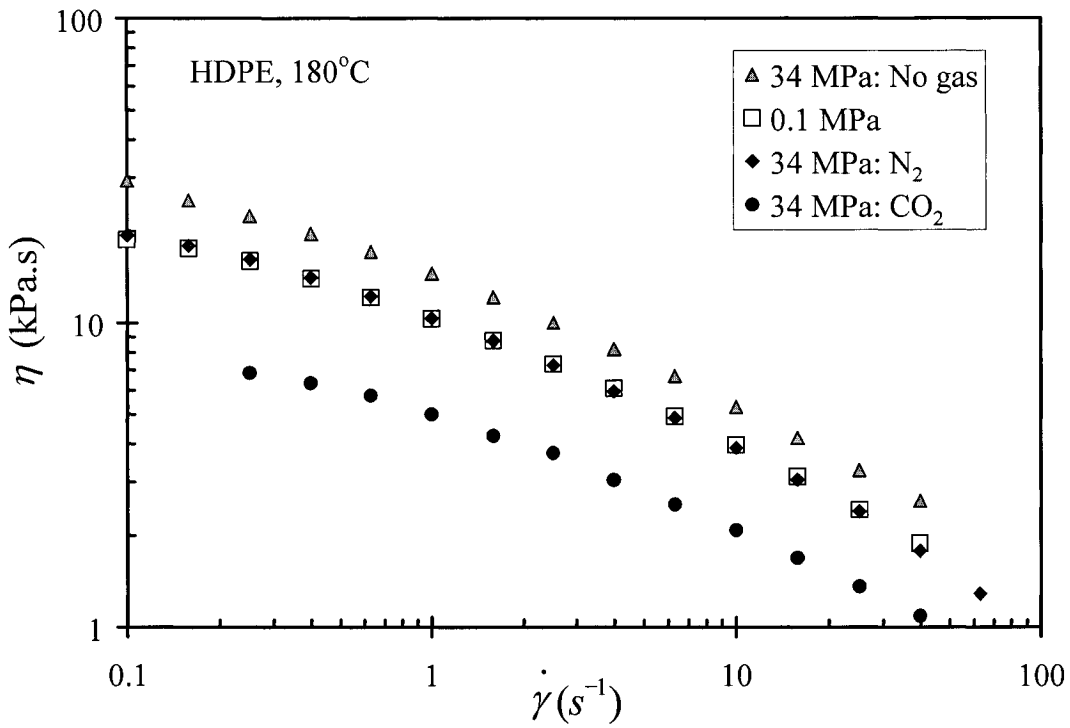

Figure 6.73. Comparison between effects of CO_2 and N_2 on viscosity at 34 MPa.

6.7.9 Effects of Pressure and CO_2 on the Stress Growth Function

Pressure and concentration affect rheological properties as is illustrated in Fig. 6.74, and to study the effects of pressure and CO_2 on the stress growth function $\sigma^+ \equiv \sigma(\dot{\gamma},t)$, either shear rate or steady-state stress should be fixed (Fig. 6.75). Both approaches (Section 6.7.9.1) are described in this section. Stress growth data are usually reported as $\eta^+(t,\dot{\gamma}) \equiv \sigma^+(t,\dot{\gamma})/\dot{\gamma}$, but the normalization by shear rate does not provide a good description of the pressure effect, so the stress itself was used in this work. The first approach is to compare normalized $\sigma^+(t)/\sigma^+(\infty)$ curves generated at the same shear rate for various values of P and C. The vertical shift of stress was not considered because this factor will be canceled out by the normalizing stress:

$$\frac{\sigma^+(t)/b_C}{\sigma^+(\infty)/b_C} = \frac{\sigma^+(t)}{\sigma^+(\infty)} \tag{6.84}$$

The second (Section 6.7.9.2) is to compare $\sigma^+(t)/b_C$ curves for the same steady-state stress $[\sigma^+(\infty)/b_C]$ for various values of P and C. The second case is similar to a creep test, in which stress is constant, but $\sigma^+(\infty)$ is not controlled directly in the strain-controlled mode. After varying the shear rate at fixed values P and C, $\sigma^+(t)/b_C$ curves giving similar values of $\sigma^+(\infty)/b_C$ were selected for comparison. Only one set of curves was found to satisfy this criterion.

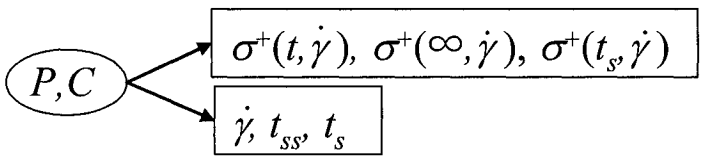

Figure 6.74. Effects of pressure and CO_2 on stress growth behavior.

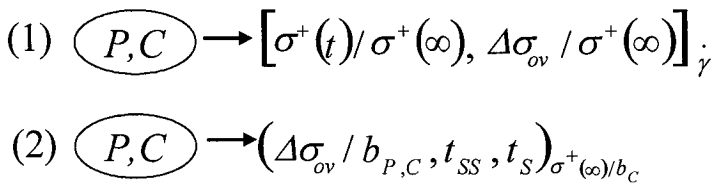

Figure 6.75. Two approaches for describing the effects of pressure and CO_2 on stress growth behavior.

6.7.9.1 Stress Growth Function at Same Shear Rate

Figure 6.76 shows the effect of pressure on $\sigma^+(t)$ at a shear rate of 25 s^{-1}. Pressure increases the maximum stress $\sigma_S \equiv \sigma^+(t_S)$ and the overshoot $\Delta\sigma_{ov} \equiv \sigma^+(t_S) - \sigma^+(\infty)$ at a given shear-rate, while CO_2 decreases these.

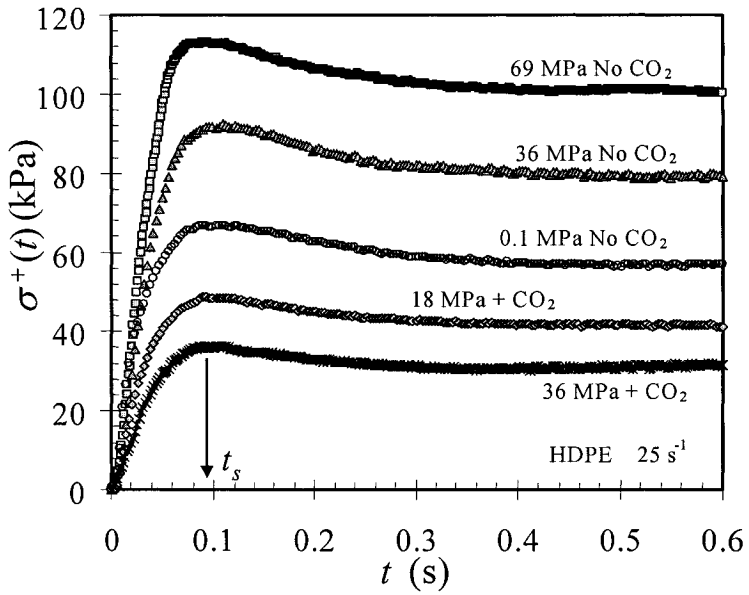

Figure 6.76. Effects of pressure and CO_2 on the stress growth function at 25 s^{-1} and 180℃.

It was found that a master curve could be made if $\sigma^+(t)$ was normalized by $\sigma^+(\infty)$ to give $\sigma^+(t)/\sigma^+(\infty)$ (Fig. 6.77). Thus, at a constant shear rate, the variation

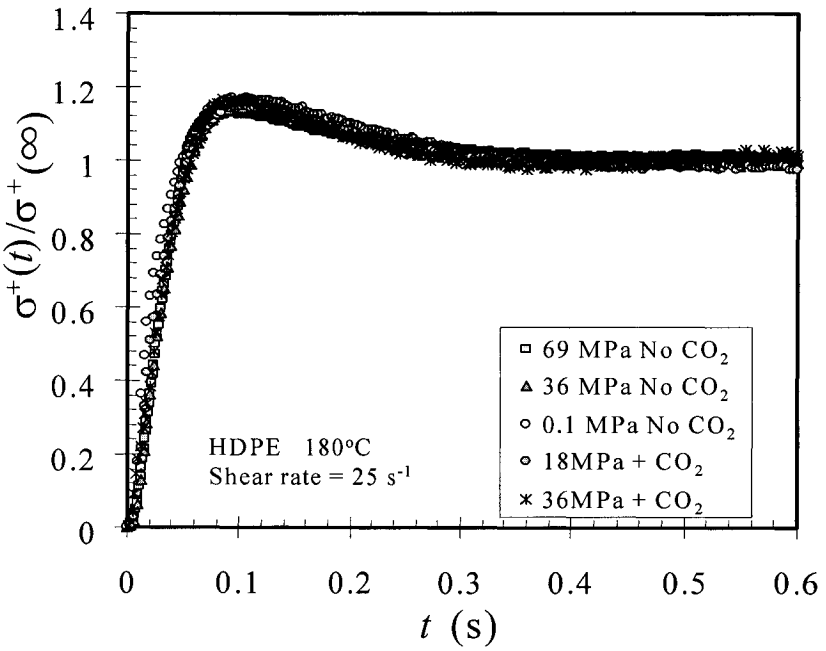

Figure 6.77. Normalized stress growth function at 25 s^{-1} at 180℃.

of $\sigma^+(t)/\sigma^+(\infty)$ with t, the time to reach the maximum stress (t_S), and the time to reach steady stress (t_{SS}) are all unaffected by CO_2 and pressure. These responses are affected only by the shear-rate. One implication of this is that at a given shear rate, the relative magnitude of the stress overshoot $\Delta\sigma_{ov}/\sigma^+(\infty)$ does not vary with pressure, and the following relationship is valid with no horizontal $a_{P,C}$ shift:

$$\left[\frac{\sigma^+(t,P_0)}{\sigma^+(\infty,P_0)}\right]_{\dot{\gamma}} = \left[\frac{\sigma^+(t,P,C)}{\sigma^+(\infty,P,C)}\right]_{\dot{\gamma}} \tag{6.85}$$

At a low shear rate of 0.63 s^{-1}, the same result can be seen in Fig. 6.76, except that the signal is noisy because of the low stress level. This behavior may be valid only for a linear polyethylene. Park [5] reported that pressure increases $\Delta\sigma_{ov}/\sigma^+(\infty)$ for a long-chain branched metallocene polyethylene (BmPE). His plots of nonlinear viscosity are shown in Figs. 6.79, which shows that the atmospheric curve does not have an overshoot, and 6.80. Thus, the effect of pressure on the stress growth function provides evidence of long-chain branching.

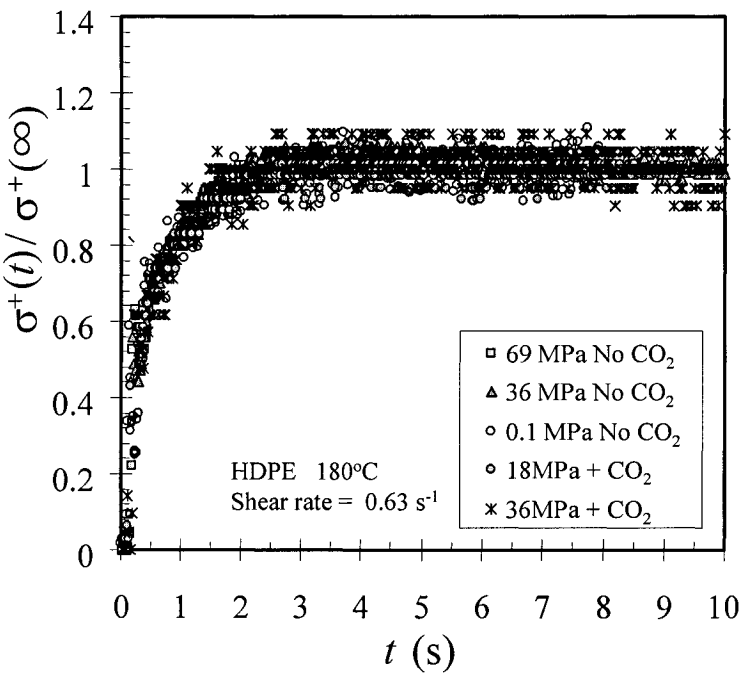

Figure 6.78. Normalized stress growth function at 0.63 s^{-1} and 180℃.

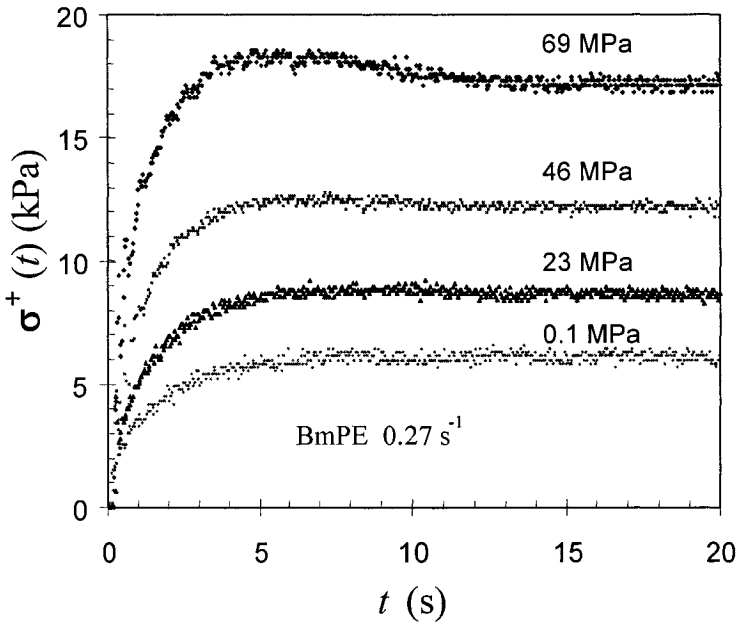

Figure 6.79. Pressure dependence of the stress growth function of BmPE at 0.27 s^{-1} and 170℃ [5].

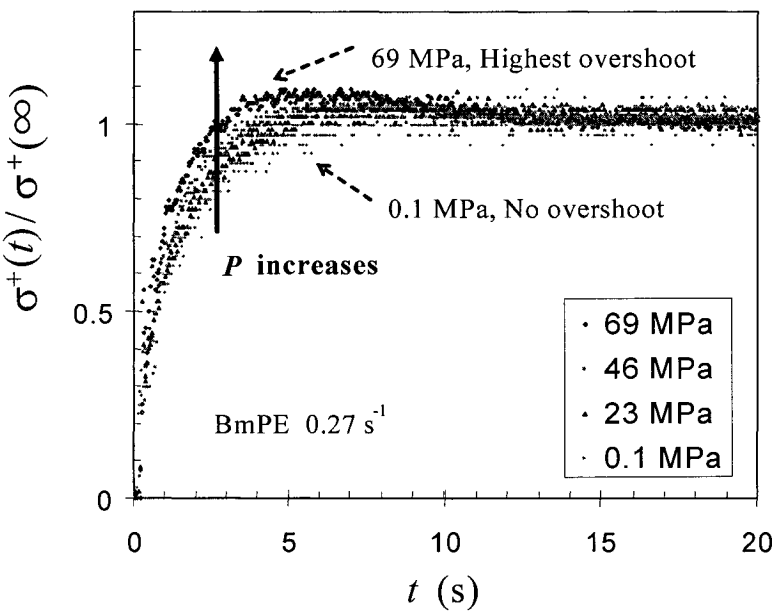

Figure 6.80. Pressure dependence of the normalized stress growth function of BmPE at 0.27 s^{-1} and 180℃ [5].

6.7.9.2 Stress Growth Function with Same Steady-state Stress

Figure 6.81 shows $\sigma^+(P,C,t)/b_C(C)$ curves for several shear rates that lead to the same steady-state stress. We see that pressure delays the response, while CO_2 accelerates it. This implies that a longer time is required to achieve the overshoot and steady state at elevated pressure, and less time is needed with CO_2, at a given pressure.

Because the shear rate varies, it is necessary to shift the time response using the shift factor obtained from viscosity measurements. Figure 6.82 shows the superposed curve. The early stage of superposition is not perfect, but other time responses, such as t_S, and t_{SS}, seem to be superposable. The following relationships can thus be established:

$$[t_S(P_0)]_{\sigma^+(\infty,P_0)} = [t_S(P,C)/a_{P,C}(P,C)]_{\sigma^+(\infty,P,C)/b_C(C)} \quad (\dot{\gamma} \text{ varies}) \tag{6.86}$$

$$[t_{SS}(P_0)]_{\sigma^+(\infty,P_0)} = [t_{SS}(P,C)/a_{P,C}(P,C)]_{\sigma^+(\infty,P,C)/b_C(C)} \quad (\dot{\gamma} \text{ varies}) \tag{6.87}$$

where $\sigma^+(\infty,P_0) = \sigma^+(\infty,P,C)/b_C(C)$, and the magnitude of the stress overshoot $\Delta\sigma_{ov}$ is affected only slightly by pressure or CO_2:

$$[\Delta\sigma_{ov}(P_0)]_{\sigma^+(\infty,P_0)} = [\Delta\sigma_{ov}(P,C)/b_C(C)]_{\sigma^+(\infty,P,C)/b_C(C)} \tag{6.88}$$

The creep test is preferable to study the effects of pressure and CO_2 on viscoelasticity at a constant stress, and creep data are presented in the next section.

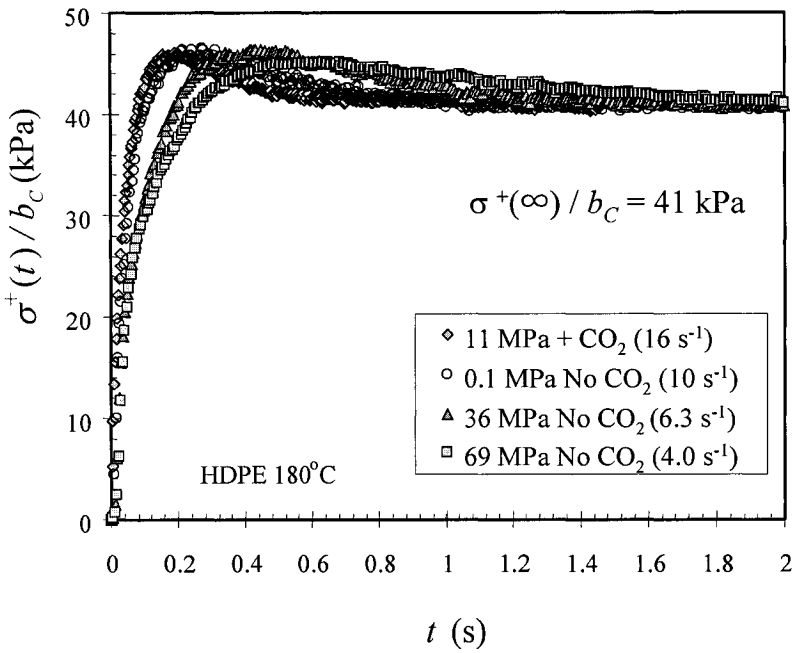

Figure 6.81. Stress growth functions that provide the same steady-state stress.

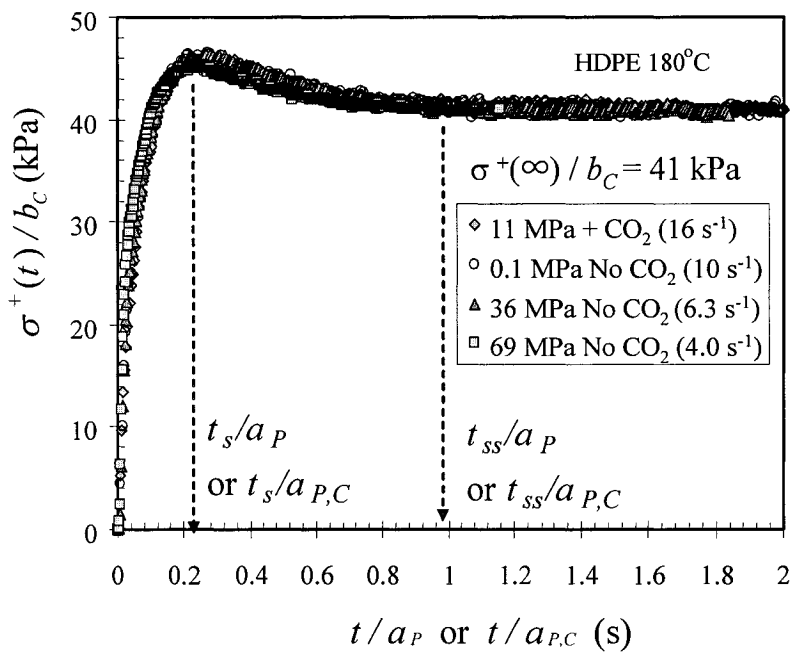

Figure 6.82. Shifted stress growth function.

6.7.10 Effects of Pressure and Concentration on Nonlinear Creep Compliance

6.7.10.1 Effect of Stress on Creep Compliance

The HPSPR system was used to make creep tests. First creep measurements were performed at several stresses at atmospheric pressure and at 180℃. Figure 6.83 shows the effect of stress on the creep compliance. The curves of 4 and 10 kPa were obtained by use of the HPSPR, and the curves with 3 and 20 Pa were obtained using the SR5000. The inset has expanded scales to show the short time behavior, which follows linear viscoelasticity. The compliance and steady-state shear rate should increase with stress, but the 3 Pa curve does not seems to exhibit this behavior. However, if the compliance is tracked to longer times, the expected behavior is observed. Thus the compliances at 3 and 20 Pa did not reach their steady states in 30s and were still curving. The data for 3 Pa cross over those for 20 Pa around 1700s (ellipse in Fig. 6.84) and eventually show the lowest slope as expected. The curves at 4 and 10 kPa are not shown, because the creep time was less than 1 min.

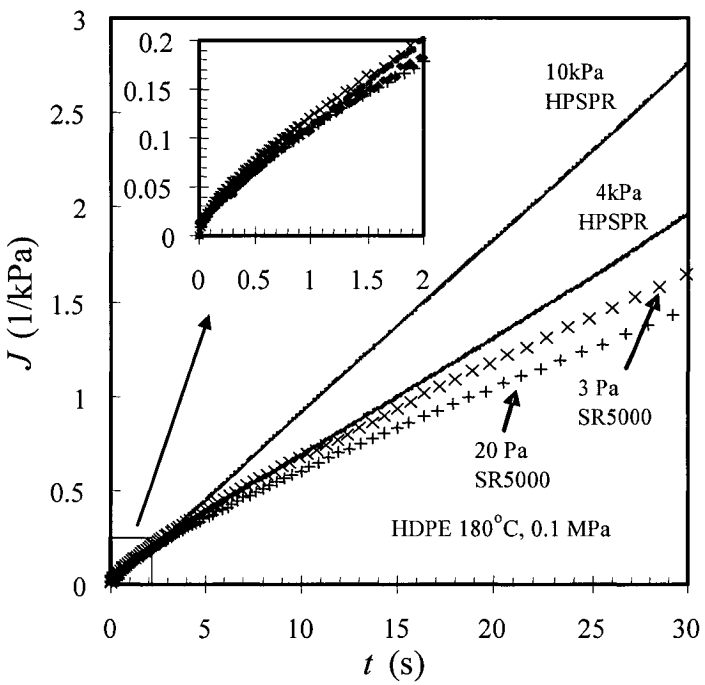

Figure 6.83. Effect of stress on $J(t)$ for a short time.

When the stress is above 10 kPa, the actuator system becomes unstable, and a reproducible compliance curve cannot not be obtained. This arises from the difficulty of using a feedback-loop based on the signal from the shear stress transducer.

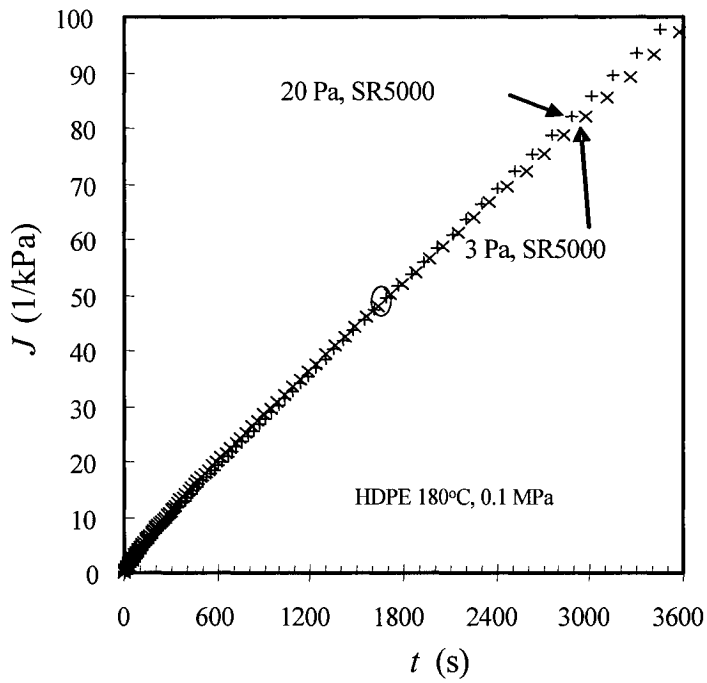

Figure 6.84. Effect of stress on $J(t)$ for a long time.

6.7.10.2 Effects of Pressure and CO_2 on Creep Compliance

Creep tests were carried out at 0.1 and 69 MPa without CO_2 and at 18 MPa with CO_2 at a stress of 4 kPa. Figure 6.85 shows that pressure delays the time response of the compliance, and CO_2 has the inverse effect. The viscosity and shear-rate were calculated from the slope of the compliance curve at steady-state, and the viscosity was found to match that from steady shear tests. Considering the difficulties of creep experiments, this agreement shows that the system can be used for creep tests with or without CO_2 at elevated pressure. Figure 6.86 shows the shifted creep compliance using pressure- and concentration-shift factors. The data at 18 MPa with CO_2 had to be shifted vertically using b_C, which pushes down the curve, and then shifted

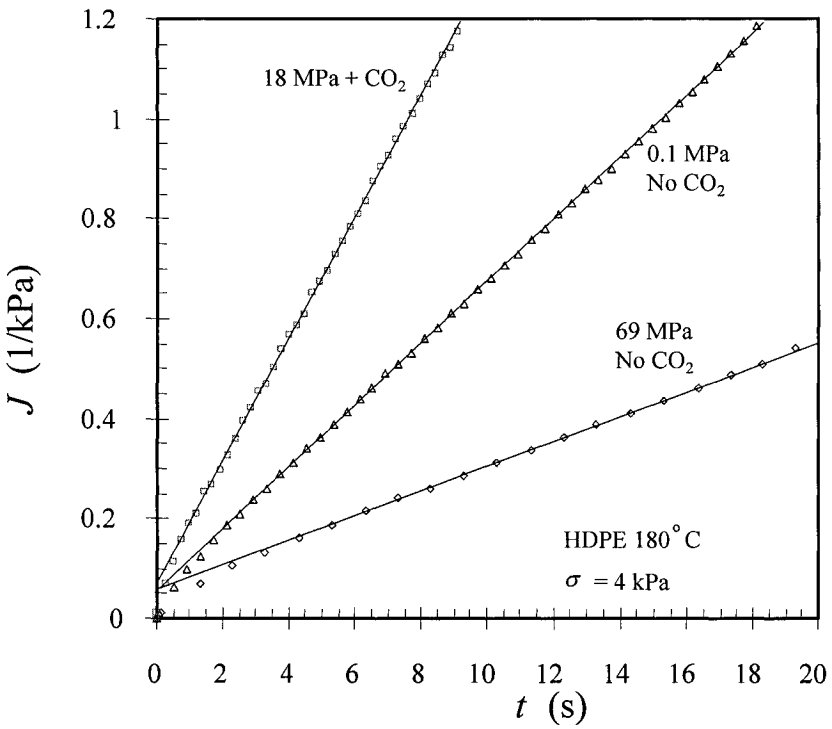

Figure 6.85. Creep compliances at different conditions with stress of 4 kPa and extension of linear portions of creep compliance.

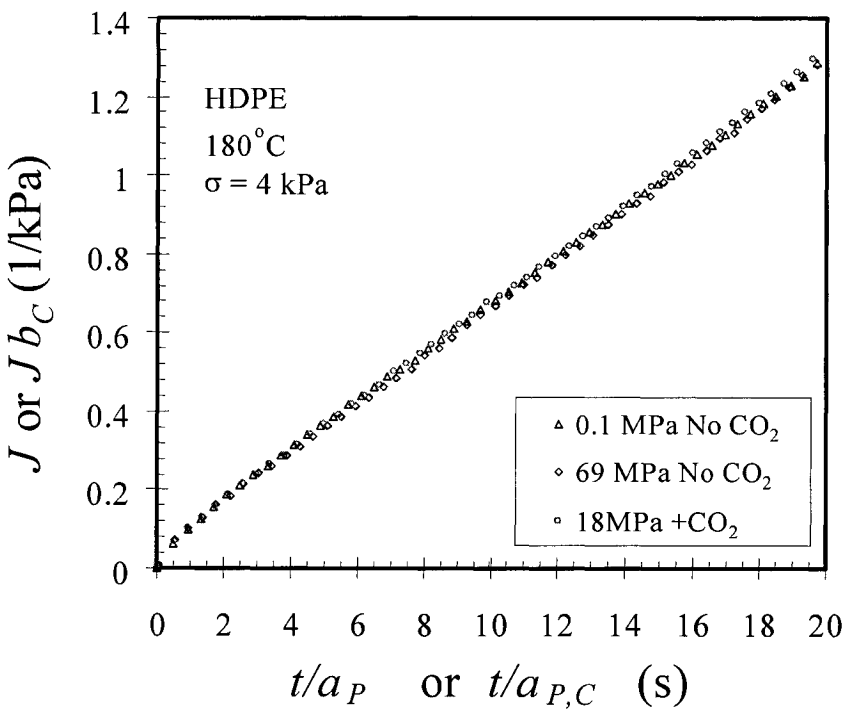

Figure 6.86. Shifted creep compliance.

horizontally by $a_{P,C}$, which pulls the curve to the right. There is a small discrepancy, but the shifted curve seems to be reasonable considering the difficulty of the creep tests. The shifted creep curve can be formulated as follows:

$$J(\sigma,P_0,t) = J[\sigma,P,C,t/a_{P,C}(P,C)]b_C(C) \tag{6.89}$$

If a protocol for tuning the control parameters can be established, it would be preferable to use creep tests at various pressures to determine the shift factors.

6.7.10.3 Effects of Pressure and CO_2 on Steady-State Compliance

To determine the effects of P and C on the steady-state compliance, the linear part of the compliance curve was extended to the y-axis, and the intercept was obtained (Fig. 6.85). Table 6.5 shows there is little effect of a pressure of 69 MPa, and a 20% increase at 18 MPa with CO_2. Because HDPE melt is not very elastic J_S is close to zero.

Table 6.5. Effects of pressure and concentration on the steady-state compliance.

	0.1 MPa, No CO_2	69 MPa, No CO_2	18 MPa with CO_2
J_S (10^{-2}/kPa)	6.0	5.9	7.3

It is clear that J_S is a very week function of P and depends only on C if the creep compliances at P and (P,C) are superposable using shift factors. The linear part of the creep curve at P_0 is described by Eq. 6.90 (The detailed procedure is given in Appendix 8.):

$$J(P_0) = \frac{1}{\eta(P_0)}t + J_S(P_0) \tag{6.90}$$

Those at P and (P,C) are given by Eqs. 6.91 and 6.92:

$$J(P) = \frac{1}{\eta(P_0)} \frac{t}{a_P(P)} + J_S(P_0)$$
$$= \frac{1}{\eta(P)} t + J_S(P) \tag{6.91}$$

$$J(P,C) b_C(C) = \frac{1}{\eta(P_0)} \frac{t}{a_{P,C}(P,C)} + J_S(P_0) \tag{6.92}$$

Equation 6.92 can be rewritten to give:

$$J(P,C) = \frac{1}{\eta(P_0)} \frac{t}{a_{P,C}(P,C) b_C(C)} + \frac{J_S(P_0)}{b_C(C)}$$
$$= \frac{1}{\eta(P,C)} t + J_S(P,C) \tag{6.93}$$

Based on Eqs. 6.91 and 6.93, the following relationships at the same stress can be derived:

$$\eta(P) = \eta(P_0) a_P(P) \tag{6.94}$$

$$\eta(P,C) = \eta(P_0) a_{P,C}(P,C) b_C(C) \tag{6.95}$$

$$J_S(P) = J_S(P_0) \tag{6.96}$$

$$J_S(P,C) = J_S(P_0)/b_C(C) \tag{6.97}$$

Equations 6.94 and 6.95 show the dependency of viscosity on P and C. Equations 6.96 and 6.97 reveal that the steady-state compliance J_S is a function of the vertical shift factor but is not that of pressure. For example, $b_C(18\text{MPa}) = 0.87$, and the predicted steady state compliance is $J_S(P,C) = 6 \times 10^{-2}/0.87 = 6.9 \times 10^{-2}\ (\text{kPa}^{-1})$. This value is close to the value in Table 6.5. This is similar to the effect temperature on J_S^0. The steady-state compliance of a highly entangled monodisperse polymer is inversely proportional to (ρT) [9]:

$$J_s^0 = \frac{0.4M_c'}{R\rho(T)T} \quad \text{for } M > M_c' \tag{4.50}$$

As was discussed in Chapter 5, $\rho(T)T$ changes little with T and has little effect on η, and J_S^0 should thus be a very weak function of temperature. If the vertical shift factors are not ignored, for a system with thermo- and piezo-rheological simplicity, J_S would shift as follows with T, P, and C:

$$J_S(T,P,C) = \frac{J_S(T_0,P_0)}{b_{T,P,C}(T,P,C)} \tag{6.98}$$

Based on Eq. 6.97 and $b_C < 1$, J_S will increase by swelling, which decreases the number of viscous and elastic elements in the unit volume [61]. This might seems to be imply contradictory considering that J_S shows elastic property. However, the prediction by the Maxwell model shows that dilution, *i.e.*, fewer elements in the unit volume, decreases the viscosity and increases the steady-state compliance. This was shown using the Maxwell model in Appendix 9.

6.7.11 Foaming Studies

To study the foamed structures in detail, experimental data at many conditions are required, because the structure is affected by the shape and distribution of gas bubbles, the concentration of gas, surface tension, and the nonlinear behavior of the polymer. To control the structure of a cell, not only ΔP but also $\Delta P/\Delta t$ should be controlled, but the present system controls only ΔP. However, the purpose of this section is to show the potential application of the HPSPR based on limited data.

6.7.11.1 Images of Foamed Structure

Figures 6.87 and 6.88 are images of the foamed structures of the HDPE and of a long-chain branched metallocene polyethylene (BmPE) with $M_w = 89\,\mathrm{kg/mol}$, $M_w/M_n = 2.3$, and $\mathrm{LCB}/10^3\mathrm{C} = 0.062$ ($\Delta P = 18\,\mathrm{MPa}$ and $-\Delta P/\Delta t = 1\,\mathrm{MPa/s}$). By use of a Nikon Eclipse E800 optical microscope, these images were taken through the raw surface without fracturing. Both have irregular shape and size distributions of gas bubbles. However, BmPE has smaller and more bubbles than HDPE, and this results from the LCB. For comparison, an elastomer was also foamed. A polybutadiene (PBD) with $M_w = 78\,\mathrm{kg/mol}$ and $M_w/M_n = 1.04$ supplied by Firestone was used. By use of a Jeol JSM 840 SEM, an image was made after fracturing the sample in liquid N_2 at -196℃ and coating it with gold/palladium. The foamed PBD sample did not flow at room temperature, and the structure did not change during taking SEM pictures. Figure 6.89 shows that the foamed PBD has more and regular cells than HDPE and BmPE. The fraction of void volume is also a larger than that of HDPE and BmPE to give low density and large cushion, which arises from the internal wrinkle structure on bores (Fig. 6.90). These aspects result from the elasticity of PBD.

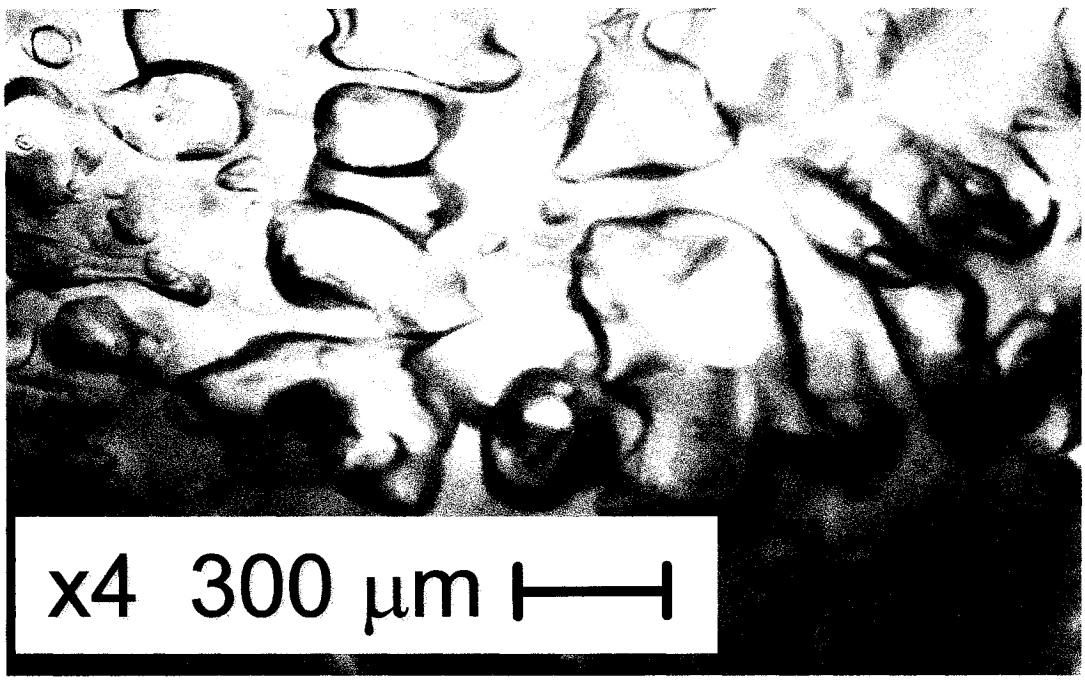

Figure 6.87. Foamed structure of HDPE by optical microscopy. Image through raw surface, $\Delta P = 18\mathrm{MPa}$; $-\Delta P/\Delta t = 1\mathrm{MPa/s}$.

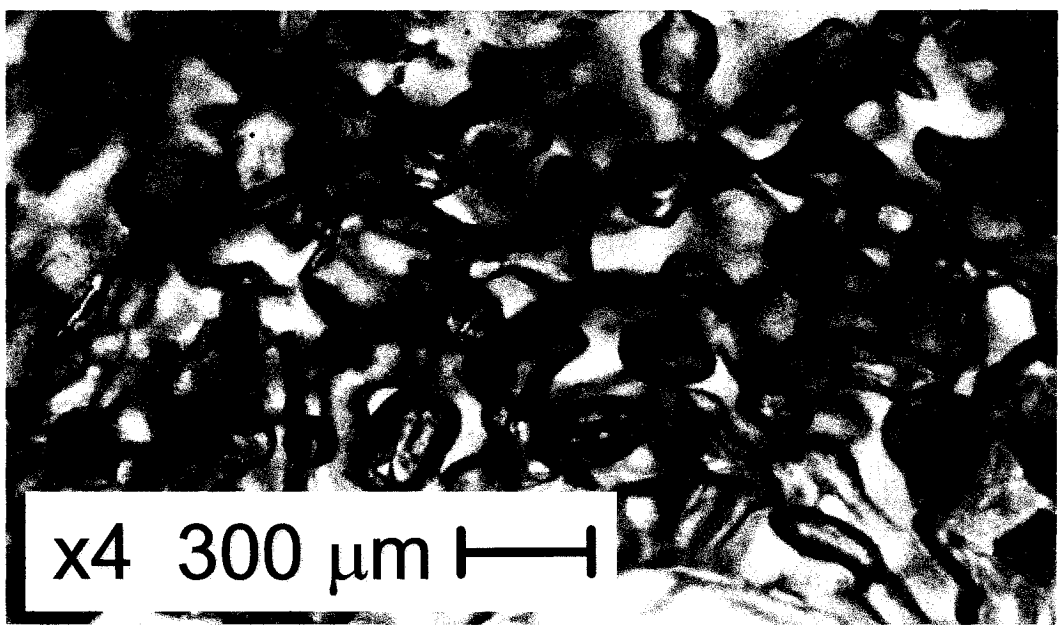

Figure 6.88. Foamed structure of BmPE by optical microscopy. Image through raw surface, $\Delta P = 18\mathrm{MPa}$; $-\Delta P/\Delta t = 1\mathrm{MPa/s}$.

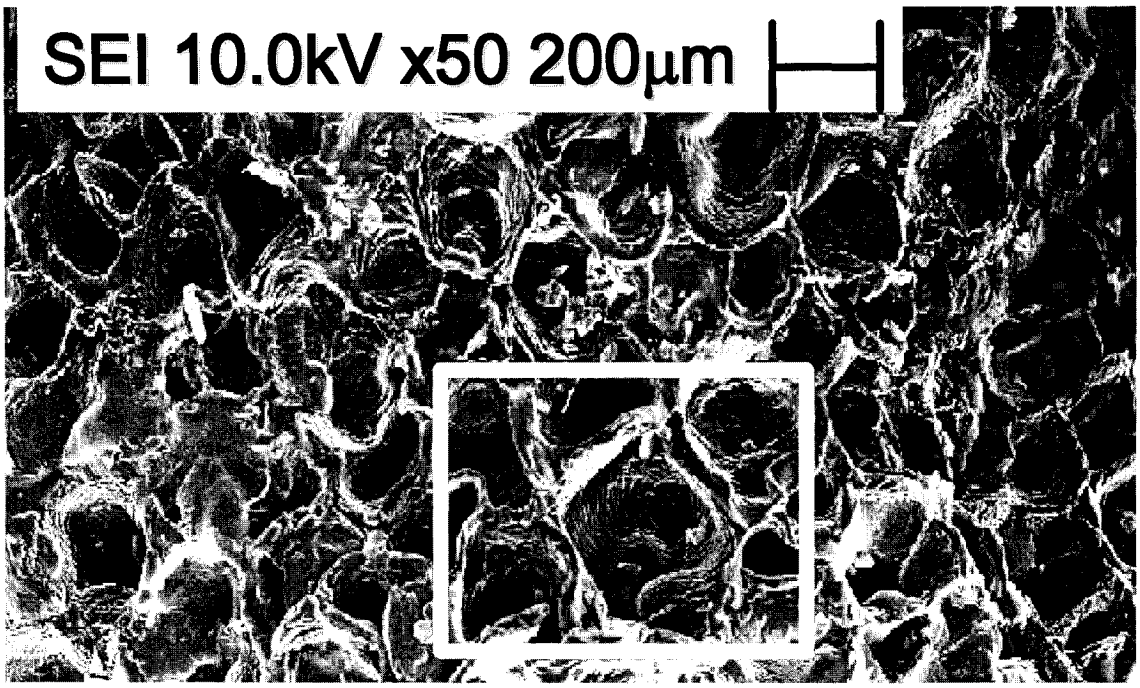

Figure 6.89. Foamed structure of PBD by SEM. Image on the fractured surface, $\Delta P = 18\mathrm{MPa}$; $-\Delta P/\Delta t = 1\mathrm{MPa/s}$.

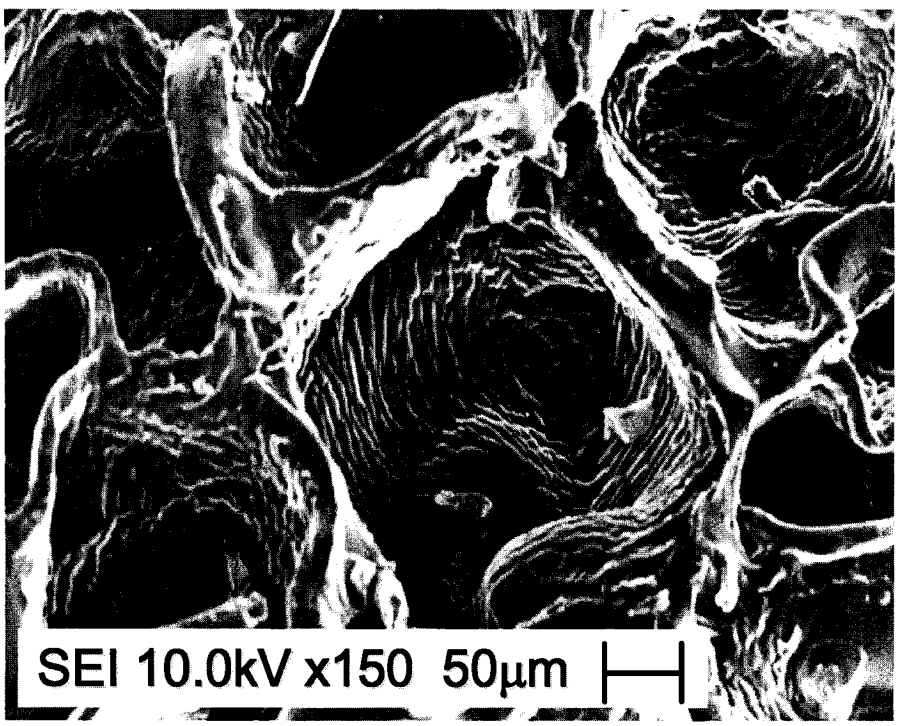

Figure 6.90. Extended foamed structure of PBD (rectangle in Fig 6.89) by SEM. Image on the fractured surface, $\Delta P = 18\mathrm{MPa}$; $-\Delta P/\Delta t = 1\mathrm{MPa/s}$.

6.7.11.2 Effect of Foamed Structure on Viscosity

After saturating a new sample with CO_2 without shearing at 18 MPa, the pressure was suddenly released ($\Delta P = 18$ MPa and $-\Delta P/\Delta t = 1$ MPa/s) to foam the sample, and the sample was then sheared at 0.4, 1.6, and 6.3 s^{-1}. Figure 6.91 shows that a steady-state stress was not obtained at 6.3 s^{-1} due to flow instability, which may arise from the foamed structure with the strain history imposed by the two previous shear deformations or at the high shear rate. The bubble structure may collapse due to rupture.

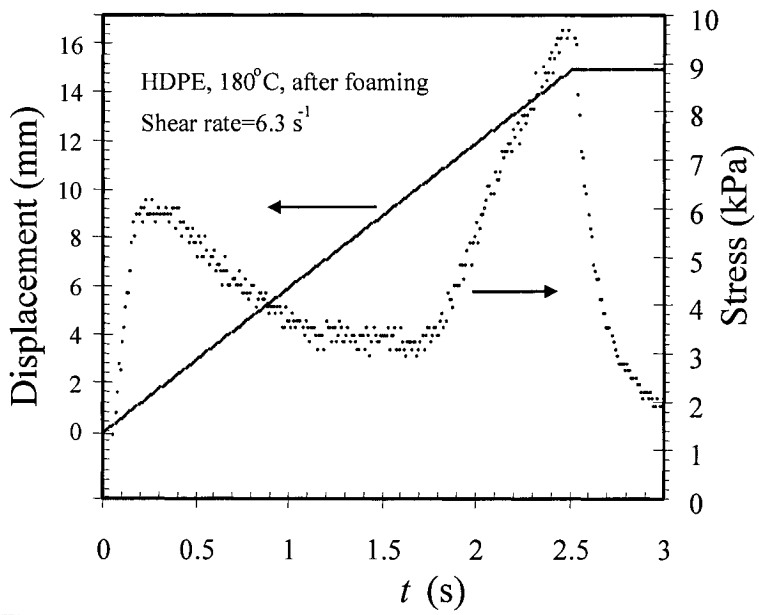

Figure 6.91. Flow instability due to foamed structure, strain history, and high shear rate.

Figure 6.92 shows the effect of foaming on the viscosity. The triangles are atmospheric data, and diamonds are data at a pressure of 18 MPa with CO_2. To obtain pressure-independent curve with CO_2, $a_P(18\,\mathrm{MPa})$ was used to shift the curve at 18 MPa with CO_2, and the squares are the shifted data, which are pressure independent. Circles show the viscosity with gas bubbles in the sample. The latter two samples are assumed to contain the same amount of CO_2, which is the solubility ($0.15\,gCO_2/gHDPE$), and the points show the viscosity at 1 atm. Dissolved CO_2 (■)

reduced the pure polymer viscosity at 1 atm (▲) by half, and CO_2 bubbles (●) reduced the viscosity of sample with dissolved gas (■) by half again. To model the effect of the foamed structure on the viscosity, more data are required, and a new sample must be used for each shear rate to obtain strain-history-independent data.

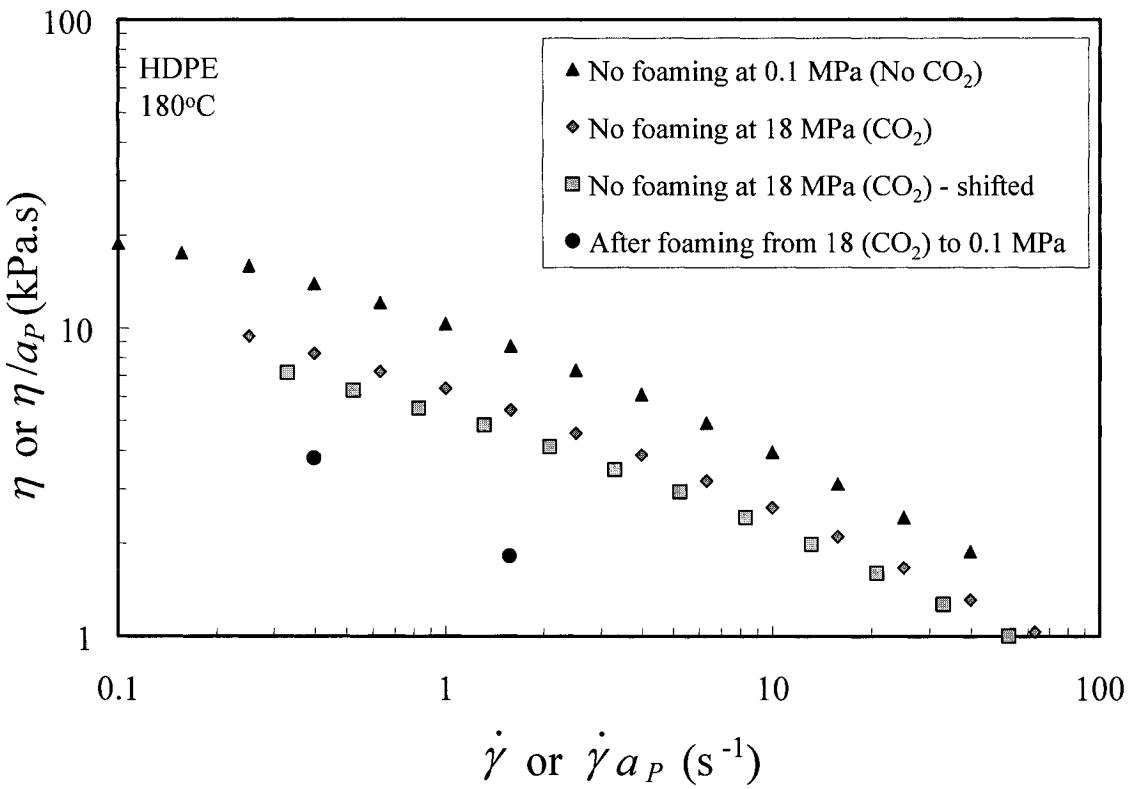

Figure 6.92. Effects of dissolved CO_2 and foam on viscosity.

6.8 Conclusions

The zero-shear viscosity was determined by the Cross model fitting using viscosity data obtained from creep tests and steady simple shear tests. A new system was developed to study the effects of pressure and CO_2 on the rheological properties of molten polymers. This system was evaluated using several types of measurement. The reproducibility was found to be excellent. Saturation with CO_2 was confirmed experimentally, and the saturation time agreed with that predicted

using Fick's diffusion equation. The effects of pressure and CO_2 on the viscosity were measured, and shift factors were determined. Pressure slows viscoelastic responses at the same steady stress, while CO_2 accelerates these. However, those depend on pressure little at the same shear rate. A vertical shift factor for concentration was found to be necessary to build a master curve. The shift factors obtained were found to be valid for other rheological properties, such as the stress growth function and creep compliance. The steady-state compliance was found to be independent of pressure but dependent of the concentration of CO_2. To establish the effect of CO_2 at constant pressure, shift factors for pressure and CO_2 concentration were assumed to be separable. The Fujita-Kishimoto free volume model was found to describe the CO_2 concentration shift factor. The temperature shift factors obtained by shear-rate sweep and SAOS tests were compared and found to be practically identical. Nitrogen shows much less effect on the viscosity than CO_2 and a different effect relative to pressure. The HPSPR can make polymeric foams, and the image of the structure can be obtained using an optical microscope and SEM. The viscosity of a sample with CO_2 bubbles is about half that of a sample saturated with the same amount of CO_2.

6.9 References

1. C.D. Han, *Multiphase flow in polymer processing*, Academic Press, New York, 1981.
2. M.M. Cross, "Deformation and Flow," in *Polymer Systems: Deformation and Flow: Proceedings of the* 1966 *Annual Conference of the British Society of Rheology*, Edited by R.E Wetton and R.W. Whorlow, Macmillan, London, 1968.
3. P.J. Carreau, "Rheological equations from molecular network theories," Doctoral Thesis, University of Wisconsin, Wisconsin, 1969.
4. K.Y. Yasuda, R.C. Armstrong, and R.E. Cohen, "Shear flow properties of concentrated solutions of linear and star branched polystyrenes," *Rheol. Acta* 20:163 (1981).
5. H.E. Park, "Effect of pressure on the rheological properties of three polyethylenes," Master's Thesis, McGill University, Montreal, 2001.
6. E.B. Bagley, "End correction in the capillary flow of polyethylene," *J. Applied Physics* 28:624 (1957).
7. B. Rabinowitch, "Über die viskosität und elastizität von solen (Over the viscosity and elasticity from brine)," *Zeitschrift für Physikalische Chemie* 145:1 (1929).
8. C.D. Han, *Rheology in polymer processing*, Academic Press, New York, 1976.
9. J.M. Dealy and K.F. Wissbrun, *Melt Rheology and Its Role in Plastics Processing*, Chapman and Hall, London, 1995.
10. R.F. Westover, "The significance of slip in polymer melt flow," *Polymer Engineering and Science* 83 (1966).
11. M.R. Kamal and H. Nyun, "The effect of pressure on the shear viscosity of polymer melts," *Transactions of the Society of Rheology*, 17:271 (1973).
12. M.R. Kamal and H. Nyun, "Capillary viscometry: A complete analysis including pressure and viscous heating effects," *Polymer Engineering and Science*, 20:109 (1980).
13. V.-H. Karl, "Über die druckabhängigkeit der viskoelastischen und physikalisch-chemischen eigenschaften von polymeren, 8 (Over the pressure dependence of the viscoelastic and physicochemical characteristics of polymer, 8)," *Die Angewandte Makromolekulare Chemie* 79:11 (1979).
14. P.D. Driscoll and D.C. Bogue, "Pressure effects in polymer melt rheology," *J. Applied Polym. Sci.* 329:1755 (1990).
15. F.S. Baker and M. Thomas, "The effect of hydrostatic pressure on the flow properties of various polymers," *Makromol. Chem., Macromol. Symp.* 68:13 (1993).
16. M.R. Mackley, R.T.J. Marshall, and J.B.A.F. Smeulders, "The multipass

rheometer," *J. Rheology* 39:1293 (1995).

17. S. Chakravorty, M. Rides, C.R.G. Allen, and C.S. Brown, "Polymer melt viscosity increases under pressure: simple new measurement method," *Plast., Rubber Compos. Pcocess. Appl.* 25:260 (1996).
18. D.M. Binding, M.A. Couch, and K. Walters, "The pressure dependence of the shear and elongational properties of polymer melts," *J. Non-Newt. Fluid Mech.* 79:137 (1998).
19. K. Walters, *Rheometry*, Chapman and Hall, London, 1975.
20. H.M. Laun, "Polymer melt rheology with a slit die," *Rhologica Acta*, 22:171 (1983).
21. S.E. Kadijk and Van den Brule, "On the pressure dependency of the viscosity of molten polymers," *Polym. Engineering and Science* 30:1535 (1994).
22. H.C. Langelaan, A.D. Gotsis, and A.P. de Boer, "On the linearity of the pressure drop during flow of thermotropic LCPs in slits and capillaries," *J. Rheology* 38:1353 (1994).
23. M. Mooney, "A shearing disk plastometer for unvulcanized rubber," *Industrial and Engineering Chemistry,* 6:147 (1934).
24. V. Semjonow, "Rotational viscometer for the measurement of the pressure dependence of the viscosity of high-polymer melts," *Rheologica Acta* 2:138 (1962).
25. F.N. Cogswell, "Influence of pressure on the viscosity of polymer melts," *Plastics and Polymers* Feb:39 (1973).
26. S. Bair, W. O. Winer, and F. Qureshi, "Lubricant rheological properties at high pressure," *Lubrication Science* 5:189 (1993).
27. S. Bair, M. Khonsari, and W.O. Winer, "High-pressure rheology of lubricants and limitations of the Reynolds equation," *Tribology International* 31:573 (1998).
28. P.M. Khandare, J.W. Zondlo, P.B. Stansberry, and A.H. Stiller, "Rheological investigation of pitch materials Part I: Design and development of a high-temperature high-pressure (HTHP) rheometer," *Carbon* 38:881 (2000).
29. D.J. Highgate and R.W. Whorlow, "End effects and particle migration effects in concentric cylinder rheometry," *Rheologica Acta* 8:142 (1969).
30. R.G. Foltz, K.K. Wang, and J.F. Stevenson, "An experiment to measure the pressure dependence of the zero-shear-rate viscosity," *J. Non-Newt. Fluid Mech.* 3:347 (1978).
31. R. Sobczak, "Viscosity measurement by spheres falling in a magnetic field," *Rheologica Acta* 25:175 (1986).
32. M. Gahleitner and R. Sobczak, "A new apparatus for measuring high viscosities," *J. Physics E: Scientific Instruments* 21:1074 (1988).
33. W. Hermann and R. Sobczak, "A new inductive detection for the magnetoviscometer," *J. Applied Polymer Science* 37:2675 (1989).

34. J.-P. Mattischek and R. Sobczak, "A new cell for measurement of viscosity under high pressure," *Meas. Sci. Technol.* 5:782 (1994).

35. J.-P. Mattischek and R. Sobczak, "High-pressure cell for measuring the zero-shear viscosity of polymer melts," *Rev. Sci. instrum.* 68:2101 (1997).

36. A.J. Giacomin, "A sliding plate melt rheometer incorporating a shear stress transducer," Doctoral Thesis, McGill University, Montreal, 1987.

37. A.J. Giacomin, T. Samurkas, and J.M. Dealy, "A novel sliding plate rheometer for molten plastics," *Polym. Eng. Sci.* 29:499 (1989).

38. F. Koran, "Thee effect of pressure on the rheology and wall slip of polymer melts," Doctoral Thesis, McGill University, Montreal, 1998.

39. F. Koran and J.M. Dealy, "A high pressure sliding plate rheometer for polymer melts," *J. Rheology*, 43:1279 (1999).

40. J.M. Dealy and A.J. Giacomin, "Sliding Plate and Sliding Cylinder Rheometers," Chapter 8 in *Rhelogical Measurement* 2nd Ed., Edited by A.A. Collyer and D.W. Clegg, Chapman & Hall, London, 1998.

41. J.M. Dealy, *Rheometers for molten plastics*, Van Nostrand Reinhold, New York, 1982.

42. J.M. Dealy, "Method of measuring shear stress," U.S. Patent No. 4,464,928 (1984).

43. J.M. Dealy and R.S. Jeyaseelan, "Frequency response of a shear stress transducer installed in a sliding plate rheometer," *J. Rheology* 42:833 (1998).

44. J.M. Dealy, K.R. Bubic, and S.R. Doshi, "Method and apparatus for measuring shear stress," US Patent No. 5,094,100 (1992).

45. J.A. Brydson, *Plastics Materials*, 7th Ed., Butterworth Heinemann, Oxford. 1999.

46. S.P. Sawan, Y-T. Shieh, J.-H. Su, G. Manivannan, and W.D. Spall, "Evaluation of supercritical fluid interactions with polymeric materials," Chap. 6 in *Superciritical Fluid Cleaning - Fundamentals, Technology, and Applications*, Edited by J. McHardy and S.P. Sawan, Noyes Publications, Westwood, 1997.

47. A. Fick, "Ueber diffusion," *Ann. Physik* 94:59 (1855).

48. H.S. Carslaw and J.C. Jaeger, *Conduction of Heat in Solids*, 2nd ed., Clarendon press, Oxford, 1959.

49. J. Crank and G.S. Park, *Diffusion in Polymers*, Academic Press, London, 1968.

50. J. Crank, *The Mathematics of Diffusion*, Second Edition, Clarendon Press, Oxford, 1975.

51. A.L. Hines and R.N. Maddox, *Mass Transfer Fundamentals and Applications*, Prentice Hall, Englewood Cliffs, 1985.

52. Y. Sato, K. Fujiwara, T. Takikawa, Sumarno, S. Takishima, and H. Masuoka, "Solubilities and diffusion coefficients of carbon dioxide and nitrogen in polypropylene, high-density polyethylene, and polystyrene under high pressures and temperatures," *Fluid Phase Equilibria* 162:261-276 (1999).

53. Y. Sato, T. Takikawa, S. Takishima, and H. Masuoka, "Solubilities and diffusion coefficients of carbon dioxide in poly(vinyl acetate) and polystyrene," *J. of Supercritl Fluids* 19:187 (2001).

54. W.P. Cox and E.H. Merz, "Correlation of dynamic and steady flow viscosities," *J. Poly. Sci.* 28:619 (1958).

55. S. Kim, "A criterion for gross melt fracture of polyolefins and its relationship with molecular structure," Doctoral Thesis, McGill University, Montreal, 2000.

56. F. Smillo, "Wall slip and spurt of molten polymer," Master's Thesis, McGill University, Montreal, 2004.

57. J. Xu, "Nonlinear viscoelasticity and wall slip of molten polymers," Master's Thesis, McGill University, Montreal, 2005.

58. P. Schümmer and R.H. Worthoff, "An elementary method for the evaluation of a flow curve," *Chem. Eng. Sci.* 33:759 (1978).

59. F.N. Cogswell, *Polymer Melt Rheology*, Woodhead Pub., Cambridge, 1996.

60. H. Fujita and A. Kishimoto, "Diffusion-controlled stress relaxation in polymers. II. Stress relaxation in swollen polymers," *J. Polym. Sci.* 28, 547 (1958).

61. J.D. Ferry, "Mechanical properties of substances of high molecular weight. VI. Dispersion in concentrated polymer solutions and its dependence on temperature and concentration," *J. of the Am. Chem. Soc.* 72:3746 (1950).

7. Effect of Molecular Structure on Temperature and Pressure Sensitivity of Viscosity

7.1 Introduction

In recent decades, much has been learned about the effect of molecular structure on rheological properties. A major subject of interest is the effect of long-chain branching (LCB), which is very strong, whereas short-chain branching (SCB) has been known to have little effect. Münstedt *et al.* [1] reported that LCB in polystyrene (PS) has little effect on temperature sensitivity, while LCB in PE has a large effect. Thus, in addition to LCB, a large side group such as a benzene ring can also enhance temperature sensitivity. To observe the effects of LCB, SCB, and a benzene side group, several polymers were chosen for this project. The major features of interest were the pressure and temperature sensitivities of the viscosity. These effects are described by shift factors, $a_P(P)$ and $a_T(T)$ as function of P or T; the higher the slope of the function, the stronger the dependency of the viscosity on P or T.

7.2 Materials

Four PEs, one PP, and two PSs were chosen for this study. The HDPE is thought to be purely linear with no side group. A linear, low-density PE (LLDPE), a linear metallocene PE (LmPE), and a slightly long-chain branched metallocene PE (BmPE) also have short-chain branching. A PP has methyl side groups on every second back-bone carbon and is also treated here as a short-chain branched linear PE. A linear PS (LPS) and a star PS (BPS) were also studied. The basic properties of the LLDPE, LmPE, and BmPE were reported by Kim [2], and those of LPS and BPS have been reported by Ferri and Lomellini [3]. The properties of all these materials are shown in Table 7.1.

Table 7.1. Physical properties of the materials studied, 1 atm.

Code	Code in the original literature	Manufacturer	T_m (℃)	T_g (℃)	M_w (kg/㏖)	M_w/M_n	Comonomer	LCB/10^3C
HDPE	HDPE	Japan Polyolefins	133		111	13.6		0
LLDPE	LLDPE	Dow Chem.	126		120	3.8	Octene	0
LmPE	L-mPE-3	Exxon	105		109	2.3	Butene	0
BmPE	B-mPE-3	Dow Chem.	104		89	2.3	Octene	0.062
PP	PP	Dow Chem.	163		367	4.7		0
LPS	X1			100	185	1.7		0
BPS	X5			101	868	3.6		0.33

7.3 Experiments

For the effect of pressure, viscosity data $\eta(\dot{\gamma},P)$ were acquired by use of the HPSPR as described in the previous chapter. Data for HDPE, PP, LPS, and BPS were determined in this study, and data for LLDPE, LmPE, and BmPE were obtained in an earlier study by Park [4]. The effect of temperature on $|\eta^*(\omega,T)|$ was determined using SAOS tests at 1 atm. Data for HDPE, PP, LPS, and BPS were obtained in this work. Experiments on LLDPE, LmPE, and BmPE were carried out by Kim [2]. After shear-rate or frequency sweep tests were done, the data were fitted to the Cross or Yasuda models, and the stress data were shifted to the reference curve for the reference temperature and pressure to determine the pressure and temperature shift factors. The dependency of $a_P(P)$ on P and of $a_T(T)$ on T were determined by use of the Barus, Arrhenius, and WLF equations. The operating conditions and models used are summarized in Table 7.2. It was assumed that the shift factors for temperature and pressure are independent, and this yielded excellent superpositions.

Table 7.2. Molecular structures, models, and test conditions.

ID	Code	Side group	Model and Test Conditions [data source] (data from this study if not specified.)					
			Effect of P (P_0=0.1MPa)			Effect of T (T_0=highest test T)		
			$\eta(\dot{\gamma}, P)$	$a_P(P)$	P(MPa), T(℃)	$\lvert\eta^*(\omega, T)\rvert$	$a_T(T)$	1 atm, T(℃)
1	HDPE	None	Cross	Barus	0.1-69, 180	Yasuda	Arrhenius	160-210
2	LLDPE	A few hexyl group	" [4]	"	0.1-69, 170	Cross [2]	"	150-200
3	LmPE	A few ethyl group	" [4]	"	0.1-69, 170	Cross [2]	"	130-170
4	BmPE	A few hexyl group & very few LCB	" [4]	"	0.1-69, 170	Yasuda [2]	"	130-170
5	PP	Many methyl group	"	"	0.1-34, 180	Yasuda	"	170-220
6	LPS	Many Benzene rings	"	"	0.1-69, 200	Cross	WLF	170-230
7	BPS	Many Benzene rings & a few LCB	"	"	0.1-69, 200	Yasuda	WLF	170-230

7.4 Results and Discussion

7.4.1 Temperature Sensitivity

The temperature dependence of the viscosity for LPS and BPS could be described by the WLF equation, which is shown as Eq. 7.1:

$$\ln\left[a_{1,T}(T)\right] = \frac{-(1/f_{T_0})(T-T_0)}{f_{T_0}/\alpha_0 + (T-T_0)} \tag{7.1}$$

where f_{T_0} is the fractional free volume at T_0, and α_0 is the isobaric thermal expansion coefficient of the free volume. For the PE and PP the Arrhenius equation was found to be suitable:

$$\ln[a_T(T)] = \frac{E_a}{R}\left(\frac{1}{T} - \frac{1}{T_0}\right) \tag{7.2}$$

Wood-Adams and Costeux [6] reported that BmPE exhibits thermorheological complexity, and an average value over the frequency range was chosen for the shift factor. Since the molecular weight has a small effect on $a_T(T)$, even though all the polymers have different molecular weights, the effect of molecular weight is not discussed here.

As a reference material, HDPE (ID 1) was chosen. Figure 7.1 presents $a_T(T)$ for the PEs and PP. The slope of the line is the activation energy, E_a in kJ/mol, which is a measure of the temperature sensitivity of the viscosity. The random SCB in the LLDPE increased E_a only slightly (ID 2), while the regular SCB in PP increased E_a much more (ID 1 and 5), so that not only the existence of SCB but also the amount of SCB affects the temperature sensitivity. Very little LCB together with a little SCB (the BmPE has both LCB and SCB.) increased E_a very much (ID 4). From the above observations, we conclude that any branching increases the temperature sensitivity, and that even a small amount of LCB has a strong effect for PE.

Figure. 7.2 shows the temperature shift factors for all the polymers and reveals that E_a is a function of T for the PSs, while those of the PEs and the PP are independent of T. This difference results from the different flow physics, which can be described in terms of the free volume theory and/or the absolute rate theory. The two PSs show identical shift factors and have values of E_a that are higher than the other polymers, and this implies that the bulky benzene side group strongly increases the temperature sensitivity of $a_T(T)$. However, no increase of E_a for PS due to a little LCB (ID 7) can be seen. It can thus be inferred that the regular large side groups has more effect on E_a than LCB.

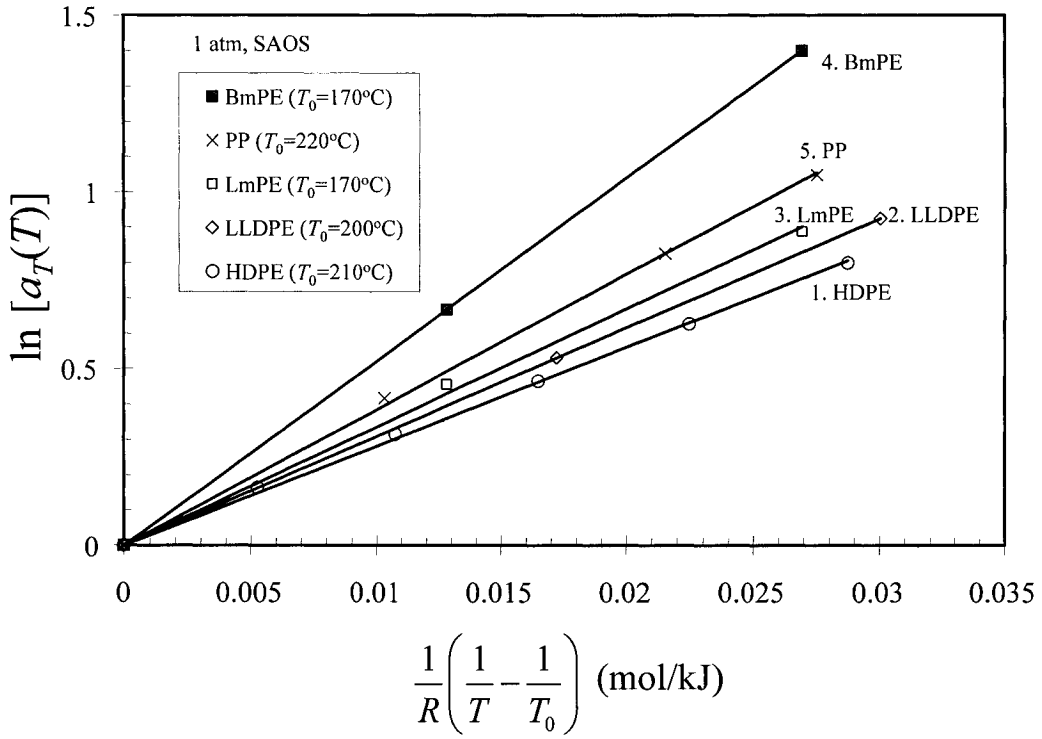

Figure 7.1. Temperature shift factors for PEs and PP.

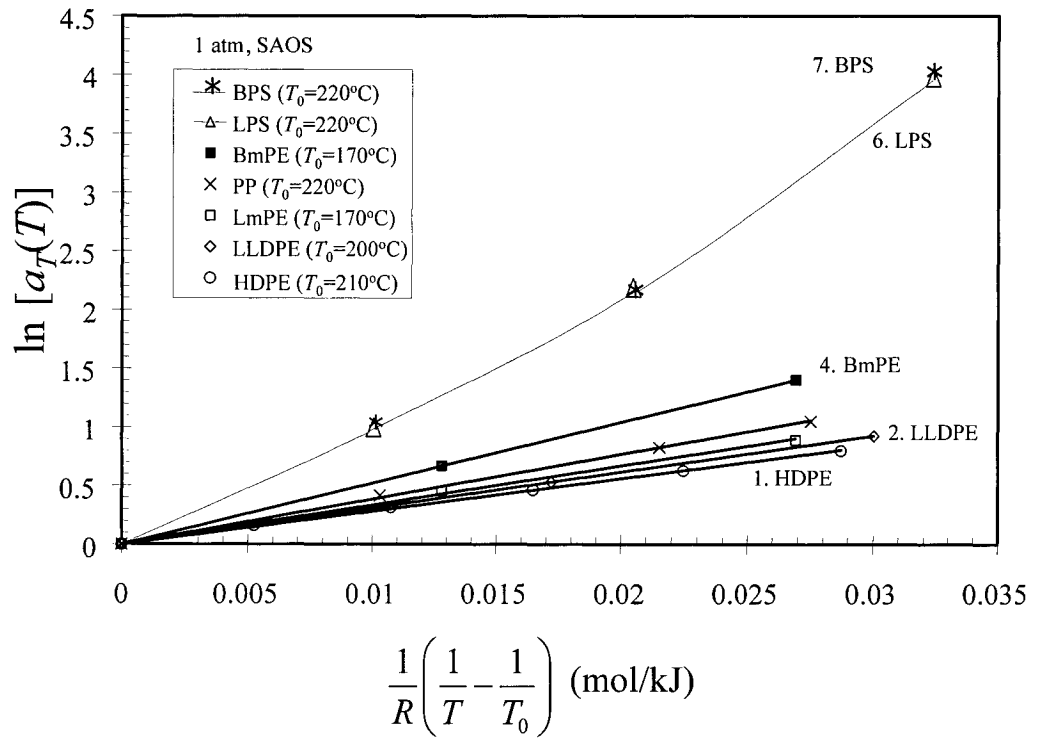

Figure 7.2. Temperature shift factors for all polymers.

7.4.2 Pressure Sensitivity

The pressure dependence of the viscosity of all polymers, including the polystyrenes, could be described by the Barus equation:

$$\ln[a_P(P)] = \beta(P - P_0) \tag{7.3}$$

and this implies that a_T and a_P of PS have different dependencies on T and P within the experimental window. The parameter β (GPa^{-1}) of Eq. 7.3 represents the pressure sensitivity, and results are shown in Figs. 7.3 and 7.4. The trends are similar to those for temperature sensitivity. Short-chain branching increases β (ID 2), and the more SCB the polymer has the more β increases (ID 5). Long-chain branching at a very low level has a large effect (ID 4).

Pressure sensitivity differed from temperature sensitivity in two more ways. One is that β for PP is higher than that of BmPE, and this means that a high level of SCB has stronger effect on the pressure sensitivity than a very low level of LCB, while the temperature sensitivity shows the opposite result. These differences are further analyzed by considering the relative influence of pressure and temperature in the next section. The other is that the relative influence of regular SCB and little LCB differs on temperature and pressure sensitivities.

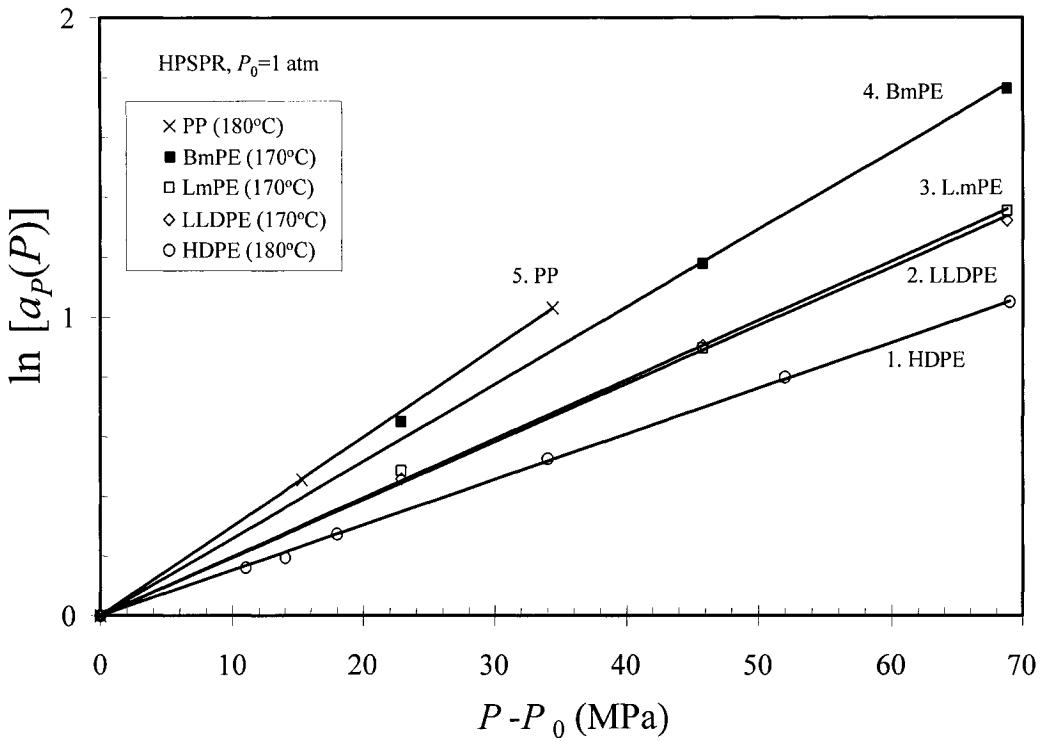

Figure 7.3. Pressure shift factors for PEs and PP.

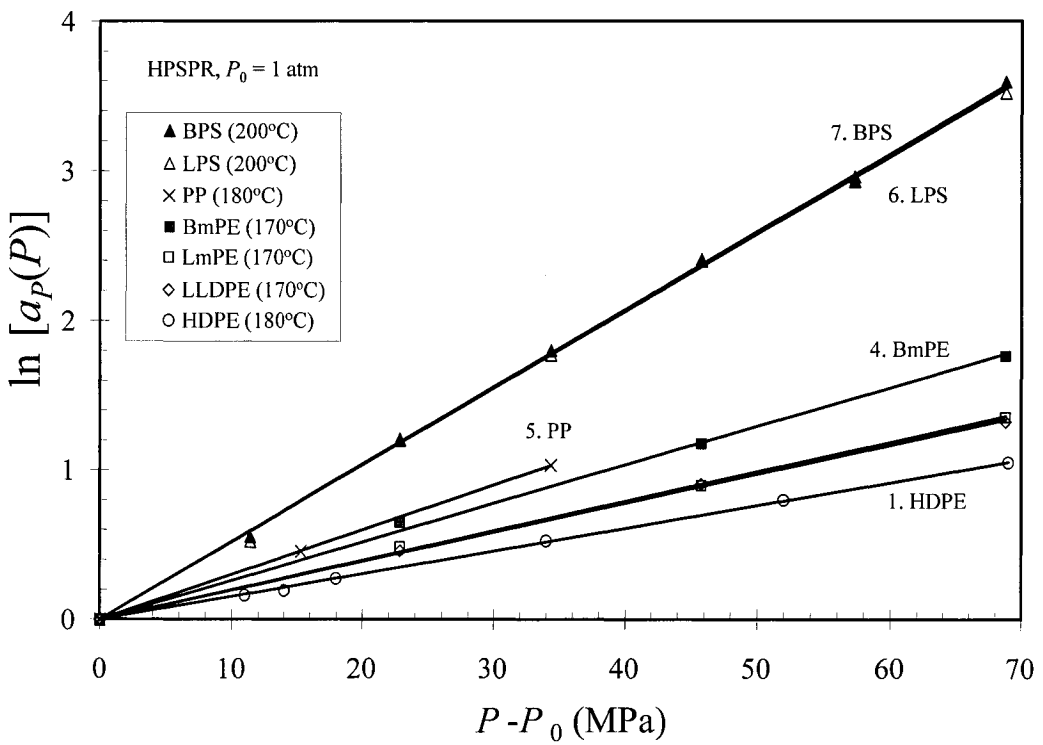

Figure 7.4. Pressure shift factors for all polymers.

7.4.3 Relative Influence of Temperature and Pressure

The relative influences of temperature and pressure are described using the exponential Barus and Arrhenius equations except BPS and LPS. Equation 7.4 is based on those two relationships (Section 6.7.6):

$$\left(\frac{\partial T}{\partial P}\right)_{\eta_0} = \frac{R\beta}{E_a} T^2 \text{ (K/MPa)} \tag{7.4}$$

For BPS and LPS the Barus and WLF equations are used, and assuming that the effects of T and P are separable, the zero-shear viscosity can be modeled assuming the effects of temperature and pressure are separable as:

$$\eta_0(T,P) = \eta_0(T_0,P_0)\exp\left[a+\frac{b}{c+(T-T_0)}\right]\exp[\beta(P-P_0)] \tag{7.5}$$

where $b = 1/\alpha_0$, and $c = f_{T_0}/\alpha_0$. Taking derivative of both sides leads to the following expressions:

$$\left[\frac{\partial \eta_0(T,P)}{\partial P}\right]_T = \eta_0(T_0,P_0)\beta\exp\left[a+\frac{b}{c+(T-T_0)}\right]\exp[\beta(P-P_0)] \tag{7.6}$$

$$\left[\frac{\partial \eta_0(T,P)}{\partial T}\right]_P = -\eta_0(T_0,P_0)\frac{b}{[c+(T-T_0)]^2}\exp\left[a+\frac{b}{c+(T-T_0)}\right]\exp[\beta(P-P_0)] \tag{7.7}$$

Now we seek the change in temperature that results in the same change in the viscosity as a given change in pressure:

$$d\eta_0 = \left(\frac{\partial \eta_0}{\partial T}\right)_P dT + \left(\frac{\partial \eta_0}{\partial P}\right)_T dP = 0 \tag{7.8}$$

or

$$\left(\frac{\partial T}{\partial P}\right)_{\eta_0} = -\left(\frac{\partial \eta_0}{\partial P}\right)_T \Big/ \left(\frac{\partial \eta_0}{\partial T}\right)_P \tag{7.9}$$

The final equation for BPS and LPS is obtained by combining Eqs. 7.6 through 7.9:

$$\left(\frac{\partial T}{\partial P}\right)_{\eta_0} = \frac{\beta}{b}(c + T - T_0)^2 \text{ (K/MPa)} \tag{7.10}$$

Both Eqs. 7.4 and 7.10 are functions of temperature, so that the equivalence ratio is a function of temperature. Figure 7.5 shows $(\partial T/\partial P)_{\eta_0}$ for all the polymers.

In the previous section, it was seen that PP had the highest pressure sensitivity except for the PSs but did not have the highest temperature sensitivity. This can be explained in terms of $(\partial T/\partial P)_{\eta_0}$. The larger this quantity, the greater the relative sensitivity to pressure at a given T. The highest $(\partial T/\partial P)_{\eta_0}$ is found for the case of PP, and this implies that the high degree of SCB causes the pressure to have a stronger effect on viscosity than temperature. The difference in β between PP and HDPE is larger than that between BmPE and LmPE, while the opposite trend is found for E_a *i.e.*, for temperature. This implies that the relative influence of regular SCB and little LCB differs on temperature and pressure sensitivities.

Figure 7.5 proves that $(\partial T/\partial P)_{\eta_0}$ is also structure dependent. Values for each polymer at 170℃ (ellipse in Fig. 7.5), which was the common test temperature. are shown in Table 7.3, and we see that the relative effect of P and T is a complex phenomenon.

While the two PSs have the smallest $(\partial T/\partial P)_{\eta_0}$ value, 0.5, the other polymers have values around 1 at 170℃. This shows that the relative influence of pressure for PS is smaller than that for the other polymers. Short-chain increases $(\partial T/\partial P)_{\eta_0}$ while long-chain branching decreases that. The effects of structure on $(\partial T/\partial P)_{\eta_0}$ are summarized in Table 7.4.

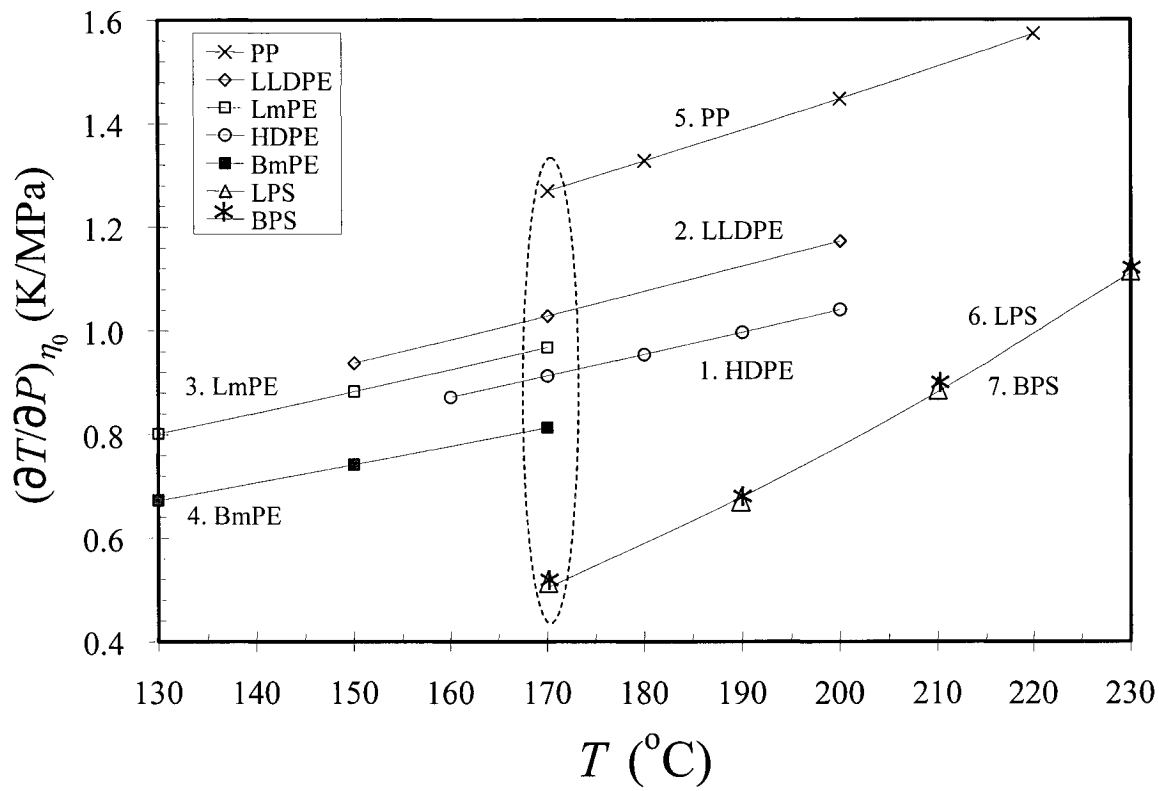

Figure 7.5 Relative influence of temperature and pressure as a function of T.

Table 7.3. Parameters of models and relative influence of T and P at 170℃.

ID	Code	$a_P(P)$	$a_T(T)$		$\left(\frac{\partial T}{\partial P}\right)_{\eta_0}$ (℃/MPa) at 170℃
		Barus Eq. β (GPa^{-1})	Arrhenius Eq. E_a (kJ/mol)	WLF Eq. b(K), c(K)	
5	PP	30.1	38.7		1.27
2	LLDPE	19.4	30.8		1.03
3	LmPE	19.8	33.4		0.97
1	HDPE	15.4	27.5		0.91
4	BmPE	25.9	52.0		0.81
6	LPS	51.6		1000, 164	0.50
7	BPS	51.9		1000, 164	0.50

Table 7.4. Effects of structure on the relative influences of T and P at 170℃.

ID	Structure	$(\partial T/\partial P)_{\eta_0}$ or Relative sensitivity to pressure
1 & 5	Many regular SCB	↑↑↑
1 & 2 or 1 & 3	Few SCB	↑↑
6 & 7	A few LCB with benzene ring	↓
3 & 4	Few LCB w/o benzene ring and w/ SCB	↓↓
1 & 6	Many benzene rings	↓↓↓

7.5 Conclusions

The effects of molecular structure on the rheological properties were described by comparing $a_P(P)$, $a_T(T)$, and $(\partial T/\partial P)_{\eta_0}$ of the polymers. Any branching structure or side group increases both the pressure and temperature sensitivities. The benzene side group has the largest effect. Long-chain branching has a strong effect, and short-chain branching also has its own effect, but long-chain branching does not show effect with a regular benzene side group. The comparison of the effects of pressure and temperature was carried out by calculating $(\partial T/\partial P)_{\eta_0}$, and this quantity was found to be strongly structure dependent. Short-chain branching increases the function, and long-chain branching and a benzene side group decrease it at 170℃.

7.6 References

1. H. Münstedt, C. Gabriel, and J. Hepperle, "Comparison of rheological properties of long-chain branched polyethylenes and long-chain branched polystyrenes," *72nd Annual Meeting*, Society of Rheology, 2001.
2. S. Kim, "A criterion for gross melt fracture of polyolefins and its relationship with molecular structure," Doctoral Thesis, McGill University, Montreal, 2000.
3. D. Ferri and P. Lomellini, "Melt rheology of randomly branched polystyrenes," *J. Rheology* 43:1355 (1999).
4. H.E. Park, "Effect of pressure on the rheological properties of three polyethylenes," Master's Thesis, McGill University, Montreal, 2001.
5. P. Wood-Adams and S. Costeux, "Thermorheological behavior of polyethylene: effects of microstructure and long chain branching," *Macromolecules* 34:6281 (2001).

8. Conclusions

1. The Tait model fits the pressure-volume-temperature (*PVT*) data of pure polymer better than the Sanchez-Lacombe equation.
2. The solubility of CO_2 in HDPE at 34 MPa is 0.32 g-CO_2/g-HDPE, and the volume of the HDPE/CO_2 mixture at 34 MPa is 38% higher than that at 1 atm.
3. The four-parameter Yasuda model describes the dependence of complex viscosity on frequency very well.
4. The Arrhenius type equation describes the temperature dependency of the shift factors of HDPE.
5. The use a vertical shift factor $b_T(T)$ or $b_P(P)$ based on *PVT* density data is not necessary to build a master curve.
6. The temperature shift factors obtained by shear rate sweep and dynamic tests (SAOS) were in good agreement.
7. The Barus equation describes the pressure dependency of the shift factors of HDPE.
8. The HPSPR can be used to determine effects of pressure and CO_2 on rheological properties.
9. A vertical shift factor for concentration of HDPE is necessary to build a master curve.
10. The shift factors for pressure and concentration appear to be independent. The Fujita-Kishimoto free volume model describes the concentration shift factor.
11. Nitrogen shows much less effect on the viscosity than CO_2 and a different effect relative to pressure.
12. Pressure slows viscoelastic responses of polymer at the same steady stress, while CO_2 accelerates these. However, those depend on pressure little at the same shear rate.
13. The pressure and concentration shift factors based on viscosity are valid also for the stress growth function and creep compliance.

14. The steady-state compliance is independent of pressure but increases with the concentration of CO_2.
15. The effects of molecular structure on the rheological properties can be expressed by comparing $a_P(P)$, $a_T(T)$, and $(\partial T/\partial dP)_{\eta_0}$ for the various polymers. Any branching or side group increases the pressure and temperature sensitivities.
16. The side group of benzene has the largest effect on temperature and pressure sensitivities of viscosity. Long-chain branching also has a strong effect, and short-chain branching has its own effect, but long-chain branching does not show effect with a regular benzene side group.
17. The comparative effects of temperature and pressure are clearly revealed by calculating $(\partial T/\partial dP)_{\eta_0}$, and this ratio is strongly structure-dependent. Short-chain branching increases $(\partial T/\partial dP)_{\eta_0}$, and long-chain branching and benzene group decrease it at 170℃.
18. The HPSPR can be used to make polymeric foams; an elastic PBD yields more foaming and more regular cell structure than HDPE and BmPE.
19. The viscosity of a sample with CO_2 bubbles is half that saturated with the same amount of CO_2.

9. Original Contributions to Knowledge

1. Determined CO_2 solubility in HDPE up to 34 MPa.
2. Confirmed that Fick's law of diffusion describes dissolution process.
3. Developed an apparatus and procedure to study the effects of pressure and dissolved CO_2 on the rheological properties of molten polymers and batch foaming.
4. Determined the effects of pressure and CO_2 on viscosity, stress growth function, and creep compliance up to 69 MPa without CO_2 and up to 34 MPa with CO_2.
5. Compared effects of CO_2 and N_2 on the viscosity of molten HDPE.
6. Confirmed that temperature shift factors from dynamic measurements and those from steady simple shear are in substantial agreement.
7. Found that a vertical shift factor for concentration of HDPE is necessary but that vertical factors for pressure and temperature are not.
8. Determined the dependency of the steady-state compliance on pressure and dissolved CO_2.
9. Determined the effects of short- and long-chain branching and a benzene side group on the pressure and temperature sensitivities of rheological properties.
10. Demonstrated the relative influences of temperature and pressure on rheological properties.

Appendix 1. Density Determination

To determine the *PVT* behavior of the polymer and the solubility of CO_2, the density of the pure polymer must be known. The density of a solid or a liquid can be determined by means of Archimedes' principle (buoyancy method). Archimedes' principle states that a body immersed in a fluid loses weight by an amount equal to the weight of the fluid it displaces. The density is determined by using a liquid of known density, and water was used for this study. A Mettler Toledo AB204 Balance (Fig. A.1 and Table A.1) with a density determination kit (part number 33360) was used to determine the density of HDPE.

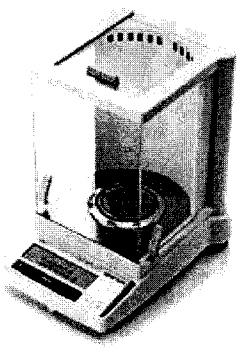

Figure A.1. Mettler Toledo AB204 Balance

Table A.1. Specifications of Mettler Toledo AB204 Balance.

Temperature Sensitivity	2.5 ppm/°C
Readability	0.1 mg
Repeatability	0.1 mg
Linearity +/-	0.3 mg
Maximum capability	210 g

The sample is first weighed in air [Fig. A.2 (b)] and then weighed in water [Fig. A.2 (c)]. The air buoyancy of the sample is not taken into account. The density of the sample is:

$$\rho_s \equiv \frac{W_{pol}}{V_s} \tag{A.1}$$

where W_{pol} is the sample weight, and V_s is the sample volume. The weight loss due to buoyancy is:

$$W_b = \rho_w V_s \tag{A.2}$$

where ρ_w is the density of water, and

$$1/V_s = \rho_w / W_b \tag{A.3}$$

The density of the sample can thus be determined by

$$\rho_s = \frac{W_{pol}}{V_s} = \frac{W_{pol}}{W_b}\rho_w \tag{A.4}$$

If the density of the sample is lower than that of water, $W_b > W_{pol}$.

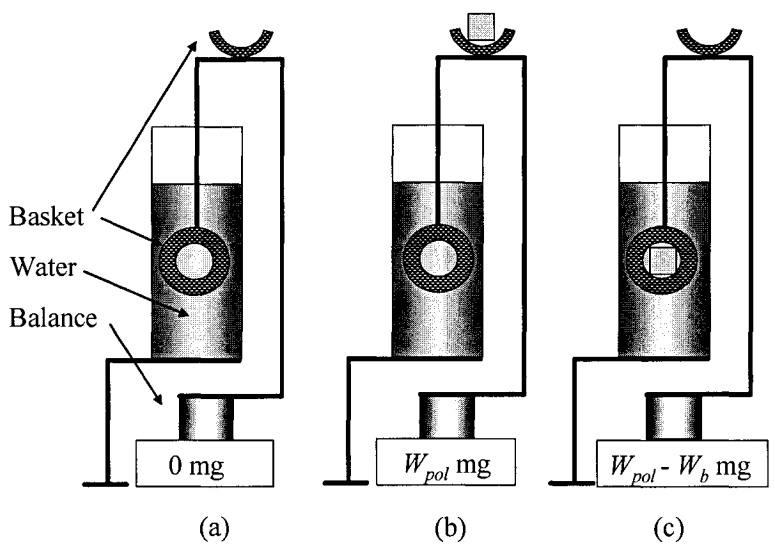

Figure A.2. Density measurement of solid: (a) tare (b) weighing sample (c) weighing immersed sample.

Appendix 2. Ozone-depleting Substances and Greenhouse Gases

Ozone depletion is reduction of the concentration of ozone (O_3) in the upper atmosphere (stratosphere) markedly in polar regions, and this results from uses of human-made ozone-depleting substances (ODSs). To quantify the effect of an ODS on ozone depletion, an ozone depletion potential (ODP) [1] (Table A.2) was introduced and is defined as the total steady-state ozone destruction, vertically integrated over the stratosphere, that caused by a unit mass of a substance per year relative to that of CFC-11.

Global warming or the greenhouse effect is a temperature increase in the lower atmosphere (troposphere), which is cooled by emitting heat, *i.e.*, infrared radiation to the space, but greenhouse gasses absorb and reflect the heat back to the earth resulting in the greenhouse effect. This effect has been keeping moderate temperature on the earth, otherwise the average temperature of the earth would be around -22℃. However, dramatic increases of greenhouse gases are causing climate changes. To quantify the effect of a greenhouse gas on global warming, a global warming potential (GWP) [2] (Table A.2) was introduced. The GWP is the relative contribution of 1 kg of a gas to the effect of 1 kg of CO_2 integrated over a fixed time period such as 100 years.

Chlorofluorocarbons (CFCs) and hydrochlorofluorocarbons (HCFCs) are strong ODSs having both a high ODP and a high GWP, while other greenhouse gases such as CO_2, hydrocarbons, nitrous oxide (N_2O), and Hydrofluorocarbons (HFCs) contribute to global warming without contributing to ozone depletion.

Table A.2. Global warming potential and ozone depletion potential of selected materials.

Common Name / Code	Systematic Name	Formula	GWP (100years) [3,4]	ODP [1]	Major Uses [1]
Water		H_2O	0	0	
	Carbon dioxide	CO_2	1	0	
	Methane	CH_4	25	0	
	Ethane	C_2H_6	3	0	
	Propane	C_3H_8	3	0	
	Butane	C_4H_{10}	3	0	
	Nitrous oxide	N_2O	320	0	
Freon-11, R-11 / CFC-11	Trichlorofluoromethane	$CFCl_3$	4000	1	Foams (60%) Aerosols (30%)
Freon-12, R-12 / CFC-12	Dichlorodifluoromethane	CF_2Cl_2	8500	1	Refrigerant (45%) Aerosols (35%) Foams (13%)
R-22 / HCFC-22	Chlorodifluoromethane	CHF_2Cl	1700	0.055	Refrigerant (85%)
HFC-23	Trifluoromethane or Fluoroform	CHF_3	12100	0	
HFC-32	Difluoromethane	CH_2F_2	580	0	

The decoding system for CFC-@#$& is as follows:

@ = number of double bonds (omitted if zero)

= number of carbon atoms - 1 (omitted if zero)

$ = number of hydrogen atoms + 1

% = number of fluorine atoms

& = number of chlorine atoms replaced by Bromine ("B" prefix added)

Appendix 3. Two Theories of Temperature and Pressure Dependency

Two approaches have been proposed to describe the T and P dependence of the rheological properties of polymers. The absolute reaction rate theory is associated with the change of the activation energy with T and P and correlates the activation energy with the viscosity, while the free volume theory is based on the change of free-volume with pressure or temperature and correlates the free volume with the viscosity. Figure A.3 summarizes the difference between the two approaches.

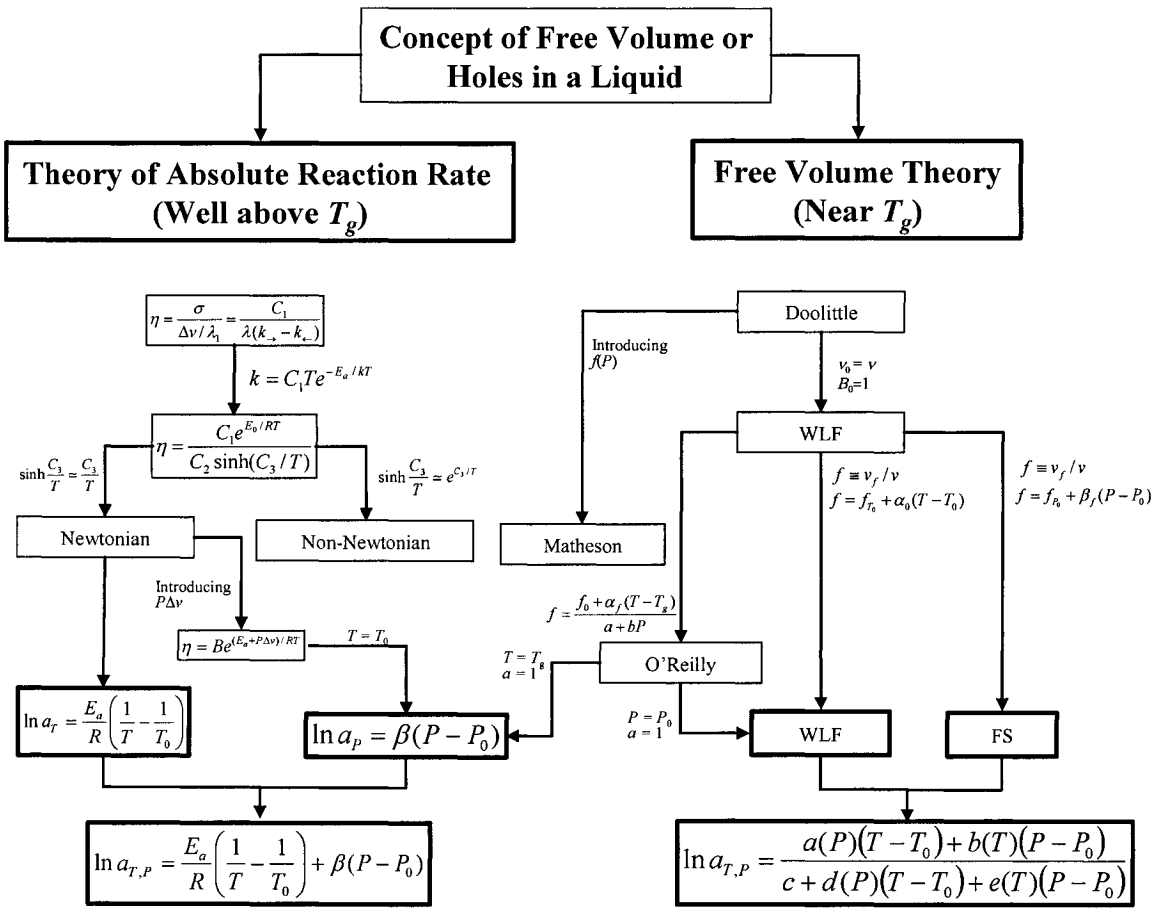

Figure A.3. Schematic diagram of derivation and relationship between two approaches.

A.3.1 The Absolute Rate Theory

The theory of absolute rates of chemical reaction was developed after Arrhenius [5] proposed the concept of an activated molecule and potential energy barriers in 1889. In the 1930's researchers tried to apply this concept to physical problems involving viscosity, diffusion, and plasticity. They combined Arrhenius' equation, which is the relationship between chemical reaction rate and temperature, with equations that describe physical flow to describe the temperature dependency of the viscosity. The theory assumes that a liquid contains free volume or holes that jump or move about in a material, and flow results from these jumps, which occur with the same probability in every direction. This situation is treated as a process of transporting a molecule from one equilibrium position to another over a potential barrier [6], and the process is thus similar to a chemical reaction (Fig. A.4). The theory also assumes that while the potential barrier changes with pressure but not temperature, the rate changes with both P and T.

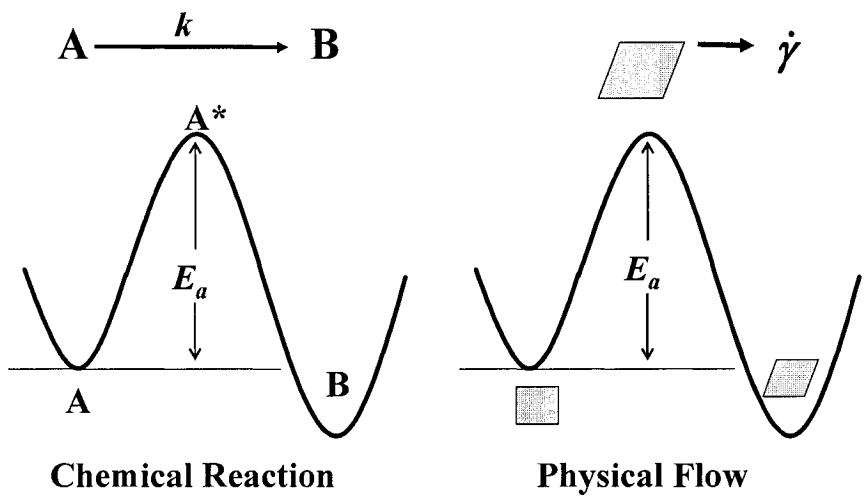

Figure A.4. Similarity of energy profiles of the paths of a chemical reaction system and a physical flow process.

If no velocity gradient exists in a liquid sample, the energy profile can be expressed by the dashed curve in Fig. A.5. A molecule will diffuse equally to the

right or to the left at a rate, k_1, which has units of reciprocal time [6]:

$$k_1 = C_1 T e^{-\Delta E_a/kT} \tag{A.5}$$

where k is the Boltzman constant, C_1 is a constant, and $\triangle E_a$ [1] is the activation energy for diffusion; there is no net flow. If a shearing force is applied to the right, there will be a decrease in the activation energy of $\sigma\delta$ in the direction to the right, where δ is a constant, and an equal increase in the opposite direction. The rates of flow in each direction are:

$$k_{\rightarrow} = C_1 T e^{-(\Delta E_a - \sigma\delta)/kT} = k_1 e^{\sigma\delta/kT} \tag{A.6}$$

$$k_{\leftarrow} = C_1 T e^{-(\Delta E_a + \sigma\delta)/kT} = k_1 e^{-\sigma\delta/kT} \tag{A.7}$$

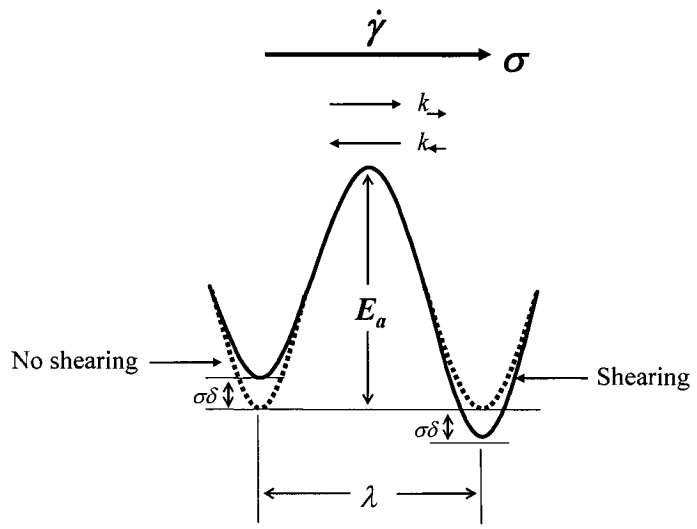

Figure A.5. Energy profile for the path of a flowing molecule.

1) ΔE_a is the activation energy per molecule, and Ea is the activation energy per mole. Since $k=R/N$, $\Delta E_a/k = N\Delta E_a/R = E_a/R$.

The net velocity is then:

$$\Delta v = \lambda(k_{\rightarrow} - k_{\leftarrow}) \tag{A.8}$$

where λ is the distance between equilibrium positions in the direction of flow. The viscosity is given by:

$$\eta = \frac{\sigma}{\Delta v/\lambda_1} = \frac{\sigma\lambda_1}{\lambda(k_{\rightarrow} - k_{\leftarrow})} \tag{A.9}$$

where λ_1 is the perpendicular distance between adjacent layers of molecules (Fig.A.6).

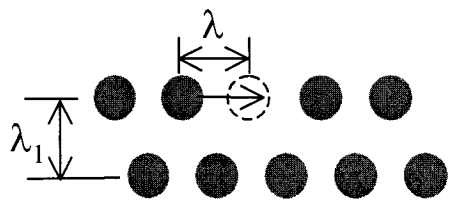

Figure A.6. Distance between molecules in a liquid.

By combining Eqs. A.6 through A.9, Eq. A.9 can be rewritten as:

$$\eta = \frac{\sigma\lambda_1}{\lambda k_1 \sinh(\sigma\delta/kT)} \tag{A.10}$$

Eyring [6] derived equations for Newtonian and non-Newtonian liquids from Eq.A.10. In the Newtonian case $\sigma\delta \ll kT$, and all terms having higher powers than the first in the Taylor series expansion of $\sinh(\sigma\delta/kT)$ are negligible, and $\sinh(\sigma\delta/kT)$ is very close to $\sigma\delta/kT$. Equation A.10 can then be simplified by eliminating the stress term:

$$\eta = \frac{\lambda_1 kT}{\lambda k_1 \delta} \tag{A.11}$$

In the case of a non-Newtonian fluid, if $\sigma\delta$ is sufficiently large, the diffusion flow to the left can be neglected in comparison with the flow in the shearing direction, and $\sinh(\sigma\delta/kT)$ can be approximated by $e^{\sigma\delta/kT}$, and Eq. A.10 becomes:

$$\eta = \frac{\sigma\lambda_1 k}{\lambda k_1 e^{\sigma\delta/kT}} \tag{A.12}$$

Substituting Eq. A.5 into Eqs. A.11 and A.12 gives the following equations:

$$\eta = \frac{\lambda_1 k e^{\Delta E_a/kT}}{\lambda\delta C_1} \quad \text{for Newtonian fluid} \tag{A.13}$$

$$\eta = \frac{\sigma\lambda_1 k e^{(\Delta E_a - \sigma\delta)/kT}}{\lambda T C_1} \quad \text{for non-Newtonian fluid} \tag{A.14}$$

Laidler and Eyring [7] derived the following equation from Eq. A.13 [2]:

$$\eta_0(T) = \left(\frac{hN}{V} e^{-\Delta S^*/R}\right) e^{\Delta H^*/RT} \tag{A.15}$$

where h is Planck's constant, N is Avogadro's number, V is the molar volume, and ΔS^* and ΔH^* are the entropy and enthalpy for viscous flow. Eyring assumes that the molar volume varies little with temperature and that ΔS^* is also independent of temperature. The terms inside the brackets in Equation A.15 can thus be reduced to a constant, and the equation can be rewritten as:

$$\eta_0(T) = Be^{E_a/RT} \tag{A.16}$$

where E_a is the activation energy per mol for flow, and B is a constant. This kind of relationship was proposed empirically by de Guzmán [8], da Andrade [9], and

2) Only the viscosity equations for Newtonian liquids will be discussed further, since the pressure dependence of the viscosity will be discussed in terms of the zero-shear viscosity.

Arrhenius [3] [10]. Ewell and Eyring [11] introduced a pressure term by assuming that additional work must be done against external pressure in order to make a hole in a liquid. The additional work is a result of the additional activation energy necessary for a molecule to overcome the increased barrier to flow (Fig. A.7). The quantity $P\Delta v$ was thus added to the activation energy:

$$\eta_0 = Be^{(E_a + P\Delta v)/RT} \tag{A.17}$$

where Δv is an increase of volume per mol for flow at external P and represents formation of a hole for a mol of molecule to flow into. According to the absolute rate theory, the viscosity can be expressed in terms of the activation energy and a pre-exponential factor.

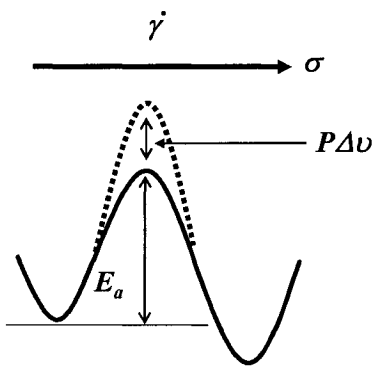

Figure A.7. Increase of the activation energy due to external pressure.

From Eq. A.13 Laidler and Eyring [7] derived the following expression involving free volume without assuming it to be independent of T and P:

$$\eta = \frac{N}{V}\sqrt{2\pi mkT}\sqrt[3]{v_f}e^{(E_a + P\Delta v)/RT} \tag{A.18}$$

3) de Guzman reported a model similar to Eq. A.16 prior to Arrhenius, but this equation is called "the Arrhenius equation" since the Arrhenius equation for chemical reaction rate is popular.

where m is the mass of a molecule, and v_f is the free volume. However, this equation is rarely used.

A.3.2 The Free Volume Theory

Another approach to the theory of T and P dependence of viscosity involves the change of free volume with temperature and pressure. Each choice of relationship between free volume and T or P leads to a different prediction. The idea that the fluidity of a liquid is due to the presence of free volume was first advanced by Batschinski [12] and extensively developed by Doolittle [13-15]. Free volume increases with increasing temperature and decreasing pressure, and fluidity increases with increasing free volume. Batschinski [12] proposed a direct relationship between viscosity and free volume:

$$\eta = \frac{C_2}{v_f} = \frac{C_2}{v - v_0} \tag{A.19}$$

where v is the total specific volume, v_f is the free volume, and v_0 is the specific volume occupied by molecules or the limiting specific volume extrapolated to 0K at 1 atm(Fig. A.8).

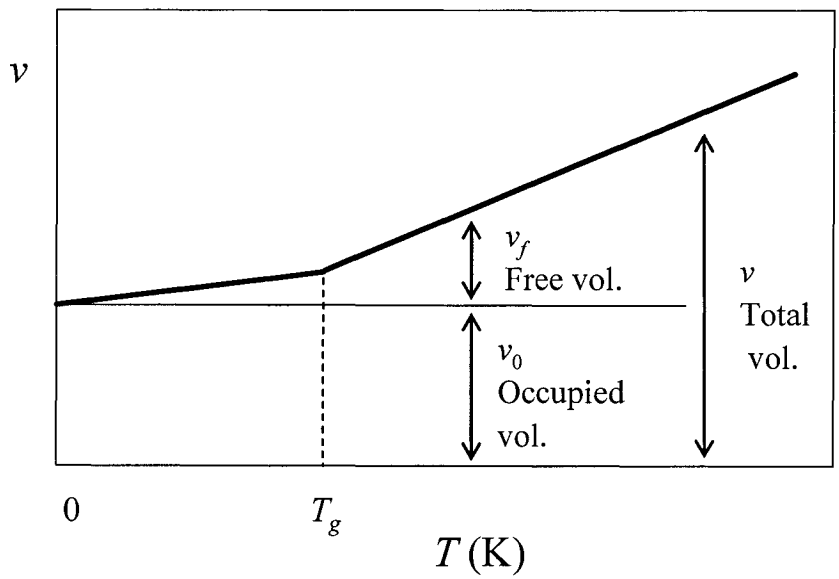

Figure A.8. Schematic of the volume of a polymer above and below T_g.

The free volume theory as formulated at present is based on the observations of Doolittle, who measured the viscosities of *n*-alkanes and found their dependence on free volume. He proposed that specific free volume rather than temperature should be the primary variable for viscosity. Such a relationship is expressed by the following equations, often called the Doolittle equations:

$$\eta = Ae^{B_0 v_0 / v_f} \tag{A.20}$$

$$\ln\eta = A' + B_0 \frac{v_0}{v_f} = A' + B_0 \frac{v_0}{v - v_0} \tag{A.21}$$

where A, A', and B_0 are constants. For the temperature to be explicitly introduced into Eq. A.20, the temperature dependence of the free volume is required. Williams, Landel, and Ferry [16] assumed B_0 is unity, and replaced v_0 with v since $v_f \ll v$ and $v \simeq v_0$:

$$\eta = Ae^{v/v_f} \tag{A.22}$$

They further suggested the following form for the temperature dependency of the free volume:

$$v_f = v_{f,g} + \alpha_0 v (T - T_g) \tag{A.23}$$

where T_g is the glass transition temperature, v_f is the free volume at T, $v_{f,g}$ is the free volume at T_g, and α_0 is the coefficient of thermal expansion of free volume. The following equation is obtained by combining Eqs. A.22 and A.23:

$$\ln\eta = A' + \frac{v}{v_{f,g} + \alpha_0 v (T - T_g)} \tag{A.24}$$

This equation is valid when $T_g < T < T_g + 100℃$. It is usually assumed that when $T < T_g$ the free volume remains unchanged and equal to $v_{f,g}$ due to the freezing of the

conformation [4] of polymeric chains at temperatures below T_g. Thus, when $T < T_g$, a change of volume occurs only as a result of a change in the volume occupied by the molecules, *i.e.* $\Delta v \cong \Delta v_0$.

It is well known that the viscosities of ordinary liquids increase at elevated pressures [17], and the same effect has been observed for polymers [18]. Matheson [19] discussed this behavior qualitatively in terms of the relation between free volume, temperature and pressure. He suggested that an increase of pressure at constant temperature leads to a decrease in v_0 and that the compressibility of a liquid has the same mathematical form as that found by Bridgman [17] for solids:

$$v_0^P = v_0(-aP + bP^2) = v_0 f(P) \tag{A.25}$$

where v_0^P is the limiting specific volume of the liquid at the pressure P. Matheson showed that by substituting v with v^P and v_0 with v_0^P respectively, Eq. A.24 can be rewritten as:

$$\ln\eta = A' + B_0 \frac{v_0 f(P)}{v^P - v_0 f(P)} \tag{A.26}$$

where v^P is the specific volume of the liquid at the pressure P. According to the free volume theory, the viscosity can be expressed in terms of the free volume as a function of T and P.

4) Conformation and configuration are often used interchangeably to mean the spatial arrangement of atoms in a molecule. However, in this work these terms have different meanings. A change of conformation requires rotation about a single bond, while a change in configuration requires breaking or reforming a bond.

Appendix 4. Origin of Method of Reduced Variables

The method of reduced-variables has been useful in rheological measurement. Data at various conditions can be reduced to a single master curve by shifting on to that at the reference condition. During construction of the master curve, the shift factors are obtained, and these factors show the quantitative dependency of the variables on the state variables T, P, and C. One of the most used reduced-variable method is the time-temperature superposition. There have been many reports of its validity and limitations. Time-concentration superposition has been less successful, and very few data regarding time-pressure superposition have been published.

A.4.1 Temperature Shift Factor for Incompressible Materials

To provide a mathematical framework for time-temperature superposition, Ferry [20] used the generalized Maxwell model (Fig. A.9 [21]) in which spring element G_i is relaxed by dashpot $\eta_i \equiv \lambda_i G_i$, and λ_i is the relaxation time of element i. The zero-shear viscosity is given by Eq. A.27:

$$\eta_0(T_0) = \sum_i \lambda_i(T_0) G_i(T_0) \tag{A.27}$$

where subscript 0 indicates the reference state. Ferry made two assumptions: (1) All relaxation mechanisms have the same T dependence, and the relaxation times thus all have the same dependency on temperature, which can be expressed in terms of the temperature shift factor a_T:

$$\lambda_i(T) = \lambda_i(T_0) a_T \tag{A.28}$$

(2) The spring elements have rubberlike elasticity, and G_i is thus proportional to T:

$$G_i(T) = \frac{T}{T_0} G_i(T_0) \tag{A.29}$$

The above two relationships along with Eq. A.27 yield the zero-shear viscosity at T_0 in terms of the parameters evaluated at T:

$$\eta_0(T_0) = \sum_i [\lambda_i(T)/a_T] \left[G_i(T) \frac{T_0}{T} \right] \tag{A.30}$$

From Eq. A.27, the zero-shear viscosity at T can be expressed as:

$$\eta_0(T) = \sum_i \lambda_i(T) G_i(T) \tag{A.31}$$

Using Eq. 31, Eq. A.30 can be rearranged to give:

$$\eta_0(T_0) a_T \frac{T}{T_0} = \sum_i [\lambda_i(T)] [G_i(T)] = \eta_0(T) \tag{A.32}$$

and finally the temperature shift factor is:

$$a_T = \frac{\eta_0(T)}{\eta_0(T_0)} \frac{T_0}{T} \tag{A.33}$$

Ferry proposed that this equation was valid for incompressible materials. Because a unit volume contains fewer elastic and viscous elements if the system expands thermally, this equation needs a density correction for a compressible system and is discussed in Section A.4.3.

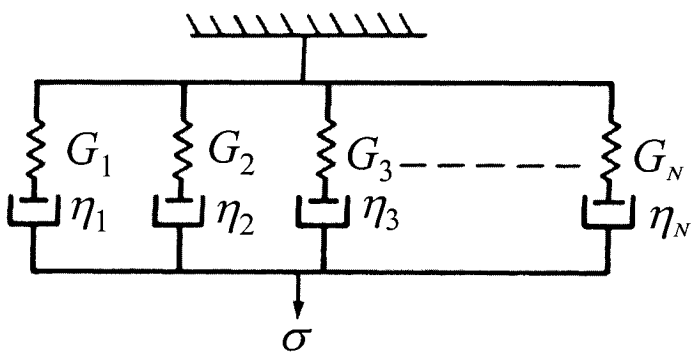

Figure A.9 Generalized Maxwell model.

A.4.2 Concentration Shift Factor

Ferry [20] carried out an analysis of the concentration (C) shift factor. Again, it was assumed that all relaxation mechanisms have the same C dependence and that the relaxation time is:

$$\lambda_i(C) = \lambda_i(C_0)a_C \tag{A.34}$$

where C is the concentration of diluent, and a_C is the C shift factor. It cannot be assumed that the diluent changes the rigidity of each spring, but by fitting data, he found that G_i is proportional to the density of the polymer :

$$G_i(C) = \frac{\rho_{pol}(C)}{\rho_{pol}(C_0)} G_i(C_0) \tag{A.35}$$

where $\rho_{pol}(C)$ is the density of polymer at the concentration C, and $\rho_{pol}(C_0)$ is the density of pure polymer and is simply ρ_{pol}. The concentration shift factors can then be obtained as:

$$a_C = \frac{\eta_0(C)}{\eta_0(C_0)} \frac{1}{b_C(C)} \tag{A.36}$$

$$b_C(C_{pol}) \equiv \frac{\rho_{pol}(C)}{\rho_{pol}} \tag{A.37}$$

Since the density of polymer at diluent concentration C can be described as the concentration of the polymer C_{pol}, Eq. A.37 can be formulated as:

$$b_C(C_{pol}) = \frac{C_{pol}(C)}{\rho_{pol}} \tag{A.38}$$

A.4.3 Temperature Shift Factor for Compressible Materials

Thermal expansion and dilution can be treated in a similar manner as described above, where G_i is proportional to the density and T. To account for thermal expansion, G_i can be modified to give:

$$G_i(T) = \frac{T\rho(T)}{T_0\rho(T_0)} G_i(T_0) \tag{A.39}$$

This equation leads the well known the temperature shift factor:

$$a_T(T) = \frac{\eta_0(T)}{\eta_0(T_0)} \frac{T_0\rho(T_0)}{T\rho(T)} = \frac{\eta_0(T)}{\eta_0(T_0)} \frac{1}{b_T(T)} \tag{A.40}$$

The modified Rouse model [22, p.76] predicts a specific form for Eq. A.39:

$$G(t,T) = \frac{R\rho(T)T}{M} \sum_{p=1}^{N} e^{-t/\lambda_p} \tag{A.41}$$

where λ_p is a function of chemical structure and friction coefficient. However, $b_T \equiv T\rho(T)/T_0\rho(T_0)$ changes little with T, and $b_T(T)$ is usually set equal to unity.

Appendix 5. Observation of Need of Vertical Shift Factor

Figure A.10 illustrates the case of necessity of $b_T(T)$. Stress data at T_0 are circles, and solid curve indicates these at T. While dash-dot curve shifted by only $a_{1,T}(T)$ deviates from the data at T_0, dotted curve shifted by $a_T(T)$ and $b_T(T)$ is on the reference data. If $b_T(T)$ is small, or shear thinning occurs little, *i.e.*, stress has a almost linear relationship with frequency, shift by $b_T(T)$ makes no difference for superposition. Otherwise, $b_T(T)$ is necessary to build a master curve.

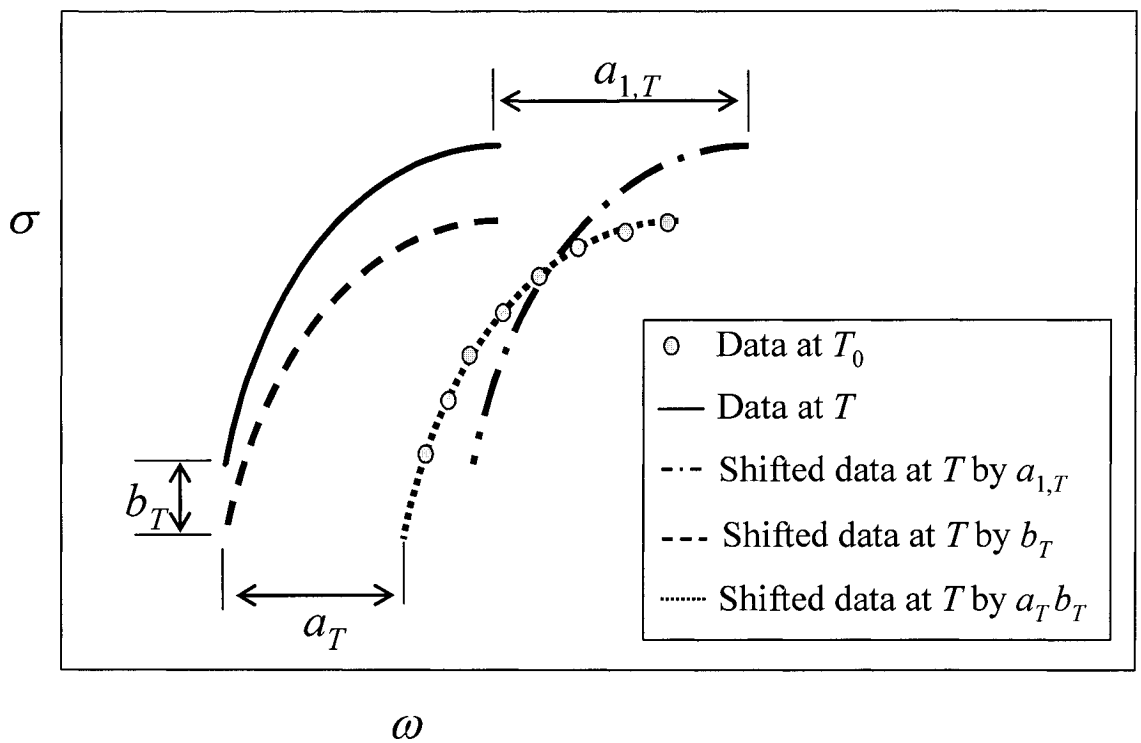

Figure A.10. Illustration of validity of using b_T.

Appendix 6. Selecting O-ring Material and Modifying O-ring

Several factors are important in selecting an O-ring material from the many that are available: chemical resistance, price, delivery time, and maximum operating *P* and *T*. Most of the available data on chemical resistance were obtained at ambient conditions, so after acquiring O-rings, they had to be tested in a SC-CO_2 environment in the HPSPR. An important factor is temperature. There are several choices for temperatures higher than 200℃: Aflas™ (Copolymer of tetrafluoro -ethylene/propylene), Viton® (Fluorocarbon), Silicone, Fluorosilicone, Kalrez® (perfluoroelastomer), Chemraz®, and Teflon®. Aflas™, Kalrez®, and Chemraz® were excluded due to high price and long delivery time despite their good chemical resistance. Viton® and Fluorosilicone showed weak CO_2 resistance. Finally Teflon was found to have better SC-CO_2 resistance than silicone, but it was not possible to use it in the HPSPR due to the difficulty of making a rectangular shape, which is the shape of the O-ring groove on the HPSPR cover place. Moreover, the contour length of the O-ring groove is between generic O-ring sizes of 369 and 370. A generic Teflon O-ring, which is plastic rather than rubber, would not fit the groove. Thus, Teflon was excluded.

A Teflon encapsulated silicone (TES) O-ring (Figs. A.11 and A.12) was considered next. This type of O-ring has flexibility from the silicone rubber and chemical resistance from the Teflon. After one use of this type of O-ring, the shape conformed to that of the O-ring groove (Fig. A.13), and it could thus be easily reinstalled. However, it was found that with repeated usage, a few parts of the O-ring were damaged (Fig. A.14). The price of this type of O-ring is U$39.13, and it can be considered disposable, but if damage occurred during an experiment, it could cause severe leaks of CO_2. This type of O-ring was therefore excluded.

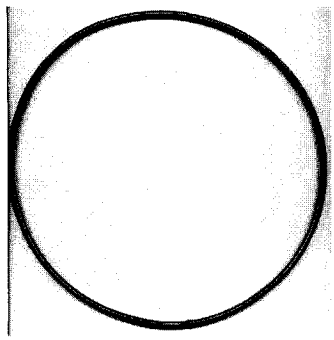

Figure A.11. TES O-ring.

Figure A.12. Enlarged part of TES O-ring.

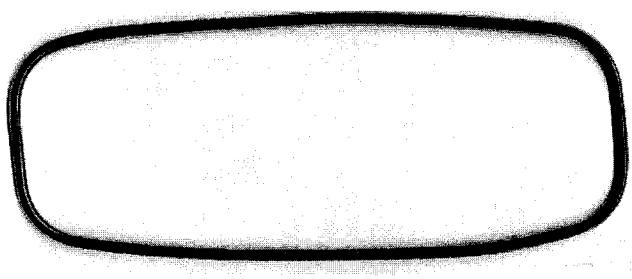

Figure A.13. Changed shape of O-ring.

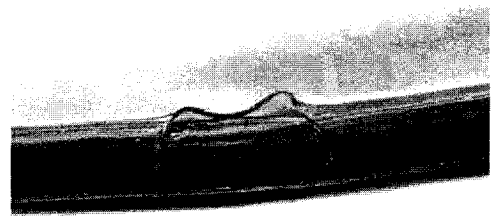

Figure A.14. Damaged part of O-ring.

Then, the use of a pure Teflon O-ring having a generic size re-considered. (A custom Teflon O-ring between sizes 369 and 370 has long a delivery time of 2-3 weeks and a high cost of U$123.) It was thought that a Teflon O-ring could be compression-molded like a TES O-ring. A "custom" Teflon O-ring was thus made from a generic Teflon O-ring of size 369 (U$33). It was tested five times with SC-CO_2 and exhibited no problem. The performance of this O-ring was even better than the TES O-ring. The method of making a custom Teflon O-ring for the HPSPR is as follows:

(1) A No. 369 Teflon O-ring is placed in the oven to make it flexible. (Fig.A.15).

(2) When the O-ring is flexible, it is bent and stretched to fit in its groove (Fig. A.16).

(3) After a couple of hours in a SC-CO_2 environment, the O-ring is no longer circular but rectangular with rounded corners (Fig. A.17).

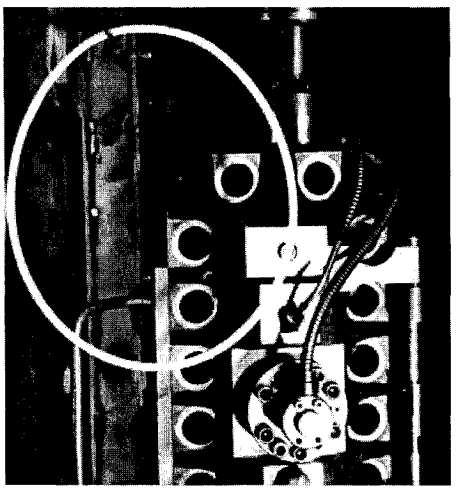

Figure A.15.Heating up O-ring.

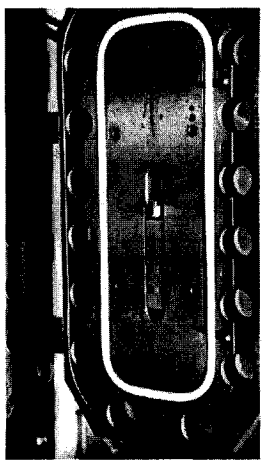

Figure A.16.
Placed O-ring.

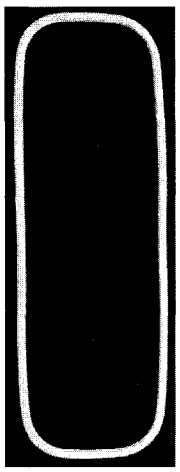

Figure A.17.
Shape change.

(4) If the O-ring has been at room temperature, it is shorter than its groove and cannot be mounted in the groove (Fig. A.18).

(5) To make the cold O-ring fit its groove, it needs to be placed in the hot oven for a while prior to loading (Fig. A.19).

(6) Then, the O-ring fits the groove well (Fig. A.20).

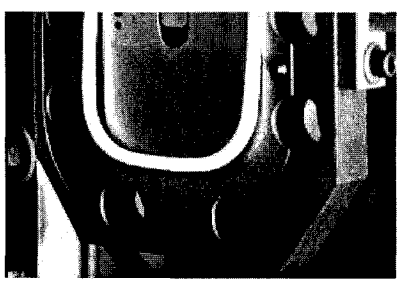

Figure A.18.O-ring does not fit.

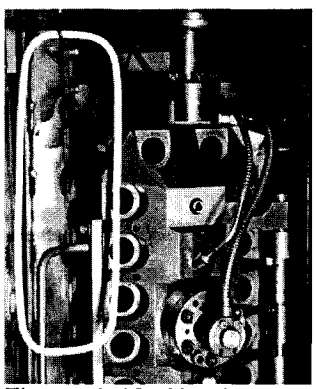

Figure A.19. Heating up.

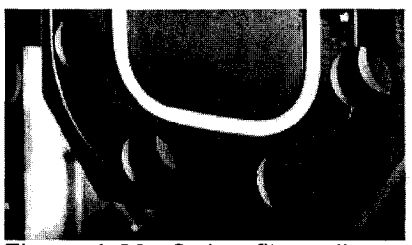

Figure A.20. O-ring fits well.

Appendix 7. Experimental Procedures of HPSPR

A.7.1 Preliminary Checking

(1) The following items need to be inspected to verify that they are clean and oil-free:

a) Fixed and moving plates
b) SST active face head
c) Mating surfaces
d) Actuating rods
e) Set screws

(2) The following items need to be checked to see that they are clean and well lubricated:

a) O-ring groove on the cover plate of the pressure vessel:
b) O-ring
c) 7/8-inch bolts

(3) The following items need to be checked to see that they are connected correctly:

a) Servo-valve and shear stress cables to the controller cards on the computer
b) SST capacitance probe line to Capacitec(R) amplifier
c) Thermocouple to the temperature readout (Fig. A.21)
d) Position of the rheometer selector of hydraulic pump oil (Fig. A.22)

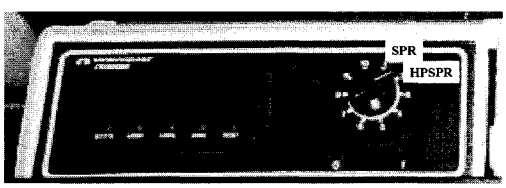

Figure A.21. Temperature readout.

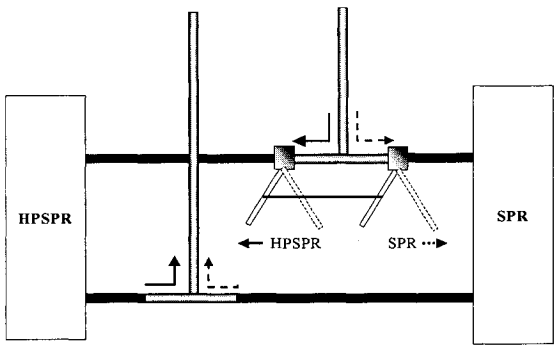

Figure A.22. Rheometer selector for hydraulic oil.

(4) Warming-up and tuning

a) Warm-up the actuator by sinusoidal linear movement.

b) Tune the control parameters (PIDO).

(5) Heating

a) Close the oven.

b) Turn on the heater (Figure A.23).

c) Set the temperature at the test temperature plus 20℃.

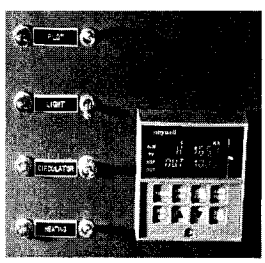

Figure A.23. Heating controller panel.

A.7.2 Adjusting the Control Parameters

The Proportional, Integral, Differential, and Offset (PIDO) parameters of the operating software, QuikTest, are adjusted to obtain a good match between command and feedback. A triangular mode of displacement can be used to adjust the controller parameters. The general procedure for adjusting the PIDO for controlled strain is as follows:

(1) After loading a dummy sample or without a sample, impose an appropriate frequency and amplitude for a triangular displacement.

(2) Set the I, D, and O parameters to zero.

(3) P governs the difference between the maximum and minimum values of the triangular displacement (Fig. A.24). Start the test. Adjust P until the desired response is achieved, and the difference between the maximum and minimum of the command and that of the feedback will the same.

(4) Adjust I to match the maximum and minimum of the command and those of the feedback (Fig. A.25).

(5) Adjust D to eliminate an overshoots when P is high. (usually zero).

(6) After stopping the test and turning off the I and D terms, adjust O to match the feedback and the command (Fig. A.26).

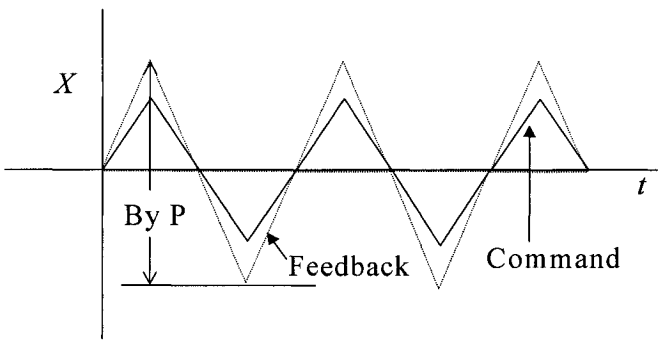

Figure A.24. Triangular displacement and effect of P parameter.

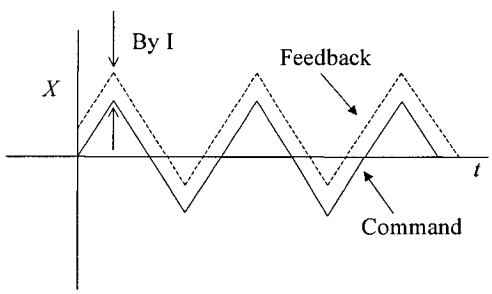

Figure A.25. Triangular displacement and effect of I parameter.

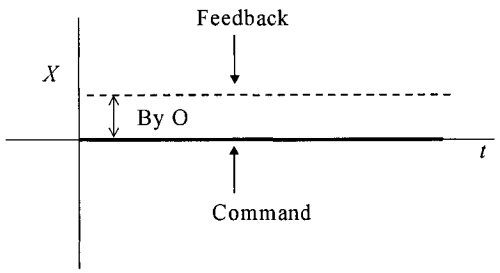

Figure A.26. Ambient command and effect of O parameter.

The procedure for adjusting the PIDO parameters for a controlled-stress run is much more difficult and cannot be performed using a triangular displacement. The parameters can be adjusted using a ramp displacement, but this is a very laborious trial-and-error procedure, and control can easily be lost if the trial is in wrong direction, and parameters or command stress are too high. Stress exceeding 10 kPa was found to make the system unstable up-to-date. However, once optimized parameters are found at a certain condition for a sample, parameters at another condition for the sample are not far from the previous one and can be determined much easier than the first parameter set.

A.7.3. Assembly and Sample Loading

(1) Turn off the heater.

(2) Install the moving plate.

(3) Install the SST active face head.

(4) Install the fixed plate.

(5) Locate a sample of 1cm×8cm at the center of the fixed plate.

(6) Insert the O-ring in the groove.

A.7.4. Closing the HPSPR

(1) Close the cover plate.

(2) Insert the 7/8-inch bolts into the threaded holes.

(3) Change the air inlet value to torque wrench mode.

(4) Set the pressure value of the air regulator for the torque wrench.

(5) Turn on air inlet.

(6) Tighten the bolts with the torque wrench.

(7) Close the oven.

(8) Turn on the heater and set a test temperature.

A.7.5. Pressurizing

(1) Change the air inlet value to oil-filling mode.

(2) Turn on air inlet to fill HPSPR with Krytox oil.

(3) Close every valve after the filling is finished.

(4) Pressurize HPSPR with the hand pump until the desired pressure is reached.

A.7.6. Operating

Usually the set-point temperature can be reached one hour after loading the sample. Two hours after loading the sample, a run can be carried out.

A.7.6.1. Controlled-Stress Mode

(1) Enter a value of the speed of stress change to reach a desired stress under 'rate' in the Quiktest operating software.

(2) Enter a value for the desired stress under 'level'.

(3) Press 'start'.

A.7.6.2. Controlled-Strain Mode

Two ramp displacements, one upward and the other return, at constant speed are required to determine the viscosity.

(1) Enter a value of the desired speed of the moving plate under 'rate'.

(2) Enter a value of the desired total displacement under 'level'.

(3) Press 'start'.

A.7.7. Depressurizing

(1) Turn off the heater

(2) Open the release valve to 5°on the hand pump.

(3) Close every valve connected to the hand pump.

(4) Change air inlet value to oil-emptying mode.

(5) Turn on air inlet to push oil out of the HPSPR.

A.7.8. Opening the HPSPR

(1) Change air inlet value to torque wrench mode.

(2) Open the oven.

(3) Turn on air inlet.

(4) Untighten the bolts with the torque wrench.

(5) Remove 7/8-inch bolts.

(6) Close the cover plate.

A.7.9. Disassembly and Sample Removal

(1) Remove and clean the O-ring.

(2) Remove the sample with an aluminium bar.

(3) Remove the fixed plate

(4) Remove the SST active face head

(5) Remove the moving plate

A.7.10. Cleaning

(1) Wipe out the inside of the HPSPR.

(2) Cool down the plates and the SST active face head

(3) Clean the plates and the SST active face head with Easy-off oven cleaner.

(4) Rinse off Easy-off completely to prevent the corrosion of metal parts that are not made of stainless steel, such as the SST beam. Warm, around 60℃, xylene can be used to clean the plates and the SST head. It is a good solvent for polyethylene and does not corrode any metal. However, a ventilation system is required to use xylene since it is volatile and toxic, and xylene was not used for this study.

Appendix 8. Formulation of Linear Portion of Creep Compliance

The equation of a linear portion of a curve [Fig. A.27 (1)] is:

$$y = mt + n \tag{A.42}$$

where m is the slope, and n is the y-intercept. A line can be stretched or shrunk by a nonrigid transformation [23, p.104] by multiplying each coordinate value by a factor. A horizontal nonrigid transformation [Fig. A.27 (2)] of a curve obtained by multiplying h will give the following line:

$$y = m\left(\frac{t}{h}\right) + n \tag{A.43}$$

A vertical nonrigid transformation [Fig. A.27 (3)] by multiplying by v will make a line as:

$$\left(\frac{y}{v}\right) = mt + n \tag{A.44}$$

and Eq. A.44 can be rewritten as:

$$y = vmt + vn \tag{A.45}$$

If a multiplying factor is between 0 and 1, the transformation shrinks the original function towards origin. If the factor is greater than 1, the transformation stretches the function away from origin. Equations A.42, A.43, and A.45 show that a horizontal nonrigid transformation does not change the intercept, but a vertical transformation changes it by a factor of v.

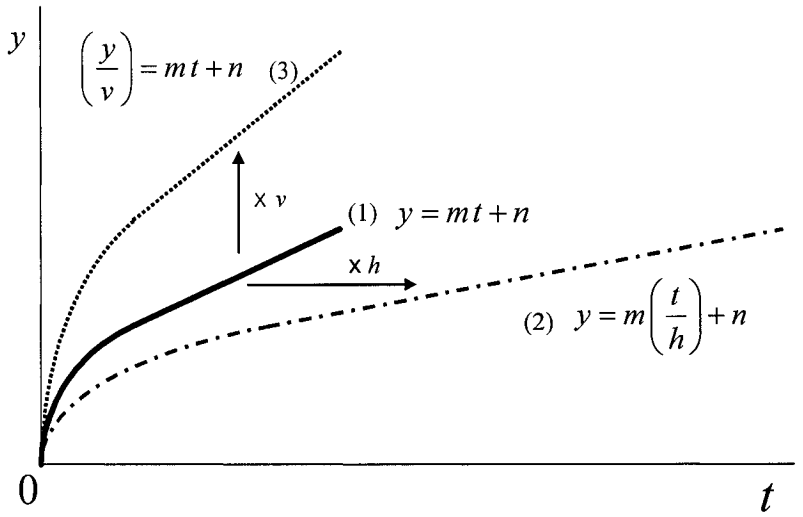

Figure A.27. Nonrigid transformation of line by a factor.

For creep compliance at P_0, the linear portion of the curve can be described by letting $y = J$, $m = 1/\eta$, and $n = J_S$ in Eq. A.42 to give:

$$J(P_0,t) = \frac{1}{\eta(P_0)}t + J_S(P_0) \tag{A.46}$$

If the sample is piezorheologically simple, *i.e.*, superposable by a shift factor or two factors, the linear portion of the creep curve at P can be predicted from that (Eq. A.46) at P_0 by setting $h = a_P(P)$ in Eqs. A.42 and A.43:

$$J(P,t) = \frac{1}{\eta(P_0)}\frac{t}{a_P(P)} + J_S(P_0) \tag{A.47}$$

Since $J(P,t) = t/\eta(P) + J_S(P)$, the following relationships can be found:

$$J_S(P) = J_S(P_0) \tag{A.49}$$

$$\eta_0(P) = \eta_0(P_0)a_P(P) \tag{A.50}$$

The linear portion at P and C can be predicted from that (Eq. A.46) at P_0 by letting $h = a_{P,C}(P,C)$ and $v = 1/b_C(C)$ in Eqs. A.42, A.43, and A.45 as:

$$J(P,C,t)b_C(C) = \frac{1}{\eta(P_0)}\frac{t}{a_{P,C}(P,C)} + J_S(P_0) \tag{A.51}$$

and Eq. A.51 can be rearranged to give:

$$J(P,C,t) = \frac{1}{\eta(P_0)}\frac{t}{a_{P,C}(P,C)b_C(C)} + \frac{J_S(P_0)}{b_C(C)} \tag{A.52}$$

Because $J(P,C,t) = t/\eta(P,C) + J_S(P,C)$, the following relationships can be shown:

$$J_S(P,C) = J_S(P_0)/b_C(C) \tag{A.54}$$

$$\eta_0(P,C) = \eta_0(P_0)a_{P,C}(P,C)b_C(C) \tag{A.55}$$

Appendix 9. The Maxwell Model for the Steady-state compliance

Two Maxwell models are compared to study the effect of dilution on the steady-state compliance: (A) One consists of one element set, and (B) the other has two sets (Fig. A.28), which represent more elements in the same unit volume than the former case. Each set has the same spring and dashpot elements:

$$G_A = G_{B1} = G_{B2} \tag{A.56}$$

$$\eta_A = \eta_{B1} = \eta_{B2} \tag{A.57}$$

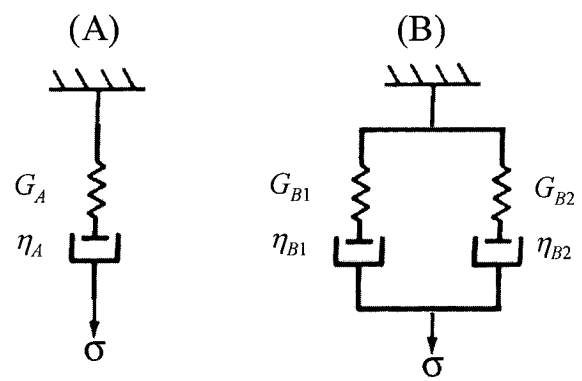

Figure A.28. The Maxwell models with one and two element-sets.

The analytical expressions for stress and strain are as follows:

$$\gamma_A(t) = \frac{\sigma}{G_A} + \frac{\sigma}{\eta_A}t \tag{A.58}$$

$$\sigma = \sigma_{B1} + \sigma_{B2} = 2\sigma_{B1} \tag{A.59}$$

$$\gamma_B(t) = \gamma_{B1}(t) = \frac{\sigma_{B1}}{G_{B1}} + \frac{\sigma_{B1}}{\eta_{B1}}t = \frac{\sigma}{2G_{B1}} + \frac{\sigma}{2\eta_{B1}}t \tag{A.60}$$

The creep compliance for A and B can be formulated as:

$$J_A(t) \equiv \frac{\gamma_A(t)}{\sigma} = \frac{1}{G_A} + \frac{1}{\eta_A}t = J_{S,A} + \frac{1}{\eta_A}t \tag{A.61}$$

$$J_B(t) \equiv \frac{\gamma_B(t)}{\sigma} = \frac{1}{G_B} + \frac{1}{\eta_B}t = J_{S,B} + \frac{1}{\eta_B}t \tag{A.62}$$

and combining Eqs. A.56 and A.60 gives Eq. A.63:

$$J_B(t) = \frac{1}{2G_{B1}} + \frac{1}{2\eta_{B1}}t = \frac{1}{2G_A} + \frac{1}{2\eta_A}t = \frac{1}{2}J_{S,A} + \frac{1}{2\eta_A}t \tag{A.63}$$

The following relationships are established by Eqs. A.62 and A.63:

$$J_{S,B} = \frac{1}{2}J_{S,A} \tag{A.64}$$

$$\eta_B = 2\eta_A \tag{A.65}$$

More generally, the steady-state compliance and the viscosity can be predicted by the Maxwell model with N identical sets of elements as follows:

$$J_{S,1} = NJ_{S,N} \tag{A.66}$$

$$\eta_1 = \frac{1}{N}\eta_N \tag{A.67}$$

where subscript 1 indicates the Maxwell model with one element set, and N indicates that with N sets in the same unit volume. This shows that the viscosity will decrease and the steady-state compliance will increase due to dilution, *i.e.*, fewer elements in the unit volume. This is the same results shown in Appendix 8.

Appendix 10. Nomenclature

Roman Letters

a	Length to width ratio
a,a_0,a_1,a_2	Constants
a_C	Horizontal concentration shift factor
$a_{1,P}$	Horizontal pressure shift factor considering b_P as one
a_P	Horizontal pressure shift factor
$a_{1,P,C}$	Horizontal pressure and concentration shift factor considering $b_{P,C}$ as one
$a_{P,C}$	Horizontal pressure and concentration shift factor
$a_{1,T,P,C}$	Horizontal temperature, pressure, and concentration shift factor considering $b_{P,C}$ as one
$a_{T,P,C}$	Horizontal temperature, pressure, and concentration shift factor
$a_{1,T}$	Horizontal temperature shift factor considering b_T as one
a_T	Horizontal temperature shift factor
A	Surface area of the active face of shear stress transducer
A,A_1,A'	Constants
b_0,b_1	Constants
b_C	Vertical concentration shift factor
b_P	Vertical pressure shift factor
$b_{P,C}$	Vertical pressure and concentration shift factor
b_T	Vertical temperature shift factor
$b_{T,P,C}$	Vertical temperature, pressure, and concentration shift factor
B,B_0,B_1,B'	Constants
C	Concentration of dissolved gas or constant
C_0	Initial gas concentration

C_1, C_2	Constants
C_1	Gas concentration on interface
C_{pol}	Concentration of polymer
D	Differential parameter
D	Diffusion coefficient
D_0	Diameter of a capillary
e	Bagley end correction,
E_a	Activation energy
f	Fractional free volume
F	Shear force
$\vec{F}$	Flux vector
F_x	x-Component of flux vector
F_y	y-Component of flux vector
F_z	z-Component of flux vector
g	Acceleration of gravity
G	Gibbs free energy
$G(t)$	Relaxation modulus
G'	Storage modulus
G''	Loss modulus
G_d	Amplitude ratio
G_i	Modulus of Maxwell spring element i
G_m	Gibbs free energy of mixture
GWP	Global warming potential
h	Gap between two plates or Planck's constant
H	Enthalpy
ΔH^*	Enthalpy for viscous flow
i	Shear-rate or frequency index
I	Integral parameter
j	Pressure and concentration index

J	Creep compliance
J_s^0	Steady-state compliance of linear viscoelasticity
J_S	Steady-state compliance of nonlinear viscoelasticity
k	Boltzman constant, reaction rate constant, linear swell factor
k_1	Rate of a diffusing molecule
$k_{\leftarrow}$	Rate of a molecule diffusing to the left
$k_{\rightarrow}$	Rate of a molecule diffusing to the right
K_{12}	Interaction parameter
L	Length or width of a sample
L_0	Length of a capillary
LCB	Level of long-chain branching
m	Mass of a molecule or constant
$M(t)$	Total amount of diffusing substance absorbed at time t
$M(\infty)$	Total amount of diffusing substance absorbed after infinite time
M	Torque or molecular weight
M_c, M_c'	Critical molecular weights
M_m	Molecular weight of mixture
M_n	Number average molecular weight
M_w	Weight average molecular weight
n	Power-law index or constant
N	Avogadro's number or number of data
N_1	First normal stress difference
N_2	Second normal stress difference
O	Offset parameter
ODP	Ozone depletion potential
P	Proportional parameter
P	Pressure
$\tilde{P}$	Reduced pressure
P^*	Characteristic pressure

P_0	Initial pressure or reference pressure
ΔP_{cap}	Pressure drop in the capillary
$\tilde{P}_m$	Reduced pressure of mixture
P_0, P_r	Reference pressure
P_a	Environmental pressure
P_c	Critical pressure
P_d	Driving pressure
ΔP_{ent}	Entrance pressure drop
ΔP_{ex}	Exit pressure drop
Q	Volumetric flow rate
r	Number of mers per molecule or constant
R	Gas constant or Radius of a capillary
RD	Relative difference between two quantity
S	Solubility, error sum for the least square method, or entropy
ΔS^*	Entropy for viscous flow
S_T	Solubility calculated using a theory
S_{TE}	Solubility calculated using a theory and experimental data
t_S	Onset time for maximum stress
t_{SS}	Onset time for steady-state stress
T	Temperature
$(\partial T/\partial P)_{\eta_0}$	Relative influence of temperature and pressure on the zero-shear viscosity
$\tilde{T}$	Reduced temperature
T^*	Characteristic temperature
T_0, T_r	Reference temperature
T_c	Critical temperature or crystallization temperature
$T_{c,e}$	Crystallization temperature from the end of the peak in the endothermic curve
$T_{c,h}$	Crystallization temperature from the peak in the endothermic curve

T_g	Glass transition temperature
T_m	Melting temperature
$T_{m,e}$	Melting temperature from the end of the peak in the endothermic curve
$T_{m,h}$	Melting temperature from the peak in the endothermic curve
$\tilde{T}_m$	Reduced temperature of mixture
v	Specific volume
v^*	Characteristic volume
$v(0,T)$	Zero-pressure isotherm
v_0	Specific volume occupied by molecules or the limiting specific volume extrapolated to 0K and 1 atm
v_0, v_1	Constants
v_0^P	Limiting specific volume of the liquid at the pressure P
v_c	Critical volume
v_f	Free volume
v_{f_g}	Free volume at T_g
v_{f_0}	Free volume at T_0
v_{mp}	Model-predicted specific volume
v_{pol}	Specific volume of polymer
Δv	Net velocity of a molecule or increase of volume per mol for flow at external P
V	Molar volume or velocity of a moving plate
V_{body}	Volume of an immersed body
V_g	Volume of gas
V_{holder}	Volume of sample holder
V_m	Volume of mixture
V_{pol}	Volume of polymer
V_s	Sample volume

V_{sw}	Swollen volume of sample
w_1, w_2	Weight fractions
W_b	Weight loss due to buoyancy
W_{body}	Actual weight of an immersed body
W_g	Weight of gas
W_{pol}	Weight of polymer
W_R	Weight reading or net weight
W_{R1}	Weight reading with no sample/sample holder and no sinker
W_{R2}	Weight reading with the sample/sample holder but no sinker
W_{R3}	Weight reading with the sample/sample holder and sinker
W_{sinker}	Weight of a sinker
x^*	Schümmer shift factor
X	Displacement of a moving plate

Greek Letters

α	Isobaric thermal expansion coefficient or Constant
α_0	Coefficient of thermal expansion of free volume
β	Isothermal compressibility or pressure coefficient
γ_0	Strain amplitude,
γ	Strain
$\dot{\gamma}$	Shear rate
$\dot{\gamma}_a, \dot{\gamma}_A$	Apparent shear rate
$\dot{\gamma}_w$	True wall shear rate
δ	Phase angle or constant
ϵ^*	Interaction energy
η	Shear viscosity
η^*	Complex viscosity
η_0	Zero-shear viscosity
η_a, η_A	Apparent viscosity

$\eta(\infty)$	Viscosity at saturation with dissolved gas
η^*_{mp}	Model-predicted complex viscosity
η_i	Maxwell dashpot element *i*
η_R	Relative viscosity
Θ	Cone angle
λ	Distance between equilibrium positions in the direction of flow or Characteristic time
λ_1	Perpendicular distance between adjacent layers of molecules
λ_i	Relaxation time of Maxwell element *i*
μ	Chemical potential
μ_1^m, μ_g^m	Chemical potential of gas in polymer/gas mixture phase
μ_g^g	Chemical potential of gas in the gas phase
ρ	Density or density of polymer
ρ^*	Characteristic density
$\tilde{\rho}$	Reduced density
ρ_g	Density of gas
$\tilde{\rho}_m$	Reduced density of mixture
$\tilde{\rho}_c$	calculated reduced density
ρ_{pol}	Density of polymer
ρ_s	Density of sample
ρ_w	Density of water
ϕ	Cone diameter
ϕ_1, ϕ_2, Φ	Volume fractions
σ	Stress
σ_0	Stress amplitude
$\sigma^+(t)$	Stress growth function
σ_{mp}	Model-predicted stress
$\Delta\ \sigma_{ov}$	Stress overshoot

σ_S	Maximum stress
$\sigma_{SS}, \sigma^+(\infty)$	Steady-state stress
σ_w	True wall shear stress
$\underline{\tau}$	Stress tensor
ω	Frequency
Ω	Angular velocity

Appendix 11. References

1. E.A. Parson, *Protecting the Ozone Layer*, Oxford University Press, Oxford, 2003.
2. Panel on Policy Implications of Greenhouse Warming, *Policy Implications of Greenhouse Warming*, National Academy Press, Washington, D.C., 1992.
3. W.J. Collins, R.G. Derwent, C.E. Johnson, and D.S. Stevenson, "The oxidation of organic compounds in the troposphere and their global warming potentials," *Climatic Change* 52:453 (2002)
4. J.T. Houghton, L.G.M. Filho, B.A. Callander, N. Harris, A. Kattenberg, K. Maskell, *Climate Change* 1995: *The Science of Climate Change*, Cambridge University Press, Cambridge, 1996.
5. S. Arrhenius, "Über die reaktionsgeschwindigkeit bei der inversion von rohrzucker durch säuren (On the reaction rate with the inversion of sucrose by acids),", *Zeitschrift für Physickalische Chemie* 226 (1889).
6. H. Eyring, "Viscosity, plasticity, and diffusion as a examples of absolute reaction rates," *J. Chem. Phys.* 4:283 (1936).
7. K.J. Laidler and H. Eyring, *The Theory of Rate Processes*, McGraw-Hill, New York, 1940.
8. J. de Guzmán, "Relación entre la fluidez y el calor de fusión (Relation between the fluidity and the heat of fusion)," *Anales de la Sociedad Espanola de Fisica Y Quimica*, 11:353 (1913).
9. E.N. da C. Andrade, "The viscosity of liquids," *Nature* 125:309 and 582 (1930).
10. S. Arrhenius, "Die theoretische deutung von viskositäts-messungen kolloidaler lösungen (The theoretical interpretation of viscosity measurements of colloidal solutions)," *Meddelanden Från K. Vetenskapsakademiens Nobelinstitut* 3:1 (1916).
11. R.H. Ewell and H. Eyring, "Theory of the viscosity of liquids as a function of temperature and pressure," *J. Chem. Phys.* 5:726 (1937).
12. A.J. Batschinski, "Untersucungen über die innere reibung der flüssigkeiten, I (Investigations on the internal friction of the liquids, I)," *Zeitschrift fur Physickalische Chemie* 84:643 (1913).
13. A.K. Doolittle, "Newtonian flow. II. The dependence of the viscosity of liquids on free space," *J. Applied Physics* 22:1471 (1951).
14. A.K. Doolittle, "Newtonian flow. III. The dependence of the viscosity of liquids on molecular weight and free space (in homologous series)," *J. Applied Physics* 23:236 (1952).
15. A.K. Doolittle, "Newtonian flow. V. Further verification of the free-space viscosity equation," *J. Applied Physics* 28:901 (1957).

16. M.L. Williams, R.F. Landel, and J.D. Ferry, "The temperature dependence of relaxation mechanisms in amorphous polymers and other glass-forming liquids," *J. American Chemical Society* 77:3701 (1955).

17. P.W. Bridgman, *The Physics of High Pressure*, Dover Publications, New York, 1931.

18. Von K.H. Hellwege, W. Knappe, F. Paul, and V. Semjonow, "Pressure-dependence of the viscosity of some polystyrene melts," *Rhol. Acta* 6:165 (1967).

19. A.J. Matheson, "Role of free volume in the pressure dependence of the viscosity of liquids," *J. Chem. Phys.* 44:695 (1966).

20. J.D. Ferry, "Mechanical properties of substances of high molecular weight. VI. Dispersion in concentrated polymer solutions and its dependence on temperature and concentration," *J. of the Am. Chem. Soc.*, 72:3746 (1950).

21. S.L. Rosen, *Fundamental Principles of Polymeric Materials*, 2nd Ed., New York, John Wiley & Sons, Inc., 1993.

22. J.M. Dealy and K.F. Wissbrun, *Melt Rheology and Its Role in Plastics Processing*, Chapman and Hall, London, 1995.

23. R.E. Larson and R.P. Hostetler, *Precalculus: A graphing Approach*, D.C. Heath and Company, Lexington, 1993.